Advances in Civil Engineering

Construction and Management of Urban Rail Transit Systems

Lead Guest Editor: Yuan Mei
Guest Editors: Jian Xu, Song-He Wang, and Annan Zhou

Construction and Management of Urban Rail Transit Systems

Advances in Civil Engineering

Construction and Management of Urban Rail Transit Systems

Lead Guest Editor: Yuan Mei
Guest Editors: Jian Xu, Song-He Wang, and Annan Zhou

Contents

Hindawi
Advances in Civil Engineering
Volume 2022, Article ID 9359268, 8 pages
https://doi.org/10.1155/2022/9359268

Research Article

Research on the Method of Ground Stress Balance under Complex Conditions Based on Geometric Tracing

Ge Wang

Xi'an Traffic Engineering Institute, Xi'an 710300, Shaanxi, China

Correspondence should be addressed to Ge Wang; wanggeaza@163.com

Received 24 February 2022; Revised 26 March 2022; Accepted 7 April 2022; Published 14 May 2022

Academic Editor: Yuan Mei

The accuracy of the initial ground stress balance determines the accuracy of the finite element analysis of geotechnical problems. The traditional ground stress balance method has a good balance effect for simple geotechnical models but has strong limitations when the structure and soil interact with each other, the geometry of the model is complex, or the constraints are complicated. To deal with such problems, this paper proposes a general ground stress balance method based on geometric tracing by iteratively superimposing the static displacement field of the numerical model with the initial node coordinates of the numerical model. Two commonly used methods as well as the proposed method were tested with a model which contains both soil elements and structural elements and a case study. Test results show that the proposed method is capable of dealing with a complex model in which the commonly used methods fail to. Furthermore, the proposed ground stress balance method was demonstrated to be clear and has rapid convergence and high accuracy for complex stratum-structure geotechnical problems.

1. Introduction

Ground stress is the natural stress that exists in the Earth's crust undisturbed by engineering, also known as the geostatic stress, absolute stress or original rock, and soil stress, which is the fundamental force that causes the deformation and damage of underground engineering [1–4]. Therefore, in the numerical simulation process involving geotechnical materials, the ground stress balance should usually be performed on the finite element numerical model first. The purpose of ground stress balance is to find the ground stress field that can make the initial displacement field close to zero under the action of initial load and boundary conditions [5–7]. The accuracy of the ground stress balance process determines the accuracy of numerical simulation results.

The commonly used ground stress balance techniques include the automatic method, keyword definition method, ODB import method, and nodal force method. The pros and cons of each method are clear [8, 9]. Using these methods or their variants, scholars have conducted a lot of fundamental research. Wang et al. [10] proposed a method for stratum-structure geotechnical problems, which is applicable to the problems that have a contact feature. Zavriyan [11] derived a theoretical formulation for the initial stress of rod element in ground stress analysis. He et al. [12] and Xiao et al. [13] use the element birth and death technique to achieve ground stress balance in ABAQUS, which effectively alleviates the convergence difficulties of the ground stress balance problem. Xu [14] proposed a method by applying nodal loads directly to the finite element model. Guo [15] carried out a finite element analysis of the ground stress field process with stress concentration problem. Yu et al. [16] established a convenient superposition model that can be used to simulate the stress and displacement fields around cracks. Fu et al. [17], Zhang et al. [18], Xie et al. [19], and Meng et al. [20] performed regression inversion analysis of the ground stress field for different types of models. The above studies on the ground stress balance are mostly dealing with simple models, and the application of their methods is limited. When the interaction between structures and soil is involved or the constraints are complex, the existing methods often fail to work or have low accuracy [21].

To address the above-mentioned problem, this paper discards the conventional idea of adding a stress field to the

model or applying nodal force to mesh nodes and proposes a more general method based on geometric tracing to quickly achieve ground stress balance for complex finite element models. The basic idea of this method is that the displacement field after the static analysis of the numerical model is superimposed with the initial node coordinates of the numerical model and reconstructed the model iteratively until it meets the citation, so as to achieve the purpose of setting the displacement field to zero. The proposed method can avoid the failure of ground stress balance due to the difficulties of too many structures and complex interactions in the model, since it only reconstructs the node coordinates and did not change the original stress field.

2. Analysis of Commonly Used Ground Stress Balance Methods

In ABAQUS, four types of ground stress balance methods are often used, including the automatic method, keyword definition method, ODB import method, and nodal force method. For the numerical model with few materials and simple boundary conditions, the calculation results of all four methods can meet the requirements. Among them, the results obtained by the automatic method are the most ideal and should be preferred when available [22]. In practical engineering, structures such as underground diaphragm walls or buildings coexisting with foundations are often involved and interact with the soil foundation. These problems can be collectively referred to as stratum-structure geotechnical problems [23], for which commonly used methods are often unable to converge or have poor balance results. [24].

To demonstrate stratum-structure geotechnical problems, a ABAQUS model is established as shown in Figure 1. The basic size of the foundation is $50\,\text{m} \times 50\,\text{m} \times 50\,\text{m}$ ($X \times Y \times Z$). The foundation material is clay. A concrete frame structure is set on the foundation. The foundation soil adopts the elastic-plasticity model using the Mohr-Coulomb yield criterion, while the concrete adopts the linear elasticity model. The material parameters are shown in Table 1. The frame structure is bound with the foundation using TIE constraints in ABAQUS, so that the upper surface of the foundation is fully coupled with the frame structure in all degrees of freedom (fully constrained displacement in x, y, and z directions). Normal displacement at the sides of the soil cube is constrained, while the bottom has pined. The automatic method and the ODB import method were used to perform the ground stress balance for the established model since these two methods have been proved to be the most effective and adaptive.

According to the test results, the automatic method fails to converge during the calculation because of the complexity of the model. Figures 2 and 3 show the calculation results of the ODB method in the static analysis stage and the ground stress balance stage, respectively. Figure 4 shows the relationship curve between the iteratively import times and the maximum absolute displacement.

It can be seen from Figures 2 and 3 that the maximum absolute value of displacement of the result of the import

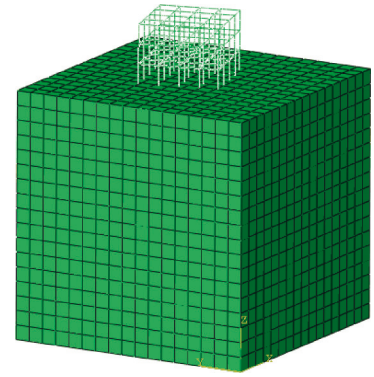

Figure 1: Finite element model of a stratum-structure geotechnical problem.

method is $3.9 \times 10^{-4}\,\text{m}$, which is barely acceptable. But the stress results changed dramatically before and after the balance process. This happens because the concept of the ODB import method is to apply the initial load and boundary conditions to the model, obtain the stress field through static analysis, and import the obtained stress field into the ground stress balance process as the initial stress field with one or more iterations. This process may constantly alter the initial stress state of the model, which is contrary to the original purpose of ground stress balance and affects the accuracy of subsequent calculations of the model. From Figure 4, it can be seen that with the increase in the number of ODB import, the absolute value of the maximum displacement of the model decreases rapidly before 15 times, changes slowly afterwards, and tends to converge at $3.9 \times 10^{-4}\,\text{m}$ at the 35th iteration. This phenomenon shows that the ODB import method may converge at a nonzero value of the maximum absolute value of displacement. After certain iteration times, the results may not become better afterwards, which makes the method very tedious and has strong limitations.

3. Ground Stress Balance Method Based on Geometric Tracing

3.1. Steps of the Proposed Method. When dealing with geotechnical engineering problems in ABAQUS, there are often cases where soil and structures exist at the same time and interact with each other, such as the foundation excavation deformation analysis, pile-soil interaction analysis, and simulation of tunneling under existing buildings [25]. For these so-called stratum-structure geotechnical problems, the existing commonly used ground stress balance methods may converge slowly or even unable to converge. Traditional methods usually use external loads or add stress fields to the numerical model in the ground stress balance process [15]. Therefore, they can handle simple problems because the stress field is simple and can converge easily. But when the model is complex, the stress field will be complex too, and convergence problem may take place.

Considering the above shortage of the traditional methods, we discard the stress-based concept and proposed a ground stress balance method based on geometric tracing,

Table 1: Material parameters of the numerical model.

Materials	Modulus of elasticity (kPa)	Poisson's ratio	Cohesion (kPa)	Angle of friction (°)	Gravity load (kN/m^3)
Clay	1.5×10^4	0.3	32	14	20
Concrete	3.15×10^7	0.2	—	—	25

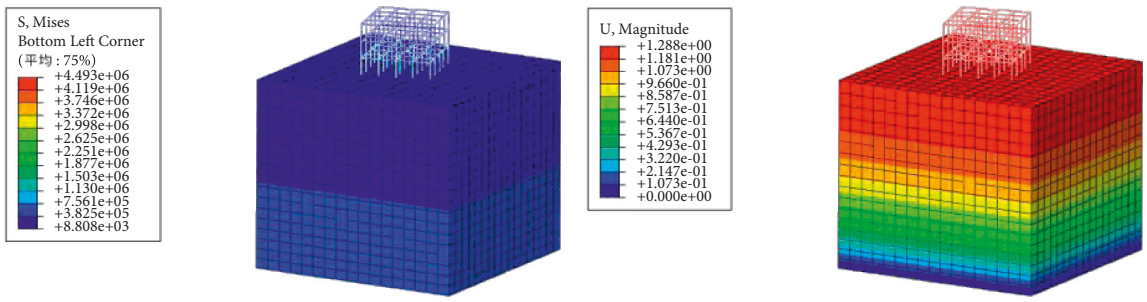

Figure 2: Calculated results of static analysis of the stratum-structural model. (a) Stress nephogram. (b) Displacement nephogram.

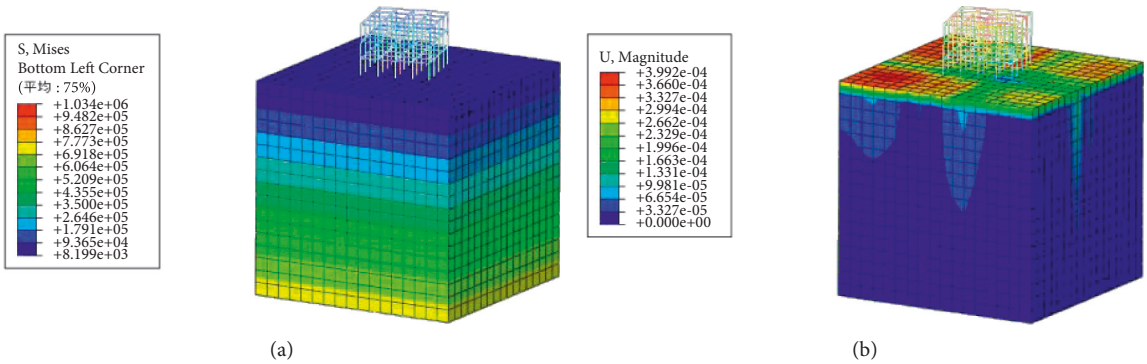

Figure 3: Ground stress balance calculation results of the stratum-structural model using ODB import method. (a) Stress nephogram. (b) Displacement nephogram.

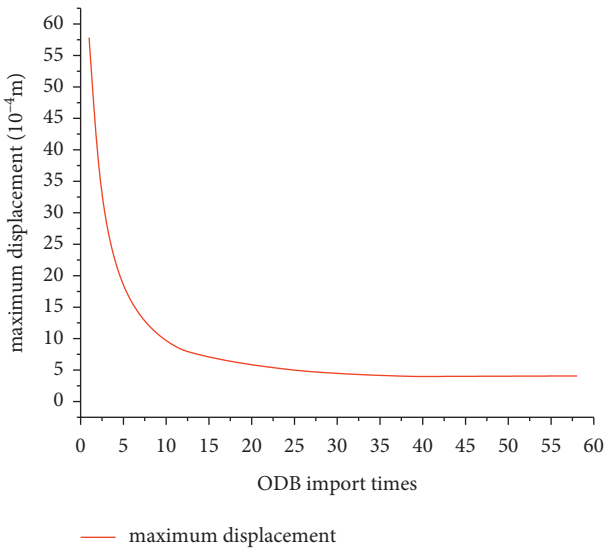

Figure 4: Import times-maximum displacement curve.

in which the position coordinates of the nodes in the model change iteratively which will be referred to as the reconstruction process since the model is altered after each iteration. After a few iterations, the model would be different from the original one since the node coordinates have been altered. By adding loads and boundary conditions, the model will deform to a state that is similar to the original model. When the deformation difference between nodes is small enough, the ground stress balance can be considered established. The proposed method generated the initial ground stress of the model without changing the stress field of the model and can better simulate the initial stress state of the finite element model even though the model is complex. The proposed method is demonstrated based on FEM software ABAQUS, but the concept can be used for any other software. Specific steps of the method are as follows .

Step 1. Using ABAQUS to establish the geometric model of the engineering structure. Apply loads and boundary conditions to the numerical model. Then, run a static analysis to obtain the displacement field of

the model. Meanwhile, record the initial position coordinates of all nodes as L_i^j from the INP file of the numerical model.

$$L_i^j = \left(l_{ix}^j, l_{iy}^j, l_{iz}^j\right), \quad i = 0, 1, 2, \ldots, N;\ j = 0, 1, 2, \ldots, M, \tag{1}$$

where L_i^j is the position coordinates sequence of the the i-th node in j-th iteration of the reconstruction. l_{ix}^j, l_{iy}^j, and l_{iz}^j are the coordinate of x, y, and z, respectively. N is the total number of nodes in the numerical model. M is the total number of iterative reconstructions.

Step 2. The displacement fields result from the static analysis of the numerical model, which is extracted to obtain the displacement vector sequences of all nodes in the numerical model. The expressions of the displacement vector sequences of all nodes in the numerical model are

$$V_i^j = \left(v_{ix}^j, v_{iy}^j, v_{iz}^j\right), \quad i = 0, 1, 2, \ldots, N;\ j = 0, 1, 2, \ldots, M, \tag{2}$$

where V_i^j is the displacement vector of the i-th node in j-th iteration of the reconstruction. v_{ix}^j, v_{iy}^j, and v_{iz}^j are the displacement vector sequence of x, y, and z, respectively.

Step 3. Determine whether the maximum absolute value of the displacement of all nodes satisfies the preset convergence condition, if it does, the ground stress balance process stops and returns the stress field, and if not, proceed to step4. The maximum absolute value of the displacement of all nodes can be calculated by the following equation:

$$\begin{aligned} &\max\left(\left|L_i^j + V_i^j - L_i^0\right|\right) \\ &= \max \\ &\left(\sqrt{\left(l_{ix}^j + v_{ix}^j - l_{ix}^0\right)^2 + \left(l_{iy}^j + v_{iy}^j - l_{iy}^0\right)^2 + \left(l_{iz}^j + v_{iz}^j - l_{iz}^0\right)^2}\right), \end{aligned} \tag{3}$$

where $\max(|L_i{}^j + V_i{}^j - L_i{}^0|)$ is the maximum absolute value of the displacement of all nodes in the numerical model after the j-th iteration of reconstruction of the numerical model. $L_i{}^0$ is the vector of initial position coordinates of the i-th node in the numerical model. l_{ix}^0, l_{iy}^0, and l_{iz}^0 are the i initial value of x, y, and z of the coordinates of node i. It is generally considered that when the order of stress before and after balance remains unchanged, and the soil displacement is below 10^{-4} m, the ground stress balance process can be considered acceptable and will not have an impact on the subsequent analysis. This is because the effective displacement caused by foundation excavation, and tunneling construction is usually above 10^{-3} m. Therefore, the preset convergence condition of this method is set to

$$\max\left(\left|L_i^j + V_i^j - L_i^0\right|\right) \le 10^{-4}. \tag{4}$$

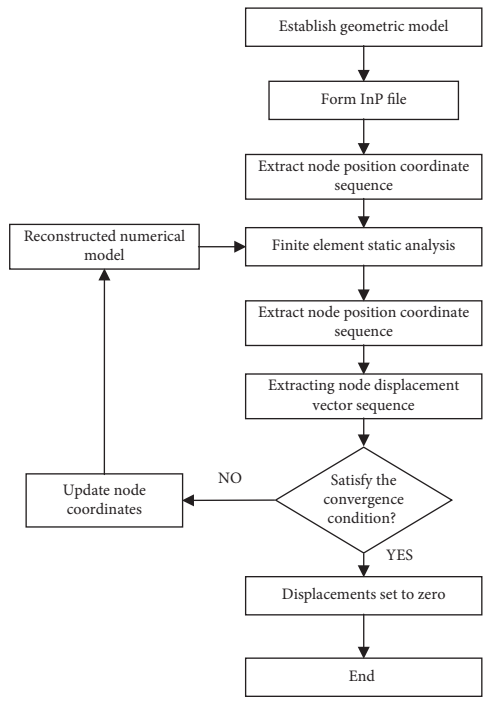

Figure 5: Ground stress balance process.

Step 4. The displacement vector of all nodes in step 2 is then superimposed backwards with the corresponding node position coordinate in step1, using the following equation:

$$L_i^{j+1} = L_i^j - V_i^{j-1}, \tag{5}$$

where L_i^{j+1} is the position coordinates sequence of the i-th node in $j+1$-th iteration of the reconstruction. $V_i{}^{j-1}$ is displacement vector of the i-th node in $j-1$-th iteration of the reconstruction.

After the superposition, the nodes of the numerical model are reconstructed to obtain a new numerical model. The static analysis of the reconstructed numerical model is carried out to obtain the displacement field of the reconstructed numerical model. Meanwhile, the loads and boundary conditions applied to the reconstructed numerical model were kept unchanged [5–7] for each iteration of the static analysis process.

Step 5. Repeat Step 4 until the maximum absolute value of the displacement of all nodes in the reconstructed numerical model satisfies the preset convergence condition. Then, the results of the last iteration were obtained as the result of the ground stress balance process.

It should be noted that the proposed method extracts the node coordinates and node displacements from the model INP file and the model result ODB file directly, forms the new node coordinates after backwards superposition, and then replaces the node coordinates in the INP file of the former model to generate the new model during iteration. Therefore, the accuracy of the ground stress balance process of the proposed method

algorithm 1 Geometric tracing" geostatic stress field procedure for complex model

Input: Numerical model for initial in-situ stress balance;

Output: Numerical model meeting the requirements of initial in-situ stress balance;

function MERGERSORT($Array, left, right$)
  Conventional static analysis of the initial numerical model;
  for $j = 0$ to M **do**
    Accessing model data in model InP file $(modeldata)$ Get node coordinates;
    SET:$L_i^j = (l_{ix}^j, l_{iy}^j, l_{iz}^j) \leftarrow iisthenumberofmodelnodes$
    Accessing the result data in the model ODB file$(resultdata)$The displacement field is obtained;
    SET:$V_i^j = (v_{ix}^j, v_{iy}^j, v_{iz}^j) \leftarrow iisthenumberofmodelnodes$
    $max\ (|L_i^j + V_i^j - L_i^0|) = max\ (\sqrt{((l_{ix}^j + v_{ix}^j - l_{ix}^0)^2 + (l_{iy}^j + v_{iy}^j - l_{iy}^0)^2 + (l_{iz}^j + v_{iz}^j - l_{iz}^0)^2)})$;
    if $max\ (|L_i^j + V_i^j - L_i^0|) < 10^{-4}$ **then**
      Numerical model after balance completion and output balance
    else
      The numerical model is reconstructed
      $L_i^{j+1} = L_i^0 - V_i^{j-1}$
      $L_i^{j+1} \leftarrow \mathrm{INP}_{j+1}$
    end if
    Importing INP_{j+1} in ABAQUS

Figure 6: Pseudocode of the proposed method.

will not be affected regardless of the complexity of the boundary conditions or load conditions of the numerical model, and thus, the noncoverage or low efficacy problems were addressed.

Step 6. The final step is to set the displacement field of the result in Step 5 to zero so that the geotechnical engineering simulation can proceed. Figure 5 shows the flow chart of the proposed method.

3.2. Method Implementation. The proposed method is codified through the Python interface provided by ABAQUS, so that after the model is built, the Python script can be used to complete the ground stress balance process, which greatly improves the work efficiency. [26–28] In order to achieve the aforementioned ground stress balance, we first need to export the coordinates of each node of the initial numerical model by accessing the model data generated by ABAQUS, that is, the INP file. The ODB file of the first static analysis was accessed to record displacement field data of all nodes. Then, equation (4) will be calculated to determine whether the process stops. If the coverage citation is not met, the backwards superimpose will be carried out to form a new geometry model in ABAQUS and run the next round of iterations until the coverage citation is met.

The above calculation process is placed in a for loop statement that breaks only when (4) is satisfied. Thus, the ground stress balance process was carried out in an iterative way. Figure 6 shows the pseudocode of the algorithm [29].

4. Case Study

In the simulation of geotechnical engineering problems, there are often cases where soil and structures exist simultaneously and interact with each other, such as the analysis of foundation excavation [29], the pile-soil interaction simulation, and the tunneling construction under existing buildings [30], which usually contain complex soil layer forms and stratigraphic parameters. In order to verify the effectiveness and superiority of the proposed method, the ground stress balance process of the following simulation of the tunneling construction under the existing building will be carried out in ABAQUS.

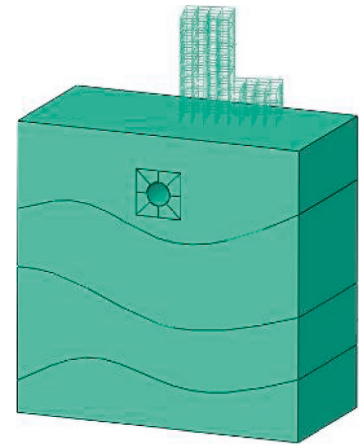

Figure 7: Schematic diagram of finite element model.

The geometry of the model is shown in Figure 7. The ideal elastoplastic model with Mohr-coulomb yield criterion and elastic model were used for the soil layers and the structure, respectively. The dimensions of the foundation model are 100 m × 50 m × 100 m. The soil foundation contains silty clay, silty sand, sandy soil, and moderately weathered sandstone from top to bottom. The diameter and thickness of the tunnel are 8 m and 0.15 m, respectively. The buried depth of the tunnel is 15 m. Above the foundation is a building that has a 15° angle with the tunnel direction. The building structure and foundation are bound by tie constraints. The bottom of the model is fully constrained (x, y, and z directions), while the normal displacement is constrained for four sides. The finite element model is shown in Figure 7, and the material parameters are shown in Table 2.

Table 2: Model material property parameters.

Materials	Modulus of elasticity (kPa)	Poisson's ratio	Cohesion	Angle of friction (°)	Gravity (kN/m^3)
Powdered clay	1.5×10^4	0.3	32	14	20
Powdered sand	1.8×10^4	0.35	35	16	21
Sandy soil	2.0×10^4	0.35	36	20	23
Mesothermal sandstone	1.0×10^6	0.2	70	35	24
Concrete	3.15×10^7	0.2	—	—	25

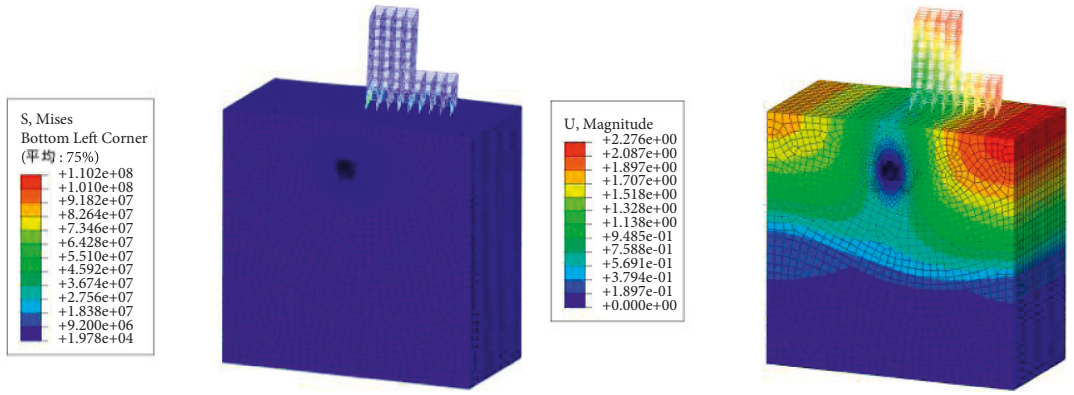

Figure 8: First static analysis results of the tunneling model. (a) Stress cloud diagram. (b) Displacement cloud map.

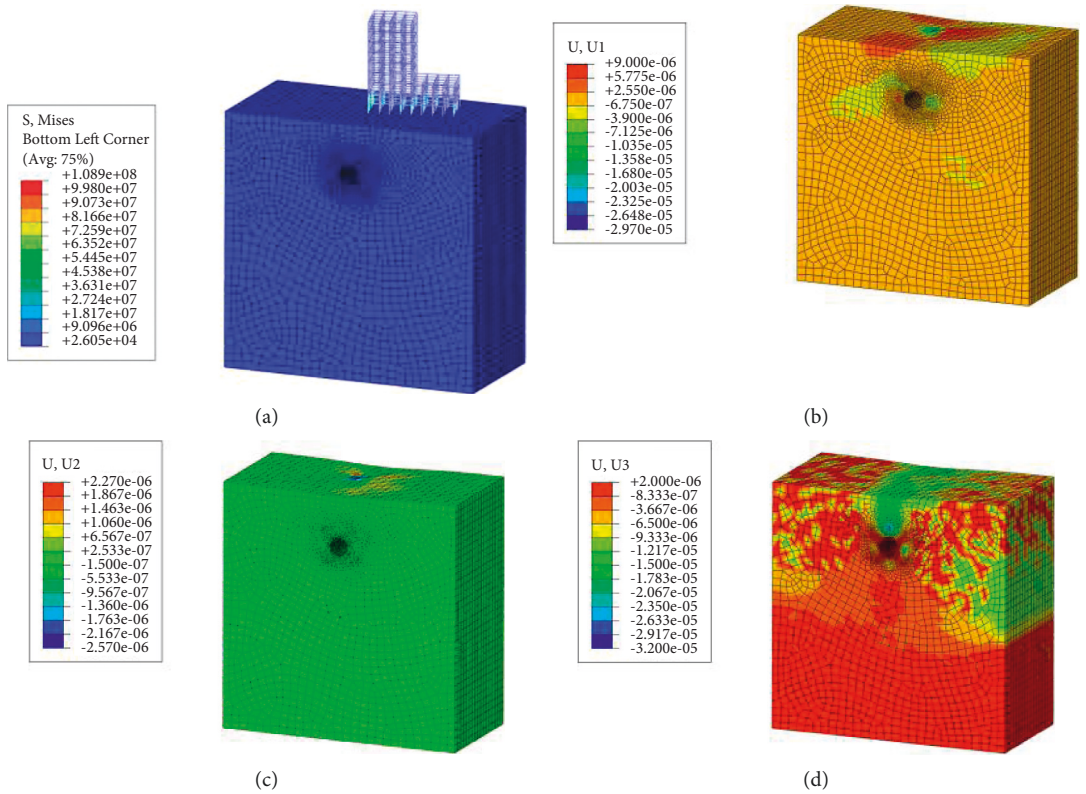

Figure 9: Calculated results of the tunneling model. (a) Stress cloud diagram. (b) x-direction displacement. (c) y-direction displacement. (d) z-direction displacement.

The results of the first static analysis of the model are shown in Figure 8. The ground stress balance result using the proposed method in this paper based on geometric tracing is applied to the model, and the calculation results are shown in Figure 9. For simplicity of observing the effect of ground stress balance, the upper frame is hidden.

It can be seen from Figures 8 and 9 that after applying the proposed ground stress balance method to the model, the displacements of the model are kept in the order of 1×10^{-6} m, and the stress results are similar to those of static analysis, without obvious stress concentration and stress shift. It was proved that the ground stress balance method based on geometric tracing proposed in this paper is clear, converges fast, has high accuracy, and can better meet the requirements of ground stress balance for complex models.

5. Conclusion

(1) This paper studied the adaptiveness of the commonly used ground stress balance method, that is, the ODB import method and the automatic method, for the stratum-structure geotechnical problems. Analysis results show that the automatic method fails to coverage. For the ODB import method, as the iteration increases, the maximum displacement of the model will converge to a certain value and will no longer decrease. The converge speed and the accuracy are both low.

(2) Based on the analysis of the commonly used method, this paper proposed a general ground stress balance method based on the concept of geometric tracing which iteratively reconstructs the model according to the displacement field results of the static analysis and the node coordinates of the numerical model.

(3) A case study was carried out to test the performance of the proposed method. Test results show that the proposed method is capable of dealing with the stratum-structure geotechnical problems with complex geometry efficiently.

There are also some limitations in the paper that should be addressed or discussed in the future.

(i) The proposed method has not been applied to a constitutive model other than the elastic-plasticity model using the Mohr-Coulomb yield criterion. The adaptiveness of the method should be further investigated.

(ii) Structures such as existing buildings may also be affected by the method. This issue should be addressed in the future.

Data Availability

The data used to support the findings of this study are available from the first author upon request.

Conflicts of Interest

The authors declare that there are no conflicts of interest regarding the publication of this paper.

References

[1] M. F. Cai, *Principles and Techniques of Ground Stress Measurement*, Science Press, Beijing, China, 1995.

[2] D. Jianju, Q. Xianghui, Z. Qingli, L. Zhang, and Q. Chen, "Estimation of the present-day stress field using in-situ stress measurements in the Alxa area, Inner Mongolia for China's HLW disposal," *Engineering Geology*, vol. 220, 2017.

[3] J. A. Hudson, F. Cornet, and R. Christiansson, "Methods for rock stress estimation-Part 1: strategy for rock stress estimation," *International Journal of Rock Mechanics and Mining Sciences*, vol. 40, no. 7, 2003.

[4] Y. Shuxin, H. Luyuan, X. Furen, and C. Xiaofeng, "Quantitative analysis of the shallow crustal tectonic stress field in mainland China based on in situ stress data," *Journal of Asian Earth Sciences*, vol. 85, 2014.

[5] M. X. Hou and X. R. Ge, "Research on the method of analyzing the initial ground stress field of rock masses," *Geotechnical Mechanics*, vol. 13, no. 8, pp. 1626–1630, 2007.

[6] K. Matsuki, S. Nakama and T. Sato, Estimation of regional stress by FEM for a heterogeneous rock mass with a large fault," *International Journal of Rock Mechanics and Mining Sciences*, vol. 46, no. 1, 2009.

[7] S. Ove and Z. Arno, "ISRM suggested methods for rock stress estimation-Part 5:establishing a model for the in situ stress at a given site," *Rock Mechanics and Rock Engineering*, vol. 45, no. 6, 2012.

[8] C. M. Hu, Y. L. Yuan, and Y. Mei, "Research on ground stress balance method based on ABAQUS stratigraphic-structural method model," *Modern Tunneling Technology*, vol. 55, no. 04, pp. 76–86, 2018.

[9] R. Dai, Z. Li, and J. Wang, "Research on the initial ground stress balance method based on ABAQUS," *Journal of Chongqing University of Technology and Business (Natural Science Edition)*, vol. 29, no. 09, pp. 76–81, 2012.

[10] X. Wang, Y. Yuan, C. Hu, and Y. Mei, "Research on the geostatic stress field procedure under complex conditions," *Advances in Civil Engineering*, vol. 2021, Article ID 6674369, 15 pages, 2021.

[11] E. G. Zavriyan, "Determination of the initial stresses in mine working supports by the relief method," *Soviet Mining Science*, vol. 6, no. 5, pp. 589-590, 1970.

[12] L.-L. He, R. Jia, and Y. Jiao, "Research on automatic ground stress balance method for port structure calculation model based on ABAQUS," *Water Transport Engineering*, vol. 55, no. 11, pp. 178–185, 2021.

[13] G. Xiao, S. Ma, and Y. Liu, "Research on equilibrium ground stress method based on ABAQUS raw and dead unit technology," *Journal of Water Resources and Construction Engineering*, vol. 19, no. 04, pp. 47–52, 2021.

[14] L. Xu, "A general method for achieving accurate equilibrium of complex initial ground stress fields," *Journal of Three Gorges University (Natural Science Edition)*, vol. 34, no. 03, pp. 30–33, 2012.

[15] Y. H. Guo, W. S. Zhu, and X. P. Li, "An improved initial ground stress field regression method based on FLAC~(3D)," *Journal of Geotechnical Engineering*, vol. 36, no. 05, pp. 892–898, 2014.

[16] P. Yu, L. Yongming, and Z. Jinzhou, "A novel approach to simulate the stress and displacement fields induced by hydraulic fractures under arbitrarily distributed inner pressure," *Journal of Natural Gas Science and Engineering*, vol. 35, 2016.

[17] C. Fu, W. Wang, and S. Chen, "Study on the inversion analysis of the initial ground stress field in the dam area of Xiluodu Hydropower Station," *Journal of Rock Mechanics and Engineering*, vol. 25, no. 11, pp. 2305–2312, 2006.

[18] J. G. Zhang, Q. Y. Zhang, and W. D. Yang, "Inverse analysis of the initial ground stress field in the dam area of Dagangshan

Hydropower Station," *Geotechnics*, vol. 30, no. 10, pp. 3071–3078, 2009.

[19] H. Xie, J. He, and M. Xiao, "Regression inversion analysis of three-dimensional ground stress field in a large hydropower plant," *Geotechnics*, vol. 30, no. 08, pp. 2471–2476, 2009.

[20] W. Meng, C. He, and J. Zhang, "Inverse analysis of initial ground stress field of rock masses under high ground temperature and high ground stress," *Journal of Rock Mechanics and Engineering*, vol. 39, no. 04, pp. 749–760, 2020.

[21] M. Wei and H. Chuan, "Back analysis of the initial geo-stress field of rock masses in high geo-temperature and high geo-stress," *Energies*, vol. 13, no. 2, 2020.

[22] J. Y. Yang, J. B. Lei, and Y. Q. Zou, "An analysis of the initial ground stress balance method of composite foundation with cap pile based on ABAQUS," *Journal of Nanchang Aviation University (Natural Science Edition)*, vol. 31, no. 04, pp. 73–78, 2017.

[23] W. Q. Ding, L. Zhu, and Y. C. Peng, "3D numerical analysis of immersed tube tunnel based on stratigraphic-structural method," *Journal of Geotechnical Engineering*, vol. 35, no. S2, pp. 622–626, 2013.

[24] I. L. Pan Kov, "Physical simulation and theoretical estimate of gravity-induced horizontal stress in rocks," *Journal of Mining Science*, vol. 52, no. 5, pp. 892–898, 2016.

[25] L. Qingbin, L. Jiang, and L. Jie, "ParaView visualization of Abaqus output on the mechanical deformation of complex microstructures," *Computers & Geosciences*, vol. 99, 2017.

[26] B.-B. Ren, L.-J. Su, and C.-L. Zhang, "Development of automated algorithms for slope reliability calculation based on Python language and Abaqus platform," *Journal of Civil & Environmental Engineering*, vol. 41, no. 05, pp. 67–72, 2019.

[27] X. Cui, X. Han, S. Duan, and G. R. Liu, "An ABAQUS implementation of the cell-based smoothed finite element method (CS-FEM)," *International Journal of Computational Methods*, vol. 17, no. 02, 2020.

[28] J. Q. Zhang, Y. M. Mou, and C. H. Zhang, "A control flow-based approach to analyze the consistency of software design and implementation," *Computer Applications*, vol. 40, no. 10, pp. 3025–3033, 2020.

[29] J. Q. Zhang, Y. M. Mou, and C. H. Zhang, "Research on deformation law of deep foundation pit of station in core region of saturated soft loess based on monitoring," *Advances in Civil Engineering*, vol. 202216 pages, Article ID 848152, 2022.

[30] X. Y. Wang, Z. Ma, and Y. T. Zhang, "Research on safety early warning standard of large-scale underground utility tunnel in ground fissure active period," *Frontiers of Earth Science*, vol. 10, no. 9, Article ID 828477, 2022.

Hindawi
Advances in Civil Engineering
Volume 2022, Article ID 3268150, 12 pages
https://doi.org/10.1155/2022/3268150

Research Article

Quantitative Evaluation of the Adaptability of the Shield Machine Based on the Analytic Hierarchy Process (AHP) and Fuzzy Analytic Hierarchy Process (FAHP)

Jiangsheng Xie,[1] Bo Liu ,[1,2] Lu He,[3] Weiling Zhong,[1] Haiqing Zhao,[1] Xingzhi Yang,[1] and Tianrui Mai[3]

[1]*China Railway 20th Bureau Group Co. Ltd., Xi'an, Shaanxi 710016, China*
[2]*Post-doctoral Research Workstation, China Railway 20th Bureau Group Co. Ltd., Xi'an, Shaanxi 710016, China*
[3]*Shaanxi Metallurgical Design & Research Institute Co., Ltd., Xi'an, Shaanxi 710018, China*

Correspondence should be addressed to Bo Liu; liubo208@xauat.edu.cn

Received 18 January 2022; Revised 9 March 2022; Accepted 15 April 2022; Published 10 May 2022

Academic Editor: Qian Chen

Tunnel engineering based on the shield method is an extremely complex project. During the construction process, many uncertain factors are often faced, which makes it difficult to effectively and quantitatively evaluate the effectiveness of the shield machine. To solve this problem, this paper proposes an adaptability evaluation method for shield machines based on the fuzzy analytic hierarchy process (FAHP) and analytic hierarchy process (AHP). First, the selection and equipment matching of Earth pressure balance shield machines in the shield interval between Tashuiqiao Station and Erxianqiao Station of Chengdu Metro Line 17 are introduced. Then, using APH for screening, the final evaluation indices of the adaptability of the shield machines in this project are determined. Next, referring to the existing research results and fuzzy mathematics method, the membership function of the evaluation indices and adaptability evaluation model of the shield machine are constructed. Finally, the rationality and accuracy of the fuzzy comprehensive evaluation model of shield adaptability are verified through onsite shield construction, and the evaluation results are consistent with the actual situation.

1. Introduction

In recent years, with the growth of the urban population and continuous expansion of the urban scale, urban development has gradually shifted to underground space development [1–5]. The forms of underground space utilization include underground parking lots, underground shopping malls, underground drainage pipelines, underground railways, etc [6–8]. As an emerging public transportation mode, subways have the advantages of large transportation capacity and fast speed. Since subways can effectively relieve the pressure of ground transportation, they have been incorporated into the construction planning of increasingly many cities. The construction methods of subway tunnels mainly include the open-cut method, sallow buried-tunnelling method, and shield method [9]. Due to its safety, efficiency, convenient construction, and low impact on the surrounding strata and the environment, the shield method has become the main method to build urban subway tunnels. Selecting a suitable shield machine is a key step in shield construction. If the machine type is not suitable, it can cause major delays and injury to shield drivers and ultimately may stop the project. In addition, it is necessary to analyse the adaptability of shield machines by adopting a reasonable method to ensure safe and smooth construction [10, 11].

Adaptability refers to the ability to adapt to different internal and external environments and objective conditions [12–14]. The system is composed of several different and related factors and can realize an organic collection with certain functions. When an important factor in the system changes, it will be directly affected and restricted by other factors in the system and affect other factors. Therefore, to maintain the overall function of the system, important factors must adapt to one another. To perform the adaptability evaluation, the evaluation index system must be determined

first. The evaluation index system depends on the evaluation object. Generally, when establishing an index system that can be used for adaptability evaluation, the principles of hierarchy, validity, and simplicity should be followed.

The selection of an inappropriate shield machine will lead to low construction efficiency and abnormal phenomena such as downtime during construction and difficulty in excavation. Many scholars have performed a series of studies on the qualitative evaluation of shield machines. Rengshausen et al. [15] discussed the advantages and disadvantages of a TBM-S with Earth pressure balanced face support (EPB-TBM) and a TBM-S with slurry face support (Mix-Shield TBM) for the C310 Thames Tunnels after the contract award and a comparative risk assessment. Song et al. [16] studied the adaptability of the soil pressure balance shield in the expansive clay stratum for Xuzhou metro urban rail transit line 2, and they proposed the targeted design of the shield selection and the selection of excavation parameters. Edalat et al. [17] introduced the process of choosing tunnel boring machines for Tabriz urban railway line 2 using the multicriteria analysis method and identified some technical, economical, and environmental parameters that affected the tunnel boring machines type. Considering the disintegration of fines from cohesive soil within free water, such as slurry, Hollmann et al. [18] proposed an assessment method of logging in mechanised tunneling. Hyun et al. [19] discussed the potential risk of undesirable events that occurred during tunneling with the application of a shield tunnel boring machine. Based on the numerical computations results, Ramoni and Anagnostou [20] investigated the problem of shield jamming and analysed the effects of possible countermeasures. Based on the TOPSIS method, Wu et al. [21] carried out a study on the shield selection for subway construction and selected Wuhan Rail Transit Line 2 for example analysis to verify the feasibility of the method. Huang et al. [22] applied the statistical analysis method to the shield selection for Chengdu Metro Line 18. However, these studies mostly use qualitative methods for analysis. The adaptability analysis of a shield machine does not the link one phenomenon to another but comprehensively considers various uncertainty indices. Therefore, it is urgent to seek a quantitative evaluation method of the adaptability of the shield machine.

In this paper, the adaptability of the shield machine in the shield interval between Tashuiqiao Station and Erxianqiao Station of Chengdu Metro Line 17 is analysed by combining the fuzzy analytic hierarchy process (FAHP) and the analytic hierarchy process (AHP). Based on the analysis of the adaptability evaluation indices of the shield machine and the determination of the membership function of the evaluation indices, a quantitative evaluation model for the adaptability of the shield machine is constructed. The quantitative evaluation method of the proposed shield machine adaptability in this paper can improve the reliability and scientificity of evaluation results.

2. Project Overview

2.1. Project Introduction. The shield interval between Tashuiqiao Station and Erxianqiao Station (TS-ES) of Chengdu Rail Transit Line 17 is located in the third section of Jianshe North Road, Chenghua District, Chengdu, between the Second Ring Road and the Middle Ring Road. Figure 1 shows the plane position of the tunnels in the TS-ES section. The TS-ES section contains two shield tunnels: the left and right lines from Tashuiqiao Station to Erxianqiao Station. The demarcation mileage of the right-line tunnel in the TS-ES section is YDK92 + 649.748~YDK94 + 345.700, with a total length of 1696.391 m (the long chain is 0.439 m). The demarcation mileage of the left-line tunnel in the TS-ES section is ZDK92 + 649.749~ZDK94 + 345.700, with a total length of 1691.308 m (the short chain is 4.643 m). The buried depth of the interval tunnel is 19.9~30 m, and the minimum horizontal curve radius and vertical curve radius of the line are 450 m and 5000 m, respectively. The TS-ES shield section starts by airlifting in the undercut section of the tunnel and traverses many major risk sources, including the existing buildings and pipelines. Due to the poor geological self-stability of shield tunnels, the excavation surface easily overdig, which results in excessive surface settlement, cracks, and even ground collapse. The shield construction of this project has great risk.

The TS-ES shield section adopts prefabricated circular reinforced concrete segments. The inner diameter and outer diameter of the circular segment are 7500 mm and 8300 mm, respectively, and the circular segment is 400 mm thick. The concrete strength grade for circular segments is C50, and the impermeability grade is P12. The circular segment adopts a three-part staggered assembly mode of a standard lining ring, a left-turning wedge ring, and a right-turning wedge ring. The staggered assembly of the circular segment is connected by M30 bolts. The joints of the circular segment adopt the waterproof form of a composite elastic water-swellable rubber water stop belt.

2.2. Geological and Hydrogeological Survey. The area along the shield track in the TS-ES shield section is mainly located in dense pebbly soil and moderately weathered mudstone, stratum, and it partially passes through fully weathered mudstone strata and strongly weathered mudstone strata, including lenticular fine sand strata. The geological structure of the shield section is simple. The bad geology is mainly the sand and gravel layer contaminated by the leakage of the sewage pipe. The geological composition of the TS-ES interval is shown in Figure 2.

The TS-ES shield section belongs to the hydrogeological unit of the plain area. Quaternary loose deposits are widely distributed, with good water permeability and water abundance. According to the types of water-bearing media and characteristics of water-bearing voids, the ground water in the site is mainly divided into three types: upper stagnant water deposited above the clay layer, pore water of the Quaternary loose soil layer, and fissure water of the bedrock.

3. Selection and Matching of the Shield Machine

3.1. Selection of the Shield Machine. The type selection of the shield machine is generally based on the geological conditions of the tunnel passing through the stratum,

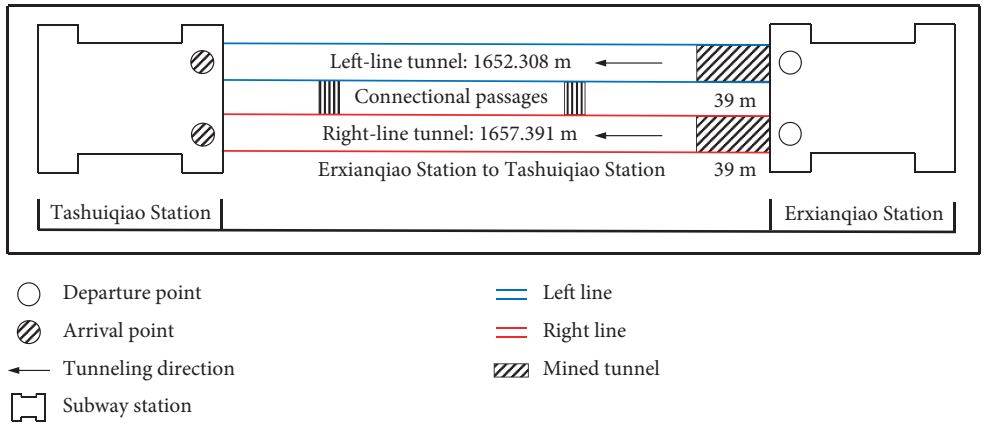

Figure 1: Plane position of the tunnels in the TS-ES section.

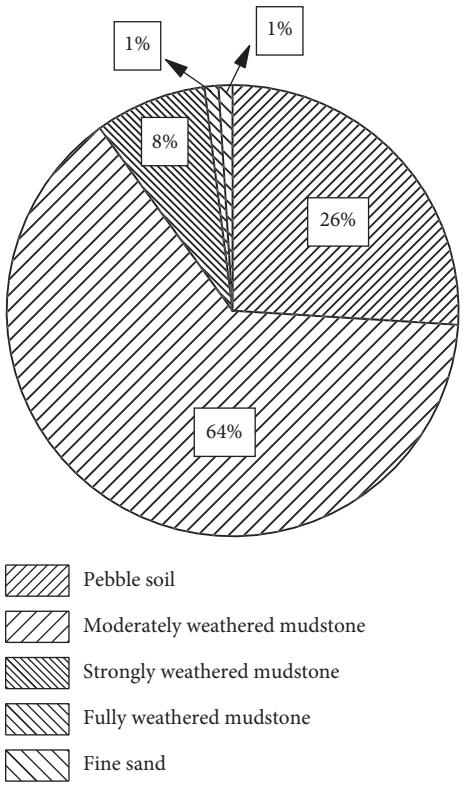

Figure 2: Geological composition of the tunnels in the TS-ES section.

environmental conditions, equipment reliability, construction period requirements, economic benefits, and engineering and technical experience. Combined with similar geological construction experience in the Chengdu area, two ZTE8600 large-diameter composite Earth pressure balance shield machines manufactured by the China Railway Construction Heavy Industry Corporation were selected to construct this shield tunnel. The crossing strata are dense cobble strata and moderately weathered mudstone strata. During the construction process, improper operation or abnormal tunneling parameters can easily make the tunnel structure float up and the road surface settle and collapse, which will affect the surrounding buildings, pipelines, and traffic safety. A single shield machine is equipped with two train groups, which adopt a single-group transportation mode; i.e., one train group will complete all transportation in a cycle to ensure the continuity of propulsion. The main performance parameters of the shield machine are shown in Table 1. The optimal parameters for the trial excavation of the shield tunnel in this project are as follows: the thrust range is 8440~10750 kN, the cutter head torque range is 1284~2440 kN m, the excavation speed is 48~65 mm/min, and the grouting pressure is 0.2~0.3.

3.2. Main System of the Shield Machine. The main system of the shield machine selected for this project is introduced as follows.

3.2.1. Configuration of the Cutter Head and Cutting Tools. The cutter head with a compound design adopts the structure form of spokes and panels. The excavation diameter and opening ratio of the cutter head are 8630 mm and 36%, respectively. The cutter head is equipped with knives, including hobs, cutting knives, shell knives, and edge scrapers. Among them, there are 6 double hobs with a knife height of 180 mm and a knife spacing of 101.5 mm; 34 front hobs with a knife height of 180 mm and a knife spacing of 78 mm; 12 edge hobs; 1 supercut tooth knife with a maximum over-xcavation of 50 mm; 52 cutting knives with a knife height of 115 mm and a knife spacing of 200 mm; 6 shell knives with a knife height of 140 mm high; and 12 pairs of edge scrapers with a knife height of 115 mm. According to different geological conditions, the hobs can be completely or partially replaced by the tooth knife. All detachable cutters can be replaced from the back of the cutter head. When the tunnel is excavated in the full section, the shield machine can realize the forward and reverse rotations of the ballast.

3.2.2. Main Drive. The main drive is a high-torque variable frequency drive composed of 14 drive units, and a single motor has a drive power of 250 kW. The relationship between rotation speed and torque is shown in Figure 3. The

Table 1: Performance parameters of the shield machine.

Serial number	Technical parameters	Parameter configuration	Unit
1	Model number of shield machine	ZTE8600	—
2	Excavation diameter	8630	mm
3	Opening ratio of cutter head	≈37	%
4	Maximum excavation speed	80	mm/min
5	Maximum thrust	81895	kN
6	Segment size (outside diameter/inside diameter – width)	8300/7500–1500	mm
7	Length of main machine of shield machine	≈11	m
8	Total length of shield machine	≈106	m
9	Total weight of shield machine	≈1200	t
10	Installed power	≈5050	kW
11	Horizontal turning radius	350	m
12	Longitudinal climbing ability	±50	‰

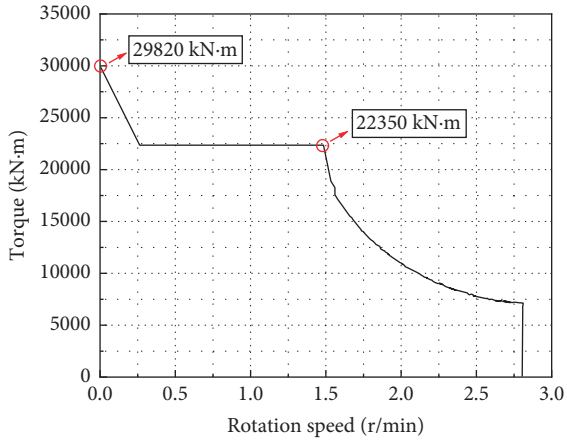

Figure 3: Relationship between rotation speed and torque.

nominal torque of the main drive can reach 22350 kN m, and the relief torque can reach 29820 kN m. It has sufficient torque reserve to achieve long-term overload and is more suitable for the geological conditions of mudstone and pebble soil in this section. To improve the pressure-bearing capacity of the main drive, polyurethane is used to seal the main drive system. After sealing, the pressure-bearing capacity of the main drive system can reach 10 bar.

3.2.3. Shield Body System. The shield machine is composed of a front shield, a middle shield, and a tail shield. The main structure of the shield machine is made of Q345 B carbon alloy steel. The outer diameter of the front shield is designed to be 8600 mm, and the notch is welded with a 5-mm wear-resistant layer to increase the wear resistance. To improve the fluidity of the muck, 4 passive stirring arms are installed on the pressure-resistant partition of the soil bin. A mud injection system is added to the middle shield to inject improved materials around to prevent the shield body from being wrapped. The designed diameter of the tail shield is 8570 mm. The connection between middle shield and tail shield adopts a passive articulation design, and the articulation adopts two rubber seals, which can satisfy the tunneling requirements of the $R = 400$ m turning radius.

3.2.4. Propulsion system. The propulsion system is divided into six groups, including 38 propulsion cylinders. The maximum thrust of the propulsion system is 81895 kN. The cylinder diameter, rod diameter, and stroke specifications of the propulsion cylinder are 280 mm, 240 mm, and 2600 mm, respectively. The pressure of the six groups of cylinders can be independently adjusted. The propulsion speed is regulated by a flow control valve, and the actual maximum excavation speed of the propulsion system is limited to 80 mm/min. By adjusting the propulsive pressure and speed of each cylinder, the excavation direction of the shield machine can be corrected and adjusted.

3.2.5. Screw Conveyor. The shield machine adopts a shaft-type screw conveyor with an inner diameter of 1020 mm. The installation angle of the screw conveyor is 22°, and it is fixed on the sleeve flange at the bottom of the front shield, which can realize the functions of forward and backward telescoping. The maximum capacity of the screw conveyor to transport muck is 581 m^3/h. When the shield machine is tunneling at the maximum excavation speed, the required capacity to transport muck is 421 m^3/h. Thus, the capacity of the screw conveyor to transport muck can satisfy the requirements of shield construction.

3.2.6. Installation system of shield segments. First, the full-ring segment is transported by the segment-transport vehicle from outside the tunnel to the unloading work area. After the unloading operation is completed, the segment-transport vehicle exits the unloading work area. The segment crane transports the segments to the storage area. Then, the segments are sent to the segment-assembly machine by the segment feeder. The segment-assembly machine is installed on the tail shield and consists of a pair of heavy lifting cylinders, a large swing mechanism, a grasping mechanism, and a translation mechanism. The segment-assembly machine has two control methods: remote control and wire control, both of which can be individually and flexibly controlled for each action. The segment-assembly machine has 6 degrees of freedom. Its rotation speed is 0~1.3 r/min and can be fine-tuned. The longitudinal movement stroke of

the segment-assembly machine is 3200 mm, and the rotation angle is ±200°. Using these equipment, the segments can be installed in an accurate position.

3.2.7. Muck improvement system. The shield is equipped with a 9-way single-tube foam injection system, which is sprayed to the spout in front of the cutter head through a rotary joint. The foaming method is changed from direct foaming in the original pipeline to foaming pumped by the foam pump after the mixing box has been fully mixed. Thus, the foaming effect can be enhanced, and the foam consumption can be reduced. The bentonite system uses two hoses as injection pumps. Generally, two pumps are separately injected, one of which is used for muck improvement and the other for lubrication outside the shield shell. When a large flow is required under special circumstances, two pumps can also be used together for muck improvement. The equipped bentonite injection system can inject bentonite or clay from the outside of the shield shell, which can effectively reduce the friction resistance of the shield body and prevent the shield from jamming.

3.2.8. Grout injection system. The shield machine is equipped with 3 sets of hydraulically SCHWING grouting pumps, which inject the mortar into the annular gap between the excavation diameter and the outer diameter of the segment through the grouting pipe at the tail shield. The grouting pressure and pumping frequency of the grouting pump can be continuously adjusted within the adjustable range, and the pressure change is monitored by the pressure sensor. The shield tail is equipped with 12 grouting pipes, and the grouting capacity is 30 m^3/h.

3.2.9. Guidance system. A set of automatic guidance systems is installed on the shield machine, which can accurately measure and display various postures of the shield machine in tunneling and the line and position relationship. The angle-measuring precision of the automatic guidance system is 2 seconds, and the effective working distance is 200 m. The operator can adjust the tunneling direction and posture of the shield machine in a timely manner based on the information provided by the guidance system.

4. Adaptability Evaluation

4.1. Evaluation Methodology. The fuzzy analytic hierarchy process (FAHP) is a type of systematic analysis method that combines qualitative analysis and quantitative analysis based on a fuzzy number or fuzzy judgement matrix [23, 24]. The analytic hierarchy process (AHP) has certain limitations for testing the judgement matrix, while FAHP overcomes this defect and is a more effective comprehensive evaluation method. The analytical process of the FAHP is shown in Figure 4.

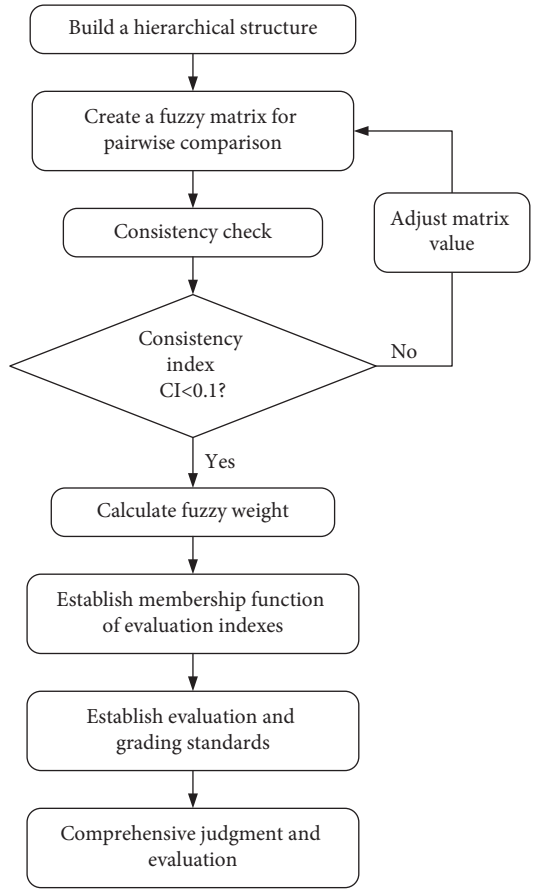

Figure 4: Analytical process of FAHP.

4.2. Evaluation Process

4.2.1. Evaluation Index. By analysing the application status of the shield machine, the evaluation of its adaptability can be divided into four grades, as shown in Table 2.

According to the FAHP, basic requirements, and basic elements of the shield-type selection, the evaluation indices for the adaptability of shield-type selection are initially formed, as shown in Table 3. The evaluation indices include 4 major categories and 24 subcategories. The primary evaluation indices for the adaptability evaluation are relatively complicated, and the factors considered involve all aspects of the project. However, the factors that have a decisive influence on the adaptability evaluation of shield selection are limited. If all primary evaluation indices are considered, it likely negatively affects the comprehensive evaluation and increase unnecessary influencing factors. Eventually, the evaluation results lose their theoretical significance and practical value.

To objectively and accurately evaluate the adaptability of the shield selection of this project, the AHP is used to screen the primary evaluation indices. The weight of each index is arranged to form a reasonable evaluation index system. The calculation results and scores of AHP for primary evaluation indices are shown in Tables 4–7, where λ_{max} is the largest eigenvalue of the weight matrix for the evaluation index, CI is the random consistency index, and CR is the consistency

Table 2: Evaluation grade of the adaptability of the shield machine.

Evaluation grade	Fitness value	Adaptability evaluation	Supplementary instruction
I	(0.9, 1.0]	High degree of adaptability	The shield machine selected can satisfy the engineering requirements.
II	(0.8, 0.9]	Moderate degree of adaptability	The shield machine selected basically satisfies the engineering requirements. Engineers should do a good job in equipment maintenance, ground measurement and other related work.
III	(0.7, 0.8]	Low degree of adaptability	The follow-up risk of the selected shield machine is relatively large. It is necessary to pay attention to the performance status of the shield machine every day and to monitor the tunnelling of the shield machine at all times.
IV	≤0.70	Inadaptation	The selected shield machine is not feasible.

Table 3: Primary evaluation indices.

Target layer	Rule layer	Scheme layer
Evaluation method of shield-type selection (T)	Geological conditions (C_1)	Stratigraphic characteristics (u_{11})
		Distribution of groundwater (u_{12})
		Distribution of harmful gases (u_{13})
		Bad geology and geological disasters (u_{14})
		Specific rock and soil (u_{15})
	Environmental conditions (C_2)	Existing building (u_{21})
		Underground pipelines (u_{22})
		Existing urban rail transit and railways (u_{23})
		Surface water body (u_{24})
		Urban planning land (u_{25})
		Vibration and noise (u_{26})
		Ground traffic (u_{27})
		Disposal of sludge and soil (u_{28})
	Shield construction (C_3)	Propulsion speed (u_{31})
		Rotation speed of the cutter head (u_{32})
		Grouting pressure (u_{33})
		Soil pressure (u_{34})
	Design of shield machine (C_4)	Total thrust (u_{41})
		Main drive torque (u_{42})
		Grouting ability (u_{43})
		Number of muck improvement openings (u_{44})
		Type of cutting tools (u_{45})
		Slagging quantity of screw conveyor (u_{46})
		Spacing design of cutting tool (u_{47})

Table 4: Weights and rank of the adaptability evaluation indices.

Evaluation indices	C_1	C_2	C_3	C_4
C_1	1	1/2	1/3	1/5
C_2	2	1	1/3	1/4
C_3	3	3	1	1/3
C_4	5	4	3	1
Weight	8.333%	12.777%	12.777%	12.777%
Rank	4	3	2	1

$\lambda_{max} = 4.109$; CI = 0.036; CR = 0.041 < 0.1.

ratio. The specific calculation methods and calculation steps of these parameters can be found in the literature [25, 26].

In general, a smaller CR value corresponds to better consistency of the judgement matrix. If the CR value is less than 0.1, the judgement matrix satisfies the consistency test. Conversely, if the CR value is greater than 0.1, there is no consistency, and the judgement matrix should be appropriately adjusted and analysed again. Taking Table 4 as an example, the calculated CR value is 0.041 < 0.1, which implies that the judgement matrix in this study satisfies the consistency test, and the calculated weights are consistent. According to the calculation results in Tables 4–7, if all primary evaluation indices are used, the evaluation index system appears too complicated, and the advantages of the FAHP cannot be fully utilized. The indices with a greater impact on the evaluation results, i.e., a weight value greater than 10%, are selected as the final evaluation indices, as shown in Table 8.

4.2.2. Membership Function. There is incommensurability in the indices of shield adaptability. To solve the problem of commensurability for the evaluation indices, it is necessary to quantify the evaluation indices. The degree of adaptation between each evaluation index and the shield selection is represented by a certain value in [0, 1]. When a certain evaluation index does not satisfy the shield adaptation

Table 5: Weights and rank of the environmental conditions.

Evaluation indices	u_{21}	u_{22}	u_{23}	u_{24}	u_{25}	u_{26}	u_{27}	u_{28}
u_{21}	1	1/3	2	2	2	2	2	2
u_{22}	3	1	2	2	2	2	2	2
u_{23}	1/2	1/2	1	1	1	1	1	1
u_{24}	1/2	1/2	1	1	1	1	1	1
u_{25}	1/2	1/2	1	1	1	1	1	1
u_{26}	1/2	1/2	1	1	1	1	1	1
u_{27}	1/2	1/2	1	1	1	1	1	1
u_{28}	1/2	1/2	1	1	1	1	1	1
Weight	17.747%	23.242%	9.835%	9.835%	9.835%	9.835%	9.835%	9.835%
Rank	2	1	3	3	3	3	3	3

$\lambda max = 8.120;\ CI = 0.017;\ CR = 0.012 < 0.1.$

Table 6: Weights and rank of the shield construction.

Evaluation indices	u_{31}	u_{32}	u_{33}	u_{34}
u_{31}	1	1/3	1/3	3
u_{32}	3	1	1/2	3
u_{33}	3	2	1	3
u_{34}	1/3	1/3	1/3	1
Weight	17.028%	30.315%	42.902%	9.755%
Rank	3	2	1	4

$\lambda_{max} = 4.220;\ CI = 0.073;\ CR = 0.082 < 0.1.$

Table 7: Weights and rank of the shield machine design.

Evaluation indices	u_{41}	u_{42}	u_{43}	u_{44}	u_{45}	u_{46}	u_{47}
u_{41}	1	1	2	3	3	3	5
u_{42}	1	1	2	2	2	3	5
u_{43}	1/2	1/2	1	1	1	1	2
u_{44}	1/3	1/2	1	1	1	1	2
u_{45}	1/3	1/2	1	1	1	1	2
u_{46}	1/3	1/3	1	1	1	1	2
u_{47}	1/5	1/5	1/2	1/2	1/2	1/2	1
Weight	27.628%	24.620%	11.254%	10.610%	10.610%	10.020%	5.257%
Rank	1	2	3	4	4	5	6

Table 8: Final evaluation indices.

Target layer	Rule layer	Scheme layer
Evaluation method of shield-type selection (T)	Environmental conditions (C_2)	Existing building (u_{21})
		Underground pipelines (u_{22})
	Shield construction (C_3)	Propulsion speed (u_{31})
		Rotation speed of the cutter head (u_{32})
		Grouting pressure (u_{33})
	Design of shield machine (C_4)	Total thrust (u_{41})
		Main drive torque (u_{42})
		Grouting ability (u_{43})
		Number of muck improvement openings (u_{44})
		Type of cutting tools (u_{45})
		Slagging quantity of screw conveyor (u_{46})

standard, the weight of the evaluation index is quantified as 0, i.e., the membership degree is set to 0. Conversely, when a certain evaluation index fully satisfies the shield adaptation standard, the weight of the evaluation index is 1. The linear relationship is used to determine the specific membership degree of each evaluation index. The evaluation standard for each index is shown in Table 9, and its membership function is shown in Figure 5. In Table 9, v represents the propulsion speed, q represents the flow rate of the propulsion system, A represents the total area of the propulsion cylinder, F represents the total thrust, n represents the number of cylinders, p represents the thrust of the cylinder, d represents the

Table 9: Evaluation standard for the evaluation indices.

Scheme layer	Calculation basis	Evaluation standard		
		Low degree of adaptability	Moderate degree of adaptability	High degree of adaptability
Existing building (u21)	Based on expert experience	≥20	10~20	≤10
Underground pipelines (u22)	Based on expert experience	≥10	5~10	≤5
Propulsion speed (u31)/(mm/min)	$v = q/A$	≤40 or ≥80	40~45 or 70~80	45~70
Rotation speed of the cutter head (u32)/(r/min)	Based on expert experience	≤0.25 or ≥2.75	0.25~0.5 or 1.5~2.75	0.5~1.5
Grouting pressure (u33)/(MPa)	Based on expert experience	≤0.10 or ≥0.55	0.10~0.25 or 0.50~0.55	0.25~0.50
Total thrust (u41)/kN	$F = np\pi d^2/4$	≤69520	69520~81895	≥81895
Main drive torque (u42)/(kN·m)	$T = \alpha D^3$	≤10000	10000~22350	≥22350
Grouting ability (u43)/(m3/h)	Based on expert experience	≤15	15~25	≥25
Number of muck improvement openings (u44)/(pcs)	Based on expert experience	≤1	1~3	≥3
Type of cutting tools (u45)/(pcs)	Based on expert experience	≤1	1~4	≥4
Slagging quantity of screw conveyor (u46)/(m3/h)	$Q = 15\pi\psi n_{sc} S_{sc} (D_{sc}^2 - d_{sc}^2)$	≤350	350~421	≥421

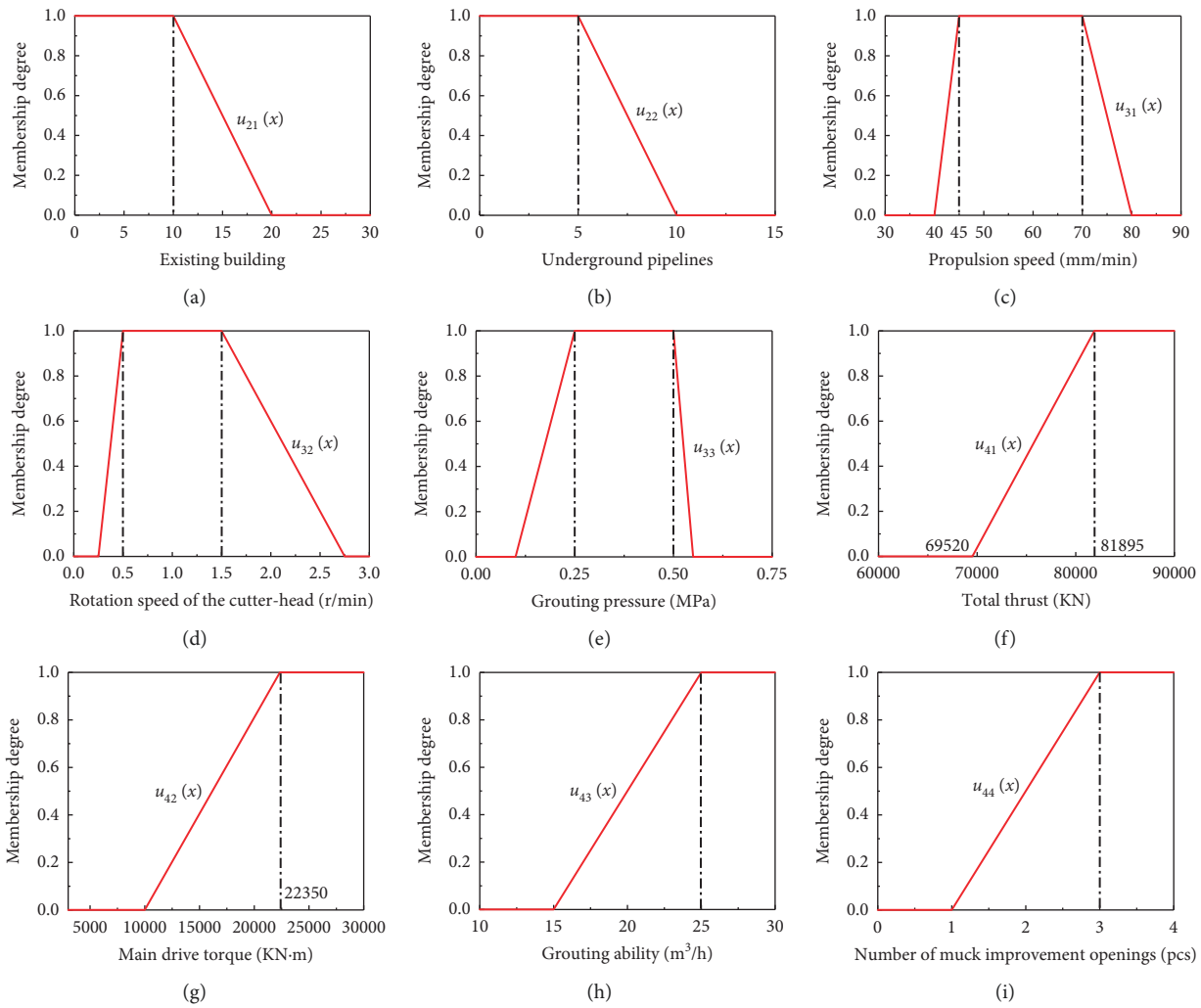

Figure 5: Continued.

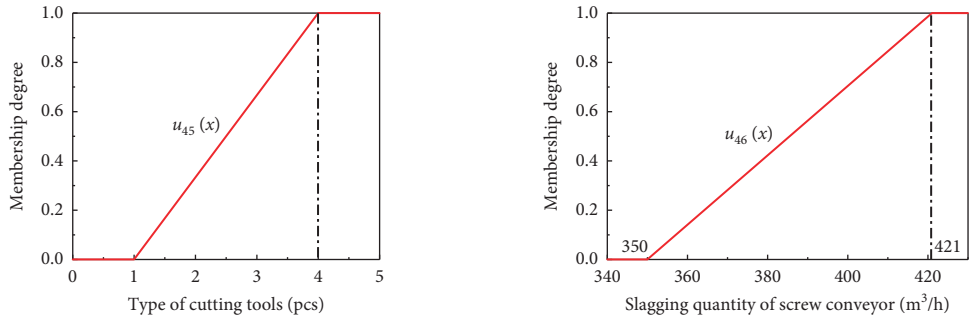

Figure 5: Membership function for the evaluation indices. (a) Existing building. (b) Underground pipelines. (c) Propulsion speed. (d) Rotation speed of the cutter head. (e) Grouting pressure. (f) Total thrust. (g) Main drive torque. (h) Grouting ability. (i) Number of muck improvement openings. (j) Slagging quantity of the screw conveyor.

diameter of the cylinder piston, T represents the main drive torque, α represents the torque coefficient, D represents the outer diameter of the shield machine, Q represents slagging quantity of screw conveyor, n_{sc} represents the rotation speed of the screw conveyor, S_{sc} represents the screw pitch, D_{sc} represents the barrel inner diameter of the screw conveyor, d_{sc} represents the screw diameter of the screw conveyor, and ψ represents the filling coefficient.

4.2.3. Evaluation Results. The evaluation indices are scored according to the methods of consulting experts in the industry and conducting seminars; then, the judgement matrices of each evaluation index areobtained. Tables 10–13 show the corresponding weights calculated by the judgement matrices. These tables show that the CR value of each judgement matrix is less than 0.1, so the single-level comparison of the evaluation index passes the consistency test, and the weights of the judgement matrices are reasonably set.

The weight of each evaluation index at the scheme layer is ranked in total, and the results are shown in Table 14. From this table, the total rank of the final 11 evaluation indices that affect the adaptability of the Earth pressure balance shield machine in this project is the total thrust, main drive torque, grouting pressure, rotation speed of the cutter head, underground pipelines, grouting ability, number of muck improvement openings, type of cutting tools, slagging quantity of screw conveyor, existing building, and propulsion speed.

The combined weight set A of each index from Table 14 is

$$A = [0.0400, 0.0800, 0.0385, 0.0908, 0.1428, 0.1787, 0.1561, 0.0730, 0.0682, 0.0682, 0.0638]. \quad (1)$$

According to the engineering data of this project, the evaluation matrix R of the shield machine is established:

$$R = [0.7, 0.8, 1, 1, 0.9, 0.9, 1, 1, 0.5, 1, 1]^T. \quad (2)$$

The adaptability evaluation indices of the shield machine and the corresponding evaluation system have been determined in a previous article. Based on the above content, the adaptability of the Earth pressure balance shield machine in the shield interval between Tashuiqiao Station and Erxianqiao Station of Chengdu Metro Line 17 is evaluated, and the type-selection judgement value S of the shield machine is obtained:

$$\begin{aligned} S &= A \cdot R \\ &= [0.0400, 0.0800, 0.0385, 0.0908, 0.1428, 0.1787, \\ &\quad 0.1561, 0.0730, 0.0682, 0.0682, 0.0638] \\ &\quad \cdot [0.7, 0.8, 1, 1, 0.9, 0.9, 1, 1, 0.5, 1, 1]^T \\ &= 0.91. \end{aligned} \quad (3)$$

Based on the FAHP, the fitness value of the Earth pressure balance shield machine in this project is 0.91, i.e., the evaluation grade is I. The selected shield machine can satisfy the requirements of the current project.

The shield construction effect is evaluated by monitoring the land subsidence, the shield tunneling attitude, and the stability of the tunnel face. In the section where the tunnel passes through the house, a measuring point is arranged every 3 m along the direction of shield tunneling, and the monitoring results are shown in Figure 6. It can be seen from Figure 6 that

Table 10: Judgement matrix of the target layer to the rule layer (T-C).

T-C	C_2	C_3	C_4
C_2	1	1/3	1/4
C_3	3	1	1/3
C_4	4	3	1
Weight	11.994%	27.210%	60.796%

$\lambda max = 3.074$; CI = 0.037; CR = 0.071 < 0.1.

Table 11: Judgement matrix of the rule layer to the environmental conditions (C_2-u).

C_2-u	u_{21}	u_{22}
u_{21}	1	1/2
u_{22}	2	1
Weight	33.333%	66.667%

$\lambda_{max} = 2.000$; CI = 0.000; CR = 0.000 < 0.1.

Table 12: Judgement matrix of the rule layer to the shield construction (C_3-u).

C_3-u	u_{31}	u_{32}	u_{33}
u_{31}	1	1/3	1/3
u_{32}	3	1	1/2
u_{33}	3	2	1
Weight	14.156%	33.377%	52.468%

$\lambda_{max} = 3.054$; CI = 0.027; CR = 0.052 < 0.1.

Table 13: Judgement matrix of the rule layer to the design of the shield machine (C_4-u).

C_4-u	u_{41}	u_{42}	u_{43}	u_{44}	u_{45}	u_{46}
u_{41}	1	1	2	3	3	3
u_{42}	1	1	2	2	2	3
u_{43}	1/2	1/2	1	1	1	1
u_{44}	1/3	1/2	1	1	1	1
u_{45}	1/3	1/2	1	1	1	1
u_{46}	1/3	1/3	1	1	1	1
Weight	29.388%	25.684%	12.009%	11.215%	11.215%	10.490%

$\lambda_{max} = 6.037$; CI = 0.007; CR = 0.006 < 0.1.

Table 14: Total rank of the evaluation index weight.

u	C_2 11.994%	C_3 27.210%	C_4 60.796%	Total weight of rule layer to scheme layer	Rank
u_{21}	33.333%	0	0	0.0400	9
u_{22}	66.667%	0	0	0.0800	5
u_{31}	0	14.156%	0	0.0385	10
u_{32}	0	33.377%	0	0.0908	4
u_{33}	0	52.468%	0	0.1428	3
u_{41}	0	0	29.388%	0.1787	1
u_{42}	0	0	25.684%	0.1561	2
u_{43}	0	0	12.009%	0.0730	6
u_{44}	0	0	11.215%	0.0682	7
u_{45}	0	0	11.215%	0.0682	7
u_{46}	0	0	10.490%	0.0638	8

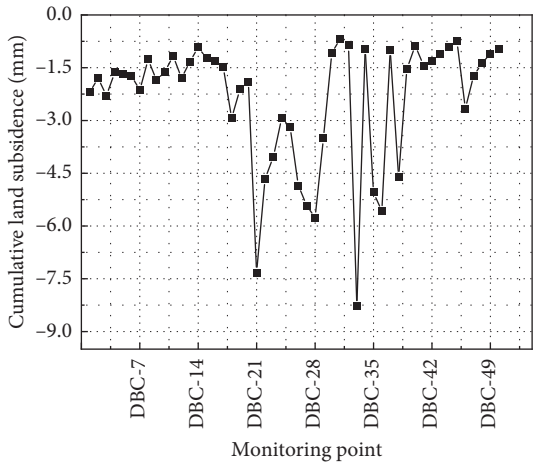

Figure 6: Monitoring value of cumulative land subsidence.

the cumulative land subsidence of each monitoring point meets the requirement that the cumulative land subsidence is less than or equal to 20 mm. To date, the shield machine has been driving steadily with good attitude control, and no engineering accidents have occurred. The shield tunneling project of Chengdu Rail Transit Line 17 has been smoothly performed, and the onsite shield construction matches well with the evaluation results of the proposed evaluation method.

5. Conclusions

A quantitative adaptability evaluation method of shield machines based on the fuzzy analytic hierarchy process (FAHP) and analytic hierarchy process (AHP) is proposed in this paper, and it is applied to the selection evaluation of shield machines in the shield interval between Tashuiqiao Station and Erxianqiao Station of Chengdu Metro Line 17. From this study, the following conclusions are drawn:

(1) The total rank of the final 11 evaluation indices that affect the adaptability of the Earth pressure balance shield machine in Chengdu Metro Line 17 is as follows: total thrust, main drive torque, grouting pressure, rotation speed of the cutter head, underground pipelines, grouting ability, number of muck improvement openings, type of cutting tools, slagging quantity of screw conveyor, existing building, and propulsion speed.

(2) The fitness value of the Earth pressure balance shield machine used in Chengdu Metro Line 17 is 0.88, i.e., the evaluation grade is I. The rationality and accuracy of the fuzzy comprehensive evaluation model of shield adaptability are verified through onsite shield construction, and the evaluation results are consistent with the actual situation.

The proposed quantitative evaluation method of the shield machine adaptability based on AHP and FAHP in this paper can provide a reference for similar projects. When analysing a specific project case, the evaluation indices and weights of specific projects should be determined again to satisfy the new analytical problem.

Data Availability

All data included in this study are available upon request by contact with the corresponding author.

Conflicts of Interest

The authors declare that there are no conflicts of interest regarding the publication of this paper.

Acknowledgments

This work was financially supported by the Key Research and Development Program of Shaanxi Province (No. 2022SF-375).

References

[1] D. V. L. Hunt, I. Jefferson, and C. D. F. Rogers, "Assessing the sustainability of underground space usage — A toolkit for testing possible urban futures," *Journal of Mountain Science*, vol. 8, no. 2, pp. 211–222, 2011.

[2] Z. L. Chen, J. Y. Chen, H. Liu, and Z. F. Zhang, "Present status and development trends of underground space in Chinese cities: Evaluation and analysis," *Tunnelling and Underground Space Technology*, vol. 71, pp. 253–270, 2018.

[3] X. Y. Wang, Z. Ma, and Y. T. Zhang, "Research on Safety Early Warning Standard of Large-scale Underground utility tunnel in Ground Fissure Active Period," *Frontiers of Earth Science*, vol. 10, pp. 1–9, 2022.

[4] Y. W. Zhang, S. Y. Fan, D. H. Yang, and F. Zhou, "Investigation about variation law of frost heave force of seasonal cold region tunnels: a case study," *Frontiers of Earth Science*, vol. 9, pp. 1–9, 2022.

[5] N. F. Liu, N. Li, C. B. Xu, G. F. Li, Z. P. Song, and M. Yang, "Mechanism of secondary lining cracking and its simulation for the Dugongling tunnel," *Rock Mechanics and Rock Engineering*, vol. 53, no. 10, pp. 4539–4558, 2020.

[6] Y. W. Zhang, Z. P. Song, and X. L. Weng, "A constitutive model for loess considering the characteristics of structurality and anisotropy," *Soil Mechanics and Foundation Engineering*, vol. 29, no. 1, pp. 32–42, 2022.

[7] N. F. Liu, L. Cui, and Y. Wang, "Analytical assessment of internal stress in cemented paste backfill," *Advances in Materials Science and Engineering*, vol. 2020, Article ID 6666548, 13 pages, 2020.

[8] X. Y. Wang, Q. Y. Song, and H. Gong, "Research on Deformation Law of Deep Foundation Pit of Station in Core Region of Saturated Soft Loess Based on Monitoring," *Advances in Civil Engineering*, vol. 2022, Article ID 7848152, 16 pages, 2022.

[9] M. Li, H. Yu, H. Jin, and P. Liu, "Methodologies of safety risk control for China's metro construction based on BIM," *Safety Science*, vol. 110, pp. 418–426, 2018.

[10] C. Wan and Z. Jin, "Adaptability of the Cutter-Head of the Earth Pressure Balance (EPB) Shield Machine in Water-Rich Sandy and Cobble Strata: A Case Study," *Advances in Civil Engineering*, vol. 2020, Article ID 8847982, 1 page, 2020.

[11] W. Qian, M. Huang, C. Sun, H. Bin, G. Wang, and H. Liu, "Adaptability of earth pressure balance shield tunneling in coastal complex formations: a new evaluation method," *Geomechanics and Engineering*, vol. 27, no. 4, pp. 375–390, 2021.

[12] J. M. Blackmore and R. A. J. Plant, "Risk and resilience to enhance sustainability with application to urban water systems," *Journal of Water Resources Planning and Management*, vol. 134, no. 3, pp. 224–233, 2008.

[13] B. Smit and J. Wandel, "Adaptation, adaptive capacity and vulnerability," *Global Environmental Change*, vol. 16, no. 3, pp. 282–292, 2006.

[14] M. Yue and L. Guo, "Double closed-loop adaptive rectification control of a shield tunneling machine with hydraulic actuator dynamics subject to saturation constraint," *Journal of Vibration and Control*, vol. 22, no. 2, pp. 309–319, 2016.

[15] R. Rengshausen, R. Tauriainen, and A. Raedle, "TBM and spoil treatment selection process–case history Crossrail C310 Thames Tunnel: Slurry TBM versus EPB TBM," *Geomechanics and Tunnelling*, vol. 7, no. 1, pp. 45–54, 2014.

[16] S. Song, R. Tian, L. Li, J. Hu, C. Shen, and S. Peng, "Adaptability study of EPB shield machine in clay stratum in Xuzhou," *Geotechnical & Geological Engineering*, vol. 37, no. 4, pp. 2335–2341, 2019.

[17] K. Edalat, M. J. Vahdatirad, H. Ghodrat, S. Firouzian, and A. Barari, "Choosing TBM for Tabriz subway using multi criteria method," *Journal of Civil Engineering and Management*, vol. 16, no. 4, pp. 531–539, 2010.

[18] F. S. Hollmann and M. Thewes, "Assessment method for clay clogging and disintegration of fines in mechanised tunnelling," *Tunnelling and Underground Space Technology*, vol. 37, pp. 96–106, 2013.

[19] K. C. Hyun, S. Min, H. Choi, J. Park, and I. M. Lee, "Risk analysis using fault-tree analysis (FTA) and analytic hierarchy process (AHP) applicable to shield TBM tunnels," *Tunnelling and Underground Space Technology*, vol. 49, pp. 121–129, 2015.

[20] M. Ramoni and G. Anagnostou, "On the feasibility of TBM drives in squeezing ground," *Tunnelling and Underground Space Technology*, vol. 21, no. 3-4, pp. 262–264, 2006.

[21] X. G. Wu, J. Y. Lin, L. M. Zhang, and J. B. Zhong, "Selection of shield type for metro tunnel construction based on TOPSIS method," *Railway Engineering*, vol. 10, pp. 95–110, 2015.

[22] X. M. Huang, J. W. Zhang, X. Li, Q. B. Zhu, and Y. Q. Ren, "Shield type selection for urban metro and regionalization study of key parameters," *Tunnel Construction*, vol. 39, no. 7, pp. 1209–1216, 2019.

[23] G. Kabir and R. S. Sumi, "Power substation location selection using fuzzy analytic hierarchy process and PROMETHEE: A case study from Bangladesh," *Energy*, vol. 72, pp. 717–730, 2014.

[24] L. Wang, J. Chu, and J. Wu, "Selection of optimum maintenance strategies based on a fuzzy analytic hierarchy process," *International Journal of Production Economics*, vol. 107, no. 1, pp. 151–163, 2007.

[25] O. S. Vaidya and S. Kumar, "Analytic hierarchy process: An overview of applications," *European Journal of Operational Research*, vol. 169, no. 1, pp. 1–29, 2006.

[26] W. Ho and X. Ma, "The state-of-the-art integrations and applications of the analytic hierarchy process," *European Journal of Operational Research*, vol. 267, no. 2, pp. 399–414, 2018.

Hindawi
Advances in Civil Engineering
Volume 2022, Article ID 9233833, 14 pages
https://doi.org/10.1155/2022/9233833

Research Article

Risk Assessment of EPB Shield Construction Based on the Nonlinear FAHP Method

Xueyan Wang,[1] Hang Gong ,[2,3] Qiyu Song ,[2,3] Xiao Yan,[2,3] and Zheng Luo[2,3]

[1]*School of Urban Planning and Municipal Engineering, Xi'an Polytechnic University, Xi'an, Shaanxi 710048, China*
[2]*College of Civil Engineering, Xi'an University of Architecture and Technology, Xi'an, Shaanxi 710055, China*
[3]*Shaanxi Key Lab of Geotechnical and Underground Space Engineering, Xi'an University of Architecture and Technology, Xi'an, Shaanxi 710055, China*

Correspondence should be addressed to Hang Gong; 414385591@qq.com

Received 22 November 2021; Revised 9 January 2022; Accepted 18 March 2022; Published 7 April 2022

Academic Editor: Qian Chen

There are many risk factors in EPB shield construction. The traditional fuzzy analytic hierarchy process (FAHP) method usually uses a linear analysis method to determine the risk level, but there are often some risk factors with prominent influence, which will reduce the accuracy of the evaluation results. In this paper, a new risk assessment model of Earth pressure balance (EPB) shield construction based on a nonlinear FAHP method is established by introducing nonlinear factors into the comprehensive calculation of the traditional FAHP. First, the new model establishes the framework of EPB shield construction risk analysis based on the work breakdown structure (WBS) and risk breakdown structure (RBS) methods. Then, it constructs an EPB shield construction risk index system by coupling the units of the WBS and RBS. The model constructs a fuzzy consistent judgment matrix, which replaces the 1~9 scale. Finally, the nonlinear operator is introduced into the FAHP comprehensive calculation, considering the influence of some prominent risk factors, which improves the accuracy of the risk assessment. By applying the new model to the risk analysis of the EPB shield construction section of a tunnel project in Hangzhou, the effectiveness of the model is further verified.

1. Introduction

In China, with the continuous development of urbanization, the contradiction between limited land resources and the growing urban population has become increasingly prominent. To solve the problems of urban ground traffic congestion and land energy shortages, the development and utilization of urban underground space has become an inevitable trend of urban development to a certain stage [1, 2]. EPB shields are widely used in the underground tunnel construction of urban rail transit, utility tunnel, and other projects because of their advantages of high safety, fast excavation speed, automatic operation throughout the excavation process, and low construction labor intensity. However, EPB shield construction has the risks of water permeability, sand gushing, mud bursting, and collapse, which can easily cause large-scale surface collapse and damage to underground pipelines or surrounding buildings. Therefore, the risk assessment of urban underground space engineering has important theoretical significance to ensure the safety of construction and the surrounding environment.

In 1980, Saaty proposed analytic hierarchy process, which is a multiobjective system decision-making method combining qualitative and quantitative aspects. It is widely used in social, economic, management, military, and other fields. In 1996, Einstein outlined the basic aspects of risk analysis and decision-making, and then discussed in detail three typical rock engineering applications of risk analysis: (1) slope design, (2) fractured medium flow, and (3) tunnel excavation [3]. Fuzziness and uncertainty are one of the characteristics of risk assessment. Various uncertain factors can be expressed quantitatively by membership function, so as to realize the transformation of risk assessment from

qualitative to quantitative. Based on the uncertainty model of fuzzy mathematics, Choi et al. established a standardized underground engineering evaluation method and applied this method to the Seoul metro project in South Korea for subway construction risk evaluation, which verified its effectiveness [4]. In addition, in the field of civil engineering, the factors to be considered in risk assessment can be divided into three parts: preconstruction preparation, main construction process, and auxiliary construction process according to the construction characteristics. In this regard, many scholars have carried out corresponding research according to different engineering characteristics. Dağdeviren and Yüksel studied the safety risk of TBM construction by using the FAHP and proposed an evaluation model for the TBM dynamic performance [5]. Zhou and Cao established the comprehensive evaluation index system of the foundation pit support scheme by analyzing the influencing factors of urban deep foundation pit support in soft soil area, obtained the weight value of each risk factor by using analytic hierarchy process, determined the relative superior degree matrix by logical operation, and put forward the FAHP model suitable for the optimization of urban deep foundation pit support scheme in soft soil area [6]. Liu et al. established the construction risk evaluation index system of deep foundation pit by the WBS-RBS method and established the fuzzy level assessment model of construction risk based on the theory of triangle fuzzy mathematics [7]. Deng et al. studied the construction risk of tunnel portal based on Fuzzy AHP and analyzed the Wuguangyi highway tunnel as a case study [8]. Lu et al. used the FAHP to build a model that can be used to evaluate the probability of tunnel collapse accidents [9]. Samantra et al. proposed a comprehensive risk assessment method for urban construction projects based on the fuzzy set theory [10]. Kuchta and Ptaszyńska proposed a fuzzy risk registration method to identify risks in construction projects and evaluate their attributes [11] based on the existing risk assessment theory of urban rail transit project infrastructure. According to the translational velocity and angular velocity characteristics of the TBM, Yu et al. established the dynamic performance evaluation model of the TBM by using the FAHP to determine the weight of the evaluation model [12]. Nezarat et al. used the fuzzy analytic hierarchy process (FAHP) to rank the geological risks of Golab tunnel construction in northwestern Isfahan (Iran) [13]. Lyu et al. proposed an improved trapezoidal fuzzy analytic hierarchy process (FAHP) to evaluate the risk of infrastructure related to land subsidence in megacities and evaluated the risk of infrastructure related to land subsidence in Shanghai [14]. Hu et al. used the analytic hierarchy process and fuzzy principle to determine the weight of each index in the index system, and on this basis, finally established an evaluation system and a classification standard for the highway tunnel structure safety grade state [15]. Based on the fuzzy comprehensive evaluation theory, Zhu et al. proposed a multilevel comprehensive evaluation method for tunnel construction organizations and applied it to an example [16]. Wang et al. took surface vertical settlement, structural stress, crack displacement, and contact pressure as the early warning indicators of the underground comprehensive pipe gallery structure in the active period of ground cracks and gave the safety control value and early warning standard on the basis of the analysis results [17, 18]. Zheng et al. combined triangular fuzzy number (TFN) and analytic hierarchy process (AHP) into the geographic information system (GIS) to evaluate geological disasters along the Zhengkun railway, which not only effectively predicted the risk distribution of geological disasters in the study area in recent 10 years but also put forward risk prevention management measures [19]. Obviously, the abovementioned scholars have made different contributions to the development of underground engineering risk management, but there is less risk analysis related to EPB shield construction.

Generally, FAHP can be divided into FAHP based on fuzzy number and FAHP based on fuzzy consistent matrix [20]. FAHP based on fuzzy numbers includes interval FAHP, triangular FAHP, and trapezoidal FAHP [21]. Interval FAHP uses interval numbers to represent the relative importance of factors[22~24], while triangular/trapezoidal FAHP uses a triangle/trapezoid number to represent the relative importance in pairwise comparison [22, 23]. After constructing the judgment matrix, if the expert's reply to the questionnaire adopts the method of pairwise comparison [24], the consistency check needs to be carried out. The consistency check mainly includes three steps: (1) calculation of consistency index; (2) determination of the average random consistency index; and (3) consistency ratio calculation[25]. When the judgment matrix does not have consistency, the factors of the judgment matrix need to be adjusted to make it consistent. This does not rule out that it needs several times of adjustment and inspection to make the judgment matrix consistent. The process is cumbersome, and the amount of calculation will increase accordingly. Therefore, Lyu et al. proposed a new questionnaire, which is composed of a comprehensive table. The first column lists all factors, and the other columns list 9 scores representing the relative importance of a factor's contribution to construction risk (from 1 = lowest importance to 9 = highest importance). The fuzzy number is determined by scoring all factors directly by experts, and a consistent judgment matrix is established [26]. When experts consider a small number of factors, this method has higher efficiency and greater accuracy, but when experts must consider a large number of factors, the importance of some factors may not be more accurate than pairwise comparison. The FAHP based on the fuzzy consistent matrix first establishes the fuzzy complementary matrix, and then transforms it into the fuzzy consistent judgment matrix for risk assessment. Because the fuzzy consistent judgment matrix transformed from the fuzzy complementary judgment matrix meets the additive consistency condition, that is, the difference between the factors of any two rows is constant, so there is no need to do consistency test [27]. Therefore, by combining this method with pairwise comparison, it can not only ensure the accuracy of experts' scoring of factors but also meet the consistency conditions.

In this paper, the WBS-RBS method is introduced into the system decomposition of the tunnel construction work structure and construction risk source, and the framework structure of EPB shield construction risk analysis is constructed. By coupling the tunnel construction work breakdown structure and construction risk breakdown structure, the risk factors reflecting EPB shield construction are determined, and the EPB shield construction risk index system is built. On this basis, the expert questionnaire is collected by a pairwise comparison method, and the fuzzy consistency judgment matrix is established by transforming the fuzzy complementarity matrix, which not only meets the accuracy and consistency requirements of expert scoring but also avoids the cumbersome consistency test. Finally, the nonlinear operator is introduced into the FAHP comprehensive calculation to improve the accuracy of the risk assessment, and a new EPB shield construction risk assessment model based on the nonlinear fuzzy analytic hierarchy process is established. The new model is applied to the risk analysis of EPB shield construction section of a tunnel project in Hangzhou, and the validity of the model is verified. It also provides ideas and experience for risk assessment in the shield construction field by using nonlinear FAHP.

2. Risk Identification of EPB Shield Construction Based on the WBS-RBS Method

The WBS (work breakdown structure) is a method to divide project tasks into different levels. The basic principle of the WBS is to decompose project tasks into different levels by top-down, bottom-up, or analogy methods. The RBS (risk breakdown structure) is a method to decompose various major risk factors into the most basic risk factors by taking risk management theory as the basic theory and combining quantitative and qualitative risk grading. Hillson and Grimaldi and others first began to integrate the WBS and RBS [28]. The basic principle of the WBS-RBS method is to organically combine the specific risk factors defined in the RBS with the effective scope of work defined in the WBS to construct the risk identification coupling matrix to identify the risk of each underlying unit and establish the risk index system of the engineering project. The steps of WBS-RBS method are as follows [25]: (1) construct the WBS work breakdown structure; (2) build the RBS risk decomposition structure; and (3) associate WBS with RBS, establish WBS-RBS coupling matrix with the work package set at the bottom of WBS and the risk element set at the bottom of RBS, and then analyze the existing risks.

2.1. Establishment of the EPB Shield Construction Work Breakdown Structure. According to the WBS principle, the EPB shield construction process is decomposed into two levels.

(1) According to the main construction stages of the EPB, the first-level WBS is divided into three stages: preparation before EPB shield construction, EPB shield tunneling construction, and EPB ancillary equipment construction.

(2) Combined with the characteristics of each stage of EPB shield construction, the first-level WBS is decomposed into different second-level WBSs by distinguishing different processes.

According to the WBS method, the EPB shield construction work breakdown structure is shown in Figure 1.

2.2. Establishment of the EPB Shield Construction Risk Decomposition Structure. According to the RBS principle, the risk sources of EPB shield construction are decomposed into two levels.

(1) According to the characteristics of EPB shield construction, the first-level RBS can be divided into three types: geological condition risk source, environmental risk source along the line, and other risk sources.

(2) On the basis of the first-level risk decomposition source, the EPB shield construction risk is analyzed in detail, and the first-level risk structure is decomposed into the second-level risk structure.

The risk decomposition structure of EPB shield construction based on the RBS method is shown in Figure 2.

2.3. Establishing the Coupling Matrix of EPB Shield Construction Risk Identification. By coupling the bottom units of the WBS (Figure 1) and RBS (Figure 2), the coupling matrix of EPB shield construction risk identification can be obtained, as shown in Table 1. The result is "0" when the two couplings do not produce risk and "1" when the two couplings produce risk. The results of the EPB shield construction risk identification coupling matrix are classified as follows: (1) $W_{11}R_{11}$, $W_{11}R_{14}$, $W_{11}R_{31}$, and $W_{11}R_{33}$: end reinforcement failure of shield shaft; (2) $W_{12}R_{11}$, $W_{12}R_{14}$, $W_{12}R_{31}$, and $W_{12}R_{33}$: tunnel portal collapsed; (3) $W_{13}R_{31}$, and $W_{13}R_{33}$: backup system failure; (4) $W_{14}R_{31}$, $W_{14}R_{32}$, and $W_{14}R_{33}$: bracket deformation and instability; (5) $W_{15}R_{31}$ and $W_{15}R_{33}$: deviation of the shield tunneling route; (6) $W_{16}R_{31}$, $W_{16}R_{32}$, and $W_{16}R_{33}$: failure of the shield machine assembly and commissioning; (7) $W_{21}R_{11}$, $W_{21}R_{31}$, and $W_{21}R_{32}$: collapse of the tunnel face; (8) $W_{21}R_{21}$, $W_{23}R_{21}$, and $W_{24}R_{21}$: settlement of surface buildings; (9) $W_{21}R_{22}$, $W_{23}R_{22}$, and $W_{24}R_{22}$: buried pipelines damage; (10) $W_{21}R_{23}$, $W_{23}R_{23}$, and $W_{24}R_{23}$: deformation of underground buildings or structures; (11) $W_{21}R_{24}$, $W_{23}R_{24}$, and $W_{24}R_{24}$: road surface heave or settlement; (12) $W_{22}R_{11}$ and $W_{22}R_{14}$: water and sand gushing in tunnel face; (13) $W_{22}R_{13}$, $W_{22}R_{32}$, and $W_{31}R_{13}$: harmful gas accumulation in tunnel; (14) $W_{22}R_{31}$ and $W_{22}R_{33}$: discontinuous transportation of muck; (15) $W_{25}R_{11}$, $W_{25}R_{12}$, $W_{25}R_{31}$, and $W_{25}R_{33}$: cutting tools damage; (16) $W_{31}R_{31}$ and $W_{31}R_{33}$: poor ventilation and dust collection in the tunnel; (17) $W_{32}R_{31}$ and $W_{32}R_{33}$: tunnel lighting system failure; (18) $W_{33}R_{14}$, $W_{33}R_{31}$, and $W_{31}R_{33}$: water accumulation in tunnel; and (19) $W_{34}R_{31}$, $W_{33}R_{32}$, and $W_{31}R_{33}$: leakage of lining segment.

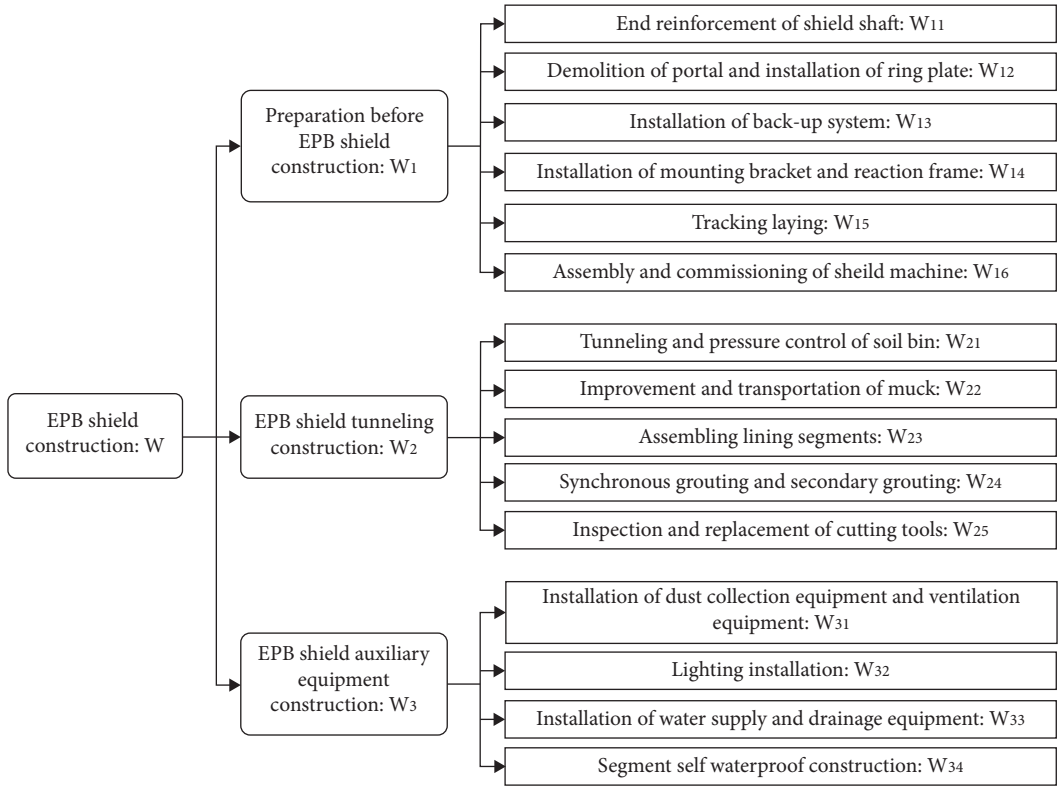

Figure 1: EPB shield construction work breakdown structure.

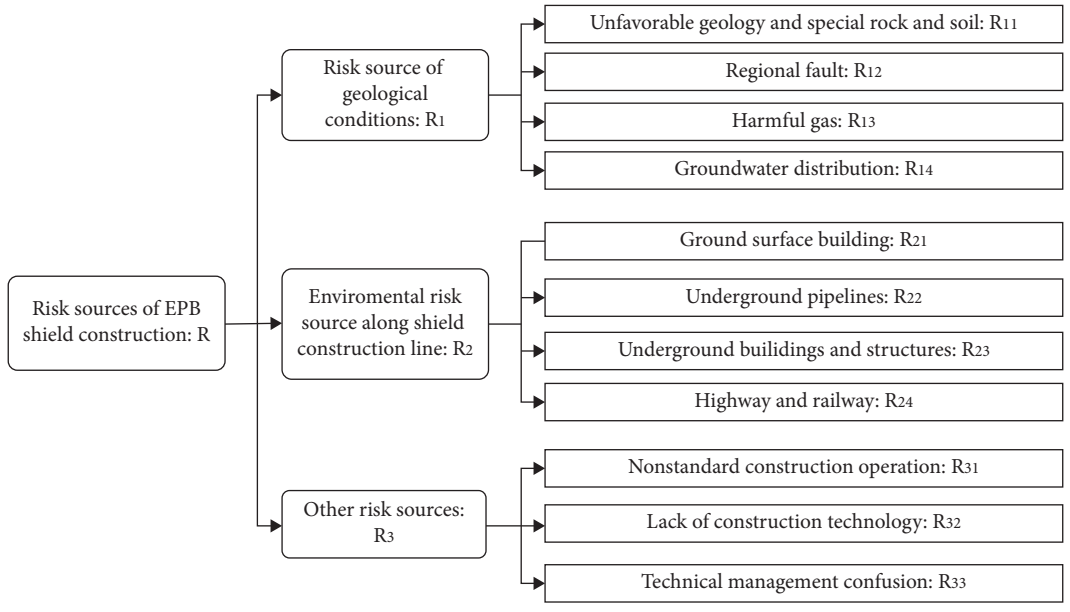

Figure 2: EPB shield construction risk decomposition structure.

2.4. Establishment of the EPB Shield Construction Risk Index System. By combining the results of the EPB shield construction risk identification coupling matrix with the experience of onsite management personnel and expert suggestions and sorting out and classifying the risks that can reflect EPB shield construction, the final EPB shield construction risk index system is shown in Figure 3.

3. EPB Shield Construction Risk Assessment

3.1. Establishment of the Fuzzy Relation Matrix

3.1.1. Establishment of the Risk Assessment Set. Risk evaluation refers to the description of risk evaluation indicators by using qualitative language. The evaluation set in this

Table 1: Coupling matrix of EPB shield construction risk identification.

		W_1						W_2					W_3			
		W_{11}	W_{12}	W_{13}	W_{14}	W_{15}	W_{16}	W_{21}	W_{22}	W_{23}	W_{24}	W_{25}	W_{31}	W_{32}	W_{33}	W_{34}
R_1	R_{11}	1	1	0	0	0	0	1	1	0	1	1	0	0	0	0
	R_{12}	0	0	0	0	0	0	0	0	0	0	1	0	0	0	0
	R_{13}	0	0	0	0	0	0	0	1	0	0	0	1	0	0	0
	R_{14}	1	1	0	0	0	0	0	1	0	0	0	0	0	1	0
R_2	R_{21}	0	0	0	0	0	0	1	0	1	1	0	0	0	0	0
	R_{22}	0	0	0	0	0	0	1	0	1	1	0	0	0	0	0
	R_{23}	0	0	0	0	0	0	1	0	1	1	0	0	0	0	0
	R_{24}	0	0	0	0	0	0	1	0	1	1	0	0	0	0	0
R_3	R_{31}	1	1	1	1	1	1	1	1	0	1	1	1	1	1	1
	R_{32}	0	0	0	1	0	1	1	1	0	0	0	0	0	0	1
	R_{33}	1	1	1	1	1	1	0	1	0	1	1	1	1	1	1

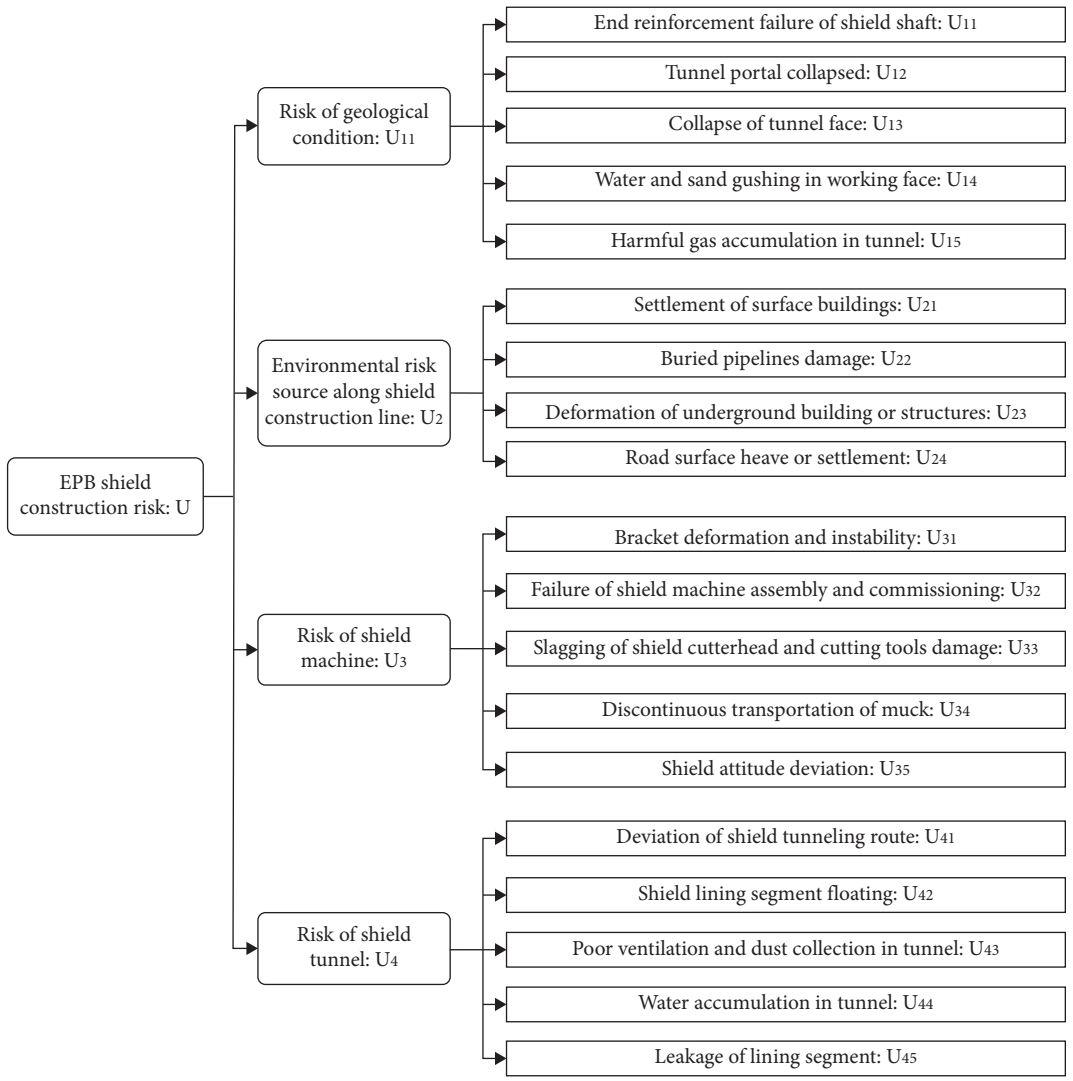

Figure 3: EPB shield construction risk index system diagram.

paper refers to the collection of comments made by judges on various construction risks of EPB shields. According to the characteristics of EPB shield construction, the comments can be divided into five levels:

$$V = \{v_1 \ v_2 \ v_3 \ v_4 \ v_5\} = \{\text{Lowest risk} \ \ \text{low risk} \ \ \text{medium risk} \ \ \text{high risk} \ \ \text{highest risk}\}. \quad (1)$$

3.1.2. Establishment of the Risk Factor Set. The factor set involved in this paper is based on the EPB shield construction risk index system. The first-level index risk factor set is as follows: $U = \{U_1, U_2, U_3, U_4\}$; the second-level index risk factor set is as follows: $U_1 = \{u_{11}, u_{12}, u_{13}, u_{14}, u_{15}\}$, $U_2 = \{u_{21}, u_{22}, u_{23}, u_{24}\}$, $U_3 = \{u_{31}, u_{32}, u_{33}, u_{34}\}$, $U_4 = \{u_{41}, u_{42}, u_{43}, u_{44}, u_{45}\}$.

3.1.3. Establishment of the Membership Vector. The expert evaluation method is a quantitative evaluation method based on quantitative and qualitative analysis, through which the target events are scored by experts. The expert group consists of 10 experts who have worked in the field of tunnel construction safety for more than 8 years, including 6 doctors and 4 masters. According to the grade of the risk evaluation, the evaluation index of each risk factor is scored, and the membership vector of EPB shield construction risk evaluation is constructed [29]. The membership vector of any risk factor concentration evaluation index u_i in the EPB shield construction risk evaluation index u to v_{ij} in the risk evaluation set V is as follows: $R_i = [r_{i1}, r_{i2}, r_{i3}, r_{i4}, r_{i5}]$.

3.1.4. Establishment of the Fuzzy Relation Matrix. According to the construction principle of the membership vector, the membership vector of each risk index to the evaluation set in the EPB shield construction risk assessment is obtained. The fuzzy relation matrix between the risk evaluation set and the factor set is obtained by combining the membership vectors corresponding to each risk index as follows:

$$R = \begin{bmatrix} r_{11} & \cdots & r_{1j} & \cdots & r_{1m} \\ \cdots & \cdots & \cdots & \cdots & \cdots \\ r_{i1} & \cdots & r_{ij} & \cdots & r_{im} \\ \cdots & \cdots & \cdots & \cdots & \cdots \\ r_{n1} & \cdots & r_{nj} & \cdots & r_{nm} \end{bmatrix}. \tag{2}$$

where $0 \le r_{ij} \le 1$ and r_{ij} is the membership of the i-th factor to the j-th risk level.

3.2. Determination of the Weight Vector. According to the established EPB shield construction risk evaluation index system, the weight of each risk factor in the EPB shield construction risk evaluation is calculated by using the analytic hierarchy process [30].

3.2.1. Establishment of the Fuzzy Complementary Judgment Matrix. The fuzzy complementary judgment matrix R represents a comparison of the relative importance of the factors related to a certain factor in the previous level. Assuming that the factor of the upper level is C and the related factor of the lower level is $a_1, a_2, \cdots, a_n$, the fuzzy complementary judgment matrix can be expressed as in Table 2.

Factor r_{ij} means that when factor a_i and factor a_j are compared with the upper level factor C, factor a_i and factor a_j have a membership degree of "more important than." By using the 0.1~0.9 scale method [31], the relative importance of any two factors in this layer to the upper layer is quantitatively described, as shown in Table 3.

Table 2: Fuzzy complementary judgment matrix.

C	a_1	a_2	...	a_n
a_1	r_{11}	r_{12}	...	r_{1n}
a_2	r_{21}	r_{22}	...	r_{2n}
...	...	...	...	...
a_n	r_{n1}	r_{n2}	...	r_{nn}

After a quantitative description with the 0.1~0.9 scale method, the following fuzzy complementary judgment matrix can be obtained by comparing the upper factor C with the related factor $a_1, a_2, \ldots, a_n$ of this layer.

$$A = \begin{bmatrix} a_{11} & a_{12} & \cdots & a_{1n} \\ a_{21} & a_{22} & \cdots & a_{2n} \\ \cdots & \cdots & \cdots & \cdots \\ a_{n1} & a_{n2} & \cdots & a_{nn} \end{bmatrix}. \tag{3}$$

3.2.2. Construction of the Fuzzy Consistent Judgment Matrix. By using the following formula to transform the fuzzy complementary judgment matrix obtained in step (1), the fuzzy consistent matrix is obtained [20]:

$$r_{ij} = \frac{r_i - r_j}{2n} + 0.5,$$

$$\begin{cases} r_i = \sum_{k=1}^{n} r_{ik} \quad i = 1, 2, \cdots, n, \\ r_j = \sum_{j=1}^{n} r_{jk} \quad j = 1, 2, \ldots n. \end{cases} \tag{4}$$

3.2.3. Weight Calculation and Ranking of the Fuzzy Consistent Judgment Matrix. The weight value has a direct impact on the final result. Let the weight values of factor $a_1, a_2, \ldots, a_n$ in the fuzzy consistent judgment matrix R be $w_1, w_2, \ldots, w_n$; then, the following relation can be obtained from the above discussion:

$$r_{ij} = a\left(w_i - w_j\right) + 0.5, \ (i, j \in K) \tag{5}$$

In the formula, a refers to a measure of the difference degree of the evaluated objects, which is related to the number and difference degree of the evaluated objects. When the number or difference degree of the evaluated objects is larger, the value of a is larger, $0\,a \le 0.5$.

When the factors in the fuzzy consistent judgment matrix R and the corresponding weights satisfy $n_j = a(w_i - w_j) + 0.5$ and $a \ge (n-1)/2$, the weights can be obtained by the following formula:

$$w_i = \frac{1}{n} - \frac{1}{2a} + \frac{1}{na} \sum_{k=1}^{n} r_{ik}, \ (i \in K). \tag{6}$$

Table 3: Coupling matrix of EPB shield construction risk identification.

Scale	Definition	Explanation
0.5	Equally important	The two factors are equally important.
0.6	Slightly more important	One factor is slightly more important than the other.
0.7	Obviously important	One factor is clearly important than the other.
0.8	Much more important	One factor is much more important than the other.
0.9	Extremely important	One factor is extremely important than the other.
0.1, 0.2, 0.3, 0.4	Converse comparison	If factor a_i is compared with factor a_j to get judgment r_{ij}, then factor a_j is compared with factor a_i to get judgment $r_{ji} = 1 - r_{ij}$

When the fuzzy complementary judgment matrix is not transformed into a fuzzy consistent matrix or a $(n-1)/2$, the least square method can be used to solve the weight vector, that is, to solve the following constrained programming problem:

$$\begin{cases} \min z = \sum_{i=1}^{n}\sum_{j=1}^{n}\left[a\left(w_i - w_j\right) + 0.5 - r_{ij}\right]^2, \\ s.t. \sum_{i=1}^{n} w_i = 1, w_i \geq 0, (i \in K). \end{cases} \tag{7}$$

By means of the Lagrange multiplier method, the constrained programming problem can be solved as follows: unconstrained programming problem:

$$\min L(w,T) = \sum_{i=1}^{n}\sum_{j=1}^{n}\left[a\left(w_i - w_j\right) + 0.5 - n_j\right]^2 + 2T\left(\sum_{i=1}^{n} w_i - 1\right). \tag{8}$$

where T is the Lagrange multiplier. The weight vector $W = [w_1, w_2, \ldots, w_n]^T$ can be obtained by solving the equations by taking the partial derivative of (L, w, T) with respect to $W_i (i \in K)$ and making it zero.

3.3. Nonlinear Comprehensive Evaluation. The fuzziness and uncertainty of the EPB shield construction process render the risk assessment nonlinear. However, in the existing fuzzy evaluation methods of the EPB shield construction risk analysis, the calculation is usually carried out by combining a linear fuzzy operator, which makes it difficult to solve the influence of the prominent index factors on the evaluation results. Therefore, this paper combined nonlinear fuzzy operator analysis to render the evaluation results more practical [32]. The nonlinear fuzzy matrix composition operator is defined as follows:

$$f(W, X, \Lambda) = \left(w_1 x_1^{\lambda_1} + w_2 x_2^{\lambda_2} + \ldots + w_n x_n^{\lambda_n}\right)^{\frac{1}{\lambda}}, \quad \lambda_i \geq 1, \quad i = 1, 2, \ldots, n, \tag{9}$$

where $W = (w_1, w_2, \ldots, w_n)$ is the risk index weight vector, $w_i \geq 0, \sum_{i=1}^{n} w_i = 1$; $X = (x_1, x_2, \ldots, x_n)$ is the factor membership vector, $x_i \in [0, 1]$; Λ is the index prominent influence degree coefficient vector, denoted as $\Lambda = (\lambda_1, \lambda_2, \ldots, \lambda_n)$, and $\lambda = \max(\lambda_1, \lambda_2, \ldots, \lambda_n)$. When the risk factors have a more prominent influence on the EPB shield construction risk assessment, the index prominent influence coefficient λ_i is larger; when the risk factors have no prominent influence on the EPB shield construction risk assessment, the index prominent influence coefficient λ_i is 1. The value method of the index prominent influence coefficient is determined according to the 1~9 scale method and λ_i value principle, and the specific value standard is shown in Table 4 [25].

In addition, when using a nonlinear operator to synthesize a fuzzy matrix, to facilitate calculation, each value of the single factor evaluation matrix should be greater than 1. Therefore, formula (8) can be used for fuzzy transformation:

$$r_{ij}^{'} = 10 \times r_{ij} \tag{10}$$

where r_{ij} is the value of the initial fuzzy evaluation matrix and $r_{ij}^{'}$ is the value of the transformed nonlinear fuzzy evaluation matrix. To keep the same proportion relationship between the evaluation matrix and the initial matrix of the nonlinear fuzzy matrix, when $r_{ij} = 0.05$, $r_{ij}^{'} = 0$ is taken; when $0.05 \leq r_{ij} = 0.1$, $r_{ij}^{'} = 1$ is taken.

3.4. New Risk Assessment Model for EPB Shield Construction. Based on the above analysis, on the basis of the EPB shield construction risk index system obtained by the WBS-RBS method, the traditional fuzzy analytic hierarchy process (FAHP) and nonlinear operator are combined for comprehensive calculation, and a new EPB shield construction risk assessment model based on the nonlinear fuzzy analytic hierarchy process is established. The specific risk assessment and analysis process of the new model is shown in Figure 4.

The new risk assessment model of EPB shield construction based on a nonlinear fuzzy analytic hierarchy process can more objectively reflect the outstanding impact of adverse risk factors on the risk assessment of EPB shield construction. By using the pairwise comparison method to collect the expert questionnaire and establishing the fuzzy complementary matrix and transforming it into the fuzzy consistent judgment matrix, it not only meets the accuracy and consistency requirements of the expert score but also avoids the complex consistency test. When this model is

Table 4: Value standard of the index prominent influence degree coefficient.

Scale	Definition
1.5	The index factors almost have no prominent influence
2.5	Index factors have a slightly prominent impact
3.5	Index factors have a significant impact
4.5	Index factors have a strong prominent impact
5.5	Index factors have extremely prominent influence
2.0, 3.0, 4.0, 5.0	The median value of adjacent scales represents the scale between two adjacent scales

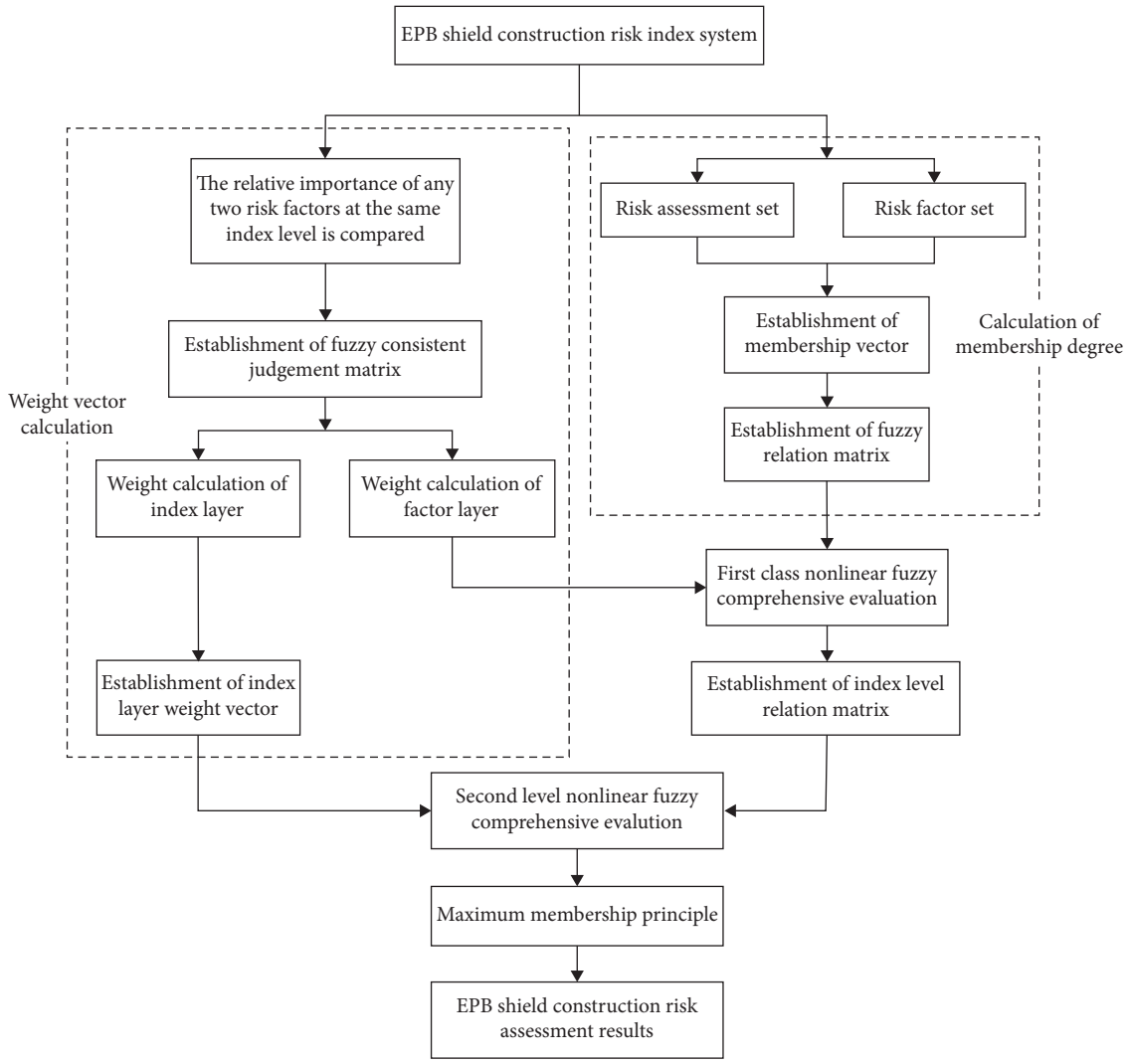

Figure 4: EPB shield construction risk assessment model.

applied to the risk assessment of EPB shield construction, the analysis results are more reasonable, feasible, and operatable.

4. Project Case Analysis

4.1. Project Overview. To verify the rationality and effectiveness of the model, it is applied to the EPB shield construction section of a tunnel project in Hangzhou. The EPB shield section is mainly located in muddy silty clay stratum. The shield passes under a DN610 mm high-pressure natural gas pipeline once, with a buried depth of approximately 5.5~8.6 m; passes under a DN500 mm medium pressure natural gas pipeline once, with a buried depth of approximately 2.2 m; passes under a 400 ∗ 200 mm optical fiber military optical cable twice, with buried depth of approximately 0.74~0.9 m. In addition, there are small and medium-sized buildings along the construction line, and the nearest building is only 10 m away from the tunnel centerline. The geological formation of the tunnel project in Hangzhou is shown in Figure 5.

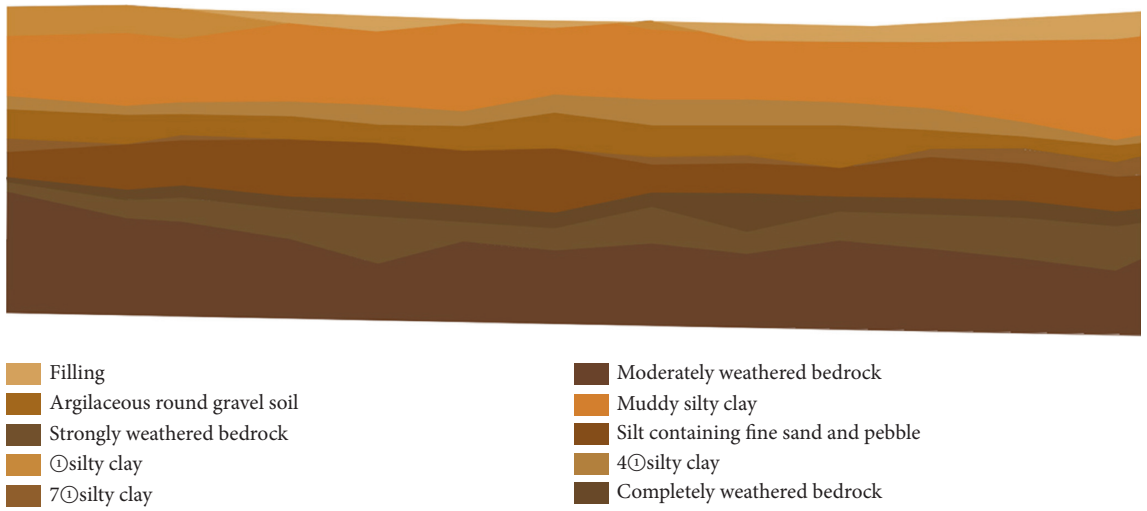

Figure 5: Geological formation of the tunnel project in Hangzhou.

4.2. Weight Vector Calculation.

Step 1: The fuzzy complementary matrix is established by using the 0.1~0.9 scale method. According to the established risk index system, the matrix between the first layer and the second layer is set as $A-B$, the matrix between the second layer and the third layer is set as $B_1-C, B_2-C, B_3-C, B_4-C$. Take $A-B$ as an example.

Step 2: The fuzzy complementary matrix is transformed into a fuzzy consistent judgment matrix according to formulas (1) and (2). (Table 5)

Step 3: Calculate the weight value of each factor in the fuzzy consistent matrix of each level through formula (4). To improve the resolution of sorting, take $a=(n-1)/2$. Then, the weight value of each factor of layer B relative to layer A is given in Table 6.

$$\begin{aligned}
w_1^1 &= \frac{1}{4}-\frac{1}{2\times 4-1/2}+\frac{1}{4\times 4-1/2}\times(0.500+0.350+0.538+0.413)=0.217,\\
w_2^1 &= \frac{1}{4}-\frac{1}{2\times 4-1/2}+\frac{1}{4\times 4-1/2}\times(0.650+0.500+0.688+0.563)=0.317,\\
w_3^1 &= \frac{1}{4}-\frac{1}{2\times 4-1/2}+\frac{1}{4\times 4-1/2}\times(0.462+0.312+0.500+0.375)=0.192,\\
w_4^1 &= \frac{1}{4}-\frac{1}{2\times 4-1/2}+\frac{1}{4\times 4-1/2}\times(0.587+0.437+0.625+0.500)=0.275,\\
w_1 &= \left(w_1^1, w_2^1, w_3^1, w_4^1\right)=(0.217, 0.317, 0.192, 0.275).
\end{aligned} \tag{11}$$

Similarly, the weight value of each factor of layer C relative to layer B is as follows:

(i) Risk of the geological condition:

$$\begin{aligned}
w_{21} &= \left(w_1^{21}, w_2^{21}, w_3^{21}, w_4^{21}, w_5^{21}\right)\\
&= (0.319, 0.288, 0.256, 0.219, 0.231).
\end{aligned} \tag{12}$$

(ii) Environmental risk sources along the shield construction line:

$$\begin{aligned}
w_{22} &= \left(w_1^{22}, w_2^{22}, w_3^{22}, w_4^{22}\right)\\
&= (0.309, 0.259, 0.233, 0.200).
\end{aligned} \tag{13}$$

(iii) Risk of the shield machine:

$$\begin{aligned}
w_{23} &= \left(w_1^{23}, w_2^{23}, w_3^{23}, w_4^{23}, w_5^{23}\right)\\
&= (0.269, 0.288, 0.238, 0.219, 0.300).
\end{aligned} \tag{14}$$

(iv) Risk of the shield tunnel:

$$\begin{aligned}
w_{24} &= \left(w_1^{24}, w_2^{24}, w_3^{24}, w_4^{24}, w_5^{24}\right)\\
&= (0.343, 0.305, 0.199, 0.218, 0.249).
\end{aligned} \tag{15}$$

According to the calculated weight value, the environmental risk along the line and the risk of the tunnel itself are the two factors that affect the safety of EPB shield

Table 5: *A*-*B* fuzzy complementary matrix.

A	B_1	B_2	B_3	B_4
B_1	0.500	0.200	0.600	0.300
B_2	0.800	0.500	0.900	0.600
B_3	0.400	0.100	0.500	0.300
B_4	0.700	0.400	0.700	0.500

Table 6: *A*-*B* fuzzy consistent matrix.

A	B_1	B_2	B_3	B_4
B_1	0.500	0.350	0.538	0.413
B_2	0.650	0.500	0.688	0.563
B_3	0.462	0.321	0.500	0.375
B_4	0.587	0.437	0.625	0.500

construction, and the other two risk factors cannot be ignored. Among the environmental risk factors along the line, the risk of surface building settlement and underground pipeline damage is greater. Among the risk factors for the tunnel itself, the risk of excavation route deviation and segment floating is greater.

4.3. Calculation of the Membership Degree. The expert evaluation method is used to score the secondary risk factors in the EPB shield construction risk assessment of a tunnel project in Hangzhou. The membership degree values of the risk factors are as shown in Table 7:

By combining the membership value of secondary risk factors for the EPB shield construction risk assessment with formula (8), the fuzzy evaluation matrix AA of the geological condition risk, the fuzzy evaluation matrix BB of the environmental risk along the line, the fuzzy evaluation matrix cc of the shield equipment risk, and the fuzzy evaluation matrix DD of tunnel risk are constructed, which can be used for the nonlinear fuzzy comprehensive calculation and are constructed as follows

$$
\begin{aligned}
R_1 &= \begin{bmatrix} 0 & 0 & 8 & 2 & 0 \\ 0 & 2 & 7 & 1 & 0 \\ 0 & 3 & 6 & 1 & 0 \\ 0 & 2 & 7 & 1 & 0 \\ 0 & 2 & 7 & 1 & 0 \end{bmatrix}, \\
R_2 &= \begin{bmatrix} 0 & 0 & 2 & 6 & 2 \\ 0 & 0 & 3 & 6 & 1 \\ 0 & 1 & 5 & 4 & 0 \\ 0 & 2 & 6 & 2 & 0 \end{bmatrix}, \\
R_3 &= \begin{bmatrix} 0 & 5 & 5 & 0 & 0 \\ 0 & 4 & 5 & 1 & 0 \\ 1 & 4 & 5 & 0 & 0 \\ 2 & 3 & 5 & 0 & 0 \\ 0 & 2 & 6 & 2 & 0 \end{bmatrix}, \\
R_4 &= \begin{bmatrix} 0 & 0 & 1 & 7 & 2 \\ 0 & 0 & 2 & 7 & 1 \\ 2 & 5 & 3 & 0 & 0 \\ 0 & 3 & 6 & 1 & 0 \\ 0 & 3 & 6 & 1 & 0 \end{bmatrix}.
\end{aligned} \tag{16}
$$

4.4. Determination of the Risk Index Prominent Influence Degree Coefficient. According to the actual situation of the EPB shield construction section of a tunnel project in Hangzhou and by combining the 1~9 scale method and λ_i value principle, the values of the prominent influence coefficient of the first-level risk factors and the prominent influence coefficient of the second-level risk factors are determined as follows in Table 8:

According to the prominent influence coefficient values of the risk factors determined in Table 9, the corresponding prominent influence coefficient vectors of risk indicators of nonlinear fuzzy evaluation matrix R_1, R_2, R_3, R_4 are constructed as follows:

$$
\begin{aligned}
\Lambda_1 &= (3.0, 3.0, 2.5, 3.0, 2.5), \\
\Lambda_2 &= (4.5, 4.0, 3.5, 3.0), \\
\Lambda_3 &= (1.52.0, 2.5, 2.5, 3.5), \\
\Lambda_4 &= (4.5, 4.0, 1.5, 1.5, 2.0).
\end{aligned} \tag{17}
$$

4.5. First-Level Nonlinear Fuzzy Comprehensive Evaluation. By substituting the obtained weight value of secondary risk factors, nonlinear fuzzy evaluation matrix, and prominent influence coefficient vector of risk index into formula (7), the following results can be obtained:

$$
\begin{aligned}
N_1 &= \mathrm{f}(W_1, R_1, \Lambda_1) \\
&= (0.319, 0.288, 0.256, 0.219, 0.231) \begin{bmatrix} 0 & 0 & 8^{3.0} & 2^{3.0} & 0 \\ 0 & 2^{3.0} & 7^{3.0} & 1^{3.0} & 0 \\ 0 & 3^{2.5} & 6^{2.5} & 7^{2.5} & 0 \\ 0 & 2^{3.0} & 7^{3.0} & 1^{3.0} & 0 \\ 0 & 2^{2.5} & 7^{2.5} & 1^{2.5} & 0 \end{bmatrix}^{1/3.0} \\
&= [0, 2.1070, 7.3046, 3.3165, 0].
\end{aligned} \tag{18}
$$

After normalization, the results can be obtained as follows: $N_1 = [0, 0.1655, 0.5739, 0.2606, 0]$

In the same way, the following result is obtained:

$$
\begin{aligned}
N_3 &= [0.1194, 0.2444, 0.4812, 0.1550, 0], \\
N_2 &= [0, 0.1075, 0.2802, 0.4663, 0.1460], \\
N_4 &= [0.0519, 0.1000, 0.1405, 0.5968, 0.1108].
\end{aligned} \tag{19}
$$

4.6. Second-Level Nonlinear Fuzzy Comprehensive Evaluation. According to the above results, a new single factor evaluation matrix $R_N = [N_1 N_2 N_3 N_4]^T$ is constructed

Table 7: Membership value table of the risk factors.

Risk level risk factor	C_{11}	C_{12}	C_{13}	C_{14}	C_{15}	C_{21}	C_{22}	C_{23}	C_{24}	C_{31}	C_{32}	C_{33}	C_{34}	C_{35}	C_{41}	C_{42}	C_{43}	C_{44}	C_{45}
Level 1	0	0	0	0	0	0	0	0	0	0	0	0.1	0.2	0	0	0	0.2	0	0
Level 2	0	0.2	0.3	0.2	0.2	0	0	0.1	0.2	0.5	0.4	0.4	0.3	0.2	0	0	0.5	0.3	0.3
Level 3	0.8	0.7	0.6	0.7	0.7	0.2	0.3	0.5	0.6	0.5	0.5	0.5	0.5	0.6	0.1	0.2	0.3	0.6	0.6
Level 4	0.2	0.1	0.1	0.1	0.1	0.6	0.6	0.4	0.2	0	0.1	0	0	0.2	0.7	0.7	0	0.1	0.1
Level 5	0	0	0	0	0	0.2	0.1	0	0	0	0	0	0	0	0.2	0.1	0	0	0

Table 8: Prominent influence coefficient of the first-level risk factors.

Evaluating indicator	B_1	B_2	B_3	B_4
Λ	3.0	4.0	2.5	3.5

Table 9: Prominent influence coefficient of the second-level risk factors.

Evaluating indicator	C_{11}	C_{12}	C_{13}	C_{14}	C_{15}	C_{21}	C_{22}	C_{23}	C_{24}	C_{31}	C_{32}	C_{33}	C_{34}	C_{35}	C_{41}	C_{42}	C_{43}	C_{44}	C_{45}
λ	3.0	3.0	2.5	3.0	2.5	4.5	4.0	3.5	3.0	1.5	2.0	2.5	2.5	3.5	4.5	4.0	1.5	1.5	2.0

and transformed by formula (8) to meet the requirements of the nonlinear fuzzy evaluation calculation. The conversion results are as follows:

$$R'_N = \begin{bmatrix} 8.486 & 16.358 & 22.990 & 97.669 & 18.157 \\ 0 & 1.075 & 2.802 & 4.663 & 1.460 \\ 1.194 & 2.444 & 4.812 & 1.550 & 0 \\ 0.519 & 1 & 1.405 & 5.968 & 1.108 \end{bmatrix}. \quad (20)$$

According to the above steps, the prominent influence coefficient matrix vector corresponding to the first-level risk factors is $\Lambda = [3.0, 4.0, 2.5, 3.5]$, and the weight vector of the first-level risk factors is $\Lambda = [3.0, 4.0, 2.5, 3.5]$. The above results are substituted into formula (7), and the results of the second-level nonlinear fuzzy comprehensive evaluation are determined as follows:

$$\begin{aligned} N &= \mathrm{f}\left(W_{A-B}, R'_N, \Lambda\right) \\ &= (0.217, 0.317, 0.192, 0.275) \circ \begin{bmatrix} 8.486 & 16.358 & 22.990 & 97.669 & 18.157 \\ 0 & 1.0755 & 2.802 & 4.663 & 1.460 \\ 1.194 & 2.444 & 4.812 & 1.550 & 0 \\ 0.519 & 1 & 1.405 & 5.968 & 1.108 \end{bmatrix}^{\frac{1}{4.0}} \\ &= [2.2134, 4.6349, 7.1873, 24.6111, 4.7076]. \end{aligned} \quad (21)$$

After normalization, the total risk evaluation vector of EPB shield construction of a tunnel project in Hangzhou is obtained as follows:

$$N = [0.0510, 0.1069, 0.1658, 0.5677, 0.1086]. \quad (22)$$

Finally, combined with the principle of the maximum membership degree, it can be judged that the overall construction risk level of the EPB shield of the tunnel project in Hangzhou is grade 4, which indicates high risk. Among them, the greater risk is the environmental risk along the line and the risk of the tunnel itself. At the same time, the risks of the geological conditions and the shield equipment cannot be ignored, which is in line with the actual situation of the EPB shield construction of the tunnel project in Hangzhou.

5. Discussion

To verify the effectiveness of the EPB shield construction risk assessment model based on the nonlinear fuzzy analytic hierarchy process, the linear fuzzy analytic hierarchy process is used to calculate the data provided by the same group of field managers and experts, that is, the prominent influence coefficient of each risk factor at all levels is 1. The fuzzy comprehensive evaluation vector of the calculation results is as follows:

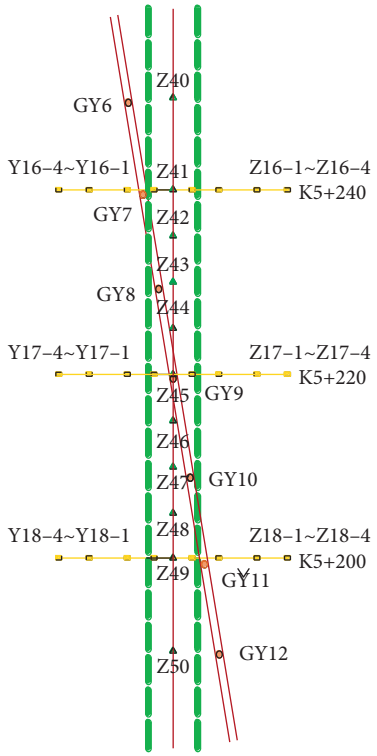

Figure 6: Layout of the surface monitoring points.

$$N' = [0.0261, 0.2347, 0.5804, 0.3242, 0.0505]. \quad (23)$$

According to the principle of maximum membership degree, the overall construction risk level of EPB shield construction section of the tunnel project in Hangzhou is grade 3, which belongs to medium risk. However, the nonlinear FAHP considers the influence of outstanding index factors on the risk level, so the risk level obtained by the nonlinear FAHP is higher than that obtained by the linear FAHP.

The surface displacement monitoring data above the pipeline of the EPB shield obliquely crossing the construction section of the high-pressure natural gas pipeline are selected for verification. The layout of surface monitoring points in the selected construction section, the surface monitoring displacement above the pipeline, and the surface monitoring displacement above the shield tunnel are shown in Figures 6–8:

This section is a construction section of EPB shield tunneling under a natural gas high-pressure pipeline at a small intersection angle of 11.4° and is mainly located at the underpass mileage of $K5 + 240 \sim K5 + 200$. According to the undercrossing range of the new tunnel in the existing pipeline, monitoring points are arranged on the surface of the upper part of the pipeline at a distance of 10 m before and after undercrossing the pipeline. It can be seen from Figures 7 and 8 that during the period of the EPB shield crossing the high-pressure natural gas pipeline obliquely, the ground surface above the pipeline and above the tunnel is greatly disturbed by the shield, showing an uplift state as a whole. Among them, the maximum uplift of the surface

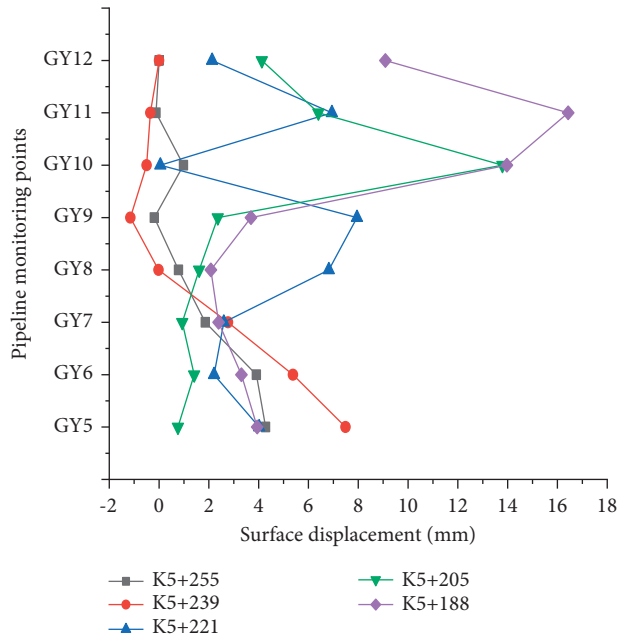

Figure 7: Surface monitoring displacement above the pipeline.

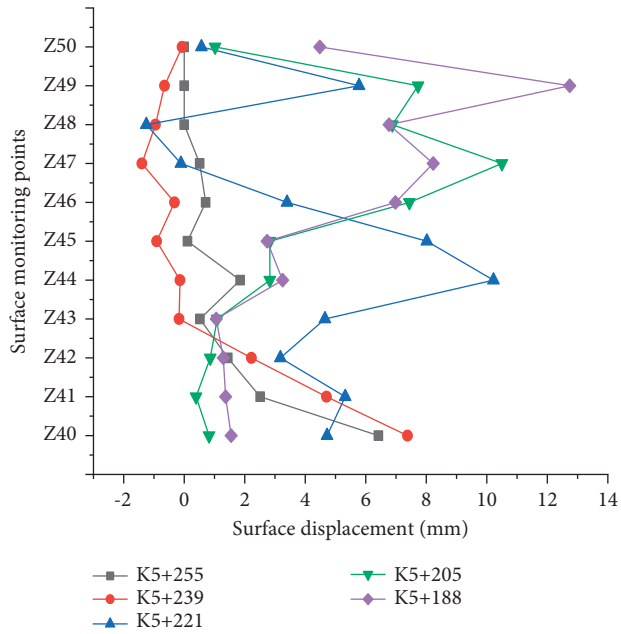

Figure 8: Surface monitoring displacement above the shield tunnel.

above the pipeline is 16.43 mm, which exceeds the control value of displacement ≤10 mm required by the control index of the underground pressure pipeline, and the maximum uplift of the surface above the shield tunnel is 12.74 mm. This finding proves that the EPB shield construction risk assessment model based on a nonlinear fuzzy analytic hierarchy process can well reflect the actual risk situation of construction and has a certain reliability and effectiveness.

6. Conclusion

The construction risk index system of an EPB shield in a soft soil area is constructed by the WBS and RBS methods, the judgment matrix is constructed by a fuzzy consistent matrix, and a nonlinear fuzzy mathematics theory is introduced to discuss the construction risk of the EPB shield:

(1) Based on the WBS-RBS method, the risk index system of EPB shield construction is constructed, which makes up for possible risk omission or incomplete identification in the expert evaluation method so that the constructed risk index system can more comprehensively reflect various risk factors and the actual situation of all levels of risk in EPB shield construction.

(2) By using pairwise comparison method to collect expert questionnaires and transforming fuzzy complementary matrix to establish fuzzy consistency judgment matrix, it not only meets the accuracy and consistency requirements of expert scoring but also avoids the cumbersome consistency test.

(3) Combining the nonlinear operator with the traditional fuzzy analytic hierarchy process, a new risk assessment model for EPB shield construction in soft soil areas based on a nonlinear fuzzy analytic hierarchy process is constructed. The outstanding influence of the risk factors is considered, and the nonlinear characteristics of the assessment process are reflected, which makes the EPB shield construction risk assessment results more reasonable. The validity of the model is verified by nonlinear calculation and linear calculation of the data provided by the same group of experts, and the results are compared with the measured data [33–35].

Data Availability

The data for the final analysis in this study are available from the corresponding author upon reasonable request.

Conflicts of Interest

The authors declare that there are no conflicts of interest regarding the publication of this paper.

Acknowledgments

This work was supported by the Key Research and Development Project in Shaanxi Province (Nos. 2020SF-373 and 2021SF-523).

References

[1] X. Li and X. Chen, "Using grouting of shield tunneling to reduce settlements of overlying tunnels: case study in shenzhen metro construction," *Journal of Construction Engineering and Management*, vol. 138, no. 4, pp. 574–584, 2012.

[2] L. Ding, L. Zhang, and X. Wu, "Safety management in tunnel construction: case study of Wuhan metro construction in China," *Safety Science*, vol. 62, pp. 8–15, 2014.

[3] H. H. Einstein, "Risk and risk analysis in rock engineering," *Tunnelling and Underground Space Technology*, vol. 11, no. 2, pp. 141–155, 1996.

[4] H.-H. Choi, H.-N. Cho, and J. W. Seo, "Risk assessment methodology for underground construction projects," *Journal of Construction Engineering and Management*, vol. 130, no. 2, pp. 258–272, 2004.

[5] M. Dağdeviren and İ. Yüksel, "Developing a fuzzy analytic hierarchy process (AHP) model for behavior-based safety management," *Information Sciences*, vol. 178, no. 6, pp. 1717–1733, 2008.

[6] H. Zhou and P. Cao, "Fuzzy analytic hierarchy process for optimization of urban deep foundation pit support scheme in soft soil area," *Journal of Central South University*, vol. 43, pp. 3582–3588, 2012.

[7] B. Liu, K. Q. Wang, M. Huang, P. Huang, and H. G. Zhang, "Study on fuzzy analytic hierarchy process of risk in subway deep foundation pit engineering," *Journal of Underground Space and Engineering*, vol. 11, pp. 257–264, 2015.

[8] X. Deng, R. Wang, and T. Xu, "Risk assessment of tunnel portals in the construction stage based on fuzzy analytic hierarchy process," *Archives of Civil Engineering*, vol. 64, no. 4, pp. 69–87, 2018.

[9] Q. Lu, Z. Huo, B. Zhao, J. Xiang, and J. He, "Tunnel collapse risk assessment based on Fuzzy AHP and consequence equivalence method," *Tunnel construction (Chinese and English)*, vol. 38, pp. 31–38, 2018.

[10] C. Samantra, S. Datta, and S. S. Mahapatra, "Fuzzy based risk assessment module for metropolitan construction project: an empirical study," *Engineering Applications of Artificial Intelligence*, vol. 65, pp. 449–464, 2017.

[11] D. Kuchta and E. Ptaszyńska, "Fuzzy Based Risk Register for Construction Project Risk Assessment," *American Institute of Physics Conference Series*, vol. 1863, 2017.

[12] H. Yu, Y. Li, and L. Li, "Evaluating Some Dynamic Aspects of TBMs Performance in Uncertain Complex Geological Structures," *Tunnelling and Underground Space Technology*, vol. 96, Article ID 103216, 2020.

[13] H. Nezarat, F. Sereshki, and M. Ataei, "Ranking of geological risks in mechanized tunneling by using Fuzzy Analytical Hierarchy Process (FAHP)," *Tunnelling and Underground Space Technology*, vol. 50, pp. 358–364, 2015.

[14] H.-M. Lyu, S.-L. Shen, A. Zhou, and J. Yang, "Risk assessment of mega-city infrastructures related to land subsidence using improved trapezoidal FAHP," *Science of The Total Environment*, vol. 717, Article ID 135310, 2020.

[15] Q. Hu, B. Zhou, F. Wang, and Z. NIU, "Safety assessment technology of highway tunnel structure based on fuzzy analytic hierarchy process," *Journal of Natural Disasters*, vol. 27, pp. 41–49, 2018.

[16] L. Zhu, M. Lei, W. Wang, M. Chen, and B. Zheng, "Fuzzy evaluation method and application of long tunnel construction organization," *Journal of Civil Engineering and Management*, vol. 37, pp. 159–164, 2020.

[17] X. Y. Wang and Z. Ma, "Research on safety early warning standard of large-scale underground utility tunnel in ground fissure active period," *Frontiers in Earth Science*, vol. 10, 2022.

[18] X. Wang and Q. Song, "Research on deformation law of deep foundation pit of station in core region of saturated soft loess based on monitoring," *Advances in Civil Engineering*, vol. 2022, pp. 1–16, Article ID 7848152, 2022.

[19] Q. Zheng, H.-M. Lyu, and A. Zhou, "Risk assessment of geohazards along Cheng-Kun railway using fuzzy AHP incorporated into GIS," *Geomatics, Natural Hazards and Risk*, vol. 12, no. 1, pp. 1508–1531, 2021.

[20] Y. Lv, "Ranking of fuzzy analytic hierarchy process based on fuzzy consistent matrix," *Fuzzy systems and mathematics*, vol. 02, pp. 79–85, 2002.

[21] M. Tavakolan and H. Etemadinia, "Fuzzy weighted interpretive structural modeling: improved method for identification of risk interactions in construction projects," *Journal of Construction Engineering and Management*, vol. 143, no. 11, 2017.

[22] Q. Zou, J. Zhou, C. Zhou, and L. Song, "Comprehensive flood risk assessment based on set pair analysis-variable fuzzy sets model and fuzzy AHP," *Stochastic Environmental Research and Risk Assessment*, vol. 27, no. 2, pp. 525–546, 2013.

[23] S. Lee, "Determination of priority weights under multiattribute decision-making situations: AHP versus Fuzzy AHP," *Journal of Construction Engineering and Management*, vol. 141, 2015.

[24] F. Li, K. K. Phoon, X. Du, and M. Zhang, "Improved AHP method and its application in risk identification," *Journal of Construction Engineering and Management*, vol. 139, 2013.

[25] Z. Song, D. Guo, T. Xu, and W. Hua, "Research on TBM construction risk evaluation model based on nonlinear fuzzy analytic hierarchy process," *Geotechnical mechanics*, vol. 42, 2021.

[26] H. M. Lyu, W. J. Sun, S. L. Shen, and A. N. Zhou, "Risk assessment using a new consulting process in fuzzy AHP," *Journal of Construction Engineering and Management*, vol. 146, 2020.

[27] J. Zhang, "Fuzzy analytic hierarchy process (FAHP)," *Fuzzy systems and mathematics*, vol. 02, pp. 80–88, 2000.

[28] D. Hillson and S. Grimaldi, "Managing Project Risks Using a Cross Risk Breakdown Matrix," *Risk Management*, vol. 8, no. 1, pp. 61–76, 2006.

[29] J. Xie and C. Liu, *Fuzzy Mathematical Method and its Application*, Huazhong University of Science and Technology Press, Wuhan, 2006.

[30] M. Yao and S. Zhang, "Fuzzy Consistent Matrix and its Application in Soft Science," *Systems engineering*, vol. 8, no. 1, 1997.

[31] W. Cao, Y. Zhai et al., "Nonlinear fuzzy evaluation method for tunnel construction risk of NATM," *Journal of Civil Engineering*, vol. 43, pp. 105–112, 2010.

[32] X. H. Zhang and Y. J. Feng, "A Nonlinear Fuzzy Comprehensive Assessment Model," *Systems Engineering-theory & Practice*, 2005.

[33] L. Tian Shy and J. Wang Mao Jiun, "Ranking fuzzy numbers with integral value," *Fuzzy Sets and Systems*, vol. 50, 1992.

[34] H.-M. Lyu and S.-L. Shen, "Inundation analysis of metro systems with the storm water management model incorporated into a geographical information system: a case study in Shanghai," *Hydrology and Earth System Sciences*, vol. 23, no. 10, pp. 4293–4307, 2019.

[35] H.-M. Lyu, S.-L. Shen, and A.-N. Zhou, "Flood risk assessment of metro systems in a subsiding environment using the interval FAHP-FCA approach," *Sustainable Cities and Society*, vol. 50, Article ID 101682, 2019.

Hindawi
Advances in Civil Engineering
Volume 2022, Article ID 6071868, 14 pages
https://doi.org/10.1155/2022/6071868

Research Article

Numerical Analysis of the Influence of Deep Foundation Pit Construction on Adjacent Subway Stations in Soft Soil Areas

Tao Yang, Shengyuan Xiong, Shuailei Liu, Yang Liu, Hao Zhao, and Yanwei Li

School of Urban Planning and Municipal Engineering, Xi'an Polytechnic University, Xi'an, Shaanxi 710048, China

Correspondence should be addressed to Tao Yang; yangtao@xpu.edu.cn

Received 16 February 2022; Revised 10 March 2022; Accepted 23 March 2022; Published 5 April 2022

Academic Editor: Yuan Mei

Deep foundation pit construction adjacent to a subway station in a soft soil area was numerically simulated with Midas GTS NX calculation software. The influence of the deep foundation pit construction on the deformation and stress of the subway station structure was studied, and the influence of the foundation pit retaining structure on the station was analyzed. The results show that during the foundation pit excavation process, the subway station slab rose as a whole and was greatly affected by the deformation of the common ground connecting wall, with the most unfavorable position changing as the excavation area changed. The excavation of foundation pits in different zones had a considerable influence on the east-to-west displacement of the common diaphragm wall outside the foundation pit. The maximum positive bending moment of the common diaphragm wall changed little, while the negative bending moment increased greatly during construction. Overall, the foundation pit excavation had a great impact on the negative moment of the common diaphragm wall. During the foundation pit excavation process, the subway station column lifted upward, and the maximum displacement, which was located at the west end of the station near the foundation pit, gradually weakened from west to east. As the foundation pit excavation process continued, the maximum axial force of the station column increased by 10.38%, and the pressure was the largest in the middle column. As the thickness of the diaphragm wall increased, the stiffness of the foundation pit retaining structure increased. After earthwork excavation and unloading, the locations in the retaining structure with high stiffnesses could resist deformations. The whole foundation pit was offset due to the high stiffness of the foundation pit retaining structure, which increased the horizontal deformation of the existing station structure. With increasing thickness, the relative horizontal deformation of the station slab gradually increased, mainly because the difference between the depths of the old and new diaphragm walls caused the embedded soil of the two same deep foundation pits to differ. Furthermore, there were great differences in the Earth pressure behind the wall. As the depth of the diaphragm wall increased, the active Earth pressure behind the diaphragm wall increased.

1. Introduction

As urban underground space and rail transit have rapidly developed, commercial and civil construction along subway lines have increased, resulting in building foundation pits becoming increasingly closer to subway stations [1]. When the soil inside a deep foundation pit is excavated, the soil stress is redistributed, and the pressure on both sides of the retaining structure becomes unbalanced, resulting in the displacement of the retaining structure inside the foundation pit, which produces additional stress on adjacent subway structures, causing the subway structure to deform and affecting the safe operation of the subway [2]. In recent years, many scholars have studied disturbances caused by foundation pit excavation in soft soil areas with numerical simulations. As an example, Jian et al. [3] used finite element analysis software and actual monitoring results from a foundation pit project to propose a generalized curve for the ground settlement behind a foundation pit support structure in a soft soil area, and they developed an applicable formula for the lateral deformation of the support structure and the ground settlement. Sun [4] used finite element analysis software to simulate the influence of deep foundation pit excavation on adjacent subway stations, and they analyzed the stress of deep foundation pit retaining structures and studied the internal force and deformation of subway

stations. Wang et al. [5] used ABAQUS software to study the deformation characteristics of an existing subway station by excavating on both sides of a deep foundation pit. The results showed that symmetrical excavation was beneficial for controlling the horizontal displacement of the subway station, while asymmetric excavation was beneficial for controlling the vertical displacement of the station. Guo et al. [6] simulated the deformation of a common diaphragm wall foundation pit during subway station transfer with ABAQUS software. In contrast to the deformation of ordinary retaining structures without underground structures, the deformation of the underground diaphragm walls in common sections was small above the foundation pit excavation surface, with the greatest lateral deformation occurring 8 m below the excavation surface.

There are few reports on the deformation mechanisms of deep foundation pit construction adjacent to subway stations in existing research. With an increasing number of underground diaphragm walls shared by subway stations and foundation pits, determining the stress change in the surrounding soil due to deep foundation pit excavation and the deformation mechanism of common wall subway stations due to changes in soil stress are major tasks, as well as a source of concern for many scholars [7, 8]. Based on a deep foundation pit project in Suzhou and simulations of different subway station structures, this paper explores the deformation relationship and internal force action mechanism of adjacent subway stations caused by deep foundation pit excavation to provide a reference for relevant projects.

2. Project Introduction

2.1. Project Profile. In a station foundation pit project in Suzhou, the total length of the foundation pit was 407.1 m, the excavation width of the standard section was 20.35 m, and the width of the docking expansion section near the end of metro line S3 was 41.7 m. The excavation depth of the station basement was 17~19 m, and the thickness of the roof soil was approximately 2.9~3.5 m. The whole foundation pit was constructed by the open-cut method. To avoid disrupting traffic, a temporary pavement system was built along Yiting Road and the S3 line, and semicover excavation was carried out. In this foundation pit, two sealing walls were installed, dividing the foundation pit into three sections. A schematic diagram of the foundation pit is shown in Figure 1.

2.2. Geological Conditions. The proposed site was located in a low-terrain region of the Tai Hu Basin, in the lower reaches of the Yangtze River. The foundation soil from the surface to a depth of approximately 70.0 m consists of loose sediments deposited from the Quaternary Holocene to the early Pleistocene era, mainly clay soil and interbedded sandy soil. The physical and mechanical parameters of the soil layer are shown in Table 1. The groundwater at the site was divided into three categories based on the occurrence condition: groundwater in the shallow filling layer, with a stable water level of 0.51~0.90 m; microconfined water in the ③$_3$ silt layer and ④$_2$ silt sand layer, with a stable water level of 0.50~0.60 m; and confined water in the ⑦$_2$ silt sand layer, with a stable water level of −2.50 to −2.80 m and an annual variation of approximately 1 m.

2.3. Foundation Pit Excavation and Enclosure Scheme. The station foundation pit was constructed by section, and the foundation pits in areas B and C at both ends were preferentially excavated. The foundation pit in area A, which was close to the station of metro line S3 and had the longest excavation length, was not initially excavated. After the integral support structures were constructed in areas B and C, the foundation pit in area A was excavated. As a result, the support stiffness of the S3 subway station was increased and the foundation pit excavation length was decreased, effectively reducing the influence of the narrow and long foundation pit excavation on the S3 subway structure and minimizing the influence of soil unloading on the S3 subway station, reducing the construction risk. The construction was carried out in strict accordance with the principle of "support before excavation, limited time support, layered excavation, and no over excavation" to minimize the exposure time and area of the foundation pit without support. Figure 2 shows a sectional construction drawing of the station foundation pit.

Given the deep foundation pit excavation, poor geological conditions, and high safety risks, an 800 mm thick diaphragm wall and an internal support enclosure scheme were designed. The length of the designed ground wall in the standard section was 29.5 m, the length of the end ground wall was 32.5 m, the length of the continuous wall under the cover was 30.64 m, and the total length of the enclosure structure completed in one week was 783 m. The inner support included both concrete support and steel support, with a section size of 800 mm × 1000 mm for the concrete support and a section diameter of 609 mm for the steel support. The excavation of the foundation pit inevitably disrupted the surrounding environment. To ensure the protection of the S3 line during construction, eight MJS (Metro Jet System) piles were set in the joint of the common ground wall for water-stop reinforcement.

3. Foundation Pit Excavation Simulation

3.1. Model Establishment. After consulting a large number of papers on numerical simulations of foundation pit excavations, the modified Mohr–Coulomb model was adopted, and Midas GTS NX software was used to simulate the project. The modified Mohr–Coulomb model was adjusted based on the Mohr–Coulomb constitutive model. This model is essentially a combination of a nonlinear elastic model and an elastic-plastic model. It is commonly used to simulate silt and sand. The modified Mohrs–Coulomb model can simulate double hardening behavior, which is not affected by shear failure or compressive yield. Table 2 shows the soil layer and structural calculation parameters.

According to the Saint-Venant principle, deformation and settlement effects at distances larger than three times the

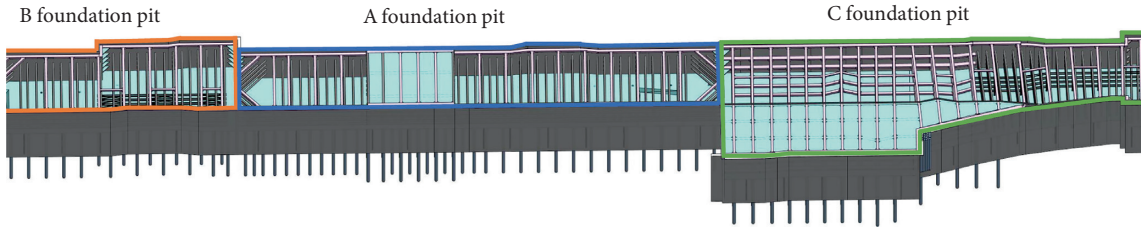

Figure 1: Schematic diagram of a foundation pit.

Table 1: Physical and mechanical parameters of the soil layer.

Soil horizon	Moisture content W (%)	Specific gravity (G_s)	Force of cohesion C (kPa)	Internal friction angle ϕ/°	Modulus of compression E_s (MPa)
①$_3$ plain fill	32.0	2.73	15	12	—
③$_1$ clay	26.9	2.74	43.0	15.5	8.10
③$_2$ silty clay	29.8	2.73	25.5	12.1	6.91
③$_3$ silt	28.6	2.69	6.0	25.4	10.69
④$_2$ sand with silt	26.3	2.69	3.8	31.8	12.50
⑤$_1$ silty clay	30.2	2.73	29.8	14.3	6.01
⑥$_1$ clay	25.8	2.74	54.9	16.1	8.36
⑥$_2$ silty clay	28.5	2.73	29.7	13.8	6.41
⑦$_1$ silty clay	31.6	2.72	27.6	15.0	5.32
⑦$_2$ silty soil with silt	28.6	2.70	10.8	23.4	9.45

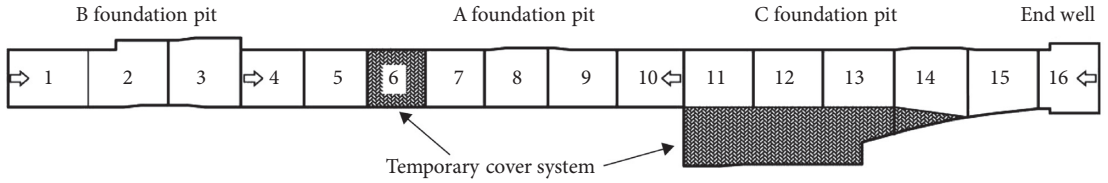

Figure 2: Sectional construction drawing of the station foundation pit.

Table 2: Soil layer and structural parameters.

Soil layer and structural	μ	C (kPa)	ϕ/°	Material type	γ (kN/m^3)	K_0	E_s/(MPa)
①$_3$ plain fill	0.43	15.0	12.0	—	18.62	0.75	—
③$_1$ clay	0.32	43.0	15.5	—	19.40	0.48	8.10
③$_2$ silty clay	0.33	25.5	12.1	—	18.91	0.50	6.91
③$_3$ silt	0.30	6.0	25.4	—	18.62	0.43	10.69
④$_2$ sand with silt	0.29	3.8	31.8	—	19.01	0.41	12.50
⑤$_1$ silty clay	0.33	29.8	14.3	—	18.91	0.50	6.01
⑥$_1$ clay	0.31	54.9	16.1	—	19.70	0.45	8.36
⑥$_2$ silty clay	0.32	29.7	13.8	—	19.21	0.47	6.41
⑦$_1$ silty clay	0.35	27.6	15.0	—	18.72	0.53	5.32
⑦$_2$ silty soil with silt	0.31	10.8	23.4	—	18.82	0.44	9.45
Crown beam	0.2	—	—	C35	25	—	30000
Underground continuous wall	0.2	—	—	C35	25	—	30000
Surrounding	0.3	—	—	Q235	78	—	210000
Concrete support	0.2	—	—	C35	25	—	30000
Steel support	0.3	—	—	Q235	78	—	210000

excavation edge of the deep foundation pit are small and can be ignored. When this result was combined with provisions in the technical code for construction safety in the Building Deep Foundation Pit Engineering (JGJ311-2013) [9], the range $0.7H$ or $H{\cdot}\tan(45^\circ{-}\varphi/2)$ from the edge of deep foundation pit was determined to be the most important influence area; the secondary influence areas were $0.7H$~(2.0~3.0) H or $H{\cdot}\tan(45^\circ{-}\varphi/2)$~(2.0~3.0) H around deep foundation pit, where H is the design depth of the deep foundation pit (m), as shown in Figure 3. In summary, a

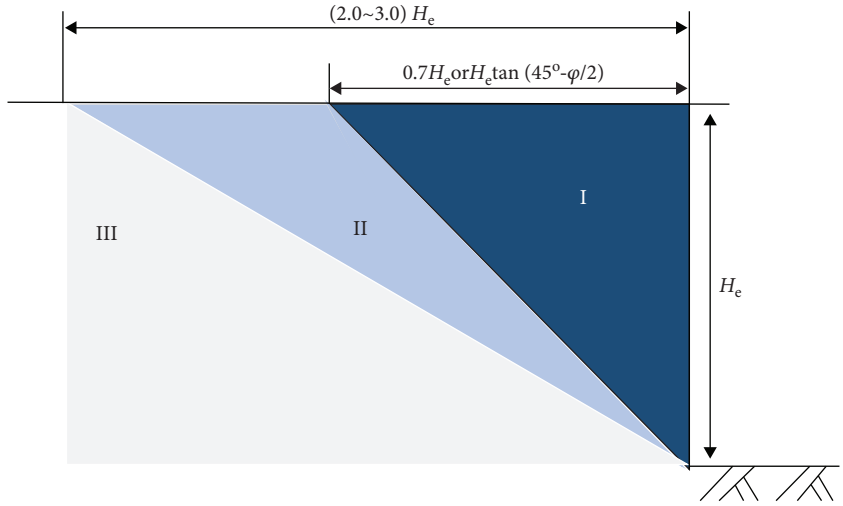

Figure 3: Impact zone of deep foundation pit engineering.

reasonable overall model size was selected based on the size of the deep foundation pit excavation in practical engineering, improving the calculation speed and the presentation of the numerical simulation results. The boundary value in the model was 510 m × 150 m × 60 m.

3.2. Construction Procedures. Midas GTS/NX software was used to simulate the dynamic construction process by activating or passivating the grid group. Deep foundation pit engineering includes the construction of long, narrow, deep foundation pits. Thus, the excavation must be completed in stages. Without changing the construction method, the construction steps were appropriately simplified, as shown in Table 3.

4. Finite Element Calculation Results

In the foundation pit excavation process, the deformation and internal force changes adjacent to the station are important guides for engineering construction. The excavated foundation pit shared a 274.5 m ground connecting wall with a station of line S3, which necessitated complex construction, a large project scale, and many construction steps. Therefore, representative working condition steps were selected for detailed analysis, such as working condition 8 (construction of the bottom plate), working condition 14 (middle stage of the excavation), and working condition 20 (backfilling and covering soil). The influence of the soft soil deep foundation pit excavation on the deformation and internal forces of the floor slab, common wall, and bearing column near the subway station were analyzed with finite element simulation in this section.

4.1. Analysis of the Deformation and Internal Force of the Station Floor Slab Caused by Excavation. Figure 4 shows the deformation of the subway station floor after each zone was excavated. Under working condition 8, the station slab of the noncommon ground wall section and common ground wall section in areas A and C tended to deform outside the foundation pit, with a maximum deformation of −1.95 mm for the overhead slab at the west end of the station. Near the excavation area in area B, the station slab deformed into the foundation pit, with a maximum deformation of 3.96 mm mainly concentrated at the bottom slab. Under working condition 14, the displacement outside the foundation pit adjacent to excavation area C was large, with a maximum deformation of −3.18 mm. The deformation trend of the station slab was consistent with that under working condition 8, with a maximum deformation of 4.31 mm near area B. Under working condition 20, the horizontal displacement of the station floor near areas A and B was large, with a maximum deformation of 5.42 mm. The horizontal deformation of the station slab showed a differential deformation trend of overall deformation inside the foundation pit and local deformation outside the foundation pit. The vertical deformation of the station slab showed a differential deformation trend of overall upward uplift and local downward settlement, with a maximum differential displacement of 8.51 mm, ensuring that the station structure can be used normally. The vertical deformation of the station slab was greatly affected by the heave and subsidence of the common ground wall. The deformation of each layer of the slab was consistent, with the maximum deformation mainly concentrated on the side of the common ground wall. As the excavation progressed, the maximum vertical deformation of the station slab successively occurred at the common ground connecting wall in areas B, C, and A, with values of 5.44 mm, 5.82 mm, and 8.30 mm, respectively. In addition, the maximum vertical displacement of the station slab was much larger than its horizontal displacement. The author believes that foundation pit excavation has a smaller impact on the horizontal direction of the station slab than on the vertical direction of the station slab. The station slab mainly produced uplift deformation and was prone to large vertical displacements due to the joint action of the uplift at the bottom of the foundation pit [10].

During the foundation pit construction process, the soil stress is redistributed, and the internal force of the existing station structure changes accordingly [11]. To further

Table 3: Key construction steps.

Working condition		Construction stage	Excavation depth (m)
1		Balance in-situ stress, building additional stress simulation, displacement clearing	—
2		Construction of diaphragm wall, column and temporary pavement system	—
3		Excavate the first layer of soil as the first concrete support	1.64
4		Excavate the second layer of soil and erect the second steel support	5.04
5		Excavate the third layer of soil and erect the third layer of steel support	7.94
6		Excavate the fourth layer of soil and erect the fourth steel support	10.84
7	Area B	Excavate the fifth layer of soil and erect the fifth steel support	13.74
8		Excavate the sixth layer of soil and construct the bottom plate	17.21
9		Remove the 4th and 5th steel supports, construct side walls and middle plates	—
10		Remove the second and third steel supports, construct side walls and top plates	—
11		Remove the first concrete support and backfill the covering soil	—
12		Excavate the first layer of soil as the first concrete support	1.64
13		Excavate the second layer of soil and erect the second steel support	5.04
14		Excavate the third layer of soil and erect the third layer of steel support	7.94
15		Excavate the fourth layer of soil and erect the fourth steel support	10.84
16	Area C	Excavate the fifth layer of soil and erect the fifth steel support	13.74
17		Excavate the sixth layer of soil and construct the bottom plate	17.21
18		Remove the 4th and 5th steel supports, construct side walls and middle plates	—
19		Remove the second and third steel supports, construct side walls and top plates	—
20		Remove the first concrete support and backfill the covering soil	—
21		Excavate the first layer of soil as the first concrete support	1.64
22		Excavate the second layer of soil and erect the second steel support	5.04
23		Excavate the third layer of soil and erect the third layer of steel support	7.94
24		Excavate the fourth layer of soil and erect the fourth steel support	10.84
25	Area A	Excavate the fifth layer of soil and erect the fifth steel support	13.74
26		Excavate the 6th layer of soil, construct the bottom plate, remove the blocking wall	17.21
27		Remove the 4th and 5th steel supports, construct side walls and middle plates	—
28		Remove the second and third steel supports, construct side walls and top plates	—
29		Remove the first concrete support and backfill the covering soil	—

explore the impact of an excavated deep foundation pit that shares a continuous wall with an existing station on the internal force of the station slab, Figure 5 shows the bending moment cloud diagram of the subway station slab during foundation pit excavation, and Figure 6 shows the maximum bending moment of each layer of the station slab during foundation pit excavation. According to the analysis in Figure 5, a negative bending moment occurred near the bottom plate of the subway station and at the beam-column joints, while a positive bending moment occurred in the middle of the plate. The bending moment was generally higher in the Y direction than in the X direction, with an average difference of 392.18 kN ∗ m. As construction progressed, the maximum bending moments of the station bottom plate were −2725.41 kN ∗ m, −2664.01 kN ∗ m, and −2740.99 kN ∗ m in areas A, B, and C, respectively, and were mainly distributed at the connection between the bottom plate and the sidewall opposite the foundation pit. The maximum positive bending moment was generally greater in the X direction than in the Y direction, with an average difference between the extreme values of 142.05 kN ∗ m. In contrast, the maximum negative bending moment was generally greater in the Y direction than in the X direction, with an average difference between the extreme values of 179.42 kN ∗ m. Under different working conditions, the bending moment changed little in the two directions of the station slab, and the excavation of the foundation pit had only a minor impact on the internal force of the adjacent station slab. The maximum bending moment of the bottom slab did not vary across different zones, and the bending moment distribution in the same direction was consistent. There were more positive bending moments in the Y direction and less positive bending moments in the X direction near the foundation pit.

4.2. Analysis of the Deformation and Internal Force of the Station Common Wall Caused by Foundation Pit Excavations. The common diaphragm wall is closely related to the outer wall of the existing subway station, and the two change approximately in coordination [12]. The deformation of the common diaphragm wall has a considerable effect on the deformation of the existing subway station [8]. Therefore, it is essential to explore the deformation and stress of the common diaphragm wall.

Figures 7 and 8 show the deformation nephogram of the horizontal deformation of the common diaphragm wall in area B in the east-west direction and north-south direction after excavating each partition. According to Figure 8, the deformation trend of the common diaphragm wall is similar to that of the station wall. After excavating the foundation pit in area B, the common diaphragm wall as a whole exhibited a deformation trend toward the foundation pit. The maximum displacement was 9.30 mm in the middle and lower parts of the adjacent excavation area, and the upper wall of the foundation pit near area A exhibited a deformation trend

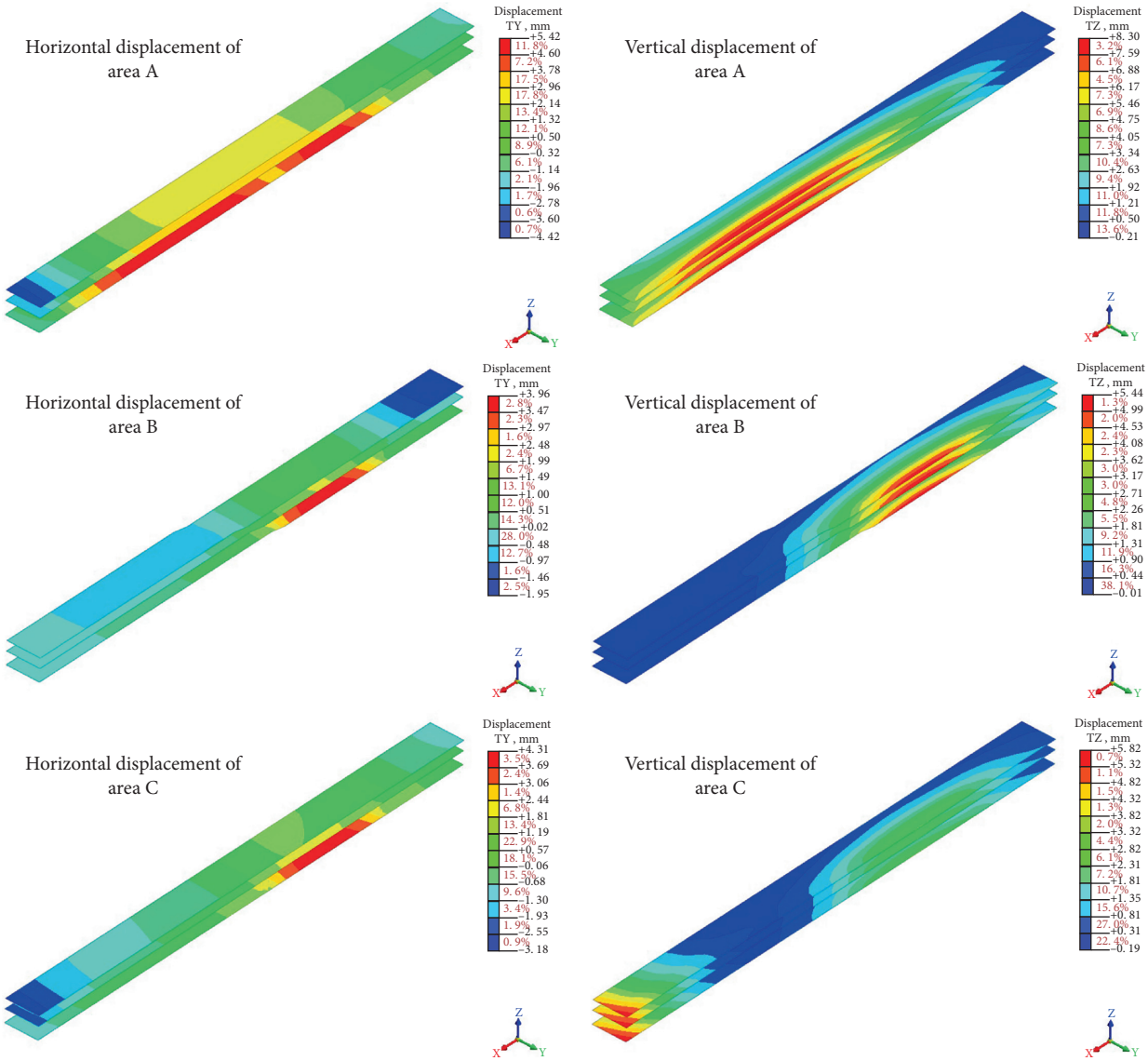

Figure 4: Horizontal and vertical displacements due to foundation pit excavation in the pit bottom station of each area.

toward the outside of the foundation pit, with a maximum deformation of −2.46 mm. After excavating the foundation pit in area C, the maximum displacement and position of the common ground connecting wall did not change, and the maximum displacement was 9.38 mm. The displacement outside the foundation pit was transferred from the upper wall of the foundation pit in area A to the middle and upper parts of the common ground connecting wall in the foundation pit excavation area, and the maximum deformation was −3.44 mm. After excavating the foundation pit in area A, the displacement of the middle and upper parts of the common ground connecting wall adjacent to area C with the outside of the foundation pit increased to −5.06 mm. At the same time, the deformation of the common diaphragm wall in the middle and lower parts of adjacent areas A and B increased, with a maximum deformation of 9.95 mm in the common diaphragm wall in the middle and lower parts of in area A. The excavation of the foundation pit in different zones had a considerable influence on the displacement of the east-west common diaphragm wall outside the foundation pit.

As shown in Figure 9, after excavating the foundation pit in area B, the maximum deformation occurred at the lower left part of the common diaphragm wall, with a maximum displacement of −0.13 mm. There was a small deformation section outside the foundation pit in the upper right part of the common diaphragm wall, with a maximum value of −0.47 mm. After excavating the foundation pit in area C, the deformation trend of the common diaphragm wall in the north-south direction was symmetrical with that after excavating the foundation pit in area B. The displacement was the largest at the lower left part of the common diaphragm wall, with a maximum value of 6.57 mm, while the deformation outside the foundation pit in the smaller section at the upper left part of the common diaphragm wall was only −5.05 mm. After excavating the foundation pit in area A, the

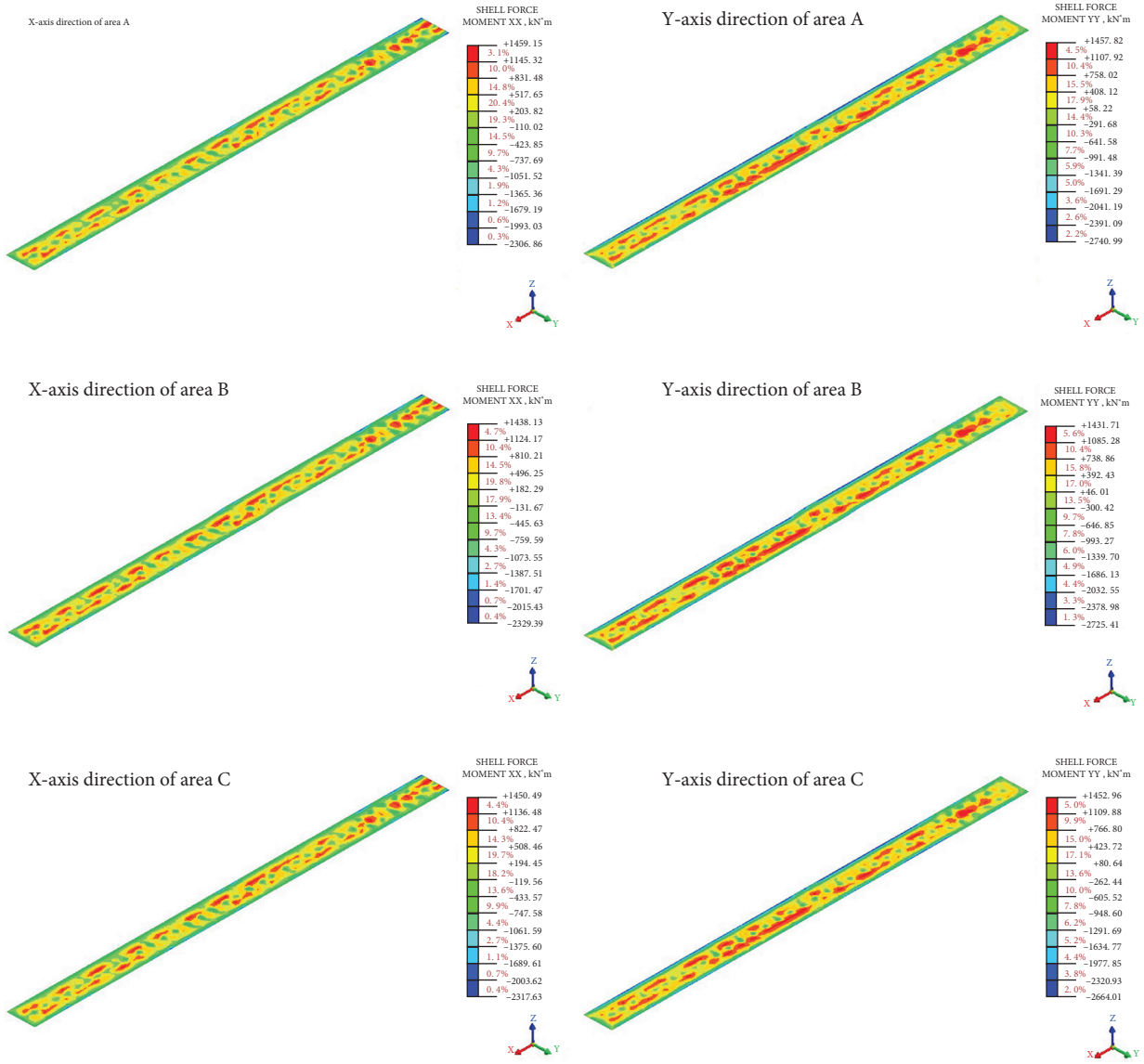

Figure 5: Distribution of bending moments in the X and Y axes from the foundation pit excavation to the station bottom plate in each area.

overall change trend was the same as that in area C, but the overall deformation was slower. The maximum displacement of the inside of the foundation pit was 2.25 mm, and the maximum displacement of the outside of the foundation pit was −3.75 mm. Based on the above analysis, the excavation of the foundation pit in area B had little impact on the north-south common diaphragm wall, mainly because area B was far from the influence area of the foundation pit. The excavation of the foundation pit in area A greatly reduced the deformation of the common diaphragm wall in the north-south direction, mainly because the excavation of the foundation pit in area A caused the common diaphragm wall to deform in the east-west direction in the foundation pit, decreasing the normal upward deformation of the common diaphragm wall in the north-south direction.

Figures 9 and 10 show the vertical deformation distribution and maximum bending moment of the common diaphragm wall before and after foundation pit excavation. Under working condition 8, the bending moment of the common underground diaphragm wall in the X direction was generally negative and small. The maximum bending moment at the junction of the partition wall in areas B and C and the bottom plate of the existing underground station was 523.75 kN ∗ m, with the minimum bending moment occurring below the bottom plate. The positive bending moment was concentrated in the middle and lower parts of the common diaphragm wall near the foundation pit in area B. The bending moment of the common diaphragm wall in the Y direction was dominated by the positive bending moment; the positive bending moment occurred above the station floor, while the negative bending moment occurred below the floor and near the partition wall and was slightly larger than the bending moment in the X direction. Under working condition 14, the bending moment distribution of the common diaphragm wall in the X direction was similar to that under working condition 8, whereas the bending

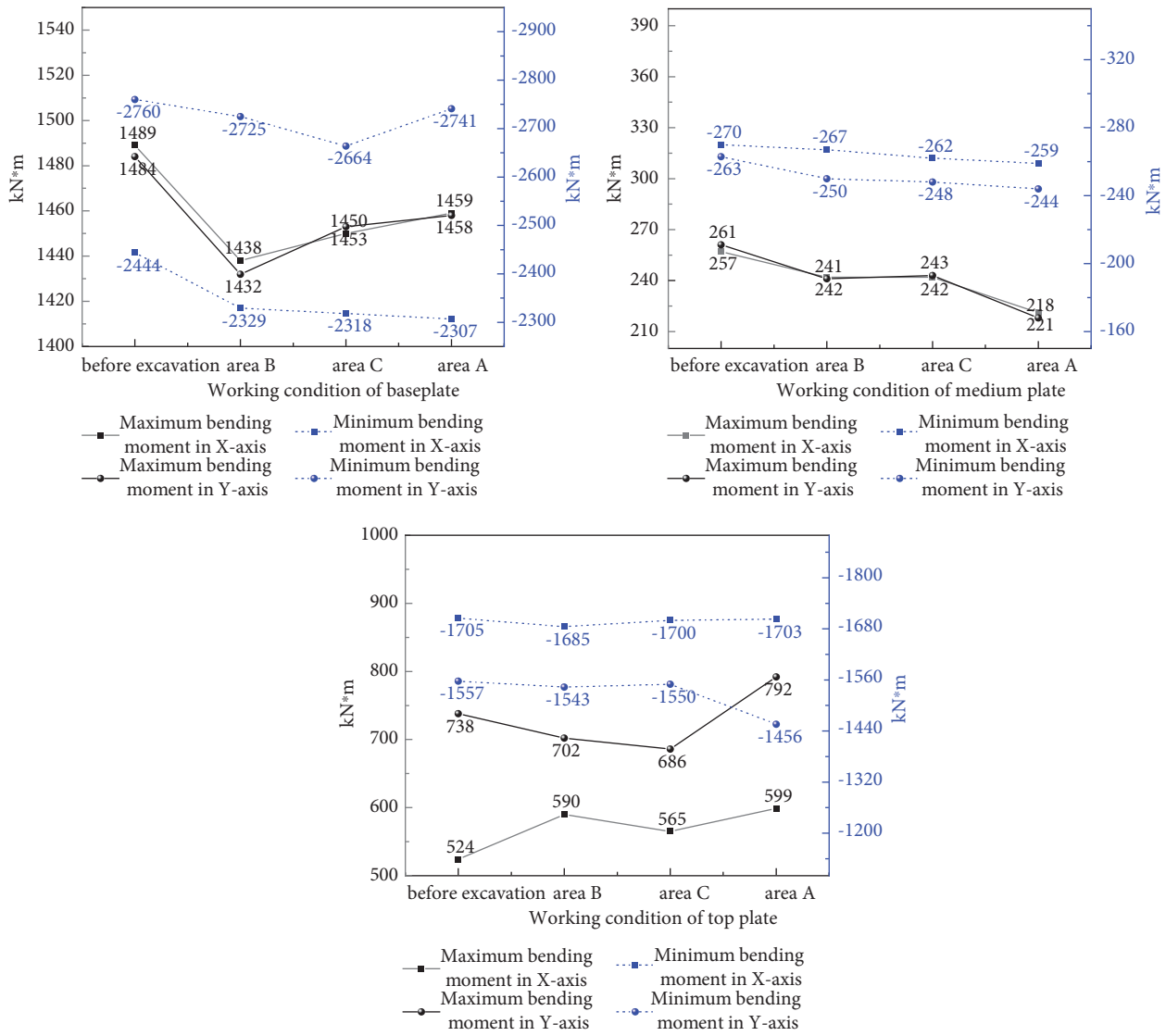

Figure 6: Maximum bending moment of the station slab from the foundation pit excavation to the pit bottom.

moment distribution of the common diaphragm wall in the *Y* direction was thinner than that under condition 8. Under condition 20, due to the influence of soil unloading, the strip positive bending moment appeared in the foundation pit excavation area and the station floor area in area A. During excavation, the maximum positive bending moment of the common diaphragm wall changed little, whereas the negative bending moment increased greatly. Compared with condition 8, the negative bending moments in the *X* direction and *Y* direction increased by 10.18% and 21.08%, respectively, under condition 14. The negative bending moment in the *X* direction under condition 20 was 12.74% larger than that under condition 14, but the change in the negative bending moment in the *Y* direction was small. Before and after excavation, the common diaphragm wall changed greatly. The positive bending moment in the *X* direction increased by 35.29% and the negative bending moment increased by 99.71%. The positive bending moment in the *Y* direction increased by 22.26% and the negative bending moment increased by 64.44%. Overall, foundation pit excavation has a considerable impact on the negative bending moment of the common diaphragm wall. In the design of similar projects, the negative reinforcement configuration of the common diaphragm wall should be considered [13].

4.3. Analysis of the Deformation and Internal Force of the Station Column Caused by Foundation Pit Excavation. Figure 11 shows the vertical deformation distributions of the subway station column before and after foundation pit excavation. Overall, the station column exhibited uplift deformation. Under working condition 8, the uplift deformation of the station column was relatively large near the foundation pit in area B, with a maximum deformation of 2.75 mm extending to both ends. The uplift deformation decreased gradually, with the smallest uplift deformation at the west end. Under working condition 14, only the station

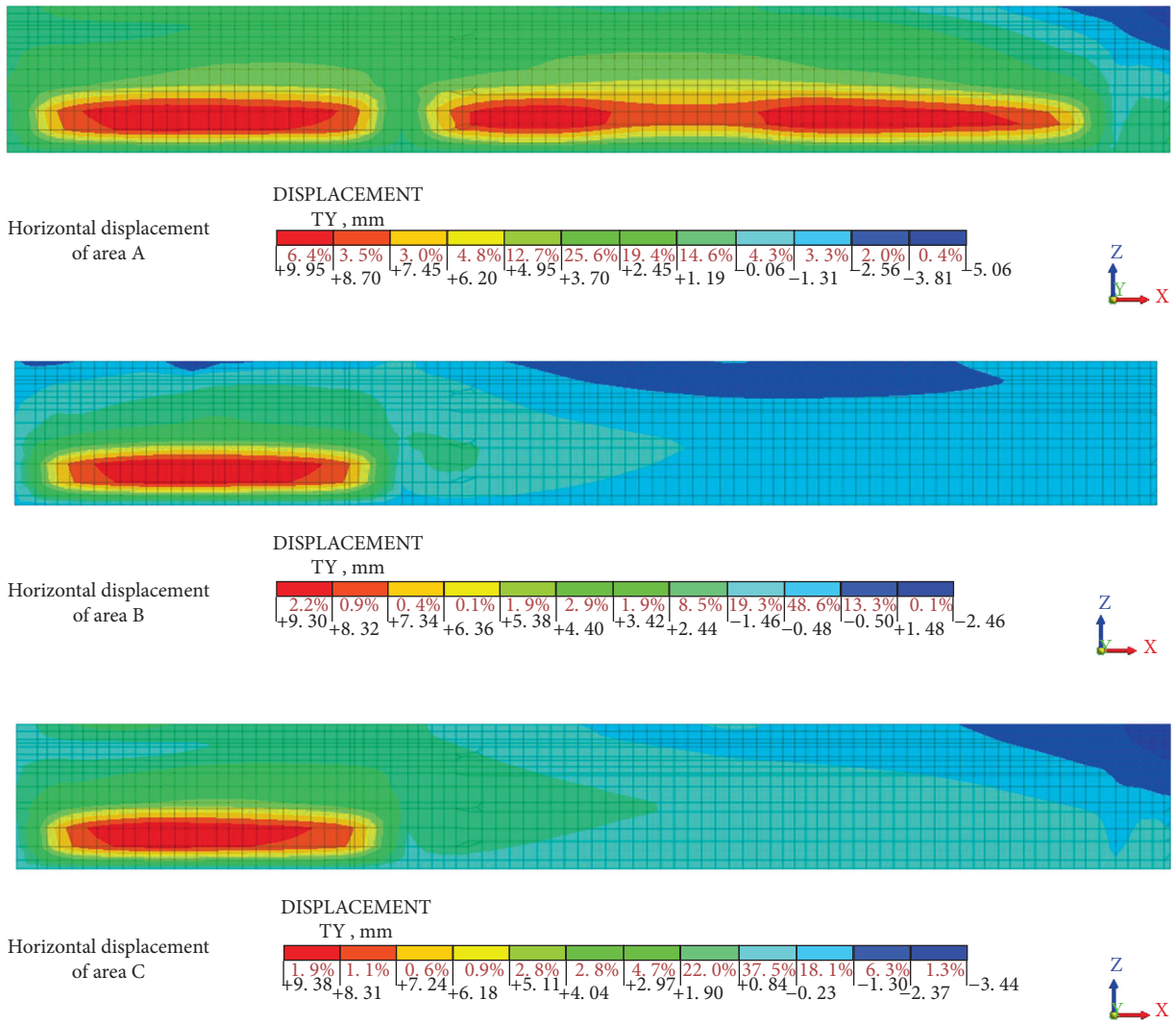

Figure 7: Deformation cloud diagram of the horizontal deformation of the common diaphragm wall in the east-west direction after excavating each partition.

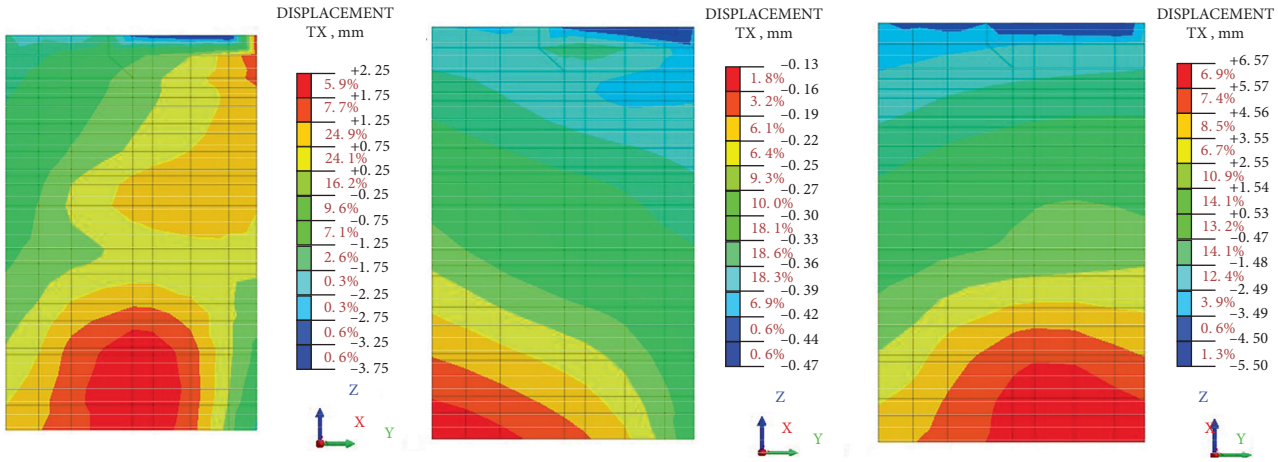

Figure 8: Horizontal displacement of the common ground wall in the north-south direction when the foundation pit in area B was excavated to the pit bottom.

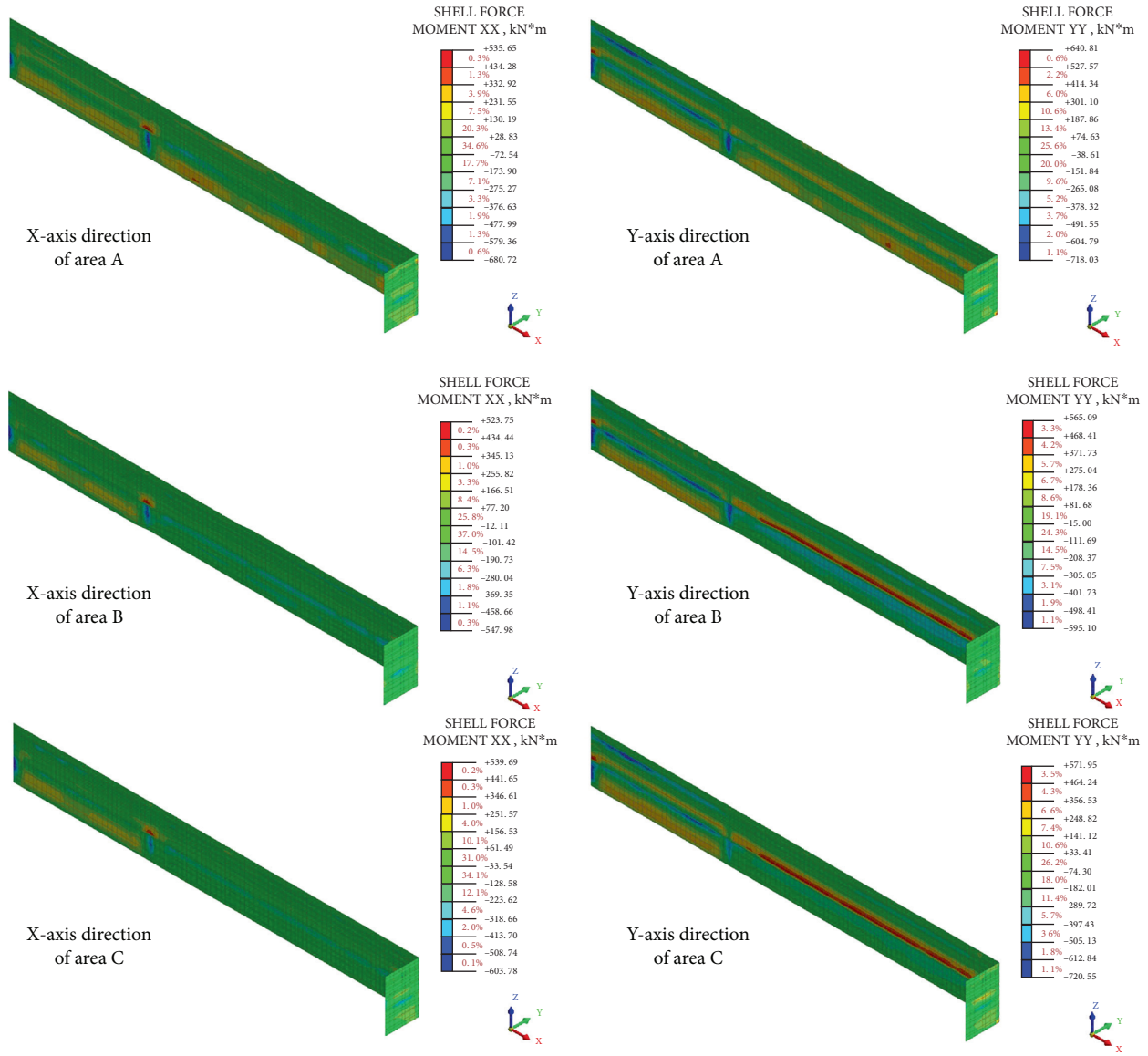

Figure 9: Bending moment distribution along the X and Y axes of the common ground wall from the foundation pit excavation to the pit bottom in each area.

column adjacent to the common ground wall had a large uplift, and the maximum deformation was 5.15 mm. The deformation far from the foundation pit excavation area was small, but the station column near the foundation pit in area B collapsed, showing a maximum deformation of 1.78 mm, which was 35% less than that before foundation pit excavation. Under working condition 20, due to the excavation of the foundation pit in area A, the deformation of the columns in the west end of the station is large, with a maximum deformation of 4.53 mm at the west end. From west to east, the uplift of the station gradually decreased. The differential settlement between the columns caused additional stress in the structure, which may lead to structural cracking and damage. Therefore, the differential settlement between the columns should be considered during foundation pit construction. Figures 12 and 13 show the axial force distributions and maximum axial forces of the columns in the subway station, which can be used to understand the variation trend of the axial force of the columns in the subway station after foundation pit excavation. Figures 12 and 13 show that the axial forces of the columns in the subway station were evenly distributed and under pressure. The column pressure was the smallest at the end of the station far from the foundation pit, and the column bottom pressure was the largest at the middle of the station. Additionally, as foundation pit excavation progressed, the maximum axial force of the station column increased from 12357.06 kN before excavation to 13639.25 kN after excavation, increasing by 10.38%. During foundation pit construction, attention should be given to the stress change of the station column, especially the stress at the bottom of the column in the middle of the station, and dynamic monitoring should be performed at all times to prevent accidents [14].

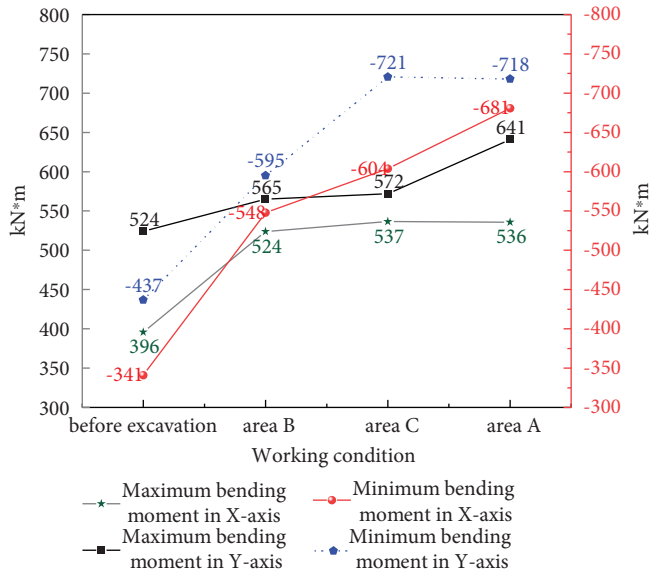

Figure 10: Maximum bending moment of the common diaphragm wall from the foundation pit excavation to the pit bottom.

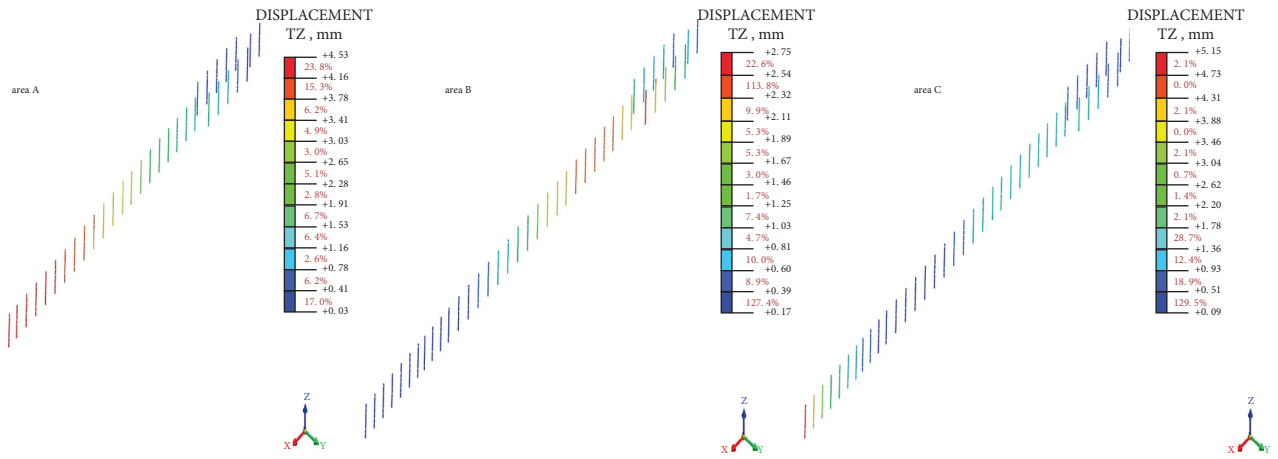

Figure 11: Vertical displacement of the station column from the foundation pit excavation to the pit bottom in each area.

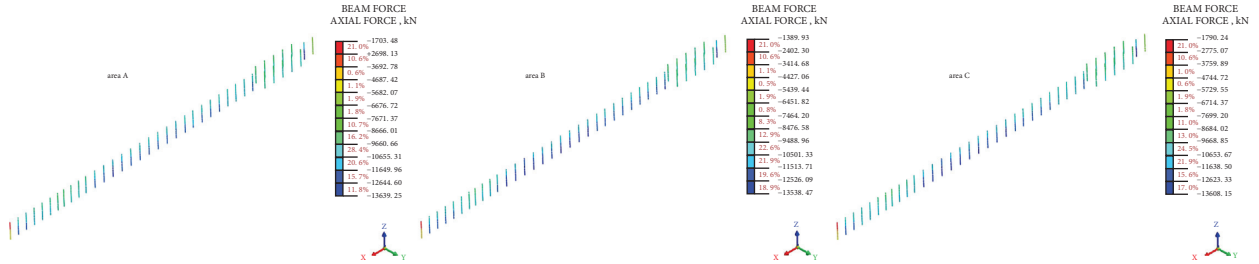

Figure 12: Axial diagram of the station column from the foundation pit excavation to the pit bottom in each area.

5. Analysis of the Influence of the Foundation Pit Retaining Structure on the Station

5.1. Analysis of the Influence of the Foundation Pit Enclosure Structure Thickness. Retaining structures with different thicknesses have various effects on foundation pit deformation [15]. The diaphragm wall of the existing station structure was 0.8 m thick. To explore the influence of the thickness of the newly built diaphragm wall of the deep foundation pit, which shares a diaphragm wall with the existing subway station, on the existing station structure, the deformations of the subway station bottom plate were

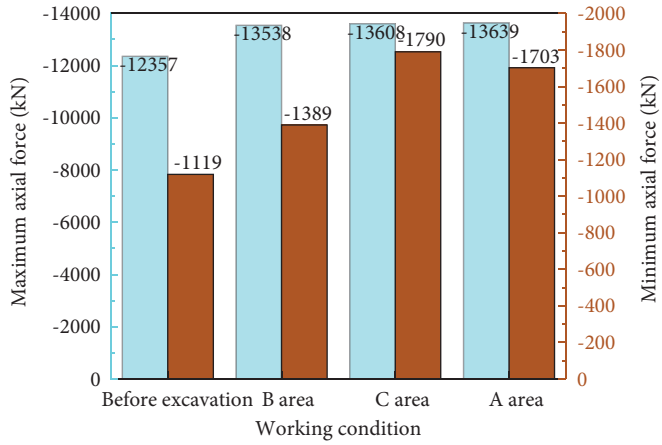

Figure 13: Maximum axial force of the station column during foundation pit excavation.

compared for eight thicknesses of 0.4 m, 0.6 m, 0.8 m, 1.0 m, 1.2 m, 1.4 m, 1.6 m, and 1.8 m with a three-dimensional model of condition 2. Figure 14 shows the horizontal and vertical displacement diagrams of the station bottom plate near the foundation pit when the foundation pit was excavated with different thicknesses. Figure 14 shows that when the thickness of the new diaphragm wall was less than that of the existing diaphragm wall, the vertical deformation of the station bottom plate first increased and then decreased with increasing thickness. When the thickness of the new diaphragm wall exceeded the thickness of the existing diaphragm wall, the vertical deformation of the station bottom plate also first increased and then decreased with increasing thickness. When the thickness exceeded 1.0 m, the reduction trend of the vertical deformation of the station bottom plate gradually slowed, and increasing the thickness of the new diaphragm wall only increased the cost and had a poor effect. When the thickness of the new diaphragm wall was 0.4 m, the vertical deformation of the station bottom plate was 7.13 mm. When the thickness of the new diaphragm wall was 0.8 m, that is, when the thickness of the new diaphragm wall was the same as that of the existing diaphragm wall, the vertical deformation of the station bottom plate was 7.09 mm. When the two thicknesses are compared, they are very similar. The author believes that the main reason for this is that the thickness of the new diaphragm wall was half the thickness of the existing diaphragm wall. In addition to resisting the deformations caused by foundation pit excavation, the Earth pressure at the bottom of the new diaphragm wall was small and less affected by the uplift of the pit bottom soil.

When the thickness of the new diaphragm wall exceeded the thickness of the existing diaphragm wall, the horizontal deformation of the station bottom plate gradually increased with increasing thickness because there was a difference in the stiffness of the retaining structure on both sides of the foundation pit. As the thickness of the diaphragm wall increased, the stiffness of the retaining structure of the foundation pit increased. After earthwork excavation and unloading, areas of the retaining structure with high stiffnesses had a strong resistance to deformation. The whole

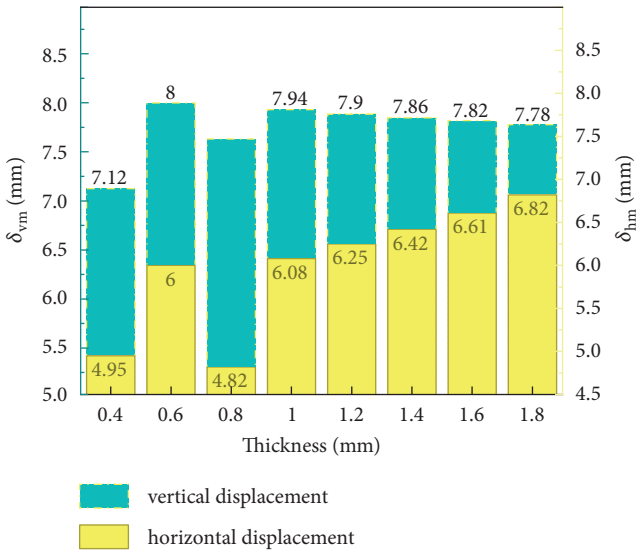

Figure 14: Horizontal and vertical displacements of the station floor near the foundation pit.

foundation pit was offset to the side due to the high stiffness of the foundation pit retaining structure, which increased the horizontal deformation of the existing station structure [16]. In summary, without considering other factors, the thickness of the new diaphragm wall should be the same as that of the existing diaphragm wall or half the thickness of the original diaphragm wall.

5.2. Analysis of the Influence of the Depth of the Foundation Pit Retaining Structure. The burial depth of the diaphragm wall has a great influence on its stiffness and bending moment, as well as the stability of the foundation pit support system [17]. When the diaphragm wall is at an insufficient depth, the supporting structure has an insufficient strength, resulting in instability and endangering the foundation pit and surrounding environment [18]. When the thickness of the diaphragm wall is known, increasing its depth can reduce the wall displacement and the uplift resistance of the soil at the

Table 4: Simulation conditions of foundation pit excavation with different depths of the diaphragm wall.

Working condition	1	2	3	4	5	6	7	8	9	10
Depth (m)	20.34	22.60	25.11	27.90	31.00	34.10	37.51	41.26	45.39	49.93

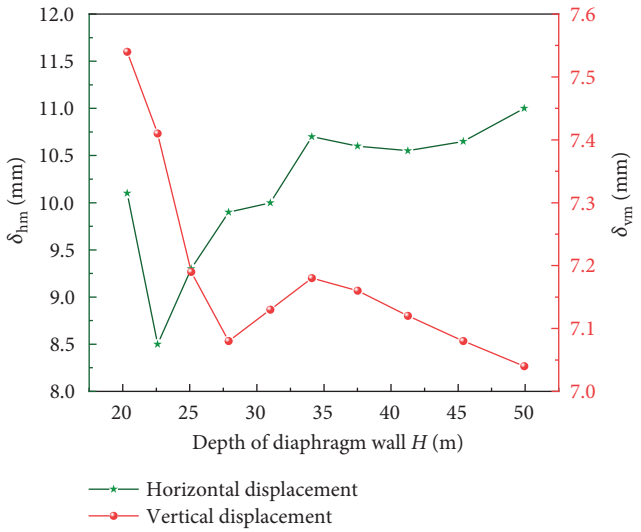

Figure 15: Vertical and horizontal displacements of the station floor structure near the foundation pit.

bottom of the foundation pit, but blindly increasing its depth increases the cost of the support structure. To explore the influence of the depth of the newly built diaphragm wall of the deep foundation pit, which shares a diaphragm wall with the existing subway station, on the structure of the existing station, a three-dimensional model of condition 2 was used, with gradual increases or decreases of 10% of the depth of the existing diaphragm wall. Ten different depth conditions were selected, as shown in Table 4.

Figure 15 shows the vertical and horizontal displacements of the station slab near the foundation pit when the foundation pit was excavated to the bottom under different working conditions. As the depth of the new diaphragm wall was gradually increased, when the depth of the new diaphragm wall exceeded the depth of the existing station diaphragm wall, the vertical deformation of the existing subway station increased slightly and then decreased gradually when the depth was increased by 10%. Before the depth of the diaphragm wall of the existing subway station was exceeded, the vertical displacement of the station first decreased and then increased slightly with as the depth of the diaphragm wall increased, and the relative horizontal deformation of the station slab first decreased and then increased with increasing depth. When the depth of the new ground wall was small, the stability of the foundation pit was poor [19]. With increasing depth, the overall stability of the foundation pit retaining structure improved. Moreover, the difference between the depth of the old and new ground connecting walls caused the embedded soil of the two deep foundation pits to differ. Furthermore, the Earth pressure behind the wall varied considerably. As the depth of the ground connecting wall increased, the active Earth pressure behind the ground connecting wall increased, posing a great challenge to the stability of the foundation pit.

6. Conclusions

Based on a deep foundation pit project in Suzhou, a numerical simulation analysis of a deep foundation pit adjacent to a subway station was performed, the deformation and stress of the subway station structure after the construction of a deep foundation pit was studied, and the influence of the foundation pit retaining structure on the station was analyzed. The following conclusions were reached:

(1) During the foundation pit excavation process, the subway station slab rose as a whole and was greatly affected by the deformation of the common ground connecting wall. The most unfavorable position shifted as the excavation area changed, mainly on the side of the common ground connecting wall. The foundation pit excavation had little effect on the bending moment of the station floor, but the floor near the wall produced a negative bending moment, which may cause cracking.

(2) The deformation trend of the station wall was the same as that of the station slab. The bottom of the station wall near the excavation area displaced into the foundation pit, the middle and upper parts of the wall and the east and west ends deformed outside the foundation pit, and the common ground connecting wall bulged upward as the foundation pit was excavated. However, there was little impact on the bending moment on the wall. The excavation of the foundation pit in different zones had little effect on the displacement of the common diaphragm wall of the foundation pit in the east-west direction, but it had a great effect on the east-west displacement of the common diaphragm wall outside the foundation pit. The stress on the common diaphragm wall changed greatly before and after excavation. The positive bending moment in the X direction increased by 35.29%, while the negative bending moment increased by 99.71%. The positive bending moment in the Y direction increased by 22.26%, while the negative bending moment increased by 64.44%. Overall, foundation pit excavation has a great impact on the negative bending moment of the common diaphragm wall. In the design of similar projects, the negative reinforcement configuration of the common diaphragm wall should be considered.

(3) During the foundation pit excavation process, the subway station column lifted upward, and the maximum displacement, which was located at the west end of the station near the foundation pit,

gradually weakened from west to east. As the foundation pit excavation process continued, the maximum axial force of the station column increased by 10.38%, and the pressure was the largest at the bottom of the middle column. Dynamic monitoring should be carried out to prevent accidents.

(4) As the thickness of the diaphragm wall increased, the stiffness of the foundation pit retaining structure increased. After earthwork excavation and unloading, areas of the retaining structure with a high stiffness could resist deformations. The whole foundation pit was offset to the side due to the high stiffness of the foundation pit retaining structure, increasing the horizontal deformation of the existing station structure. With increasing thickness, the relative horizontal deformation of the station slab gradually increased, mainly because the difference in the depths of the old and new diaphragm walls caused the embedded soil at the base of the two deep foundation pits to differ. Furthermore, there was a great difference in the Earth pressure behind the wall. As the depth of the diaphragm wall increased, the active Earth pressure behind the diaphragm wall increased.

Data Availability

The data (experimental results) used to support the findings of this study are included in the article.

Conflicts of Interest

The authors declare that there are no conflicts of interest regarding the publication of this paper.

Acknowledgments

The authors would like to thank AJE (https://www.aje.cn) for English language editing. This work was supported by the Key Research and Development Project of Shaanxi Province (No. 2021SF-523).

References

[1] Z. Ding, J. Jin, and T.-C. Han, "Analysis of the zoning excavation monitoring data of a narrow and deep foundation pit in a soft soil area," *Journal of Geophysics and Engineering*, vol. 15, no. 4, pp. 1231–1241, 2018.

[2] S. H. Ye, Z. F. Zhao, and D. Q. Wang, "Deformation analysis and safety assessment of existing metro tunnels affected by excavation of a foundation pit," *Underground Space*, vol. 6, no. 4, pp. 421–431, 2020.

[3] J. Y. Chun, *Study on Deformation Estimation of Soft Soil Foundation Pit and its Influencing Factors*, Hohai University, Nanjing, China, 2001.

[4] L. Z. Sun, "Influence analysis of foundation pit excavation on adjacent metro station," *Special Structures*, vol. 33, no. 6, pp. 52–55, 2016.

[5] Q. Wang, H. Qian, and Q. Qian, "Analysis of impact of bilateral deep foundation pit excavation on adjacent existing station," *IOP Conference Series. Earth and Environmental Science*, vol. 252, no. 5, Article ID 52049, 2019.

[6] H. Z. Guo and C. R. Bai, "Key technology analysis of shield tunneling in Luobao section of Shenzhen Metro line 13," *Modern Tunnel Technology*, vol. 57, no. S1, pp. 951–956, 2020.

[7] H. Liu, K. Li, J. Wang, and C. Cheng, "Numerical simulation of deep foundation pit construction under complex site conditions," *Advances in Civil Engineering*, vol. 2021, Article ID 6669466, 11 pages, 2021.

[8] Z. Hu, Q. Wang, S. Yang et al., "Numerical simulation of soil displacement and settlement in deep foundation pit excavations near water," *Geofluids*, vol. 2021, Article ID 5559009, 14 pages, 2021.

[9] *Technical Code for Construction Safety of Deep Foundation Pit Engineering*, China, 2013.

[10] S. Y. Fan, Z. P. Song, T. Xu, K. M. Wang, and Y. W. Zhang, "Tunnel deformation and stress response under the bilateral foundation pit construction: a case study," *Archives of Civil and Mechanical Engineering*, vol. 21, no. 3, pp. 1–19, 2021.

[11] X. Zhang, G. Wei, and C. Jiang, "The study for longitudinal deformation of adjacent shield tunnel due to foundation pit excavation with consideration of the retaining structure deformation," *Symmetry*, vol. 12, no. 12, p. 2103, 2020.

[12] C. S. Luo, Y. H. Cheng, Z. Bai, T. Shen, X. Y. Wu, and Q. G. Wang, "Study on settlement and deformation of urban viaduct caused by subway station construction under complicated conditions," *Advances in Civil Engineering*, vol. 2021, Article ID 6625429, 16 pages, 2021.

[13] H. Xing, F. Xiong, and J. Wu, "Effects of pit excavation on an existing subway station and preventive measures," *Journal of Performance of Constructed Facilities*, vol. 30, no. 6, Article ID 04016063, 2016.

[14] H. J. Zhao, W. Liu, P. X. Shi, J. T. Du, and X. M. Chen, "Spatiotemporal deep learning approach on estimation of diaphragm wall deformation induced by excavation," *Acta Geotechnica*, vol. 16, no. 11, pp. 1–15, 2021.

[15] M. N. Houhou, F. Emeriault, and A. Belounar, "Three-dimensional numerical back-analysis of a monitored deep excavation retained by strutted diaphragm walls," *Tunnelling and Underground Space Technology*, vol. 83, pp. 153–164, 2019.

[16] J. Wang, H. Xiang, and J. Yan, "Numerical simulation of steel sheet pile support structures in foundation pit excavation," *International Journal of Geomechanics*, vol. 19, no. 4, Article ID 05019002, 2019.

[17] C.-F. Zeng, X.-L. Xue, and M.-K. Li, "Use of cross wall to restrict enclosure movement during dewatering inside a metro pit before soil excavation," *Tunnelling and Underground Space Technology*, vol. 112, Article ID 103909, 2021.

[18] C. G. Zhang, X. D. Chen, and W. Fan, "Overturning stability of a rigid retaining wall for foundation pits in unsaturated soils," *International Journal of Geomechanics*, vol. 16, no. 4, Article ID 6015013.1, 2016.

[19] X. Wang, Q. Song, and H. Gong, "Research on deformation law of deep foundation pit of station in core region of saturated soft loess based on monitoring," *Advances in Civil Engineering*, vol. 2022, Article ID 7848152, 16 pages, 2022.

Hindawi
Advances in Civil Engineering
Volume 2022, Article ID 2618478, 9 pages
https://doi.org/10.1155/2022/2618478

Research Article

Experimental Study on Simulation Filling of New Underwater Cementitious Filling Material (NWC-FM)

Yanmei Ruan, Xu Luo, Shan Lin, and Xingkai Pei

Guangzhou Metro Design & Research Institute Co., Ltd., Guangzhou 510010, China

Correspondence should be addressed to Xu Luo; luolicn2003@163.com

Received 17 February 2022; Revised 10 March 2022; Accepted 14 March 2022; Published 31 March 2022

Academic Editor: Yuan Mei

To solve the problem of waste slag treatment of slurry shields, a reuse scheme in which waste shield mud is used to replace traditional karst cave grouting filling material which is proposed; thus, a new type of underwater cementitious filling material (NWC-FM) is developed. NWC-FM is convenient, inexpensive, and environmentally friendly. Its mix proportion is designed, and its mechanical performance is tested. According to the characteristics of karst caves, a semiclosed and pressurized karst cave simulation box is designed and manufactured to simulate grouting filling processes at construction sites, and an NWC-FM grouting simulation test is carried out. The results show that the fluidity of the NWC-FM slurry is good, and the strengths of the samples in the three groups of designed mix proportions meet the requirements of field construction. The underwater poured NWC-FM shows good fluidity, cohesion, nondispersibility, self-leveling, and self-compacting. After each pouring of NWC-FM material, a 2~3 cm isolation layer eventually forms on the surface due to the action of the additives, which can effectively block the contact between water and NWC-FM and ensure the flatness of the underwater poured surface of the NWC-FM material. The average compressive strength of the NWC-FM consolidated core samples at 7 d, 14 d, and 28 d are 0.56 MPa, 0.72 MPa, and 0.79 MPa, respectively, meeting the technical strength requirements of construction sites. NWC-FM has strong underwater nondispersibility and moderate strength, which can well meet the requirements of karst cave filling treatment during shield construction of urban subways. Additionally, as a low-cost and environmentally friendly material, NWC-FM will greatly reduce the project cost and minimize environmental pollution.

1. Introduction

In the process of subway tunnel shield construction, foaming agents and other lubricants are usually applied to the shield cutter head, which makes the soil difficult to consolidate, drain, and recycle because it becomes a kind of muddy waste [1–3]. The slurry output of a slurry shield is generally 2~3 times the tunnel excavation volume. At present, the disposal of waste shield mud is mainly transported to the designated spoil ground. The transportation volume is large, and its disposal cost accounts for approximately 10% of the cost of the shield tunnel. It is also difficult to find a suitable spoil ground. Due to limited urban storage sites and high personnel density, improper disposal will cause environmental pollution, land occupation, and other issues. Therefore, research on the treatment of waste shield mud has very important practical significance.

Karst commonly causes hydrogeological engineering failure in the process of subway construction in China. When a shield crosses the karst strata, it is necessary to preprocess the karst cave in advance to ensure the safety of shield construction. The traditional karst cave treatment methods mainly include the pressure-injection double-liquid slurry [4], sand grouting [5], and concrete grouting methods [6, 7], which consume large amounts of building materials. Therefore, the cost of construction cost is high, and the strength is difficult to control. Moreover, traditional backfill construction is difficult, the backfill period is long, and the backfill quality is difficult to guarantee. It is urgent to find a low-cost, convenient, and green environmental

protection material to meet the needs of karst backfill treatment.

The use of waste shield mud as an in situ prepared cave grouting filling material is one of the ways of utilizing waste shield mud as a resource, greatly saving resources, reducing urban pollution, reducing the cost of engineering construction, and realizing green construction. Scholars have studied the working performance and physical and mechanical properties of recycled slurry from abandoned shield sediment and have prepared grouting materials with a fluidity of 230 mm and a 28 d compressive strength that is greater than 2.5 Mpa; thus, this recycled slurry has achieved good comprehensive utilization results [8–12]. However, the existing research on recycled slurry of waste shield sediment mainly focuses on subgrade materials [13], slurry film-forming [14], and slurry shield synchronous grouting raw materials [15–17]. There are few reports on the use of the recycled slurry of waste shield sediment as the filling material of karst caves. Moreover, for water-filled karst caves, the filling material needs to consider the underwater dispersion resistance and other issues. In view of this, this study takes the karst cave treatment of Guangzhou metro construction as the background and takes abandoned shield mud as the main raw material. After the addition of a certain proportion of admixtures, it is fully mixed with water to form a new type of underwater cementitious filling material (NWC-FM) with pumpability and strong fluidity. Based on the characteristics of karst caves and considering the groundwater pressure, a semiclosed and pressurized karst cave simulation box is designed and manufactured, and an NWC-FM grouting simulation test is carried out to study its underwater fluidity and cohesion, thereby evaluating the engineering effect of NWC-FM karst grouting.

2. Mechanical Performance Test of NWC-FM

2.1. Raw Materials and Mix Proportions of the NWC-FM Samples. NWC-FM takes waste shield mud (taken from a shield tunnel construction site of Guangzhou Metro, the sampling depth is 5~10 m, Figures 1(a) and 1(b)) and cement as the main basic materials and selects UWB-II anti-washout admixtures of underwater concrete [18] (developed and produced by CNPC Engineering Technology R&D Company Limited, it is mainly made of sugar polymer thickener, concrete fluidizing agent, concrete setting time regulator, etc, Figure 1(c)) as the flocculating agent. An early-strength chlorine salt agent and polycarboxylate superplasticizer are added to improve the performance of NWC-FM, achieve the effect of water reduction and enhancement, and increase the strength of NWC-FM so that it meets the engineering requirements after a certain number of days of maintenance while also remaining fluid. In addition, fly ash and mineral powder are used to reduce the amount of cement, realize waste utilization, and protect the environment while saving costs. Our research group determined three groups of NWC-FM mix proportions through a large number of laboratory tests in the early stage, as shown in Table 1. The basic requirements of the design include the following four aspects:

(1) The water-binder ratio is 0.45~0.6, and the water consumption is 270~310 kg/m^3

(2) Water consumption should cause the slump of the NMC-FM mixture to reach 220 ± 20 mm, and the slump expansion should reach 350 ± 20 mm

(3) The underwater strength of NWC-FM material is 0.5 MPa

(4) When pouring the NWC-FM material, the free drop-in water is 30~50 cm

2.2. Test Process

2.2.1. Samples Preparation and Curing. NWC-FM samples were prepared according to the Chinese standard GB/T50080-2016 [19] and the Chinese standard DL/T5117-2000 [20]. Nine samples were prepared in each group. The geometric size of the sample was 70.7 mm × 70.7 mm×70.7 mm, and curing ages of 7 d, 14 d, and 28 d were used. The samples preparation steps are as follows:

(1) Configure the slurry: the original shield mud used in the test was dried, crushed, and screened, and large soil particles were removed. Then, it was mixed with cement, fly ash, mineral powder, flocculant, and other additives. Finally, this mud was with water to prepare the mixed mud.

(2) Sample preparation: to facilitate later demolding, a layer of Vaseline was evenly coated on the inner wall of the mold before loading the mixture. The prepared mixed mud was slipped into one side of the mold wall three times, poured into a 1/3 mold volume once, and vibrated for a period of time after each pouring; thus, small bubbles were released from the surface to prevent the influence of the internal bubble gap on the strength of the sample. After filling, the sample was scraped flat with a scraper and then sealed with a cover film.

(3) Sample curing: the test samples were numbered and placed in the water curing protection box of the standard curing room ($20 \pm 3^{\circ}$C, humidity >95%) for curing. Demould after 48 hours. After demoulding the test samples, continue water curing until the design age is reached (Figure 2(a)).

2.2.2. Unconfined Compressive Strength Test. After the curing of the sample was completed, unconfined compressive strength tests were performed with the consolidated bodies after 7 d, 14 d, and 28 d using a microcomputer-controlled electronic universal testing machine (Figure 2(b)) with a measuring range of 200 kN (axial strain rate of 1 mm/min). When analyzing the test strength of each group, the mean value of three horizontal samples was first calculated. If the deviation between the sample strength and mean value was greater than 10%, it was eliminated. Finally, the mean value of no less than two samples was taken as the test strength value.

(a) (b) (c) (d)

Figure 1: Photos of the undisturbed shield mud (a), shield mud sample after drying, crushing and screening (b), UWB-II anti-washout admixtures of underwater concrete (c), and fly ash (d).

Table 1: Mix proportions of the NWC-FM samples.

Number	Materials (kg)							
	Shield mud	Cement	Fly ash	Mineral powder	Flocculating agent	Early-strength agent	Water reducing agent	Water
NWC-1	1.000	0.286	0.057	0.021	0.014	0.010	0.010	0.429
NWC-2	1.000	0.357	0.071	0.021	0.014	0.010	0.010	0.357
NWC-w	1.000	0.141	0.041	0.010	0.0032	0.003	0.0045	0.351

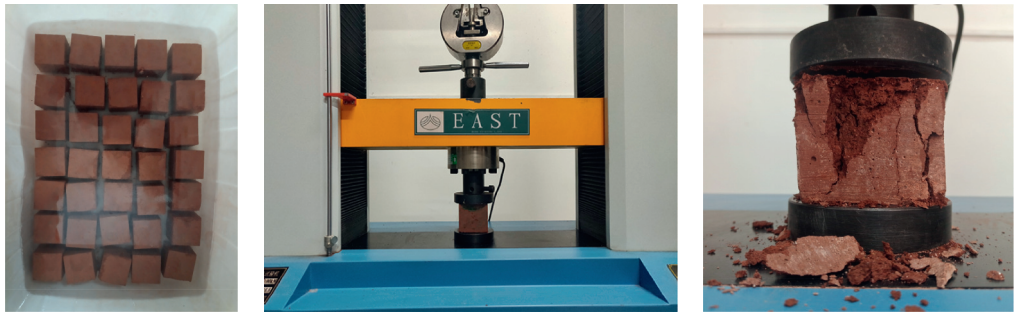

(a) (b) (c)

Figure 2: Photos of the stored samples (a), compression testing machine (b), and sample destruction (c).

2.3. Test Results and Analysis. The unconfined compressive strength of the NWC-FM sample is shown in Figure 3. It can be seen from the figure that the strength of the NWC-FM sample gradually increases with increasing curing time. Since the technical requirements of NWC-FM are to ensure the smooth advancement of the shield machine while ensuring the nondispersibility of underwater filling, the strength after filling is required to be greater than or equal to the strength of undisturbed soil, that is, the strength after the filling is approximately 0.5 MPa. The strength of the NWC-FM samples configured according to the design mix proportion of each group is higher than 0.5 MPa, meeting the engineering requirements. Moreover, the strength of the NWC-1 and NWC-2 samples is higher than that of the NWC-w sample, indicating that the strength of the NWC-FM materials is greatly affected by the amount of admixtures. The greater the amounts of additives, such as cement, the greater the strength of NWC-FM and the better the performance. Considering that many kinds of admixtures are required for the NWC-FM configuration and that too high of a strength will cause considerable waste, NWC-w is selected as the optimal mix proportion for the test based on the configuration cost and strength requirements.

3. NWC-FM Simulation Filling Test

Karst caves are underground closed spaces formed by karst in soluble rocks. The formation of karst caves is the result of the long-term dissolution of groundwater in limestone areas, which often contain a large amount of groundwater. Based on the characteristics of karst caves and considering the groundwater pressure, a semiclosed karst cave simulation box with pressure is designed and manufactured to simulate the grouting filling process at the construction site, carrying out a simulation test of grouting with NWC-FM, and study the fluidity and cohesion underwater. The engineering effect of karst grouting with NWC-FM is evaluated.

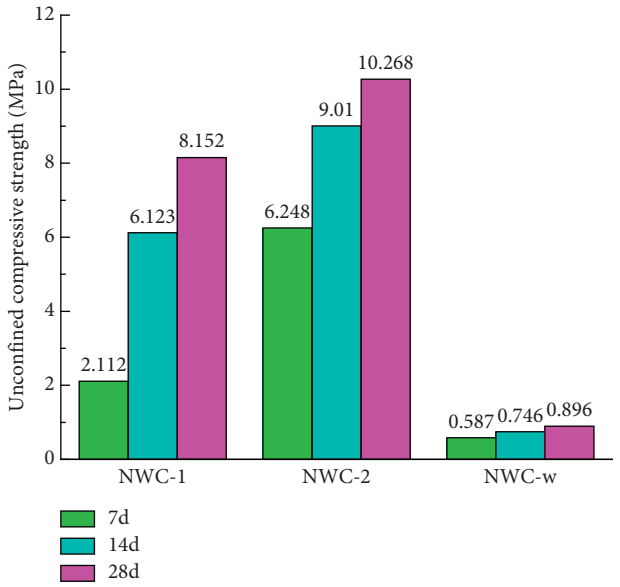

Figure 3: Unconfined compressive strength of the NWC-FM samples with different proportions and at different ages.

3.1. Design and Installation of the NWC-FM Simulation Filling Test Device. A simulation box is designed and manufactured with dimensions of 1500 mm × 800 mm × 500 mm (length × width × height); this box is filled with water to simulate a real water-filled cave. The material of the simulation box is organic glass, each side is fixed with steel strips, and the joint of the organic glass plate is blocked with a waterproof and weather-resistant silicone adhesive to ensure that the simulation box is sealed and does not leak. Three circular holes with a diameter of 100 mm are opened on the roof of the simulation box. As shown in Figure 4, holes A and B are grouting holes and hole C is a drainage hole.

The NWC-FM simulation filling test device is shown in Figure 5, which is composed of a karst cave simulation box and a pulp feeding and water drain system. The pulp feeding and water drainage system is composed of a slurry inlet pipe, a funnel, a drainage pipe, and a water holding tank. The funnel is set on the NWC-FM material feeding platform, approximately 3 m from the ground. The grouting pipe directly penetrates into the bottom of the simulation box through the reserved grouting hole in the roof, which is 200 mm from the bottom of the box; additionally, the drainage pipe is 100 mm from the roof. After reaching the roof, it is connected to the water collecting tank through the conversion elbow. Before the test, clear water is injected into the simulation box through the grouting pipe. Water is added until filling the simulation box and drainage pipe; then, the addition of water is stopped to ensure that there is a certain water pressure in the simulation box when the material is poured. In the process of NWC-FM grouting, the grouting pipes on both sides are alternately grouted to ensure the filling rate of NWC-FM. The installed karst cave simulation box is shown in Figure 6.

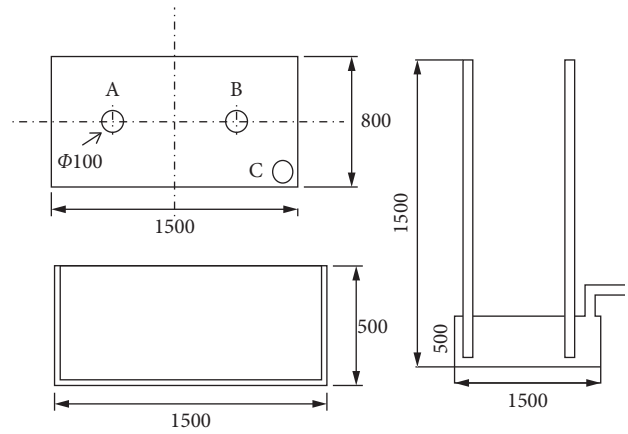

Figure 4: Schematic showing the dimensions of the simulation box. 1 and 2, slurry inlet pipe; 3, drain pipe; 4, plexiglass box; 5, funnel; 6, PVC water injection pipe; 7, water pump; 8, water holding tank; 9, floating ball; 10, traction line with scale; 11, lower floating ball.

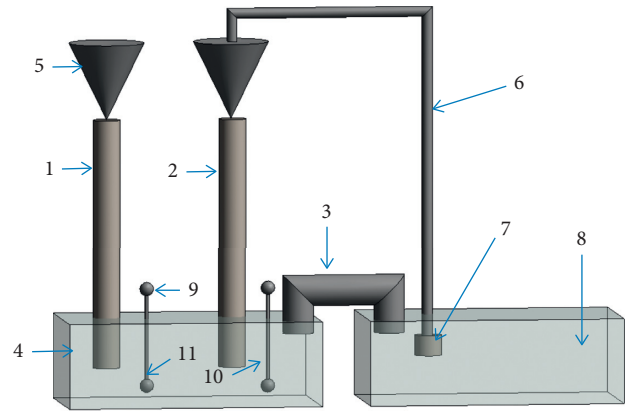

Figure 5: 3D schematic showing the simulated filling test device.

Figure 6: Completed installation of the karst cave simulation box.

3.2. Test Scheme. The NWC-w mix proportion is selected for the NWC-FM simulation test. Before the test, the shield mud and various admixtures after drying are divided into four parts and weighed for use. The test mixer with 0.3~0.5 m^3 discharge per plate ensures a continuous mixing supply of filling materials.

(1) Before the test, the grouting pipe is first inserted into grouting hole A; moreover, the drainage pipe is fixed in the simulation box. The grouting pipe is 200 mm from the bottom of the box, and the drainage pipe is 100 mm from the top surface to ensure compliance with construction at project sites.

(2) Water is injected into the simulation box through the grouting pipe. Water is added until completely filling the simulation box drainage pipe. At this point, the addition of water is stopped to ensure that there is the certain water pressure in the simulation box.

(3) After the preparation work is completed, the NWC-FM premixed shall be penetrated into the grouting pipe through the funnel to observe the decline of the new underwater agglomerating filling material in the grouting pipe. Additionally, attention should be given to the change in the liquid level of the drainage pipe, and the drainage pipe should be connected to the water collecting bucket to facilitate the smooth discharge of water.

(4) The behavior of the NWC-FM entering the water is observed, including the falling process in the water, the shape when reaching the bottom of the simulation box, and the diffusion process, fluidity, and coverage of the filling material at the bottom of the simulation box. Moreover, the changes in the surface of the filling material in the simulation box and of the water in the simulation box are observed.

(5) First, grouting is achieved through grouting pipe A. When the material filling rate drops, grouting pipe A is replaced with grouting pipe B to continue filling, and grouting pipe A is raised by 10–15 cm.

(6) The above process is repeated until all the water in the simulation box is discharged. During the test, attention is given to recording and observing the working properties of NWC-FM at each stage.

(7) After pouring, the surface treatment is carried out in time, and the test piece is wrapped for thermal insulation and moisture conservation.

The simulation filling test flowchart is shown in Figure 7.

3.3. Test Phenomena and Analysis. The NWC-FM material simulation filling test is performed by pouring continuously 4 times. When the first batch of NWC-FM materials touches the bottom plate of the simulation box, due to the impact, the NWC-FM materials will be diluted by the water and begin to slowly rise. The amount of rising slurry will increase slowly. Then, a small part of the NWC-FM is diluted, and most of it diffuses around the bottom and produces a small amount of bubbles. When the amount of NWC-FM material continues to increase, the diffusion speed of the material increases and the slurry continues to rise after touching the bottom, reaching the top of the simulation box and then moving back down to the bottom of the simulation box. At this point, the diluted slurry has diffused to half of the volume of the simulation box, the upper and left colors are light, and the color around the grouting pipe is dark due to the accumulation of the NWC-FM material. The color of the accumulated material gradually becomes lighter outward, and the slurry does not diffuse to the right side of the simulation box; thus, there is still clean water on the right side of the box (Figure 8(a)).

As the pouring is continued, NWC-FM at the grouting pipe is gradually deposited. When the deposition amount increases to a certain extent, the newly poured material squeezes the deposited NWC-FM at a certain pressure to make it evenly move around. The NWC-FM at the bottom of the box presents a distribution pattern of uniform decrease around the grouting pipe. Since grouting pipe A is located on the left side of the simulation box, when the amount of NWC-FM continues to increase, the material close to the left side first touches the sidewall of the simulation box and accumulates on the left wall. The material on the right side continues to move until they contact the right wall, and the speed at which NWC-FM accumulates on the left is significantly higher than that on the right (Figure 8(b)).

When the first pouring is complete, the distribution of NWC-FM material on the left side of grouting pipe A is basically the same, the distribution on the right side decreases gradually with increasing distance from grouting pipe A, and the overall trend is that the left side is high and the right side is low. Although the NWC-FM material that initially enters the simulation box is diluted and the whole simulation box is filled with diluted NWC-FM material, this process develops slowly. With continuous pouring, the integrity of the NWC-FM material is maintained well, and this underwater filling material, with its high fluidity and cohesiveness, forms and moves throughout the simulation box. Two minutes after the completion of the first pouring, a thin layer of white flocculent precipitates appears on the surface of the NWC-FM material at the bottom of the simulation box, and the distribution is relatively uniform. With increasing time, the white precipitates gradually increase, thicken, and clear layer. After 5 min, the thickness of the precipitates reaches approximately 1 cm, forming a milky white isolation layer (Figure 8(c)). The bottom of the simulation box is obviously divided into three layers: diluted NWC-FM solution, the white precipitate isolation layer, and the NWC-FM material from top to bottom, respectively. The isolation layer effectively isolates water from the NWC-FM material and maintains its cohesion and nondispersibility.

While NWC-FM is poured, the mixer continues to work to mix the next batch of material. There is a thick isolation layer above the NWC-FM material before the third pouring (Figure 8(d)). When the NWC-FM material falls, it must first pass through the isolation layer, which disturbs this layer at the grouting pipe and causes the material to rise; however, the isolation layer is still continuous and not dispersed. With the increase in pouring materials, the upper material and lower material gradually push the isolation layer to move around at the same time, and the isolation layer is slowly dispersed after this continuous and strong disturbance. Two minutes after the second pouring, a thin layer of white precipitates is formed on the material surface of NWC-FM. After five minutes, the amount of precipitates increases and

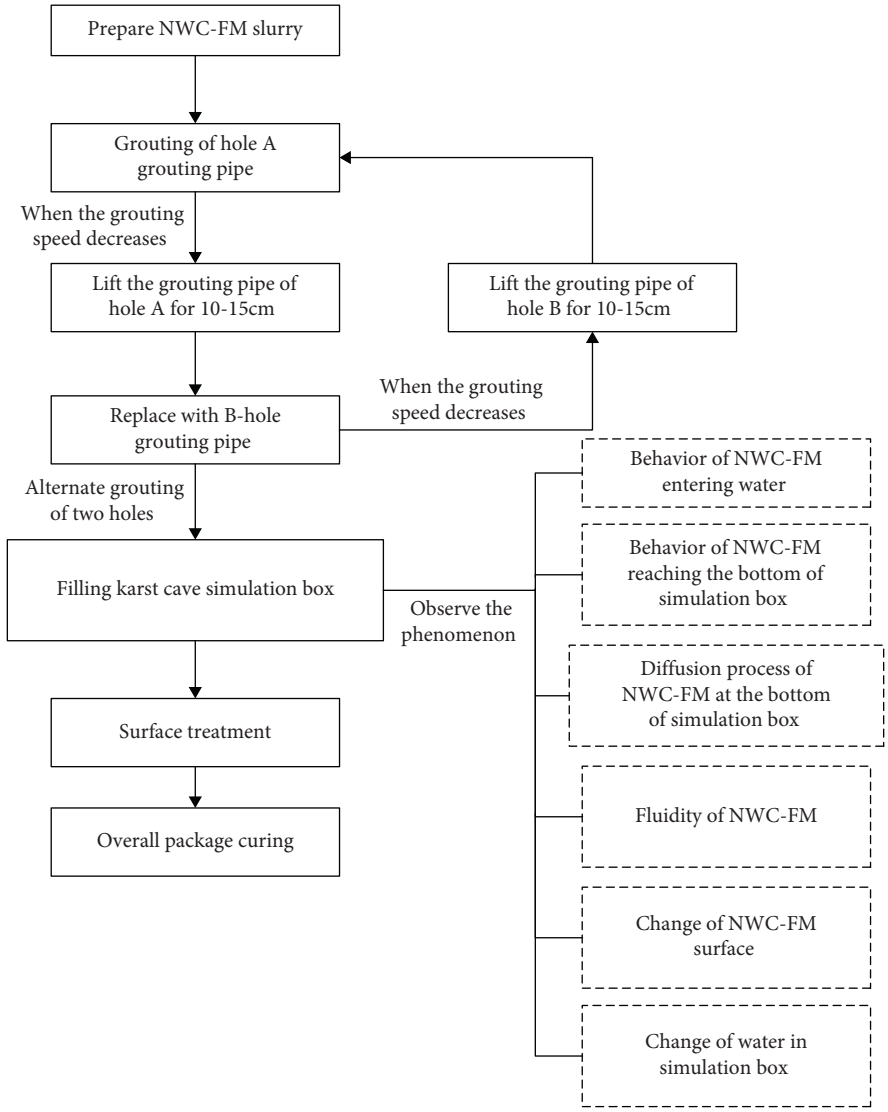

Figure 7: Flowchart of the simulation filling test.

finally forms a new isolation layer. The situation in the third and fourth pouring simulation boxes is basically the same as that in the second time. The material first passes through the isolation layer, which causes the isolation layer to slowly disperse. Then, the NWC-FM material gradually moves around and tends to be stable. Finally, a new isolation layer is formed on the surface of the NWC-FM material. The fourth pouring stops 1 cm from the top surface, completing the simulated pouring test (Figure 8(f)).

During underwater pouring, the isolation layer formed by NWC-FM can prevent the lower NWC-FM from contacting water and maintain the nondispersibility of the material. Additionally, the cementitious material of the isolation layer is continuously distributed and has a certain viscosity, which is not easily affected by the water flow. It can better maintain the cohesion and fluidity of NWC-FM and give full play to the excellent performance of NWC-FM. It can be seen from the above test phenomena that NWC-FM has strong nondispersibility underwater. Thus, even if it were to flow in the water-filled cave simulation box, there is little material separation due to water washing. Moreover, NWC-FM is viscous and plastic, and the water can gradually deposit due to its weight. Furthermore, NWC-FM has self-leveling and self-compaction properties, satisfactorily meeting the requirements of karst cave filling.

4. Mechanical Property Test of the NWC-FM Consolidated Core Sample

To study the strength performance of the NWC-FM simulated filling materials, core samples with a diameter of 100 mm and a length of 150~2200 mm are taken at 7, 14, and 28 d after the simulated filling test by the core drilling sampling method. An unconfined compressive strength test is carried out on the core samples, and the test results are shown in Table 2 and Figures 9 and 10.

At the initial stage of test loading, the deformation of each sample is small. With increasing load, fine cracks appear vertically along with the core sample, and the cracks are evenly distributed along the circumference of the core

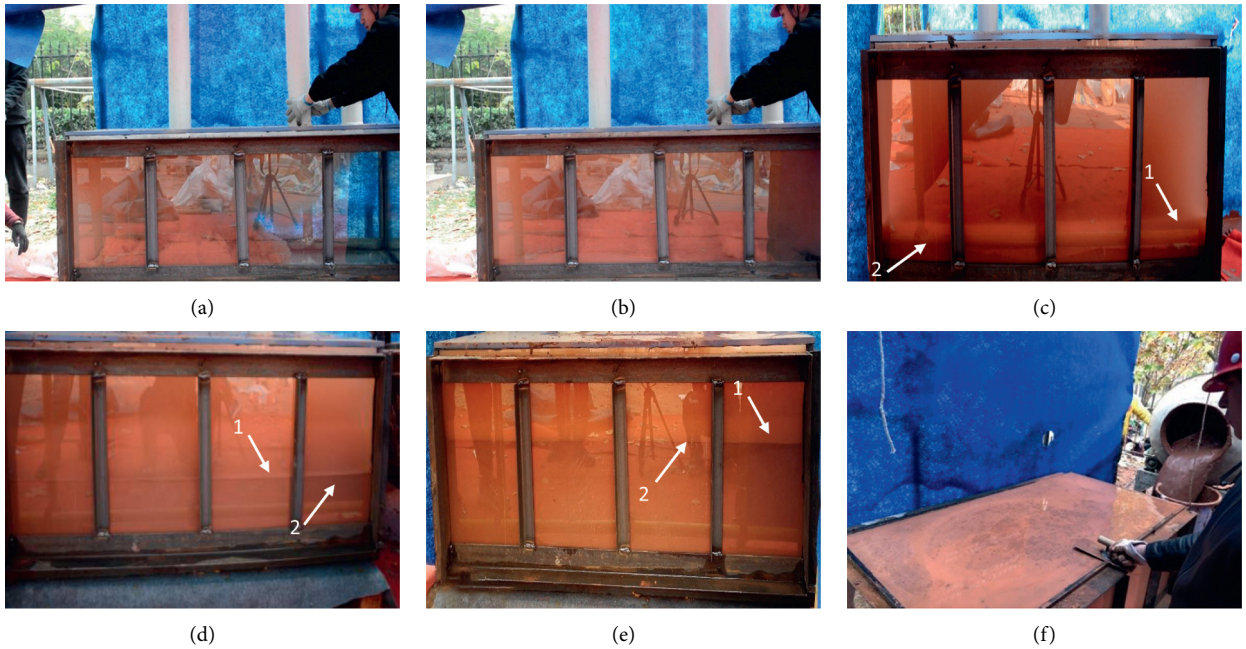

(a) (b) (c)

(d) (e) (f)

Figure 8: Photos of NWC-FM entering the simulation box (a). NWC-FM diffuses in the simulation box (b). Five minutes after the first pouring (c). Five minutes after the second pouring (d). Five minutes after the third pouring (e). After completing the pouring (f).

Table 2: Compressive strength of the core samples.

Curing age (d)	Number	Failure load (kN)	Compressive strength (MPa)	Mean value (MPa)
7	1	4.580	0.58	0.56
	2	4.378	0.56	
	3	4.214	0.54	
14	1	5.915	0.75	0.73
	2	5.920	0.75	
	3	5.291	0.67	
28	1	6.745	0.86	0.79
	2	6.036	0.77	
	3	5.884	0.75	

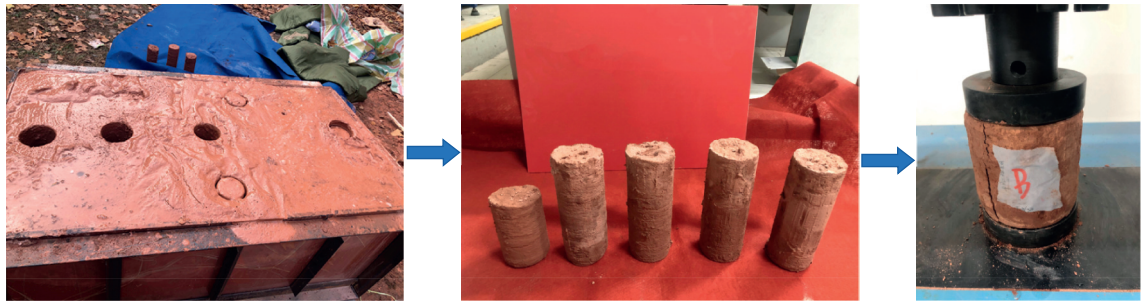

(a) (b) (c)

Figure 9: Photos of the core sampling positions (a), removed core samples (b), and sample destruction (c).

sample. As the load continues to increase, the cracks gradually extend through the top and bottom surfaces of each sample. The sample is damaged and loses its bearing capacity. The failure mode is shown in Figure 9(c). Table 2 and Figure 10 show that the strength of the consolidated core sample of the NWC-FM simulation filling test gradually increases with increasing curing time. The average compressive strength at 7, 14, and 28 days is 0.56, 0.72, and

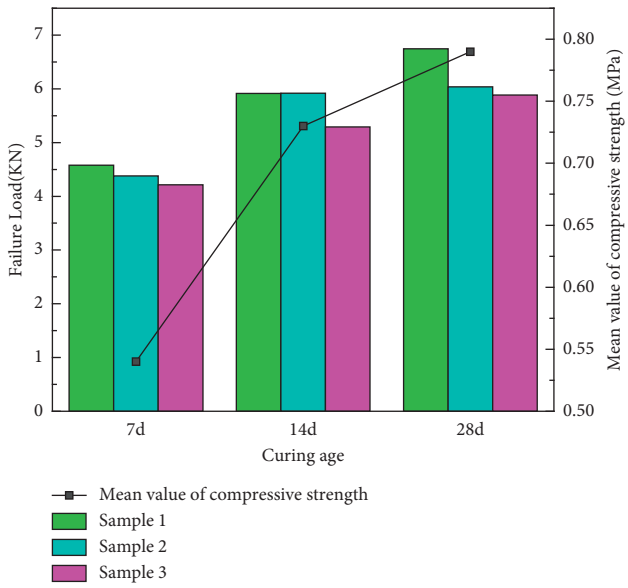

Figure 10: Test results of the unconfined compressive strength of the NWC-FM consolidated core samples.

0.79 MPa, respectively, which represents moderate strength. Therefore, this material can better meet the requirements of underwater karst cave filling at project sites.

5. Conclusions

Aiming at the resource utilization of waste shield mud and the treatment of water-filled karst caves in urban subway shield construction, a new underwater cementitious filling material that is convenient to obtain (NWC-FM), low cost, and environmentally friendly is developed. Its mix proportion is designed, and its basic properties are tested. A karst grouting simulation test is performed to study the fluidity, cohesion, and nondispersibility of NWC-FM during underwater pouring. After curing, core samples are drilled out, the strength index of the NWC-FM material is tested, and the karst grouting effect of the NWC-FM material is evaluated. The main conclusions are as follows:

(1) Through laboratory tests, NWC-FM is developed with waste shield mud, cement, flocculant, and fly ash as raw materials. The minimum 7 d-compressive strength of the three groups of mix proportion samples is 0.587 MPa, which meets the technical requirements of construction sites.

(2) The NWC-FM material initially entering the simulation box will be diluted by water, but the process is slow. Notably, the integrity of the material is maintained, and material separation due to water washing rarely occurs. Furthermore, NWC-FM has strong fluidity and cohesion and can flow in any direction underwater.

(3) After each pouring of NWC-FM material, a 2~33 cm isolation layer will eventually be formed on the surface due to the action of the admixture. The cementitious material of the isolation layer is continuously distributed and has a certain viscosity that is less affected by water flow. This layer can effectively block the contact between the water and NWC-FM material, maintain the nondispersibility, cohesion, and fluidity of the NWC-FM material, ensure the leveling of the underwater poured surface of the NWC-FM material, and prevent material loss. Thus, the NWC-FM material has good underwater service performance and meets the requirements of underwater filling.

(4) The strengths of the NWC-FM consolidated core samples at 7 d, 14 d, and 28 d are 0.56 MPa, 0.72 MPa, and 0.79 MPa, respectively, meeting the technical strength requirements of construction sites. NWC-FM has strong underwater nondispersibility and moderate strength, which can satisfactorily meet the requirements of karst cave filling treatment during urban subway shield construction. Additionally, as a low-cost and environmentally friendly raw material, NWC-FM will greatly reduce the project cost and minimize environmental pollution.

Data Availability

The data used to support the findings of this study are included within the article.

Conflicts of Interest

The authors declare that there are no conflicts of interest regarding the publication of this paper.

Acknowledgments

The authors would like to thank AJE (http://www.aje.cn) for English language editing.

References

[1] S. J. Li, Y. T. Liu, J. F. Li, and Y. M. Sheng, "Experimental study on preparation of high performance grouting material from waste sand of shield tunnel construction," *Materials Reports*, vol. 35, no. Z2, pp. 275–278, 2021.

[2] X. Y. Wang, Q. Y. Song, and H. Gong, "Research on deformation law of deep foundation pit of station in core region of saturated soft loess based on monitoring," *Advances in Civil Engineering*, vol. 2022, Article ID 7848152, 16 pages, 2022.

[3] X. Y. Wang, Z. Ma, and Y. T. Zhang, "Research on safety early warning standard of large-scale underground utility tunnel in ground fissure active period," *Frontiers of Earth Science*, vol. 10, no. 9, 2022.

[4] B. L. Sun, Q. Zhang, Q. Q. Zhang, S. Z. Liu, and Z. Q. Zhou, "Optimization scheme of comprehensive geological prediction of filling-type karst caves," *Chinese Journal of Underground Space and Engineering*, vol. 10, no. S1, pp. 1728–1734, 2014.

[5] Z. Hang, C. Y. Zhou, X. Zhang, J. S. Yang, and D. Z. Huang, "Study on construction technology of tunnel concealed excavation in the backfill of giant karst cave hall," *Modern Tunnelling Technology*, vol. 57, no. S1, pp. 1086–1092, 2020.

[6] W. B. Zhu, H. Zhang, and H. Hui, "Risk analysis and prevention countermeasures of underground engineering in red bed karst development area," *Modern Tunnelling Technology*, vol. 58, no. 5, pp. 179–186, 2021.
[7] Q. Li and S. Qin, "Study on construction technology of bedrock solution treatment of China-Laos Railway bridge pile," *Carsologica Sinica*, vol. 38, no. 4, pp. 607–611, 2019.
[8] C. Zhang, J.-S. Yang, and J.-Y. Fu, "A new clay-cement composite grouting material for tunnelling in underwater karst area," *Journal of Central South University*, vol. 26, no. 7, pp. 1863–1873, 2019.
[9] S. H. Zhou, X. Li, C. Ji, and J. H. Xiao, "Back-fill grout experimental test for discharged soils reuse of the large-diameter size slurry shield tunnel," *KSCE Journal of Civil Engineering*, vol. 21, no. 3, pp. 725–733, 2017.
[10] C. Zhang, J. S. Yang, X. T. Ye, and Z. Zhang, "Mechanism and application of controllable grouting in loose strata before shield tunneling," *Chinese Journal of Rock Mechanics and Engineering*, vol. 36, no. 9, pp. 2324–2332, 2017.
[11] J. P. Xu, W. S. Lin, and K. Xu, "Study on rapid-hardening high-performance simultaneous grouting material for shield-bored tunnels," *Tunnel Construction*, vol. 34, no. 2, pp. 95–100, 2014.
[12] H. Grohs, "Cost-efficient regeneration of bore slurry for driving of Weser tunnel," *Tunnel Construction*, vol. 27, no. 6, pp. 47–51, 2007.
[13] T. Yang, S. L. Liu, X. Y. Wang, and H. Zhao, "Analysis of the deformation law of deep and large foundation pits in soft soil areas," *Frontiers of Earth Science*, vol. 10, 2022.
[14] N. Zhang, W. Zhu, and F. L Min, "Experimental study on preparation of slurry for slurry shields: case study on Weisanlu Yangtze river tunnel in Nanjing," *Tunnel Construction*, vol. 35, no. 10, pp. 1022–1027, 2015.
[15] Y. Dai, J. S. Yang, C. Zhang, and Y. P. Xie, "Research on recycling of discarded soil produced from slurry shield in synchronous grouting materials," *Journal of Huazhong University of Science and Technology (Nature Science Edition)*, vol. 47, no. 10, pp. 40–45, 2019.
[16] R. P. Chen and W. Xin, "Experiment of slurry shield tunnel recycling waste sand in sand-pebble layer," *Advanced Materials Research*, vol. 3149, no. 919–921, pp. 1104–1109, 2014.
[17] C. G. Lin, S. M. Wu, and T. D. Xia, "Design of shield tunnel lining taking fluctuations of river stage into account," vol. 45, no. 9, pp. 107–127, 2015.
[18] X. Lin, L. H. Chen, and W. Zhou, "Properties of UWB-II anti-washout admixtures of underwater concrete," *Concrete*, vol. 27, no. 4, pp. 52-53, 2006.
[19] Gb/T50080, "Standard for test method of performance on ordinary fresh concrete," GB/T50080, China, 2016.
[20] Dl/T5117, "Test code on non-dispersible underwater concrete," DL/T5117, China, 2000.

Hindawi
Advances in Civil Engineering
Volume 2022, Article ID 6104725, 9 pages
https://doi.org/10.1155/2022/6104725

Review Article

State-of-the-Art Review on Failure Mechanism and Waterproofing Performance of Linings for Shield Tunnels

Shaoshuai Du[1] **and Jinhua Tang**[2]

[1]*State Key Laboratory of Green Building in Western China, Xi'an University of Architecture & Technology, China*
[2]*Chang'an University, Xi'an, China*

Correspondence should be addressed to Jinhua Tang; 460820272@qq.com

Received 8 December 2021; Accepted 10 February 2022; Published 8 March 2022

Academic Editor: Song-He Wang

The introduction and development of shield tunnels have led to the innovation of precast segmental linings, which has significant advantages in improving the construction speed compared with in-situ cast concrete linings. However, damage of the linings and water leakage at the lining joints highlight defects in the design and construction of the linings. In this regard, it is necessary to investigate the failure mechanism of linings for shield tunnels and evaluate the waterproofing performance and repercussions of lining joints. The relevant research results published in recent years are reviewed in this paper, focusing on the failure mechanisms of linings and the waterproofing performance of lining joints. Progressive failure and instability of linings are introduced. Progressive failure has three stages: initial elastic stage, local damage stage, and overall failure stage. The performance-based design of joint waterproofing is described in seven steps. Further opportunities for the investigation of this topic are discussed.

1. Introduction

In recent decades, the construction and operation of public transport have gradually changed from single level to multilevel, from single dimensional to multidimensional, and from manual to intelligent. A typical example of the issues modern and intelligent rail transit tries to solve is the demand to alleviate the growing traffic pressure [1–4]. Moreover, the development of better construction techniques and innovations in materials used allows for the construction of subways in almost all kinds of soil environments, such as soft soil and with water pressure [5, 6].

Tunnel, one of the main forms of subway operation, is a three-dimensional traffic building buried in the stratum. Tunnel boring machines (TBMs), as the main tunneling tool for tunnel and utility construction in urban underground spaces [7], are widely used because of their high automation, fast construction speed, and low influence on ground disturbance [8, 9]. The tunnel lining is assembled into different shapes (circular, rectangular, and mixed shapes), which are determined by the shape of the TBM to withstand the loads imposed by the interior and exterior tunnel [10, 11]. Traditionally, tunnel linings are composed of several precast concrete segments, which are connected by rigid bolts [12], and the segments are usually reinforced with steel bars to bear both exterior and interior loads [10, 13]. The application of precast concrete segments (PCS) has increased significantly owing to its high quality, low cost of installation, and low cost of raw materials [14]. Compared with in-situ cast concrete segments (CCSs), PCS can be better actively controlled during the construction process, concrete pouring, and curing. In addition, for soft and hard soils, PCS can play a role in resisting external loads as soon as possible. Therefore, the use of PCS, especially in tunnel engineering in earthquake-prone areas, is becoming increasingly popular [15, 16].

The bearing capacity and sealing performance of tunnel linings have been widely studied to ensure the safety and durability of tunnel engineering. Most previous studies focused on in situ monitoring and theoretical analysis of tunnel linings subjected to various actions [4, 16–28]. Generally, the load actions that must be considered in the

design and construction of linings include undisturbed land stress, water pressure, pavement traffic load, subgrade reaction, grouting load, and service load [29]. During a long-term operation process, segment linings are inevitably attacked by uneven subsoils, traffic loading, and groundwater leakage [26, 30–32], which finally results in extrusion deformation and leakage corrosion [3, 25, 27, 33–35].

The problems mentioned above may lead to serious or even disastrous consequences, such as weak load resistance and instability of local segments caused by extrusion deformation, and leakage and corrosion at lining joints caused by unsealing. However, there are a few experimental and numerical studies on the mechanical properties and waterproofing design for linings of shield tunnels [36]. Therefore, it is particularly important and necessary to systematically understand and master the failure mechanisms of tunnel linings and the waterproofing performance of lining joints. Corresponding failure control mechanisms and performance-based waterproofing design can be proposed only by clarifying the failure process and leakage principle of the linings.

2. Failure Mechanism of Linings

2.1. Assessment of Time-Variant Loading. Generally, linings for a shield tunnel are mainly designed using analytical and simplified numerical models [3, 5, 37, 38], which do not consider the adverse effects of nonlinear actions [39] and longitudinal bending moments [40] in actual engineering. To eliminate the limitations of the aforementioned method in the analysis of the interactions between the tunnel shell and the surrounding soil, updated design guides were proposed in reference [41], which consider and discuss the load linings that are subjected to.

Short-term loads caused by the tail gap pressure were monitored [42], and long-term loads acting around the linings, such as earth and water pressures, were also monitored [17, 43]. To further understand the variation regulations of loads with time in real time, a process-oriented model was proposed [44, 45], which can produce a more reasonable analysis of groundwater flow and slurry hardening during the construction of the linings. A typical load distribution around the tunnel linings and the temporal and spatiotemporal evolution of earth and water pressures are shown in Figures 1 and 2, respectively.

2.2. Analysis of Cracking and Deformation. From among possible damages, cracking of the lining is regarded as one of the most serious problems in tunnels, as it leads to a reduction in the durability and structural performance of the overall tunnel [47]. There are several summaries in the literature on the cracking and damage of segmental linings in the construction stage [19, 48–50]. Longitudinal cracks, a common cracking pattern in tunnel segment linings, are mainly caused by various construction loads [51]. Typical cracking patterns in tunnel construction are shown in Figure 3 and mainly include cracks formed by external force intrusion into a curved tunnel with a small radius, the

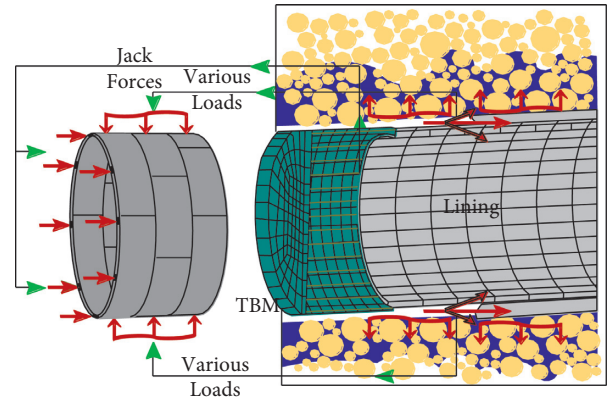

Figure 1: Various loads acting on the linings during construction (including grouting and earth and water pressures).

reaction force between jacks and adjacent segments in a tunnel with a large radius [52], and unsymmetrical pressure during mortar injection [53].

Furthermore, the deformation convergence and the state of the internal force of the linings are discussed in reference [35]. The deformation characteristics of existing linings under the actions of a foundation pit were analyzed using a hybrid model [54]. With the help of a three-dimensional nonlinear theory, a finite element model (FEM) of the hybrid shield was established, and the influence of different water pressures on the deformation performance of linings and joints was discussed [55]. Meanwhile, lateral deformation caused by lining failure has been extensively reported based on observations at construction sites [56].

2.3. Investigation of Mechanical Properties and Failure Mechanism. Once cracking and deformation occur in a tunnel lining, serious and uncontrolled consequences may be induced. It is necessary to study the mechanical properties and failure mechanisms of segmental linings. A hydraulic simulation method was proposed for analyzing the mechanical properties of tunnel linings [57]. Subsequently, the mechanical properties of precast individual segment linings are discussed, and the failure mechanism is analyzed [58]. The damage and failure mechanisms of lining joints caused by an uneven settlement of the foundations have been researched [59]. The results showed that the stress of a bolt on the section was directly proportional to the settlement depth, and an obvious dislocation phenomenon was captured at the connector of the linings. The bolts in the reverse and top positions of the segmental linings were damaged before the bolts in other positions, which can be described as a gradual failure process.

More recently, experimental research and numerical analysis of the mechanical properties of reinforced concrete linings have been performed [14, 60]. Loading tests of multiring assembled linings were carried out successively [61–63]. Compared with similar failure tests characterized by an instability failure mode, establishing predictions for lining failure based on the change rate of the tunnel diameter and ultimate displacement was proposed [61]. Failure of the

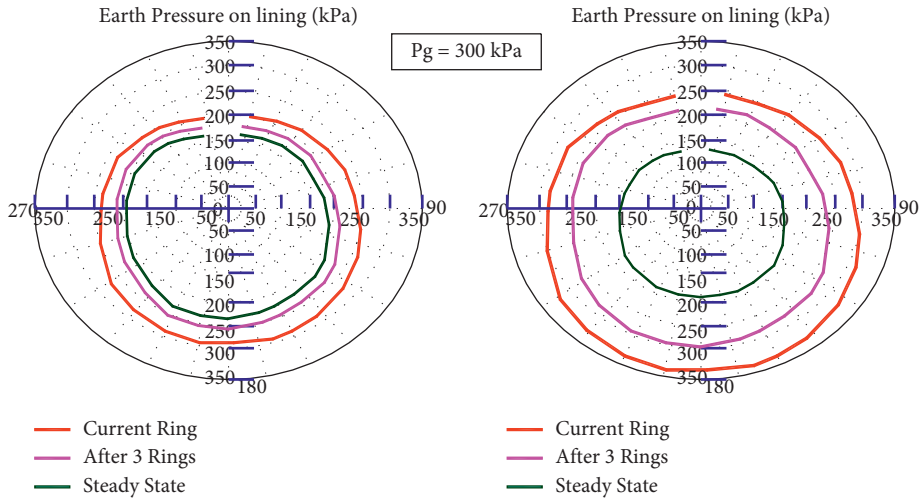

Figure 2: Spatiotemporal evolution (including earth and groundwater pressures) (reannotated based on literature [46]).

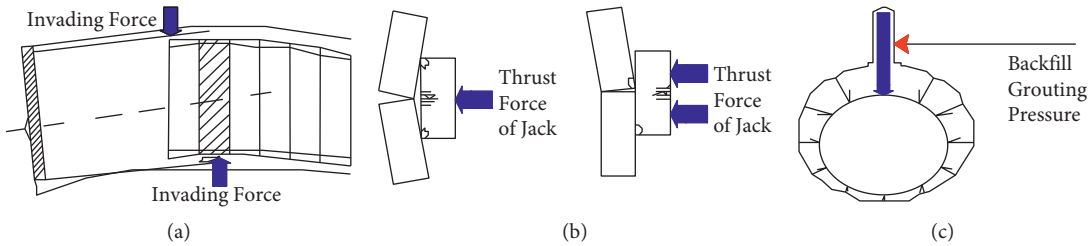

Figure 3: Typical cracking patterns in tunnel construction (reannotated based on reference [49]). (a) Invasion of shield tail. (b) Jack thrusting at deficient contacting segments. (c) Unsymmetrical pressure.

lining joints eventually led to a failure in the overall linings, but no significant damage occurred to the lining itself [62, 63]. A numerical simulation of the continuous failure process of the lining caused by local failure was performed. The results illustrate that the mechanical properties between adjacent linings can be predicted by means of existing failure criteria [64, 65].

2.4. Discussion of Progressive Failure and Instability. Although previous studies focused more on an analysis of loads, cracking and deformation, mechanical properties, and failure mechanisms, research on the progressive failure and stability of segmental linings has become increasingly popular in recent years. This research covers the experimental and theoretical analysis of the influence of sandy soil [66], soft surrounding rock [67], slope action [68], river glacier gravel [69], groundwater flow [70], water storage tunnel [71], uncorrelated flow [72], and different soil action [73] on the stability of tunnel linings. All these results contribute to further improvements in the linings in terms of preliminary design, rapid construction, operation, and maintenance.

In addition, a large number of scale tests were carried out [74] to reveal the progressive failure and instability process of linings from the aspects of assembly mode, lateral pressure, and cap block position. The progressive failure of linings consisted of three stages: initial elastic stage, local damage stage, and overall failure stage. The lining material was compacted, and the friction stress gradually increased between the equipment and the soil (points A to B). New cracks appeared one after another, and existing cracks continued to widen and elongate, implying that the microfailure of the linings was gradual rather than an instantaneous process (points B to C). Penetrating cracks were observed, and regional fractures occurred, resulting in the fracture of segmental linings along the overall section (points C to D). Subsequently, the segment linings began to rapidly lose stability until final failure occurred. The force-displacement curves of the segment linings at each characteristic point are shown in Figure 4.

3. Waterproofing Performance of Linings

3.1. Water Leakage Behavior of Lining Joints. In recent years, the advantages of precast linings, such as plain concrete (PC) and steel fiber-reinforced concrete (SFRC) linings, have been explored, which led to the promotion of its application in tunnel construction. Table 1 presents the literature on experimental studies of precast linings using different materials [14, 25, 26, 58, 75–82]. However, adverse factors in the underwater environment [83, 84], such as high-pressure water and weak seabed, lead to the weak performance of the lining (leakage water of the lining joint). Therefore, it is

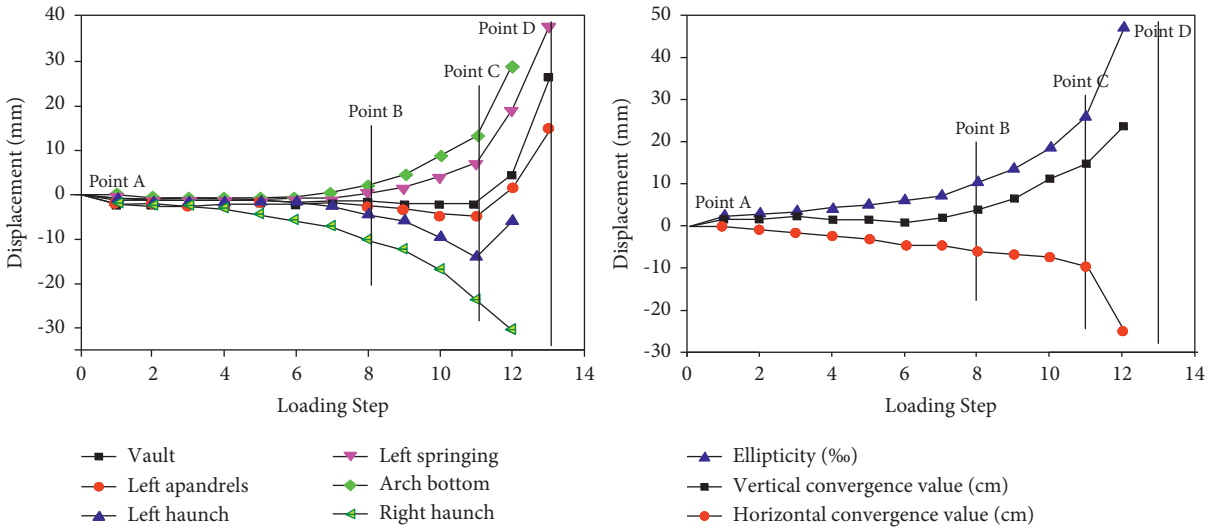

Figure 4: Force-displacement curves at each characteristic point [63].

Table 1: Summary of relevant literature on precast linings.

Objective	Material	Objective	Material
Bearing capacity [75]	PC and SFRC	Structural behavior [76]	RC and SFRC
Structural behavior [58]	RC and SFRC	Settlement behavior [14]	RC and SFRC
Structural response [77]	SFRC	Structural behavior [78]	RC and SFRC
Mechanical behavior [79]	FRHPC	Bearing capacity [80]	UHPFRC
Ductile behavior [81]	SFRC	Structural behavior [82]	RC and HFRC

where PC represents the plain concrete, RC represents the reinforced concrete, SFRC represents the steel fiber-reinforced concrete, FRHPC represents the fiber-reinforced high-performance concrete, UHPFRC represents the ultrahigh-fiber-reinforced concrete, and HFRC represents the hybrid-fiber-reinforced concrete.

necessary to master the leakage behavior of the lining joint to understand the failure mechanism and performance-based design of joint waterproofing.

It is well known that the waterproofing performance of precast linings mainly depends on the joint. A countermeasure for the failure of a joint is to install a rubber gasket. Joint leakage usually occurs at the contact surface between the rubber gasket and the groove, or between the two rubber gaskets [36, 85]. Compared with the first, the latter has a smaller contact stress value, resulting in easier water leakage between the two rubber gaskets [7]. Figures 5 and 6 illustrate the leakage point and water leakage process of the lining joint, respectively. Under the continuous action of water pressure, the two contact surfaces experienced initial separation (Figure 6(a)), contact failure (Figure 6(b)), and complete separation (Figure 6(c)), and finally formed a complete leakage path.

3.2. Failure Mechanism of Joint Waterproofing. A series of national specifications were issued [84–88], and experimental studies were carried out [6, 7, 16, 25–28, 31, 36, 89–92], aiming to further understand the behavior and mechanism of joint waterproofing of linings.

Typical joint waterproofing failure patterns are shown in Figure 7 and are mainly grouped into four failure patterns [7, 91]. In the joint opening pattern (Figure 7(a)), the waterproofing capacity of the groove interface was significantly better than that between the two gaskets, resulting in leakage often occurring between the contact surfaces of the two gaskets. In the joint offset pattern (Figure 7(b)), the joint waterproofing failure was mainly caused by displacement dislocation between the gasket and the groove. In the positive and negative rotation patterns (Figures 7(c) and 7(d)), the rate of leakage reduction was positively correlated with the rate of joint rotation. Meanwhile, within the controllable range of joint rotation, the waterproofing capacity of the interface between the gasket and the groove is due to the waterproofing capacity between the two gaskets.

3.3. Performance-Based Design of Joint Waterproofing. After mastering the leakage behavior and waterproofing failure mechanism of the lining joints, a performance-based design concept for joint waterproofing was proposed [7, 16]. The specific design process is illustrated in Figure 8. Corresponding experimental and numerical studies have verified the impact of different influencing factors on the waterproofing performance, such as gasket hardness, joint opening and rotation angle, and friction coefficient. The described design effectively simplifies the waterproofing performance evaluation of the lining joints during preliminary design and operation.

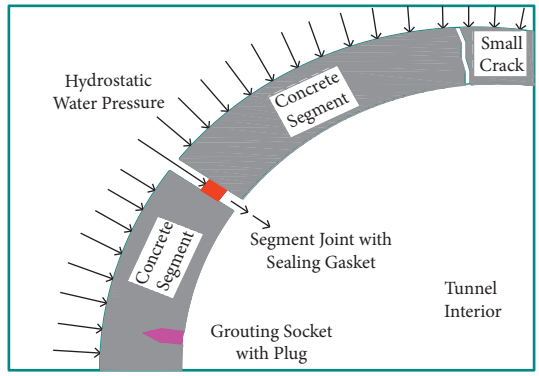

Figure 5: Illustration of leakage point (reannotated based on references [84, 86]).

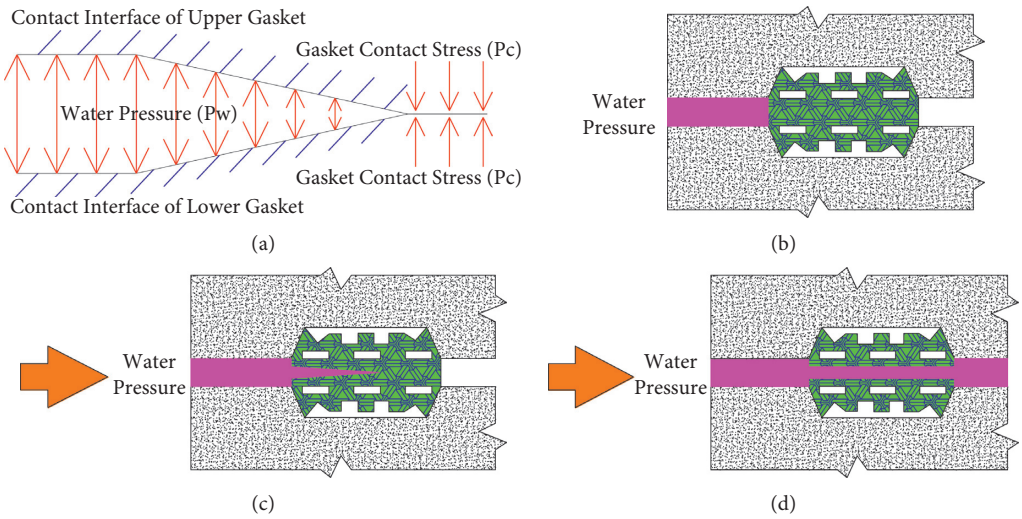

Figure 6: Water leakage process of lining joint. (a) Various loads on the gasket. (b) Initial penetration. (c) Further penetration. (d) Final leakage.

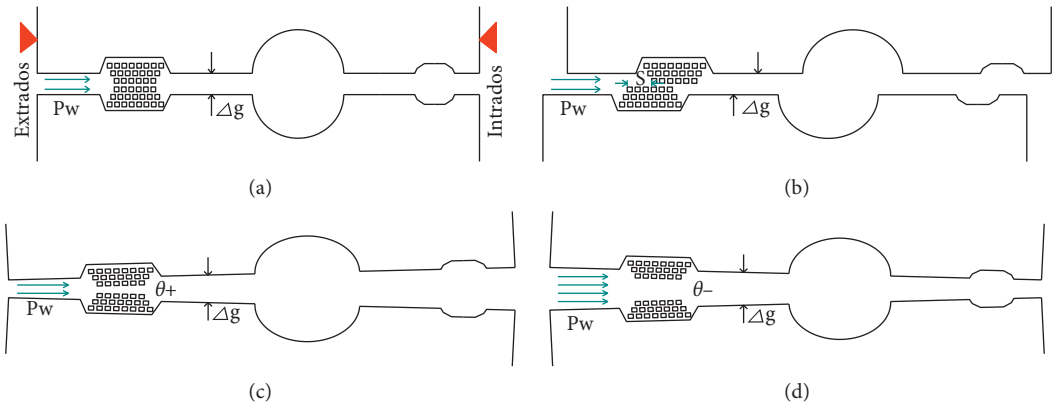

Figure 7: Failure patterns of joint waterproofing. (a) Opening of joint. (b) Offset of joint. (c) Positive joint rotation. (d) Negative joint rotation.

4. Future Works

Adverse factors in the construction process should be eliminated as much as possible, such as the pressure exerted by the jacks and unbalanced pressure between the interior and the exterior, which can effectively avoid the occurrence of initial cracks. The design of linings should focus on the weak positions rather than the overall structure, such as on lining joints, because it is often damaged at weak positions that lead to lining failure. Moreover, early warning

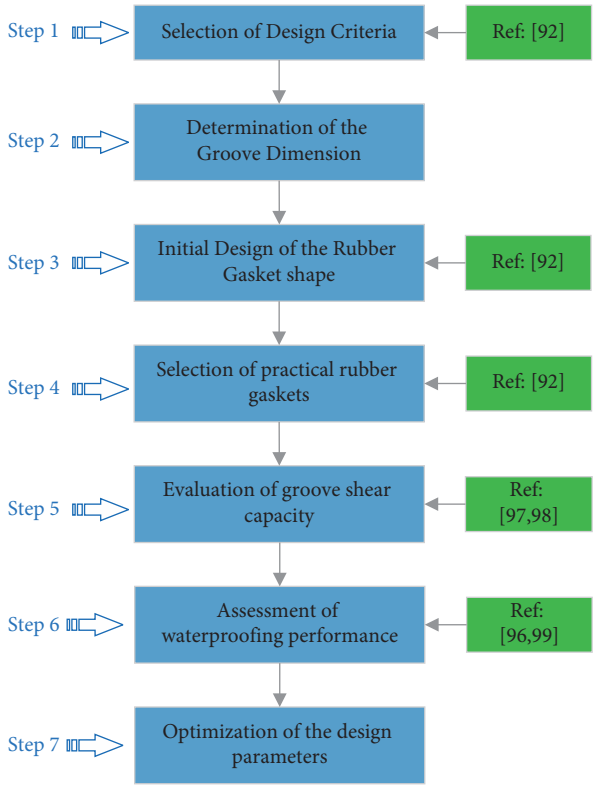

Figure 8: Specific performance-based design process for joint waterproofing.

mechanisms (EWMs) should be established [63, 93]. Once the critical value of local damage reaches point B, an early warning response (EWR) is initiated and the corresponding countermeasures are taken.

5. Conclusions

To investigate and master the failure control mechanism and performance-based design methods for linings of shield tunnels, this paper summarizes the results of the failure mechanism and waterproofing performance in the field of linings for shield tunnels. The main conclusions based on the findings of this review are as follows:

(1) Most cracks in tunnel construction are caused by external force intrusion into a curved tunnel with a small radius, by reaction force between the jacks and adjacent segments in a tunnel with a large radius, and by unsymmetrical pressure during mortar injection. Orderly construction operation and strict grouting process are essential for controlling the cracks of a tunnel.

(2) Failure of the overall linings is caused by a failure of the lining joint, and there is no obvious damage to the lining itself. The mechanical properties between adjacent linings can be predicted reasonably using the existing failure criteria. However, there are a few application cases of existing failure criteria in practical tunnel engineering. It is important to predict the mechanical response of existing lining through the proposed failure criteria.

(3) The typical waterproofing failure patterns of joints mainly include the joint opening pattern, the joint offset pattern, and patterns of positive rotation and negative rotation. At the same time, within the controllable range of joint rotation, the waterproofing capacity of the interface between the gasket and the groove mainly depends on the waterproofing capacity between the two gaskets. In order to meet the requirements of durability, it is necessary to research the mechanical properties of gaskets with new materials and new processes.

(4) In the actual tunnel engineering, the adverse factors in the construction process should be eliminated as far as possible, and the design of the weak part of the lining should be paid special attention to. In addition, comprehensive early warning mechanisms (EWMs) and solutions should be established. Once the critical value of local damage reaches the set value, EWR is initiated and the corresponding countermeasures are taken [94–96].

Conflicts of Interest

The authors declare that they have no conflicts of interest.

References

[1] J. S. Roh, H. S. Ryou, W. H. Park, and Y. J. Jang, "CFD simulation and assessment of life safety in a subway train fire," *Tunnelling and Underground Space Technology*, vol. 24, no. 4, pp. 447–453, 2009.

[2] G. Ran, A. Li, X. Hao, W. Lei, and B. Deng, "Prediction of the spread of smoke in a huge transit terminal subway station under six different fire scenarios," *Tunnelling and Underground Space Technology*, vol. 31, pp. 128–138, 2012.

[3] X. Lin, Z. Jiang, Y. Yuan, and H. A. Mang, "Numerical investigation of the mechanical behavior of deformed segmental tunnel linings, strengthened by epoxy-bonded filament wound profiles," *Tunnelling and Underground Space Technology*, vol. 78, pp. 231–244, 2019.

[4] Y. A. Fei, Q. A. Nan, L. A. Xing, and A. Ouyang, "Analyses of the defects in highway tunnels in China," *Tunnelling and Underground Space Technology*, vol. 107, p. 103658, 2020.

[5] H. Zheng, P. Li, and G. Ma, "Stability analysis of the middle soil pillar for asymmetric parallel tunnels by using model testing and numerical simulations," *Tunnelling and Underground Space Technology*, vol. 108, Article ID 103686, 2020.

[6] S. Fan, Z. Song, T. Xu, and Y. Zhang, "Investigation of the microstructure damage and mechanical properties evolution of limestone subjected to high-pressure water," *Construction and Building Materials*, vol. 316, Article ID 125871, 2022.

[7] C. Gong, W. Ding, and K. M. Mosalam, "Performance-based design of joint waterproofing of segmental tunnel linings using hybrid computational/experimental procedures," *Tunnelling and Underground Space Technology*, vol. 96, no. 2, Article ID 103172, 2020.

[8] Y. H. M. Amran, N. Farzadnia, and A. A. Abang Ali, "Properties and applications of foamed concrete; A review,"

Construction and Building Materials, vol. 101, no. DEC.30.1, pp. 990–1005, 2015.

[9] C. Zhang, J. Fu, J. Yang, X. Ou, X. Ye, and Y. Zhang, "Formulation and performance of grouting materials for underwater shield tunnel construction in karst ground," *Construction and Building Materials*, vol. 187, no. 10/30, pp. 327–338, 2018.

[10] L. Jin-Long, O. Hamza, K. Sian Davies-Vollum, and L. Jie-qun, "Repairing a shield tunnel damaged by secondary grouting," *Tunnelling and Underground Space Technology*, vol. 80, no. 10, pp. 313–321, 2018.

[11] S.-H. Tang, X.-P. Zhang, Q.-S. Liu et al., "Prediction and analysis of replaceable scraper wear of slurry shield TBM in dense sandy ground: A case study of Sutong GIL Yangtze River Crossing Cable Tunnel," *Tunnelling and Underground Space Technology*, vol. 95, Article ID 103090, 2020.

[12] Z. Zhang and Y. A. Mansoor, "Evaluating the strength of corroded tunnel lining under limiting corrosion conditions," *Tunnelling and Underground Space Technology*, vol. 38, no. 9, pp. 464–475, 2013.

[13] S. Jiang and A. Bloodworth, "Interface parameters of composite sprayed concrete linings in soft ground with spray-applied waterproofing," *Tunnelling and Underground Space Technology*, vol. 59, pp. 170–182, 2016.

[14] S. Abbas, A. M. Soliman, and M. L. Nehdi, "Experimental study on settlement and punching behavior of full-scale RC and SFRC precast tunnel lining segments," *Engineering Structures*, vol. 72, no. 8/1, pp. 1–10, 2014.

[15] G. Andreotti, G. M. Calvi, K. Soga, C. Gong, and W. Ding, "Cyclic model with damage assessment of longitudinal joints in segmental tunnel linings," *Tunnelling and Underground Space Technology*, vol. 103, Article ID 103472, 2020.

[16] Y. Qiu, X. Hu, G. Walton, C. He, C. He, and J. Woody Ju, "Full scale tests and a progressive failure model to simulate full mechanical behavior of concrete tunnel segmental lining joints," *Tunnelling and Underground Space Technology*, vol. 110, Article ID 103834, 2021.

[17] Y. Koyama, "Present status and technology of shield tunneling method in Japan," *Tunnelling and Underground Space Technology Incorporating Trenchless Technology Research*, vol. 18, no. 2/3, pp. 145–159, 2003.

[18] A. Bezuijen, A. M. Talmon, F. J. Kaalberg, and R. Plugge, "Field measurements of grout pressures during tunnelling of the sophia rail tunnel," *Soils and Foundations*, vol. 44, no. 1, pp. 39–48, 2004.

[19] J. S. Chen and H. H. Mo, "Numerical study on crack problems in segments of shield tunnel using finite element method," *Tunnelling and Underground Space Technology*, vol. 24, no. 1, pp. 91–102, 2009.

[20] M. Ramoni, N. Lavdas, and G. Anagnostou, "Squeezing loading of segmental linings and the effect of backfilling," *Tunnelling and Underground Space Technology*, vol. 26, no. 6, pp. 692–717, 2011.

[21] J.-Y. Oh and M. Ziegler, "Investigation on influence of tail void grouting on the surface settlements during shield tunneling using a stress-pore pressure coupled analysis," *Ksce Journal of Civil Engineering*, vol. 18, no. 3, pp. 803–811, 2014.

[22] G.-l. Ye, T. Hashimoto, S.-l. Shen, H.-h. Zhu, and T.-h. Bai, "Lessons learnt from unusual ground settlement during Double-O-Tube tunnelling in soft ground," *Tunnelling and Underground Space Technology*, vol. 49, no. 6, pp. 79–91, 2015.

[23] Z. Wang, L. Z. Wang, J. C. Wang, and L.-L. Li, "Case study of rehabilitation of a damaged underwater tunnel in the construction phase," *Journal of Performance of Constructed Facilities*, vol. 30, no. 1, Article ID C4014003, 2016.

[24] V. E. Gall, A. Marwan, M. Smarslik, M. Obel, P. Mark, and G. Meschke, "A holistic approach for the investigation of lining response to mechanized tunneling induced construction loadings," *Underground Space*, vol. 3, no. 1, 2018.

[25] J. Liu, C. Shi, Z. Wang, M. Lei, D. Zhao, and C. Cao, "Damage mechanism modelling of shield tunnel with longitudinal differential deformation based on elastoplastic damage model," *Tunnelling and Underground Space Technology*, vol. 113, Article ID 103952, 2021.

[26] Z. Song, T. Wang, J. Wang, K. Xiao, and T. Yang, "Uniaxial compression mechanical properties and damage constitutive model of limestone under osmotic pressure," *International Journal of Damage Mechanics*, Article ID 105678952110454, 2021.

[27] S. Y. Fan, Z. P. Song, T. Xu, K. Wang, and Y. Zhang, "Tunnel deformation and stress response under the bilateral foundation pit construction - a case study," *Archives of Civil and Mechanical Engineering*, vol. 21, no. 3, 2021.

[28] L. Li, C. Shang, K. Chu et al., "Large-scale geo-mechanical model tests for stability assessment of super-large cross-section tunnel," *Tunnelling and Underground Space Technology*, vol. 109, Article ID 103756, 2021.

[29] W. Association, "Guidelines for the design of shield tunnel lining," *Tunnelling and Underground Space Technology*, vol. 15, no. 3, pp. 303–331, 2000.

[30] J.-C. Chai, J. S.-L. Shen, M. D. Liu, and D.-J. Yuan, "Predicting the performance of embankments on PVD-improved subsoils," *Computers and Geotechnics*, vol. 93, pp. 222–231, 2018.

[31] H.-N. Wu, R.-Q. Huang, W.-J. Sun et al., "Leaking behavior of shield tunnels under the Huangpu River of Shanghai with induced hazards," *Natural Hazards*, vol. 70, no. 2, pp. 1115–1132, 2014.

[32] H.-N. Wu, S.-L. Shen, S.-M. Liao, and Z.-Y. Yin, "Longitudinal structural modelling of shield tunnels considering shearing dislocation between segmental rings," *Tunnelling and Underground Space Technology*, vol. 50, no. 8, pp. 317–323, 2015.

[33] W. F. Lee and K. Ishihara, "Forensic diagnosis of a shield tunnel failure," *Engineering Structures*, vol. 32, no. 7, pp. 1830–1837, 2010.

[34] H.-w. Huang and D.-m. Zhang, "Resilience analysis of shield tunnel lining under extreme surcharge: characterization and field application," *Tunnelling and Underground Space Technology*, vol. 51, pp. 301–312, 2016.

[35] D. M. Zhang, L. Z. Ran, and J. Y. Yan, "Effect of grouting on tunnel leakage-induced pore pressure change in saturated soft soils," *Rock and Soil Mechanics*, 2017.

[36] W. Ding, C. Gong, K. M. Mosalam, and K. Soga, "Development and application of the integrated sealant test apparatus for sealing gaskets in tunnel segmental joints," *Tunnelling and Underground Space Technology*, vol. 63, no. 3, pp. 54–68, 2017.

[37] H. Duddeck and J. Erdmann, "On structural design models for tunnels in soft soil," *Underground Space*, vol. 9, pp. 246–259, 1985.

[38] H. D. Morgan, "A contribution to the analysis of stress in a circular tunnel," *Géotechnique*, vol. 11, no. 1, pp. 37–46, 1961.

[39] H. J. Kim and Z. Eisenstein, "Prediction of tunnel lining loads using correction factors," *Engineering Geology*, vol. 85, no. 3-4, pp. 302–312, 2006.

[40] A. M. Talmon and A. Bezuijen, "Analytical model for the beam action of a tunnel lining during construction,"

International Journal for Numerical and Analytical Methods in Geomechanics, vol. 37, no. 2, pp. 181–200, 2013.

[41] C. E. Augarde and H. J. Burd, "Three-dimensional finite element analysis of lined tunnels," *International Journal for Numerical and Analytical Methods in Geomechanics*, vol. 25, no. 3, pp. 243–262, 2001.

[42] T. Hashimoto, J. Nagaya, and T. Konda, "Observation of lining pressure due to shield tunneling," in *Geotechnical Aspects of Underground Construction in Soft Ground*, R. Kastner, F. Emeriault, D. Dias, and A. Guilloux, Eds., pp. 119–124, Lyon, 2002.

[43] A. Popp, *Mortar Methods for Computational Contact Mechanics and General Interface Problems*, Technische Universität München, Germany, 2012.

[44] F. Nagel, J. Stascheit, and G. Meschke, "Process-oriented numerical simulation of shield-supported tunnelling in soft soils/. Prozessorientierte numerische Simulation schildgestützter Tunnelvortriebe in Lockerböden," *Geomechanics and Tunnelling*, vol. 3, no. 3, pp. 268–282, 2010.

[45] J. Ninic, *Computational Strategies for Predictions of the Soil-Structure Interaction during Mechanized Tunneling*, Ruhr University Bochum, Germany, 2015.

[46] J. Ninic and G. Meschke, "Simulation based evaluation of time-variant loadings acting on tunnel linings during mechanized tunnel construction," *Engineering Structures*, vol. 135, pp. 21–40, 2017.

[47] J. Zhu and Y. Li, "Quality testing and evaluation of the damaged lining of zhoulichong railway tunnel," in *Geohunan International Conference*, pp. 25–32, Hunan, China, July 2011.

[48] Japan Society of Civil Engineering (Jsce), *Tunnel Library17: Construction Loads during Shield Tunnelling*, JSCE, Tokyo Japan, (in Japanese), 2006.

[49] M. Sugimoto, "Causes of shield segment damages during construction," in *International Symposium on Underground Excavation and Tunnelling*, pp. EIT67–74, Bangkok Thailand, 2-4 Feb. 2006.

[50] Z. X. Ming, Y. W. Wei, and C. Xuan, "Seismic behavior of underground station and surface building interaction system in earth fissure environment – science Direct," *Tunnelling and Underground Space Technology*, vol. 110, 2021.

[51] G. L. Ye, L. Han, and S. K. Yadav, "Investigation on the tail brush induced loads upon segmental lining of a shield tunnel with small overburden," *Tunnelling and Underground Space Technology*, vol. 97, no. 3, pp. 1–10, 2020.

[52] S. Cavalaro, C. Blom, J. C. Walraven, and A. Aguado, "Structural analysis of contact deficiencies in segmented lining," *Tunnelling and Underground Space Technology Incorporating Trenchless Technology Research*, vol. 26, no. 6, 2011.

[53] H. Mashimo and T. Ishimura, "Numerical modelling of the behaviour of shield tunnel lining during assembly of a tunnel ring," in *Geotechnical Aspects of Underground Construction in Soft Ground-Proceedings of the 5th International Symposium TC28*, pp. 587–593, Amsterdam, the Netherlands, July 2008.

[54] C. Shi, C. Cao, M. Lei, L. Peng, and H. Ai, "Effects of lateral unloading on the mechanical and deformation performance of shield tunnel segment joints," *Tunnelling and Underground Space Technology*, vol. 51, no. 1, pp. 175–188, 2016.

[55] T. Zhao, W. Liu, and Z. Ye, "Effects of water inrush from tunnel excavation face on the deformation and mechanical performance of shield tunnel segment joints," *Advances in Civil Engineering*, vol. 2017, pp. 1–18, 2017.

[56] Y. Yang, B. Zhou, X. Xie, and C. Liu, "Characteristics and causes of cracking and damage of shield tunnel segmented lining in construction stage – a case study in Shanghai soft soil," *European Journal of Environmental and Civil Engineering*, pp. 1–15, 2017.

[57] H. Xie, X. Duan, H. Yang, and Z. Liu, "Automatic trajectory tracking control of shield tunneling machine under complex stratum working condition," *Tunnelling and Underground Space Technology*, vol. 32, no. 6, pp. 87–97, 2012.

[58] A. Caratelli, A. Meda, Z. Rinaldi, and P. Romualdi, "Structural behaviour of precast tunnel segments in fiber reinforced concrete," *Tunnelling and Underground Space Technology*, vol. 26, no. 2, pp. 284–291, 2011.

[59] Z. Wang, L. Wang, L. Li, and J. Wang, "Failure mechanism of tunnel lining joints and bolts with uneven longitudinal ground settlement," *Tunnelling and Underground Space Technology*, vol. 40, no. 2, pp. 300–308, 2014.

[60] W. C. Cheng, J. C. Ni, and S. L. Shen, "Experimental and analytical modeling of shield segment under cyclic loading," *International Journal of Geomechanics*, vol. 17, no. 6, Article ID 04016146, 2016.

[61] R. Guo and C. He, "Study on stability of segment lining structure for shield tunnel," *China Journal of Highway and Transport*, vol. 28, no. 6, pp. 74–81, 2015.

[62] X. Liu, Y. Bai, and Y. Yuan, "Experimental investigation of the ultimate bearing capacity of continuously jointed segmental tunnel linings: structure and Infrastructure Engineering," *Structure and Infrastructure Engineering*, vol. 12, no. 10, 2015.

[63] X. Liu, Z. Jiang, and L. Zhang, "Experimental investigation of the ultimate bearing capacity of deformed segmental tunnel linings strengthened by epoxy-bonded filament wound profiles," *Structure and Infrastructure Engineering*, vol. 13, no. 10, pp. 1–16, 2017.

[64] G. Zheng, T. Cui, X. Cheng et al., "Study of the collapse mechanism of shield tunnels due to the failure of segments in sandy ground," *Engineering Failure Analysis*, vol. 79, no. 79, pp. 464–490, 2017.

[65] F. Ye, C.-f. Gou, H.-d. Sun, Y.-p. Liu, Y.-x. Xia, and Z. Zhou, "Model test study on effective ratio of segment transverse bending rigidity of shield tunnel," *Tunnelling and Underground Space Technology*, vol. 41, no. 3, pp. 193–205, 2014.

[66] R.-p. Chen, J. Li, L.-g. Kong, and L.-j. Tang, "Experimental study on face instability of shield tunnel in sand," *Tunnelling and Underground Space Technology*, vol. 33, no. 1, pp. 12–21, 2013.

[67] Q. J. Zuo, L. Wu, Z. L. Lu, Y.-Z. Tun, and Q. Yuan, "Instability analysis of soft surrounding rock in shallow tunnel portal under unsymmetrical pressure by catastrophe theory," *Rock and Soil Mechanics*, vol. 36, pp. 424–430, 2015.

[68] Y.-C. Chiu, C.-H. Lee, and T.-T. Wang, "Lining crack evolution of an operational tunnel influenced by slope instability," *Tunnelling and Underground Space Technology*, vol. 65, no. 3, pp. 167–178, 2017.

[69] E. O'Connor, M. Friedman, F. Dahl, P. D. Jakobsend, D. Oosterhoutc, and M. Longe, "Assessing the abrasivity characteristics of the central Dublin fluvio-glacial gravels – a laboratory study," *Tunnelling and Underground Space Technology*, vol. 96, no. 2, pp. 1–13, 2020.

[70] S. Lee and J.-S. Moon, "Excessive groundwater inflow during TBM tunneling in limestone formation," *Tunnelling and Underground Space Technology*, vol. 96, Article ID 103217, 2020.

[71] H. Xin, L. Wei, and B. Zza, "Structural behavior of segmental tunnel linings for a large stormwater storage tunnel: insight from full-scale loading tests," *Tunnelling and Underground Space Technology*, vol. 99, Article ID 103376, 2020.

[72] P. Li, Y. Wei, M. Zhang, Q. Huang, and F. Wang, "Influence of non-associated flow rule on passive face instability for shallow shield tunnels," *Tunnelling and Underground Space Technology*, vol. 119, Article ID 104202, 2022.

[73] T. Kasper, C. Edvardsen, G. Wittneben, and G. Neumann, "Lining design for the district heating tunnel in Copenhagen with steel fibre reinforced concrete segments," *Tunnelling and Underground Space Technology incorporating Trenchless Technology Research*, vol. 23, no. 5, pp. 574–587, 2008.

[74] S. Wang, X. Wang, B. Chen, Y. Fu, Y. Jian, and X. Lu, "Critical state analysis of instability of shield tunnel segment lining," *Tunnelling and Underground Space Technology*, vol. 96, Article ID 103180, 2020.

[75] J. Poh, K. H. Tan, G. L. Peterson, and D. Wen, "Structural testing of steel fibre reinforced concrete (SFRC) tunnel lining segments in Singapore," *Scribd*, 2009.

[76] Z.-g. Yan, H.-h. Zhu, and J. W. Ju, "Behavior of reinforced concrete and steel fiber reinforced concrete shield TBM tunnel linings exposed to high temperatures," *Construction and Building Materials*, vol. 38, no. JAN, pp. 610–618, 2013.

[77] M. O. Arnau, "Experimental and analytical study of the structural response of segmental tunnel linings based on an in situ loading test.: Part 1: test configuration and execution," *Tunnelling and Underground Space Technology*, vol. 26, no. 6, pp. 764–777, 2011.

[78] S. Abbas, A. M. Soliman, and M. L. Nehdi, "Mechanical performance of RC and SFRC precast tunnel lining segments: a Case Study," *ACI Materials Journal*, vol. 111, no. 5, pp. 501–505, 2014.

[79] Y. Ding, H. Liu, F. Pacheco-Torgal, and S. Jalali, "Experimental investigation on the mechanical behaviour of the fiber reinforced high-performance concrete tunnel segment," *Composite Structures*, vol. 93, no. 4, pp. 1284–1289, 2011.

[80] M. L. Nehdi, S. Abbas, and A. M. Soliman, "Exploratory study of ultra-high performance fiber reinforced concrete tunnel lining segments with varying steel fiber lengths and dosages," *Engineering Structures*, vol. 101, no. 10, pp. 733–742, 2015.

[81] A. Caratelli, A. Meda, and Z. Rinaldi, "Design according to MC2010 of a fibre-reinforced concrete tunnel in Monte Lirio, Panama," *Structural Concrete*, vol. 13, no. 3, pp. 166–173, 2012.

[82] Z.-g. Yan, Y. Shen, H.-h. Zhu, X.-j. Li, and Y. Lu, "Experimental investigation of reinforced concrete and hybrid fibre reinforced concrete shield tunnel segments subjected to elevated temperature," *Fire Safety Journal*, vol. 71, no. 1, pp. 86–99, 2015.

[83] B. Nilsen, "Characteristics of water ingress in Norwegian subsea tunnels," *Rock Mechanics and Rock Engineering*, vol. 47, no. 3, pp. 933–945, 2014.

[84] Ø. Dammyr, B. Nilsen, K. Thuro, and J. Grøndal, "Possible concepts for waterproofing of Norwegian TBM railway tunnels," *Rock Mechanics and Rock Engineering*, vol. 47, no. 3, pp. 985–1002, 2014.

[85] F. I. Shalabi, E. J. Cording, and S. L. Paul, "Concrete segment tunnel lining sealant performance under earthquake loading," *Tunnelling and Underground Space Technology*, vol. 31, pp. 51–60, 2012.

[86] C. Gong, W. Ding, K. Soga, K. M. Mosalam, and Y. Tuo, "Sealant behavior of gasketed segmental joints in shield tunnels: an experimental and numerical study," *Tunnelling and Underground Space Technology*, vol. 77, no. 7, pp. 127–141, 2018.

[87] German Tunnelling Committee (Daub), *Recommendations for the Design, Production and Installation of Segmental Rings*, Cologne, Germany, 2013.

[88] GB/T51438-2021, *Design Standard for Shield Tunnel Engineering*, Ministry of Housing and Urban-Rural Development of the People's Republic of China, Beijing, 2021.

[89] C. Gong and W. Ding, "A computational framework to predict the water-leakage pressure of segmental joints in underwater shield tunnels using an advanced finite element method," *International Journal for Numerical and Analytical Methods in Geomechanics*, 2018.

[90] M. Wang, Y. Dong, L. Yu, L. Fang, X. Wang, and D. Liu, "Experimental and numerical researches of precast segment under radial dislocation conditions," *Tunnelling and Underground Space Technology*, vol. 92, no. 10, pp. 1–16, 2019.

[91] C. Gong, W. Ding, K. Soga, and K. M. Mosalam, "Failure mechanism of joint waterproofing in precast segmental tunnel linings," *Tunnelling and Underground Space Technology*, vol. 84, no. 2, pp. 334–352, 2019.

[92] T. Xu, Z. Song, D. Guo, and Y. Song, "A cloud model-based risk assessment methodology for tunneling-induced damage to existing tunnel," *Advances in Civil Engineering*, vol. 2020, no. 14, pp. 1–11, 2020.

[93] Y. Li and Q. Y. Wang, "Research on deformation law of deep excavation supporting structures in Beijing metro station," *Advanced Materials Research*, vol. 243-249, pp. 2338–2344, 2011.

[94] J. Lubliner, J. Oliver, S. Oller, and E. Oñate, "A plastic-damage model for concrete," *International Journal of Solids and Structures*, vol. 25, no. 3, pp. 299–326, 1989.

[95] J. Lee and G. L. Fenves, "Plastic-damage model for cyclic loading of concrete structures," *Journal of Engineering Mechanics*, vol. 124, no. 8, pp. 892–900, 1998.

[96] HG/T 3087, *Method of Accelerated Determination for Shelf-Life of Rubber Static Sealing Parts*, Ministry of Commerce of the People's Republic of China, Beijing, 2001.

Hindawi
Advances in Civil Engineering
Volume 2022, Article ID 6165563, 11 pages
https://doi.org/10.1155/2022/6165563

Research Article

Correlations between Distribution of Producer Services and Urban Built Environment in Metro Station Areas: A Case of Xi'an, China

Qi Zhang,[1,2] **Yu-Jie Zhang**,[1] **Xin Ding**,[1] **and Qiu-Ping Wang**[1,2]

[1]*School of Civil Engineering, Xi'an University of Architecture and Technology, Xi'an 710055, China*
[2]*National Experimental Teaching Center for Civil Engineering Virtual Simulation (XAUAT), Xi'an 710055, China*

Correspondence should be addressed to Qi Zhang; zhangqi-xauat@163.com

Received 6 December 2021; Accepted 3 February 2022; Published 28 February 2022

Academic Editor: Song-He Wang

Since impacts of rail transit on urban industries and space most obviously appear in metro station areas, correlations between the spatial distribution of producer services and urban built environment in metro station areas are studied in Xi'an, China. At first, the scope determining methods of a metro station area were separately proposed for both single-line station and multiline transfer station based on their construction and transportation modes. Then, when the producer services were divided into 6 categories of business, POI numbers of enterprises of each category in metro station areas were collected and weighted to calculate the distribution intensity for categories. Finally, on condition that the urban built environment of a metro station area included job and residence space, outdoor activity space, and municipal road space, correlation performances between the distribution intensity of categories and indexes representing 3 space elements of the built environment were calculated through second-order partial correlation analysis, while the corresponding mechanisms of correlations were explained too. The main conclusions of this paper indicate that there are significant positive correlations between the distribution intensity and the diversity index of job and residence space for most categories, whereas significant negative correlations between it and the openness index of outdoor activity space for most categories. Moreover, positive but weak correlations were appeared between the distribution intensity and the street network density index of municipal road space only for categories of intermediary consulting and leasing.

1. Introduction

Modern rail transit system is not only a convenient and efficient urban traffic tool but also an impetus to urban economic development. According to many studies over the world, the economic functions of rail transit systems have mainly referred to quasipublic products, positive externalizations, and economies of scale [1], while the variation and transformation of urban industrial structure and spatial structure have been deeply influenced by the rail transit system [2]. Metro station is the only operating node of the rail transit system connecting to other urban physical surroundings, so impacts of rail transit on urban industries and space firstly and most obviously appear in metro station areas [3], and industrial distribution in metro station areas is regarded as one of the most important research topics at a small scale in economic geography and urban planning. It is reported that an urban built environment around a traffic station always affects the staying time and experience of people who pass by it [4]. Accordingly, the better built environment a metro station area has, faster trips and more visits there will be both for businesses and personals [5] so that one kind of beneficial location condition is created for modern industries to survive and develop in this area. Therefore, improving the quality of the urban built environment is generally considered an effective approach to reach a successful TOD in the metro station area [6], while it also makes the space usage more intensive and efficient by industrial sectors clustering hereby and promotes urban economic growth on the whole. By the way, although the spatial distribution of most urban industries is closely correlated to their urban built environment [7], huge differences of correlation performances still appear for various industrial sectors in metro station areas. The nice built

environment surely enhances the distributing scales of commercial sectors in these areas [8], but it strongly drives factories moving away from them [9]. In contrast, correlation can seldom be found between the built environment and the public service facility distributions in metro station areas [10].

Through literature analysis, it is believed that the correlation between the urban built environment and the industrial distribution in metro station areas is full of significance, and corresponding research studies are rich in both theories and cases. However, a lot of remaining issues are ready to be studied in the long-term future because the categories of modern industrial sectors are complex and diversified. Since the producer service is now playing an increasingly dominant role in urban economies [11] and their spatial development mechanisms are quite different from those of retail commerce and common offices, correlations between the spatial distribution of producer services and urban built environment in metro station areas are studied by a case of Xi'an, China. Furthermore, both empirical reference and planning guidance can be provided to future spatial developing policies of producer services in metro station areas with outcomes gained in this paper.

2. Metro Station Areas

2.1. Scope Determining Methods of a Metro Station Area. The scope determining methods of a metro station area are proposed as following based on some relevant research studies.

2.1.1. Scope Determining for a Single-Line Station. Producer services are basically laid out in urban commercial and office buildings, while related research shows that [12] such buildings are usually distributed within a circle of 400~600 m radius from the center of the metro station site. At the same time, physical traffic activities generated by the producer services mainly depend on walking travels of pedestrians within a metro station area. According to some transportation research, [13] it is believed that the acceptable travel distance for most pedestrians is 600~900 m, while the ratio between the actual walking distance of metro passengers from their departure/arrival to the station center and straight-line distance of them is 1.53 on average in China by a recent research study [14]. In terms of this ratio, the straight-line distance can be converted to 392~588 m for walking activities from the metro station center. Through the above analysis of buildings' distribution and pedestrians' walking, it is determined that the area of a single-line metro station is a circular surface with a 500 m radius from the station center in this paper.

2.1.2. Scope Determining for a Multiline Transfer Station. When an urban metro system develops into a network stage, it is necessary to set up a transfer station at the intersections of different crossing lines for passenger transferring. The transferring modes include same point transfer and passage transfer. Same point transfer means that only one station building is constructed and used for all the crossing lines. For same point transfer, the scope of a station area is similar to a single line station because of its short transferring distance and high efficiency. Passage transfer means that various station buildings are constructed separately for crossing lines due to complex terrain features and existing surface and underground structures; then, these station buildings are connected by one or more passages for using together as a whole transfer station. For passage transfer, the scope of station areas may change largely by the length and complexity of its transferring passages.

With the help of transferring passage length recommended by some designing standards of rail transit engineering, methodological types for scope determining of a multiline transfer station area are put forward as follows:

TYPE A: same point transfer station. The condition of being the same point one includes that only one coordinate on the electronic map can be collected for its building position, and its scope determining is the same as that of the single line station.

TYPE B: short-passage transfer station. The conditions of being a short-passage one include that two or more coordinates on the electronic map can be collected for its building positions and DC (the nearest straight-line distance between any two collected coordinates) ≤100 m (walking distance ≤150 m). For its scope determining, all collected coordinates are connected to each other to form a straight line or a polygon firstly. Then, a circular surface with a 600 m radius from the midpoint of the straight line or geometric center of the polygon is considered the area of a short-passage metro station. As shown in Figure 1.

TYPE C: long-passage transfer station. The conditions of being a long-passage one include that two or more coordinates can be collected for its building positions and DC (the nearest straight-line distance between any two collected coordinates) >100 m (walking distance >150 m). For its scope determining, several circular surfaces with a 400 m radius from every coordinate are formed separately at first so that their surface union is considered the area of a long-passage metro station then, as shown in Figure 2.

2.2. Metro Station Areas in Xi'an. Xi'an is a world-famous ancient cultural capital and one of the national central cities of China. In December 2019, there was a total operating length of 126.35 kilometers of Xi'an Metro (https://www.xianrail.com/), which went through the main districts and connected most of the internal and external transportation hubs in this city. There were also a total of 89 stations of Xi'an Metro at that moment, including 6 transfer stations.

According to the above scope determining process of transfer station areas, the coordinates of each transfer station are located, while distances between any two coordinates are measured and compared to ensure its DC and scope type. Thus, 6 transfer metro station areas in Xi'an are determined by their own types, and the results are shown in Table 1.

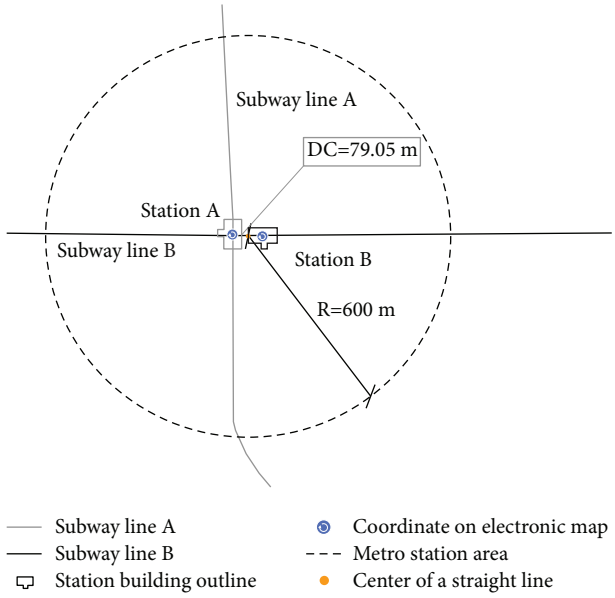

Figure 1: Area of a short-passage transfer station.

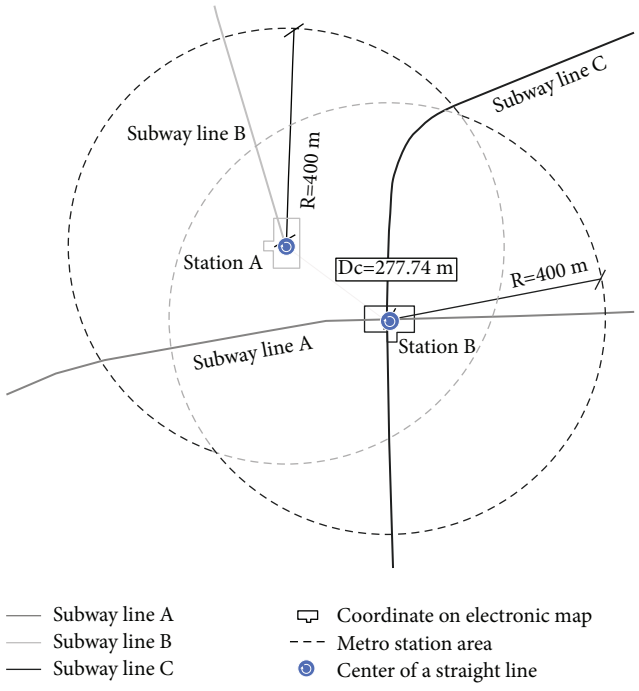

Figure 2: Area of a long-passage transfer station.

For the other 83 single-line stations of Xi'an Metro, their metro station areas are the circular surfaces with 500m radius from the center of each station coordinate. Therefore, all of the metro station areas in Xi'an can be gained, as shown in Figure 3.

3. Distribution of Producer Services

3.1. Employment of Points of Interest Data. There have been lots of research achievements about the spatial distribution of producer services on a macroscale [15, 16]. However, a few case studies on the distribution of these industrial sectors have been reported on a microscale at present due to two limitations of data collection, as well as investigation. One is that a common sample survey is not sufficient enough to establish research data since the classification of producer services is complex and their enterprise volume is very large. Another one is that building information is always too late to describe producer service activities because of their inherent flexibility from light assets while sharing uses or alternating uses in a short time of commercial offices (floors) within the same building are often happened for them.

So, point of interest (POI) data is employed in this paper to detect the distribution of producer services in order to settle the above limitations. POI data is now a widespread used spatial data source, which obtains all of real-time information data of any one point of interest on the electronic map platform through the batch search of relevant keywords, including longitude, latitude, and address [17]. As the completeness, timeliness, and accuracy of the geographical description to industrial locations on a microscale can be effectively improved by POI, it is suitable for detecting the distribution of producer services in metro station areas in Xi'an rather than data from a full enterprise sample surveying or a building information surveying.

3.2. Categories of Producer Services. The producer services were divided into 10 major types in terms of Classifying Standard issued by the National Bureau of Statistics of China (NBSC) in 2019, accompanied with 35 medium ones and 171 minor ones. 16 medium types mostly acting in urban space from the above Standard were selected and integrated into 6 categories of business in this paper. They were e-commerce, finance and insurance, scientific research and design, logistics, intermediary consulting, and leasing, as shown in Table 2.

Since categories of producer services had different scale effects and multiplier effects in the urban economy, POI numbers of enterprises of each category should be weighted to reflect their different importance of distribution. The weights for categories were determined based on the weight classification table of service facilities [18] and their applications in China [19], as shown in Table 2.

3.3. Distribution Intensity of Categories in Xi'an. Keywords of 6 categories in Xi'an city on December 8, 2019, were collected from the open port platform of AutoNavi map (https://lbs.amap.com/) with the help of Python programming. At the same time, the keyword exclusion method was used to clear the collected data so that the ones that did not belong to producer services were removed from the entry. As a result, 14,071 pieces of POI data of 6 categories were finally gained from Amap, as shown in Table 2. Each piece of data contained unique ID, name numbering, address latitude and longitude, administrative region, and other attribute information.

Both the cleared POI data of each category and the 89 metro station areas in Xi'an were located together on the ArcGIS10.5 platform so as to show the basic distributions of 6 categories in metro station areas in Xi'an, as shown in Figure 4.

Table 1: DC and scope type of 6 transfer stations of Xi'an Metro.

Transfer station	Intersecting lines	DC (m)	Types for scope determining
Beidajie	Metro line 1/line 2	0.00	TYPE A
Tonghuamen	Metro line 1/line 3	79.72	TYPE B
Xiaozhai	Metro line 2/line 3	0.00	TYPE A
Wulukou	Metro line 1/line 4	51.80	TYPE B
Xingzhengzhongxin	Metro line 2/line 4	0.00	TYPE A
Dayanta	Metro line 3/line 4	73.48	TYPE B

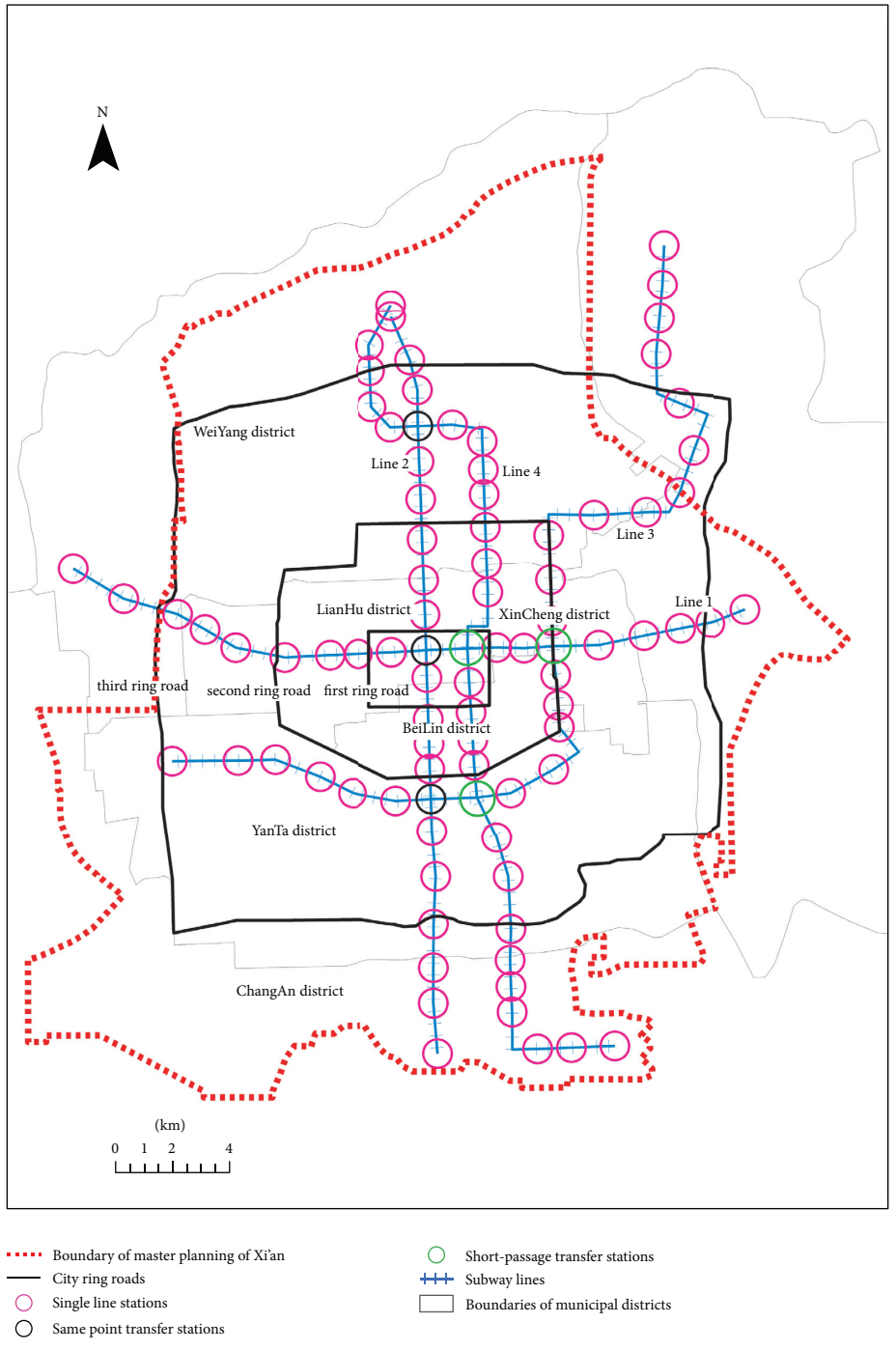

Figure 3: All metro station areas in Xi'an.

Table 2: Categories of producer services and their POI in Xi'an.

Medium type code/named by NBSC of China	Category	POI numbers (pieces)	Relevant keywords in coding table from open port platform of Amap	Weight for category
031/Information transmission service 032/Information technology services 033/e-commerce support services	E-commerce	1067	Fixed telecommunications, mobile telecommunications, internet access, information technology consulting, integrated circuit design, internet platform, and telecommunication business hall	0.9
041/Monetary and financial services 042/Capital market services 043/Productive insurance services	Finance and insurance	5388	Financial and insurance services	1.0
011/R&D and design services 014/Standard measurement service for inspection, testing, and certification 015/Productive professional technical services	Scientific research and design	567	Scientific, educational, and cultural services	1.0
025/Handling, packing, and agency services 026/National postal and express services	Logistics	5,010	Handling, packaging, cargo transport agency, postal, express, and delivery	0.8
012/Transformation services for scientific and technological achievements 013/Intellectual property rights and related legal services 072/Consulting and investigation services 073/Other productive business services	Intermediary consulting	1,368	Technical promotion service, science and technology intermediary, intellectual property, productive law, accounting, auditing, taxation, business consulting service, advertising, market management service, translation service, and credit service	0.9
062/In-kind rental service	Leasing	671	Car leasing and equipment leasing	0.8
	Total	14,071		

Then, the distribution intensity of each category in a metro station area was calculated with their POI data and corresponding weights by the following formula:

$$x = q_{ij}/q_j. \quad (1)$$

In the above formula, x is the distribution intensity, q_{ij} is the weighted POI numbers of category j in a station area i, and q_j is the total ones of category j in all metro station areas in Xi'an ($i = 1\sim89$, $j = 1\sim6$).

4. Correlations between Distribution and Built Environment

4.1. Methods of Correlation Analysis

4.1.1. Principles of Correlations. On the one hand, industrial development and its distribution within metro station areas will be differentiated due to the local construction quality level of the urban built environment. High accessibility in metro station areas not only reduces travel time cost but also brings about land appreciation and building rent premium. Thus, industrial sectors with high returns will be more suitable to be located here according to the theory of competitive rent [20]. Similarly, excellent construction standards and supporting facilities of office buildings will also be essential to locating industrial sectors with high returns [21]. Generally speaking, modernized and high-level construction quality of built environment promotes more sectors with high returns to locate in metro station areas, whereas backward construction quality hinders sectors to locate in. In addition, because there are obvious variations of operating costs and benefits in different high-return industries, industries also have different affordable rent levels when seeking for office buildings in metro station areas [22]. Accordingly, the differentiation of the rent level makes the space demand of office buildings in areas never be equally satisfied for different industries. Therefore, spatial competitions within metro station areas have unavoidably happened among high-return industries through market actions, and the winner will get the right of building space usage.

On the other hand, industrial development and its distribution within metro station areas will be differentiated due to space usage patterns of the urban built environment.

FIGURE 4: POI distributions of 6 categories of producer services in Xi'an. (a) E-commerce. (b) Finance and insurance. (c) Scientific research and design. (d) Logistics. (e) Intermediary consulting. (f) Leasing.

Metro station areas are places where various flows of economic elements converge together, so both land use and buildings hereby tend to be developed in a very high-density status [23]. However, a high-density usage pattern should not be undertaken by a single or a few very similar industrial sectors in metro station areas. Otherwise, an excessive polarization of elements integrated by these sectors or even overload may appear in a short term due to the homogeneity of the industrial chain, which often leads to adverse effects (traffic congestion, environmental pollution, inefficient information, etc.) that reduce the efficiency of industrial allocation. On the contrary, diversified usage patterns by a lot of industrial sectors are conducive to balance their demands of industry and transportation in metro station areas at different times [24], under which each sector should make proper use of land and buildings according to its own demands. Therefore, overloaded development can be avoided, and the efficiency of industrial allocation can be improved through intensive cooperation on an industrial chain in metro station areas.

In summary, these two principles of correlations between industrial distribution and built environment within metro station areas are theoretically introduced and practically adopted in the case study below.

4.1.2. Built Environment of Areas in Xi'an. Urban built environment is created by humans and made of various artificial elements. Its formation not only relies on patterns of human production and lifestyle but also affects all kinds of

human activities in itself. According to the working or living patterns and activity intensities, the urban built environment of a metro station area was divided into 3 space elements in this paper so as to carefully explain distributing activities of producer services hereby. These elements included job and residential space, outdoor activity space, and municipal road one, while their calculating methods are as follows:

(1) Job and residential space.

Diversity index is used to analyze this element, and the calculation formula is

$$D = 1 - \sum\left(\frac{\mathrm{N}_l}{N - (\mathrm{N}_O + \mathrm{N}_R)}\right)^2 \sum \text{among them: } N = \sum \mathrm{N}_l + \mathrm{N}_O + \mathrm{N}_R. \quad (2)$$

In the above formula, D is the diversity index. N is the total size of developed land in a metro station area. N_l is the land size for any planned spatial function l of jobbing or living in this area. When the function number is n, $l = 1 \sim n$. N_O is the land size for all planned spatial functions of outdoor activities in this area, such as green lands, squares, parks, and water bodies. N_R is the land size for all planned spatial functions of municipal roads in this area.

(2) Outdoor activity space.

Openness index is used to analyze this element, and the calculation formula is

$$K = \frac{\mathrm{N}_O}{N}. \quad (3)$$

In the above formula, K is the openness index, and other symbols have the same meanings as formula (2).

(3) Municipal road space.

Street network density index is used to analyze this element, and the calculation formula is

$$P = \frac{L}{N}. \quad (4)$$

In the above formula, P is the street network density index. L is the total length of municipal roads in the area, and the other symbols have the same meanings as formula (2).

4.2. Results of Correlation Analysis

4.2.1. Calculations of Correlations. Basic data about 3 space elements of the built environment was obtained through the land use planning and transportation system planning of Xi'an downtown issued by Xi'an Natural Resources and Planning Bureau. Then, the satellite images of metro station areas taken from the AutoNavi map were compared with the basic data from planning. If there were some obvious differences between them, on-site investigations should be carried out for further supplementary and calibration in order to grasp the developing status of the built environment accurately. In addition, 8 metro station areas outside the planning scope of Xi'an downtown were excluded from the next analysis of the built environment due to their non-official planning procedures and results.

All the basic data about 3 space elements of 81 remaining metro station areas in Xi'an were obtained with the help of the above steps. The diversity index D in each area was then calculated by using equation (2), openness index K by (3), and street network density index P by (4).

Since the length of the paper was limited, the calculation results of built environment of metro station areas in Xi'an were only listed with 4 examples, as shown in Table 3.

Any one of 81 metro station areas in Xi'an was used as a study sample for correlation analysis, where the distribution intensity of a certain category of producer services was used as the dependent variable, and indexes D, K, P of built environment hereby were correspondingly used as the independent variables. Meanwhile, since the total developed land of a metro station area consisted of job and residence space, outdoor activity space, and municipal road space based on formula (2), a collinear relationship surely existed among $\sum N_l$, N_O, and N_R in an area. So, a measuring tool for second-order partial correlation analysis would be adopted to calculate the coefficient in this paper so that drawbacks of collinearity among independent variables could be avoided. [25].

The calculation formula of all samples by using a second-order partial correlation tool is as follows:

$$r_{x,1,2,3} = \frac{r_{x,1,2} - r_{x,3,2} \cdot r_{1,3,2}}{\sqrt{1 - r_{x,3,2}^2} \cdot \sqrt{1 - r_{1,3,2}^2}}. \quad (5)$$

In the above formula, x is the distribution intensity of any one of 6 categories of producer services in metro station areas. r is the second-order partial correlation coefficient between x and index marked 1 expressing one of the three space elements of the built environment when the other two indexes marked 2 and 3 are controlled. When 1 is set as D, 2 and 3 are set as K and P; when 1 is set as K, 2 and 3 are set as P and D; when 1 is set as P, 2 and 3 are set as D and K. Other symbols have the same meanings as equations (1)~(4).

By formula (5), the strength and direction of net correlation between a target-dependent variable x and an independent variable index were shown through the calculating value of coefficient r at a prescribed significance level, as well as its plus sign or minus one. If the value of coefficient was large with a plus sign, the higher the positive correlation between distribution intensity of category and

Table 3: Indexes of built environment of some metro station areas in Xi'an.

Station	Line (s)	D	K	P
Zhonglou	Line 2	0.5775	0.0212	0.0092
Dayanta	Line 3, line 4	0.7140	0.1678	0.0063
Chanhe	Line 1	0.8683	0.4434	0.0059
Shizhongyiyiyuan	Line 4	0.5855	0.0836	0.0067

this index of the built environment was. On the contrary, the negative correlation between distribution intensity and index was higher when the value was large with a minus sign.

For 81 samples of metro station areas in Xi'an downtown, the second-order partial correlation coefficients between distribution intensity x of each one of 6 categories and each index of D, K, and P were completely done through 6 groups of calculations by (5). The results are shown in Table 4.

4.2.2. Explanations to Correlations. The correlation performances between the distribution intensity of each category and index D are analyzed, respectively, and compared comprehensively by rows of Table 4 and so does index K and index P. Generally speaking, the correlation mechanisms between distribution and space elements of the built environment in metro station areas are explained as follows:

(1) Significant Positive Correlations between the Distribution Intensity and Diversity of Job and Residence Space for Most Categories. On the whole, the constructions of the job and residential space are small in scale but good in quality based on the developing mode of office buildings within metro station areas. As typical industrial sectors with intensive knowledge, technology, and innovation, producer services need office buildings with a less scale but more premium decorations and in-house facilities for their daily operating, as well as high-accessible urban locations. Therefore, lots of producer services are attracted to clusters in metro station areas where locational advantages of jobbing and living are more obvious than other urban localities. What is more, because most sectors of producer service have a very wide range of industrial connections, many other sectors associated with them on industrial chains are apt to cluster near the locations of producer services. So, the more diversified development of job and residence space in a metro station area, the more varieties of office buildings can be constructed not only for the uses of producer services themselves but also for associated sectors on their industrial chains. In a word, all industries will benefit from the intensive sharing distribution in the metro station area, which leads to both well-served operations and industrial agglomerations.

The detailed explanations to correlations between the distribution of each category and job and residence space are as follows:

The largest positive and significant correlation coefficient was detected in the category of scientific research and design (0.436), and the reasons lie in its strong and multidirectional physical industrial linkages. Enterprise kinds linked with this category on industrial chains mainly include exploration and mapping, special equipment, printing and publishing, science exhibition and advertisement, and catering and accommodation. All of them expect to make a shorter trip of materials handling to or from enterprises of scientific research and design and contact their personnel conveniently through face-to-face visiting. Therefore, it is believed that the diversity of job and residence space surely helps these linked enterprises share suitable buildings in metro station areas so that their handling and visiting trips are shortened as far as possible.

The correlation coefficients were positive and significant, but the values were correspondingly reduced in the categories of intermediary consulting (0.244), finance and insurance (0.237), and e-commerce (0.213). Although enterprises of these categories also have strong industrial linkages, parts of their servicing products can be chiefly presented by information technology with digital and standardized forms. So, these categories will often communicate with the linked enterprises on industrial chains by Internet or telecommunications besides handling and visiting, while the requirement of being located in diversified job and residence space is true but declining for these categories.

The correlation coefficients were not significant in the categories of logistics and leasing. The components of logistics production chain include collection, transportation, storage, sorting, and delivery. Only some collection and delivery to initial and terminal clients can be located in metro station areas because of their little use of warehouses and transportation facilities, while other components ought to be close to urban freight hubs in suburban districts where a large number of warehouses and transportation facilities have already constructed. Similarly, since leasing subjects in producer services generally have high value or large volume, only stores responsible for soliciting leasing clients and marketing can be located in metro station areas. Other components of the leasing production chain ought to be far from metro stations, such as storage and maintenance.

(2) Significant Negative Correlations between the Distribution Intensity and the Openness of Outdoor Activity Space for Most Categories. On the whole, because the total land of a metro station area is limited, the share of land left for industrial development will be smaller when more outdoor activity spaces have developed in it, such as greening, squares, parks, and water bodies. By the way, metro station areas with both high accessibility and good nature surroundings become one of the best places for leisure and entertainment activities in urban districts and suitable for consumer services to gather their main target clients through access advantages. Therefore, on the one hand, large volume sectors of consumer services are always apt to locate in hereby, such as catering, shopping, entertainment, hotel, and fitness. On the other hand, although producer services also expect a better natural environment and living facilities for attracting talents to join in, their strong recruitment competitiveness of human resources still rely on sustainable entrepreneurial conditions and good salaries intrinsically.

Table 4: Coefficient results of second-order partial correlation.

Second-order partial correlation		Dependent variable x					
Categories		E-commerce	Finance and insurance	Scientific research and design	Logistics	Intermediary consulting	Leasing
Controlling variables	Independent variable	Group 1	Group 2	Group 3	Group 4	Group 5	Group 6
K, P	D	0.213*	0.237**	0.436***	0.039	0.244**	−0.041
P, D	K	−0.379***	−0.438***	−0.521***	−0.372***	−0.342***	−0.057
D, K	P	−0.005	0.119	0.113	−0.180	0.247**	0.219**

Note. ***means being significant at the 0.01 level, **means being significant at the 0.05 level, and *means being significant at the 0.1 level.

As a result, the more land size of outdoor activity space in a metro station area, the less developing land left for both producer services and consumer services will be, whereas more flows of clients will become increasing only for the consumer one. So, consumer services are much more competitive than producer services in building renting investments in metro station areas with high openness under the game strategies of spatial resources dominated by the market economy.

The detailed explanations to correlations between the distribution of each category and outdoor activity space are as follows:

The largest two negative and significant correlation coefficients were detected in the categories of scientific research and design (−0.521) and finance and insurance (−0.438). Specific laboratories for experimental testing and inspecting are necessities to support researching and designing on their production chains so that more quantity demands of floor areas of office buildings generate in this category. In addition, convenient and efficient services for clients are essences of enterprises in the category of finance and insurance. Thus, they must prefer a ground floor within office buildings directly toward streets so that more quality demands of floor areas generate in this category. It is suggested that scientific research and design and finance and insurance are the most vulnerable categories under the spatial competition between producer services and consumer services where the openness of outdoor activity space is high.

The quantity and quality demands of office buildings for other categories are true but less. So, the extent to which they are driven away from the areas with high openness by consumer service due to spatial competition gradually decreases and even disappears, while the correlation coefficients of these categories correspondingly become lower or even not significant.

(3) Positive but Weak Correlations between the Distribution Intensity and the Street Network Density of Municipal Road Space Only for Categories of Intermediary Consulting and Leasing. The servicing products of intermediary consulting have nonstandardized characteristics typically, while frequent face-to-face contacts between its service providers and customers are still required to establish the trust of business and reach personalized solutions then. Meanwhile, the travel proportions of rail transit in all transportation modes are 20% or less in large and medium-sized cities according to a recent research study in China [26]. So travels for face-to-face contacts on the production chain of intermediary consulting heavily rely on various patterns of streets in metro station areas, on which motor vehicles and non-motor ones run smoothly. Therefore, the greater the street network density in a metro station area, the better travel conditions for enterprises of intermediary consulting may be hereby.

Since the leasing subjects are generally of high values, clients almost never purchase such services only through online channels. For a prudent management attitude, they tend to negotiate with service providers through face-to-face contacts after online screening to finalize the order. Similarly, the greater the street network density in a metro station area, the better travel conditions for enterprises of leasing may be.

Except for the above two, frequent face-to-face contacts with personnel are seldom needed in other categories of producer services. Thus, there is little significant correlation between their distribution intensity and municipal road space in metro station areas.

5. Conclusions and Suggestions

Metro station areas in Xi'an, China, were determined, and POI data of 6 categories of producer services were empirically detected at the beginning of this study. Then, correlated spatial interactions between the distribution of each category and the space elements of urban built environments in these areas were carefully analyzed according to the calculation of second-order partial correlation coefficients.

The main conclusions include the following correlation mechanisms:

Complementary mechanism. Producer services need office buildings with a less scale but more premium facilities and high-accessible urban location, while many other sectors associated with them on industrial chains are apt to cluster together within metro station areas so as to achieve complementary development and agglomeration economy through intensive close-range connections. Thus, there are significant positive correlations between the distribution intensity and the diversity of job and residence space for most categories.

Competitive mechanism. The more openness of a metro station area, the less developing land for both producer services and consumer services will be left, whereas more flows of clients will become increasing only for

consumer one. So consumer services are much more competitive than producer services in buildings renting investments hereby, and there are significant negative correlations between the distribution intensity and the openness of outdoor activity space for most categories.

Selected supporting mechanism. On condition that more and more travels of people and goods in producer services are substituted by information technologies as a whole, only a few travels on municipal streets are preferred by categories of intermediary consulting and leasing in order to support their frequent face-to-face contacts with personnel. So, there are positive but little weak correlations between the distribution intensity and the street network density of municipal road space for these two categories.

Based on the above three mechanisms, urban planning suggestions on the built environment in metro station areas are separately developed for the newly constructed stations in Xi'an Metro for the future five years. Thus, producer services hereby can be better layout and operated. Firstly, by using the complementary mechanism, more attention should be paid to diversify the use of commercial and office lands in the area of the new metro stations in districts where important urban industrial growth poles are located, as well as the supplies of various infrastructures. Therefore, more and more related enterprises are apt to select these metro station areas as their office sites, while high-quality producer services will cluster together around their industrial chain. Secondly, by using the competitive mechanism, more public squares and greening lands should be planned and finished in the new metro station areas beside which important natural and cultural scenic spots exist, while the development of consumer services facilities should also be appropriately increased hereby. On the contrary, it is necessary to make the producer service leave for some other new metro station areas so as to avoid its inefficient spatial competition with consumer one. Thirdly, by using the selected supporting mechanism, a lot of producer service enterprises whose productions are highly dependent on intensive transportation through municipal roads are suitable to be planned in the new metro station areas in developing suburban industrial districts. As result, both the number of permanent residents and employment opportunities will greatly increase at those districts attributed to strong economic driven forces provided by newly coming producer service enterprises.

Data Availability

The data used to support the findings of this study are available from author upon request.

Conflicts of Interest

The authors declare that they have no conflicts of interest.

Acknowledgments

This work was financially supported by the Social Science Foundation of Shaanxi Province, China (grant no. 2018S39).

References

[1] R. Cervero and J. Murakami, "Rail and property development in Hong Kong: experiences and extensions," *Urban Studies*, vol. 46, no. 10, pp. 2019–2043, 2009.

[2] E. Guerra, "Mexico City's suburban land use and transit connection: the effects of the Line B Metro expansion," *Transport Policy*, vol. 32, pp. 105–114, 2014.

[3] J. X. Hu, M. Zhu, L. J. Pu, and F. F. Cai, "Progress of the research on the influence of traffic road on regional land use change," *Resources and Environment in the Yangtze Basin*, vol. 27, no. 1, pp. 205–214, 2018.

[4] T. Li, H. Jiang, P. Jing, and M. Zhang, "Analyzing the coordination relationship between urban built environment and traffic level," *Journal of Advanced Transportation*, vol. 2021, Article ID 9952306, 11 pages, 2021.

[5] M. S. Mohammad, S. K. Negin, and T. Arefeh, "A focus on the contribution of promoting TOD to increasing tehran's public spaces," *Procedia Engineering*, vol. 165, 2016.

[6] S. Hyungun and G. C. Chang, "The link between metropolitan planning and transit-oriented development: an examination of the Rosario Plan in 1980 for Seoul, South Korea," *Land Use Policy*, vol. 63, 2017.

[7] G. H. Cheng, S. C. Sun, L. L. Zhou, and G. Z. Wu, "Using Smart Card Data of Metro Passengers to Unveil the Urban Spatial Structure: A Case Study of Xi'an, China," *Mathematical Problems in Engineering*, vol. 2021, Article ID 9176501, 10 pages, 2021.

[8] T. Wang, Y. Wang, X. M. Zhao, and X. K. Fu, "Spatial distribution pattern of the customer count and satisfaction of commercial facilities based on social network review data in Beijing, Chinas," *Computers, Environment and Urban Systems*, vol. 71, 2017.

[9] M. M. I. Mohd, F. I. Ahmad, and N. H. Nordin, "Railway station facilities in rural and urban services based on observation and user feedback," *MATEC Web of Conferences*, vol. 47, 2016.

[10] K. Song, R. Zhou, H. Z. Lin, H. l. SU, and WANG, "Research on Optimal Method for Land Use Around Urban Rail Traffic Site-A Case Study of Wujiaochang Station on Shanghai Metro Line 10," *Journal of Fudan University*, no. 1, pp. 78–85, 2013.

[11] H. Hanssens, B. Derudder, S. Van Aelst, and F. Witlox, "Assessing the functional polycentricity of the mega-city-region of Central Belgium based on advanced producer service transaction links," *Regional Studies*, vol. 48, no. 12, pp. 1939–1953, 2014.

[12] A. Roukouni, S. Basbas, and A. Kokkalis, "Impacts of a metro station to the land use and transport system: the thessaloniki metro case," *Procedia - Social and Behavioral Sciences*, vol. 48, pp. 1155–1163, 2012.

[13] T. Craig and Z. John, "Built environment and pedestrian behavior at rail rapid transit stations in bangkok," *Transportation*, vol. 37, pp. 317–330, 2010.

[14] L. Wu, W. Lu, and P. J. Sun, "Research OF the walking range and flow line surrounding subway HUBS: a case study of xi'an Lu station in dalian city," *Architectural Journal*, no. S1, pp. 22–27, 2017.

[15] P. Wood, "Urban development and knowledge-intensive business services: too many unanswered questions?" *Growth and Change*, vol. 37, no. 3, pp. 335–361, 2010.

[16] S. J. Huang and C. Zhang, "The influences of the agglomeration of producer services on the urban productivity: from the perspective of industry heterogeneity," *Urban Development Studies*, vol. 23, no. 3, pp. 118–124, 2016.

[17] J. S. Li, Y. Liang, and X. R. Wang, "Spatial clustering analysis of service industries in Zhengdong New District based on POI data," *Geographical Research*, vol. 37, no. 1, pp. 145–157, 2018.
[18] D. T. Duncan, J. Aldstadt, J. Whalen, S. J. Melly, and S. L. Gortmaker, "Validation of walk score for estimating neighborhood walkability: an analysis of four US metropolitan areas," *International Journal of Environmental Research and Public Health*, vol. 8, no. 11, 2011.
[19] H. Peng, H. Xiong, and J. Y. Tian, "Urban area pedestrian accessibility study based on big data, Journal of Chongqing University of Technology (Natural Science)," vol. 33, no. 8, pp. 111–117, 2019.
[20] Y. Deng, "The spatial succession and organization model of the urban material space within the rail transit station: a case in beijing," *Scientia Geographica Sinica*, vol. 37, no. 6, pp. 817–824, 2017.
[21] L. Z. Zhang, Y. Zhuang, and Y. Ye, "A correlation analysis of transport accessibility and spatial performance aiming for synergistic development in rail transit station areas: a case study of central shanghai," *New Architecture*, no. 2, pp. 114–118, 2019.
[22] B. Shereen, K. Barendien, and K. Janine, "Location decision strategies for improving SMME business performance," *Acta Commercii*, vol. 11, no. 1, 2011.
[23] Y. J. Wang, "International studies on the interaction between urban rail transit and land use of station areas," *Urban Planning International*, vol. 33, no. 1, pp. 111–118, 2018.
[24] R. Cervero, *Transit-oriented Development in the United States: Experiences, Challenges, and prospects*, Transportation Research Board, Washington, DC, USA, 2004.
[25] Q. Zhang, B. X. Zhang, and H. Wang, "Dominance degree disparities of Chinese construction supervision enterprises," *Journal of Northwest University*, vol. 46, no. 2, pp. 298–302, 2016.
[26] Y. Yang, C. Wang, W. Liu, and P. Zhou, "Understanding the Determinants of Travel Mode Choice of Residents and its Carbon Mitigation potential," *Energy Policy*, vol. 115, 2018.

Hindawi
Advances in Civil Engineering
Volume 2022, Article ID 6484969, 8 pages
https://doi.org/10.1155/2022/6484969

Research Article

Calculation and Analysis of Vibration Stress of Guangxi Nanning Subway during Operation

Zhenchao Chang, Junhui Luo, Shihai Wang, Haifeng Huang, Peng Mo, Chunwei Wu, Laixing Liao, Yuanpeng Chen, Mian Huang, and Yuhang Wu

Guangxi Beitou Transportation Maintenance Technology Group Co. LTD, Nanning, Guangxi 530029, China

Correspondence should be addressed to Shihai Wang; wangsh214@126.com

Received 30 November 2021; Revised 31 December 2021; Accepted 15 January 2022; Published 2 February 2022

Academic Editor: Song-He Wang

In this study, based on the Mindlin solution in elastic half-space, the stress calculation formula was determined with consideration of any point in the foundation under the dynamic amplification effect. The train load was simplified as a concentrated force moving in the direction of the train, and the stress of the soil under a single wheel load was analyzed. In the state, σ_z reached a maximum value of 0.56 kPa when the axle was directly above the soil, and the stress decreased until it approached zero as the distance from the soil unit increased. Then, taking the Nanning Metro Line 1 as an example, the load was regarded as the superposition of several single-wheel loads, and the law of the soil stress change at a point directly below the moving line of the train load at different axle loads, speeds, and burial depths was studied. From the analysis of the results, it could be seen that the soil stress under different working conditions was always proportional to the train axle load, speed, and burial depths. The peak stress ratio corresponding to the depths of 9 m, 12 m, and 15 m was 1:2:11, indicating that the closer the load to the soil, the more significantly the stress of the soil element increased. Under multiple wheel loads, the soil stress always exhibited continuous cycle characteristics. The cycle period was related to the time it took for the metro to pass through the point in the soil, and the cycle period was the ratio of the distance between each axle and the vehicle speed.

1. Introduction

With the development of urban underground space, subway rail transit has gradually become the backbone of major cities. At present, there are 37 subway cities in mainland China, and four subway cities are under construction. Nanning Metro Line 1 was the first completed rail transit line in Guangxi Province, and it opened on December 28, 2016. The problem of foundation settlement caused by subway operation has become more and more prominent. The vibration and stress change of soil elements caused by the moving load of a subway have an important impact. At present, there are the Boussinesq solution, the Mindlin solution, the empirical method, and the finite element method for calculating the foundation soil stress under a traffic load. Among them, the Boussinesq solution is suitable for road engineering with a load on a surface [1]. The Mindlin formula can solve for the soil stress at any point in the elastic half-space, so it is suitable for subway engineering at any depth [2]. Ishihara [3] used the Boussinesq solution to simulate ground rail transportation to obtain the stress of a soil unit and the stress path of an inspection point. This method reflected the nature of the rotation of the main stress axis of the soil unit caused by the axle load, but soil element stress of underground traffic could not be considered. Wang et al. [4] studied a series of theoretical problems of the Boussinesq solution and Mindlin solution in depth and in detail. It is believed that the reason for the error of the Boussinesq formula is that the influence of the soil above the load surface on a stress distribution is not considered. The limitation of the Mindlin formula is that when the load surface is not a soil but a foundation, the influence on the stress distribution in the soil needs to be discussed separately. Yang et al. [5] believed that the assumptions of the empirical formula proposed by the American Railway

Engineering Association did not match the actual situation, that the calculation result was relatively high, and that the empirical formula for the calculation of the subgrade stress proposed by the Soviet Union was close to the actual measurement and the difference between the line and the actual when the line was normal or bad. Therefore, it is necessary to find a convenient and practical calculation method.

The instability of the foundation is related to the dynamic effect of a train. There is an error in the pure static solution, and it is difficult to reflect the actual stress of foundation soil. In recent years, underground rail transit has developed rapidly. With the continuous increase of the axle loads and speeds of trains, the dynamic effect has become more intense, so the study of the stress state of the soil inside a foundation under a dynamic load has drawn attention from everyone [6, 7]. Ding et al. [8, 9] analyzed and studied the foundation stress state change caused by subway train operation and the rotation of the main stress axis and the viscoelastic solution of the foundation based on the Mindlin solution in the elastic half-space without considering the effect of dynamic effects on stress. Liu et al. [10] deduced the formula of vertical dynamic stress in subgrade soil under a vehicle dynamic load. They first proposed the concept of the speed coefficient and determined the value through a simulation test. The speed coefficient had nothing to do with the size and weight of the vehicle, and it was about 0.105. The vertical dynamic stress was proportional to the load intensity and vehicle speed. Zhang et al. [11] calculated the dynamic response solution of any point under a train load based on the principle of dynamic reciprocity combined with the generalized Duhamel integral expression. The inverse Floquet transform and the Fourier inverse transform were used. After superposition, the dynamic response of any point under a train load was obtained. The expressions were in the time and frequency domains. Li et al. [12] used the complex variable method, and an analytical solution for the in-situ stress and displacement of a shallow circular tunnel in the elastic half-plane under arbitrary distributed loads in the elastic half-plane was obtained. Gu et al. [13] used the inverse conformal transformation and the Cauchy-Riemann equation. The implicit form of the exact analytical solution based on the complex variable method could be derived from the explicit form of the exact analytical solution. Eason [14] researched the dynamic response of a semi-infinite homogeneous space surface under uniform moving loads. When the velocity of the applied force was lower than the wave velocity, the displacement and stress components of the points below the load action point and the distributed load action area were given. The numerical results of the stress components at the points below the center of the distributed load zone were also given. Grundmann et al. [15] assumed a foundation to be a linear elastic layered half-space. The ordinary differential equation in the vertical direction was obtained through the Fourier transform of the time-space domain, and the wavelet transform was used for error control to analyze the different soils under the motion load of the half-space dynamic response of the layer. Barros et al. [16] proposed a method for calculating the displacement and stress in a layered viscoelastic half-space caused by uniformly moving loads at a surface or a certain depth. This method was based on the wavenumber integral representation of the complete response using the generalization of the displacement and stress fields. The accurate decomposition of the transmission and reflection coefficients took into consideration the effects of layering. Siddharthan et al. [17] studied the dynamic response of layered saturated soil under a moving load. A semi-analytical method with a higher calculation efficiency based on the Biot porous medium formula was proposed for the load under plane strain conditions, which could be used to process complex surface loads such as multiple loads, non-uniform pressure, and other types of time-varying loads. The accuracy of the model was verified through experiments. Alabi [18] gave the parametric research results of the three-dimensional model of a rail traffic vibration load and studied the dynamic response of the moving load speed, train distance, and ground depth to elastic space. The calculation results showed that the displacement was proportional to the moving speed of the load. In all cases, the displacement decreased approximately linearly with the increasing soil depth. Wang et al. [19–21] derived the displacement of the Timoshenko beam in elastic half-space under the action of a moving load and the solution of the ground surface reaction force based on the research of Eason. The steady-state stress caused by the train load in the foundation was obtained when the train speed was less than the Rayleigh wave speed response answer. Hu et al. [22] used the 2.5-dimensional finite element analysis method. The track was simplified to Euler beams, the train load was reduced to single or multiple moving axle loads, the track-embankment-foundation coupling analysis model was established, and the stress of the summarized soil unit body was summarized. The law of rotation of the path and the principal stress axis gave the dynamic response of the track structure and the ground under axial loads moving at various speeds. Chen et al. [23] simplified the vibration effect of rail transit into a uniform load and a single-wheel load, and the stress state changes of the soil element under the two simplified loads were analyzed. The research results showed that the stress path of the soil element was "apple-shaped" in the process of the load from a position close to the soil element to a position far away from the soil element.

Most of the above analyses were related to the dynamic response of a subgrade surface for a high-speed rail or road traffic, or they used pseudo-static solutions to calculate the internal soil stress of the foundation, which were difficult to apply to high-speed underground rail transportation. The greater the train axle load and speed, the violent the train dynamic effect, so the calculation of subway vibration stress considering the dynamic effect is still worthy of study. Based on the above problems, in this study the metro load was simplified as a concentrated force moving in the direction of the metro based on the Mindlin solution of elastic half-space. The stress calculation formula of the dynamic effect analyzed the stress state of the soil at a certain point directly below the moving line of the train under the load of a single axle and multiple sets of axles, and the effects of the vehicle speed, axle load, and buried depth on the stress were studied.

2. Mindlin's analytical solution considering speed

According to Mindelin's research, when the concentrated force P acted on the depth c of the elastic half-space body see Figure 1 , the stress in the soil at any point from the surface depth z in the foundation could be expressed as [24]:

$$\sigma_z = \frac{P}{8\pi(1-\mu)}\left\{\begin{array}{l}\dfrac{(1-2\mu)(z-c)}{R_1^3} - \dfrac{(1-2\mu)(z-c)}{R_2^3} + \dfrac{3(z-c)^3}{R_1^5} + \\ \dfrac{3(3-4\mu)z(z+c)^2 - 3c(z+c)(5z-c)}{R_2^5} + \dfrac{30cz(z+c)^3}{R_2^7}\end{array}\right\} \quad (1)$$

$$R_1 = \sqrt{x^2 + y^2 + (z-c)^2}$$

$$R_2 = \sqrt{x^2 + y^2 + (z+c)^2},$$

where σ_z is the stress at any depth directly under the load, z is the depth of a certain point, c is the depth of embedding of the load force, P is the concentration force, μ is Poisson's ratio of the soil layer, and x is the horizontal distance between the load acting point and the calculation point.

The vehicle load was a kind of dynamic load, and it was obviously insufficient to replace its effect on the roadbed with static force only. The stress of the wheel load on the track was related to the lateral bending of the track, the eccentric vertical load, the vehicle speed, and other factors. A dynamic wheel load would result in a dynamic stress value that was higher than the static value. The general method used to determine the wheel load was to empirically express the wheel load as a function of the static wheel load. According to the literature [25], the most comprehensive method for determining the influencing factors is the formula proposed by the International Railway Union Research and Test Office (ORE) based on the measured track results.

The influence coefficient was defined suing three dimensionless velocity coefficients α', β', γ', namely:

$$\phi = 1 + \alpha' + \beta' + \gamma'. \quad (2)$$

Among these coefficients, α' and β' are related to the average value of the impact factor, and γ' is related to the standard deviation of the impact factor. α' depended on the track level, vehicle suspension, and vehicle speed, which was expressed as:

$$\alpha' = 0.04\left(\frac{V}{100}\right)^3. \quad (3)$$

The numerical coefficient of 0.04 mainly depended on the resilience of the vehicle suspension.

According to the calculated value of the SNCF (Societe Nationale des Chemins de Fer Francaise) formula, the value range was 0.13–0.17. According to the observed value, in almost all cases, the measurement coefficient α' on the tangent trajectory was greater than the calculated $\alpha' + \beta'$. Therefore, only α' was regarded as the average value of the impact factor, and β' was ignored.

γ' was related to the vehicle speed, track age, vehicle design, etc. The data showed that γ' increased with the vehicle speed, which could be estimated with the following formula:

$$\gamma' = 0.01 + 0.017\left(\frac{V}{100}\right)^3. \quad (4)$$

By substituting α', γ' into (2), we could obtain:

$$\phi = 1.1 + 0.021\left(\frac{V}{100}\right)^3. \quad (5)$$

In the formula, φ is the dynamic coefficient, and V is the running speed of the train, in units of km/h.

Then, considering the stress of the wheel load on the track under the dynamic effect, the calculation could be simplified as $\sigma_d = \phi \cdot \sigma_z$.

3. Calculation of the vibration stress during the operation of the Nanning subway

3.1. Dynamic stress solution under a single wheel load. The force of the subway was simplified, the wheel load was treated as a concentrated force that ran at a certain speed in the direction of the subway, and the stress state of the foundation was studied based on the Mindlin solution at a certain depth under the load of a single wheel and axle.

Under the load of a single wheel, because the calculated soil element was directly below the load movement line, $y = 0$. The formula could be simplified to:

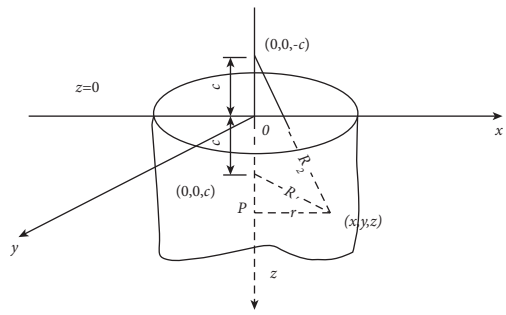

Figure 1: Concentrated force in the soil.

$$\sigma_z = \frac{P}{8\pi(1-\mu)}\left\{\begin{array}{l}\dfrac{(1-2\mu)(z-c)}{\left(x^2+(z-c)^2\right)^{3/2}} - \dfrac{(1-2\mu)(z-c)}{\left(x^2+(z+c)^2\right)^{3/2}} + \dfrac{3(z-c)^3}{\left(x^2+(z-c)^2\right)^{5/2}} + \\ \\ \dfrac{3(3-4\mu)z(z+c)^2 - 3c(z+c)(5z-c)}{\left(x^2+(z+c)^2\right)^{5/2}} + \dfrac{30cz(z+c)^3}{\left(x^2+(z+c)^2\right)^{7/2}}\end{array}\right\}. \quad (6)$$

The stress of the single-wheel load on the soil element is shown in Figure 2. The foundation soil was homogeneous soil, and the axle load depth was c = 12 m. The calculated soil element was located 4 m directly under the tunnel (x = 0, y = 0, z = 16 m). The subway ran at v = 40 km/h, and the horizontal distance between the single wheel and the calculated soil element unit was -33 m until the single wheel left the calculated soil element unit by a distance of 33 m. The distance between the load and the calculated soil element simulated the movement of the load.

According to the Mindlin solution at any point in the elastic half-space, the shear stress τ_{xy} = 0 and τ_{yz} = 0 of the soil element were directly under the load. Then only the stress state on the x-z plane was studied. As can be seen in Figure 3, the stress σ_z increased continuously as the wheel load approached the soil unit, and the stress reached a maximum value of 0.56 kPa when it was directly above the soil element. The stress value gradually decreased toward 0 when it was away from the soil unit, and its graph was symmetrical about the z-axis. The stress σ_x graph was symmetrical about the z-axis, and the stress reached a maximum value of 0.093 kPa at a distance of approximately 5 m from the soil unit. The shear stress τ_{xz} gradually increased as the train approached the soil unit, it reached a maximum value of 0.16 kPa at a distance of approximately 2 m from the soil unit, and then it was reduced to 0. The graph was antisymmetric about the z-axis. It could be seen that when the load was close to the soil element, the stress changed greatly, and σ_z was much larger than τ_{xz} and σ_x, and when the load was far from the soil unit, the stress value was small.

Based on the above research, the stress of the soil at different burial depths was calculated. Figures 4 and 5 show the calculation of the stress change of the soil unit when the burial depths were 9 m, 12 m, and 15 m. It can be seen from the figures that when the load was far away, the stress value of the soil unit was very small. Within the horizontal distance range of -2 m to 2 m from the soil unit, the stress value changed significantly, and it gradually increased as it approached the soil unit. The maximum values of σ_z and τ_{xz} were obtained at the horizontal distances of 0 m and ±1 m from the soil unit, respectively. When the buried depth was 9 m, σ_{zmax} = 0.20 kPa and τ_{xzmax} = 0.05 kPa. When the buried depth was 12 m, σ_{zmax} = 0.57 kPa and τ_{xzmax} = 0.15 kPa. At a buried depth of 15 m, σ_{zmax} = 8.74 kPa and τ_{xzmax} = 2.49 kPa. It could be seen that the soil stress was proportional to the buried depth, the greater the depth of the tunnel, the greater the stress value, and the more rapid the stress change. Therefore, the horizontal and vertical loads were smaller, the distance from the soil was smaller, and the impact on the stress state of the soil was greater.

3.2. Dynamic stress solution under multi-wheel load. The Nanning Metro Line 1 subway train used a 6B formation, which meant that the metro was arranged with six type B cars and the type B cars had a length of 19 m, a fixed distance of 12.6 m, a fixed wheelbase of 2.2 m, an axle weight of 14 t, and a maximum operating speed of 80 km/h. The train model is shown in Figure 6.

The train load acted on the foundation soil through the wheels, and the stress of the soil unit was calculated as the superposition of the stress generated by each wheel load at the point of action. The train had four pairs of wheels in each car, and the total stress value was the stress accumulation of 24 pairs of wheel pairs at the calculated point. The stress calculation formula was:

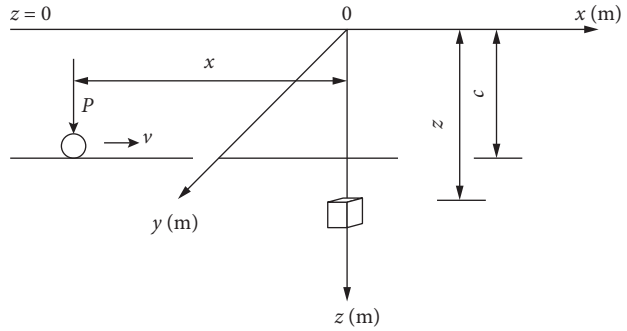

Figure 2: Stress state of the soil element under a single wheel load.

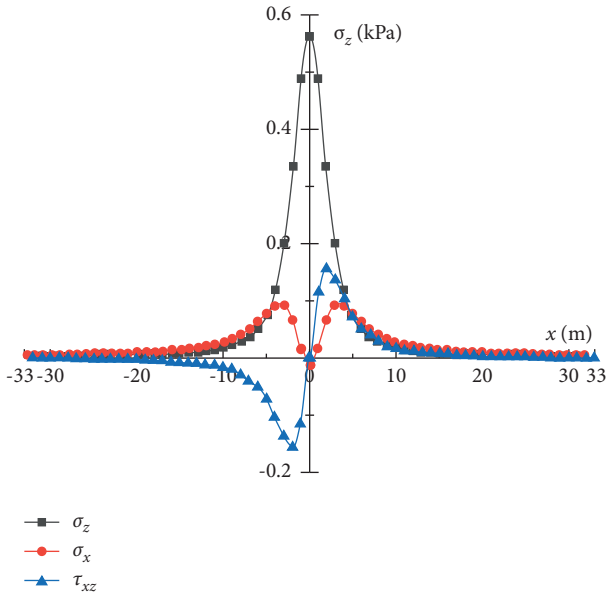

Figure 3: Changes of the soil stress state under a single wheel load.

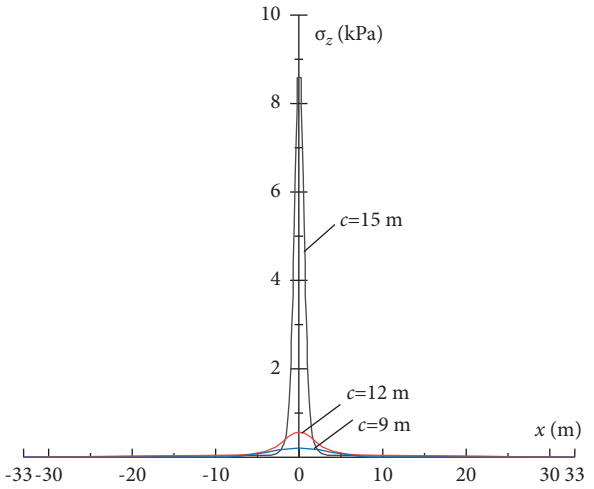

Figure 4: σ_z at different burial depths.

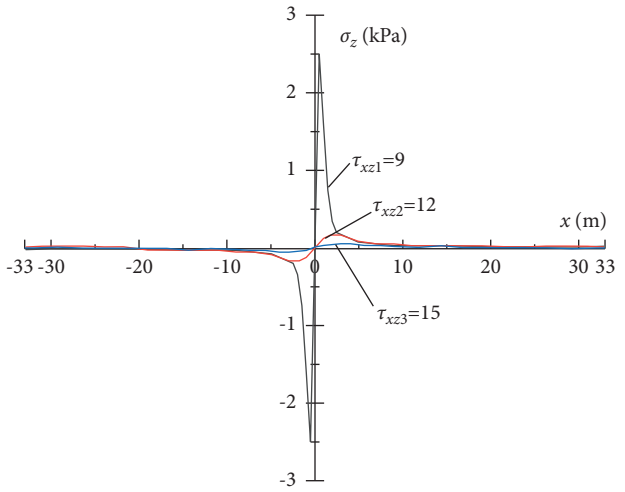

Figure 5: τ_{xz} at different burial depths.

$$\sigma_z = \sum \sigma_{z_i} = \sum \frac{P}{8\pi(1-\mu)} \left\{ \begin{array}{l} \dfrac{(1-2\mu)(z-c)}{\left(x_i^2 + (z-c)^2\right)^{3/2}} - \dfrac{(1-2\mu)(z-c)}{\left(x_i^2 + (z+c)^2\right)^{3/2}} \\ + \dfrac{3(z-c)^3}{\left(x_i^2 + (z-c)^2\right)^{5/2}} + \dfrac{3(3-4\mu)z(z+c)^2 - 3c(z+c)(5z-c)}{\left(x_i^2 + (z+c)^2\right)^{5/2}} \\ + \dfrac{30cz(z+c)^3}{\left(x_i^2 + (z+c)^2\right)^{7/2}} \end{array} \right\}. \quad (7)$$

3.2.1. Different loads. The subway train load depth was taken as c = 12 m, and it was calculated that the soil unit was located 4 m directly under the tunnel ($x = 0$, $y = 0$, $z = 16$ m). When the train ran at a speed of v = 80 km/h and when the axle weights were 11 t, 14 t, and 16 t, the stress state of the soil changed. The train ran at v = 80 km/h, and the head distance was calculated from the soil unit as -33 m until the car left the soil unit for a distance of 33 m, that is, for t =-4 s to t = 4 s. The stress state change of the soil element was calculated, and the load movement was simulated with the distance change between the load and the calculated soil element. The calculation result is shown in Figure 7.

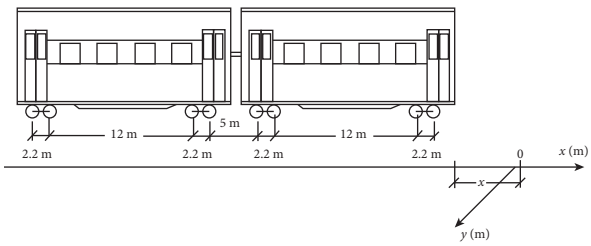

Figure 6: Schematic diagram of the vehicle model.

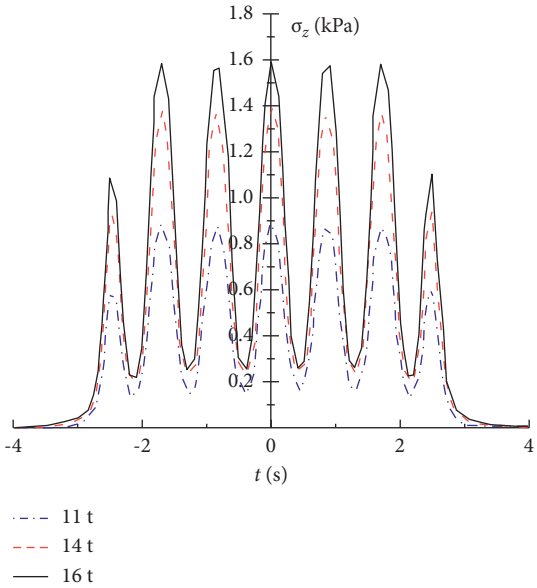

Figure 7: σ_z (o)f soil with different axes.

3.2.2. Different buried depth. The depths of the load were taken as c = 9 m, 12 m, and 15 m. The calculated soil unit was located 4 m directly under the tunnel ($x = 0$, $y = 0$, z = 16 m). The axle load of the train was 14 t. When running at a speed of v = 80 km/h, the change of the soil stress state was studied.

3.2.3. Different speeds. The axle load of the train was 14 t, and the buried depth was 12 m. The initial distance between the train and the soil unit was -33 m, when the train ran through the soil unit at speeds of 40 km/h, 80 km/h, and 120 km/h. At different speeds, the times for the vehicles passing through the soil unit at different speeds were 16 s, 8 s, and 4 s. The stress state of the calculated unit is shown in Figure 9.

It can be seen in Figures 7 and 9 that under different operating conditions, the stress of the soil unit of the metro load always had a continuous cycle characteristic, and the dynamic stress value of each cycle period was not completely equal. The stress state change at the calculation point in the process of moving away from the soil unit was symmetrical; that is, where the horizontal distance from the soil body was equal, the stress value was almost equal.

The cycle period was related to the length of the metro and the speed; that is, the faster the metro passed through the soil unit, the shorter of the cycle period. The rear wheel of each car and the front wheel of the next car were regarded as

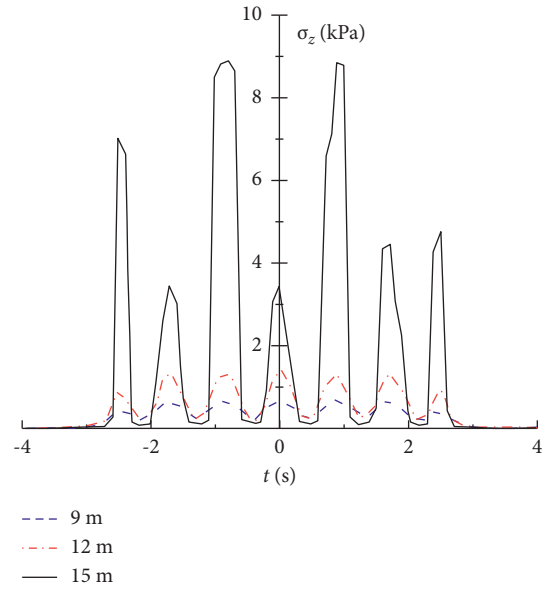

Figure 8: σ_z of soils with different depths.

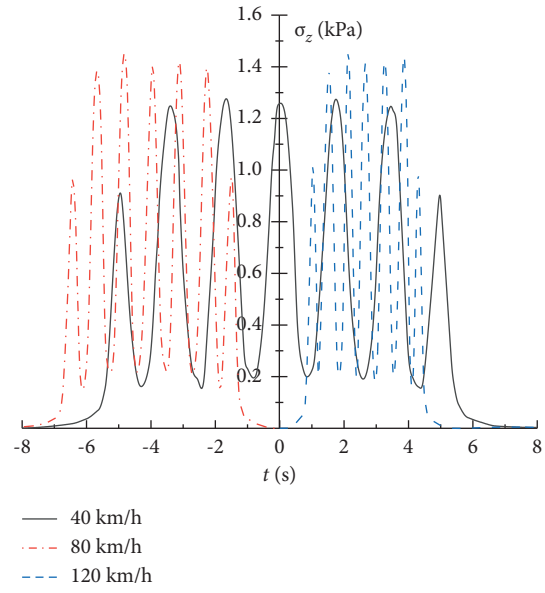

Figure 9: σ_z of soil at different speeds.

a group. Each group of the wheel axle caused a group of stress cycles. The first car front wheel and the last car rear wheel caused a group of cycles, for a total of seven cycles. The number of cycles was related to the number of wheels and axles. The peak stress in each cycle that appeared in the wheel shaft reached directly above the soil element. The closer the wheel shaft to the soil element, the greater the influence on the stress of the soil element. Therefore, the stress was related to the burial depth of the tunnel. In addition, the stress was positively related to the magnitude of the load applied to the soil. The load was related to the axle weight and speed.

It can be seen in Figure 7 that when the axle loads of the train were 11 t, 14 t, and 16 t, the corresponding peak stresses of the soil were 0.90 kPa, 1.40 kPa, and 1.60 kPa, respectively,

and the stress increased with the increase of the axle load. The stress that was exerted by the lower wheel on the track was proportional to the train speed. As shown in Figure 8, when the train speeds were 40 km/h, 80 km/h, and 120 km/h, the corresponding peak stresses of the calculated soil unit were 1.26 kPa, 1.43 kPa, and 1.60 kPa.

It can be seen in Figures 4 and 9 that the effects of different tunnel burial depths on the stresses of the soil elements under multi-wheel loads and the dynamic responses under single wheel loads showed a proportional relationship between the stress and the burial depth. Additionally, the soil stress at the depth of 15 m was significantly greater than the soil stresses at the depths of 12 m and 9 m.

4. Conclusions

In this study, based on the Mindlin solution, the change of the stress state of the foundation under a single wheel load and multiple wheel loads under different conditions was calculated. The law of the soil stress at a certain point directly below the moving line of the train load was as follows.

1. Under the load of a single wheel, the stress σ_z reached a maximum value of 0.56 kPa when the axle was directly above the soil element, and the stress decreased until it approached zero as the distance from the soil unit increased. The stress value and the burial depth had a positive correlation, and the σ_{zmax} values corresponding to 9 m, 12 m, and 15 m were 0.20 kPa, 0.57 kPa, and 8.74 kPa, respectively. Therefore, the greater the burial depth, the greater the stress value, and the more significant the stress change.

2. When a multi-wheel load was applied, the stresses of the soil passing through the soil unit under different working conditions all exhibited continuous cycle characteristics. The number of cycles was related to the number of wheels, and the cycle period corresponded to the time it took for the wheel loads to pass through the soil element, which was related to the length of the metro and the speed of the vehicle.

3. Under the load of multiple wheels, the soil stress peaked when each train axle was directly above the calculated soil element. When the metro axle weights were 11 t, 14 t, and 16 t, the corresponding peak soil stresses were 0.90 kPa, 1.40 kPa, and 1.60 kPa. When the train speeds were 40 km/h, 80 km/h, and 120 km/h, the corresponding peak stress values of the calculated soil unit were 1.26 kPa, 1.40 kPa, and 1.48 kPa, respectively. The corresponding peaks of the soil stress at the burial depths of 9 m, 12 m, and 15 m were 0.72 kPa, 1.40 kPa, and 8.9 kPa, respectively. It could be seen that the magnitude of the stress was directly proportional to the axle load, speed, and burial depth of the tunnel.

In this paper, the calculated and analyzed metro axle weights are 11 t, 14 t, and 16 t, and the metro speeds are 40 km/h, 80 km/h, and 120 km/h. The vibration stress under other metro axle weights and speeds needs to be further studied.

Data Availability

The data used to support the findings of the study are available from the corresponding author upon request.

Conflicts of Interest

The authors declare that there are no conflicts of interest regarding the publication of this paper.

Acknowledgments

The authors gratefully acknowledge the financial support for this research from the "Nanning Science Research and Technology Development Plan" (Grant No. 20173160-6), and the "Research and Application of Ecological Slope Protection Technology in Carbonaceous Rock Slopes" (Grant: AD19110124), and the Science and Technology Project of Guangxi "Research on the Key Technologies of highway construction in Guangxi carbonaceous rock area" (Grant: GuikeAC16380119), and the Key Science and Technology Project of Ministry of Transportation of The People's Government of China "Reinforcement Theory and Technology of Multi-point Restraint Anchor Cable and Monitoring Warning for Highway High Slope" (Grant: 2020-MS3-082).

References

[1] J. D. Geddes, "Stresses in foundation soils due to vertical subsurface loading," *Géotechnique*, vol. 16, no. 3, pp. 231–255, 1966.

[2] C. B. He, L. B. Wang, and G. Y. Li, "Stresses induced by vertical rectangular uniform loads within ground based on Mindlin solution," *Chinese Journal of Geotechnical Engineering*, vol. 40, no. 03, pp. 533–539, 2018.

[3] K. Ishihara, *Soil Behavior in Earthquake Geotechnics*, Oxford University Press, New York, USA, 1996.

[4] S. J. Wang, M. Zhang, and J. Z. Zhang, "On Mindlin stress formulas," *Engineering Mechanics*, vol. 18, no. 6, pp. 141–148, 2001.

[5] C. Yang and Y. Gong, "Dynamic stress and vibration of the roadbed when the train passes," *China Civil Engineering Journal*, no. 2, pp. 49–57, 1963.

[6] H. Lei, L. Zhang, Y. Xu, J. Liang, and Z. Ba, "Numerical simulation of settlement of soft soil foundation under fast metro train loads," *Chinese Journal of Geotechnical Engineering*, vol. 41, no. S1, pp. 45–48, 2019.

[7] Q. Huang, "The dynamic response analysis of the tunnel under subway train vibration load," *Subgrade Engineering*, no. 04, pp. 161–165, 2018.

[8] Z. Ding, D. W. Li, and Z. X. Xie, "Dynamic stress characteristics of viscoelastic foundations under subway train load," *China Earthquake Engineering Journal*, vol. 38, no. 6, pp. 889–895, 2016.

[9] Z. Ding, G. B. Ge, X. J. Wei, and J. Q. Jiang, "Variation of stress state of foundation soils induced by running subway," *Chinese Journal of Geotechnical Engineering*, vol. 35, no. S2, pp. 647–651, 2013.

[10] L. Wei, L. Tang, and Q. Zhang, "Research on dynamic stress of subgrade soil under vehicle loads and its diffused rule," *Journal of Chongqing Jianzhu University*, vol. 31, no. 04, pp. 799–802+823, 2012.

[11] Y. Q. Zhang, "Dynamic response of semi-infinite body under moving loads," *Rock and Soil Mechanics*, vol. 25, no. 06, pp. 955–957, 2004.

[12] Z. Li, J. Wang, and K. Han, "Analytical solution of ground stress induced by shallow tunneling with arbitrary distributed

loads on ground surface," *Symmetry*, vol. 11, no. 6, pp. 823–835, 2019.

[13] C. Guo, K. Han, H. Kong, and L. Shi, "Explicit form of exact analytical solution for calculating ground displacement and stress induced by shallow tunneling and its application," *Advances in Civil Engineering*, vol. 2019, no. 12, pp. 1–13, 2019.

[14] G. Eason, "The stresses produced in a semi-infinite solid by a moving surface force," *International Journal of Engineering Science*, vol. 2, no. 6, pp. 581–609, 1965.

[15] H. Grundmann, M. Lieb, and E. Trommer, "The response of a layered half-space to traffic loads moving along its surface," *Archive of Applied Mechanics*, vol. 69, no. 1, pp. 55–67, 1999.

[16] F. C. P. de Barros and J. E. Luco, "Response of a layered viscoelastic half-space to a moving point load," *Wave Motion*, vol. 19, no. 2, pp. 189–210, 1994.

[17] R. Siddharthan, Z. Zafir, and G. M. Norris, "Moving load response of layered soil, i: formulation," *Journal of Engineering Mechanics*, vol. 119, no. 10, 1993.

[18] B. Alabi, "A parametric study on some aspects of ground-borne vibrations due to rail traffic," *Journal of Sound and Vibration*, vol. 153, no. 1, pp. 77–87, 1992.

[19] C. J. Wang and Y. M. Chen, "Analysis of stresses in train-induced ground," *Chinese Journal of Rock Mechanics and Engineering*, vol. 24, no. 07, pp. 1178–1186, 2005.

[20] C. j. Wang, "Experimental study on deformation behavior of saturated soft clay under bidirectional cyclic loading," *China Civil Engineering Journal*, vol. 43, pp. 573–576, 2010.

[21] J. G. Qian, R. Y. Zhou, and M. S. Huang, "Dynamic stress responses to high-speed moving load on elastic saturated semi-space ground," *Engineering Mechanics*, vol. 33, no. 3, pp. 39–46, 2016.

[22] J. Hu, X. Bian, and J. Jiang, "Critical velocity of high-speed train running on soft soil and induced dynamic soil response," *Procedia Engineering*, vol. 143, pp. 1034–1042, 2016.

[23] G. X. Chen and H. Pan, "The characteristics and laboratory test simulation of stress," *China Civil Engineering Journal*, vol. 43, no. S2, pp. 340–345, 2010.

[24] R. D. Mindlin, "Force at a point in the interior of a semi-infinite solid," *Physics*, vol. 7, no. 5, pp. 195–202, 1936.

[25] N. F. Doyle, "Railway track design: a review of current practice," *Railroad Tracks*, Australian Government Publishing Service, Canberra, Australia, 1980.

Hindawi
Advances in Civil Engineering
Volume 2022, Article ID 7848152, 16 pages
https://doi.org/10.1155/2022/7848152

Research Article

Research on Deformation Law of Deep Foundation Pit of Station in Core Region of Saturated Soft Loess Based on Monitoring

Xueyan Wang,[1] Qiyu Song ,[2,3] and Hang Gong[2,3]

[1]*School of Urban Planning and Municipal Engineering, Xi'an Polytechnic University, Xi'an, Shaanxi 710048, China*
[2]*College of Civil Engineering, Xi'an University of Architecture and Technology, Xi'an, Shaanxi 710055, China*
[3]*Shaanxi Key Lab of Geotechnical and Underground Space Engineering, Xi'an University of Architecture and Technology, Xi'an, Shaanxi 710055, China*

Correspondence should be addressed to Qiyu Song; 1057250488@qq.com

Received 20 November 2021; Revised 14 December 2021; Accepted 4 January 2022; Published 24 January 2022

Academic Editor: Dawei Yin

Saturated soft loess has a large pore structure, high compressibility, low strength, fluid plastic state, and poor engineering properties. It is still one of the key problems that engineering needs to solve. In order to study the influence of deep foundation pit excavation in the saturated soft loess area on the deformation of foundation pits, the deformation laws of ground settlement, enclosure structure, and supporting axial force were clarified based on the field tests on the deformation characteristics of deep foundation pits in areas with the high-water level in saturated soft loess, combined with geological conditions and on-site construction procedures. The results indicate the following: water supply and construction process were found to be the main factor in changing the surface settlement curve of deep foundation pits in saturated soft loess; increasing the construction speed of the pit bottom floor, inverted braces, floor frame beams, and sidewall frame beams to close the structure, which is conducive to restraining the deformation of the continuous underground wall and foundation pits in similar areas. In the initial stage of support layout, the axial force of steel support tends to increase too fast or even exceed the standard control value. Therefore, a reasonable preadding axial force is an effective means to control the deformation of the continuous underground wall and the axial force of the steel support. The current research results may provide a reference for constructing deep foundation pits in similar areas.

1. Introduction

Loess is a kind of yellow silt sediment that is transported by wind. It is widely distributed in arid and semiarid areas in the Northwest of China, such as Shaanxi, Shanxi, and Gansu, as shown in Figure 1. It was deposited under special climate and geological conditions [1]. In this case, the naturally deposited loess has a typical structure, and loading and humidification can gradually destroy the loess structure [2, 3], which can cause engineering hazards [4, 5]. One type of loess is saturated after being soaked by water and loses its collapsibility, but still has a large pore structure, with greater compressibility, lower strength, flow plasticity, and poor engineering properties, and is called saturated soft loess. During precipitation excavation in saturated soft loess areas, the surrounding ground subsidence usually occurs resulting in accidents from time to time [6–8].

Saturated soft loess is mainly distributed in Xi'an, China. In recent years, the rapid development of Xi'an has increased the scale of foundation pit excavation in saturated soft loess areas. Due to the complexity and uncertainty of the site conditions of deep foundation pit excavation, the existing theory cannot consider the influence of various factors on the deformation simultaneously. On the other hand, the field monitoring data reflect the comprehensive effect of various factors in the construction process. Therefore, a thorough

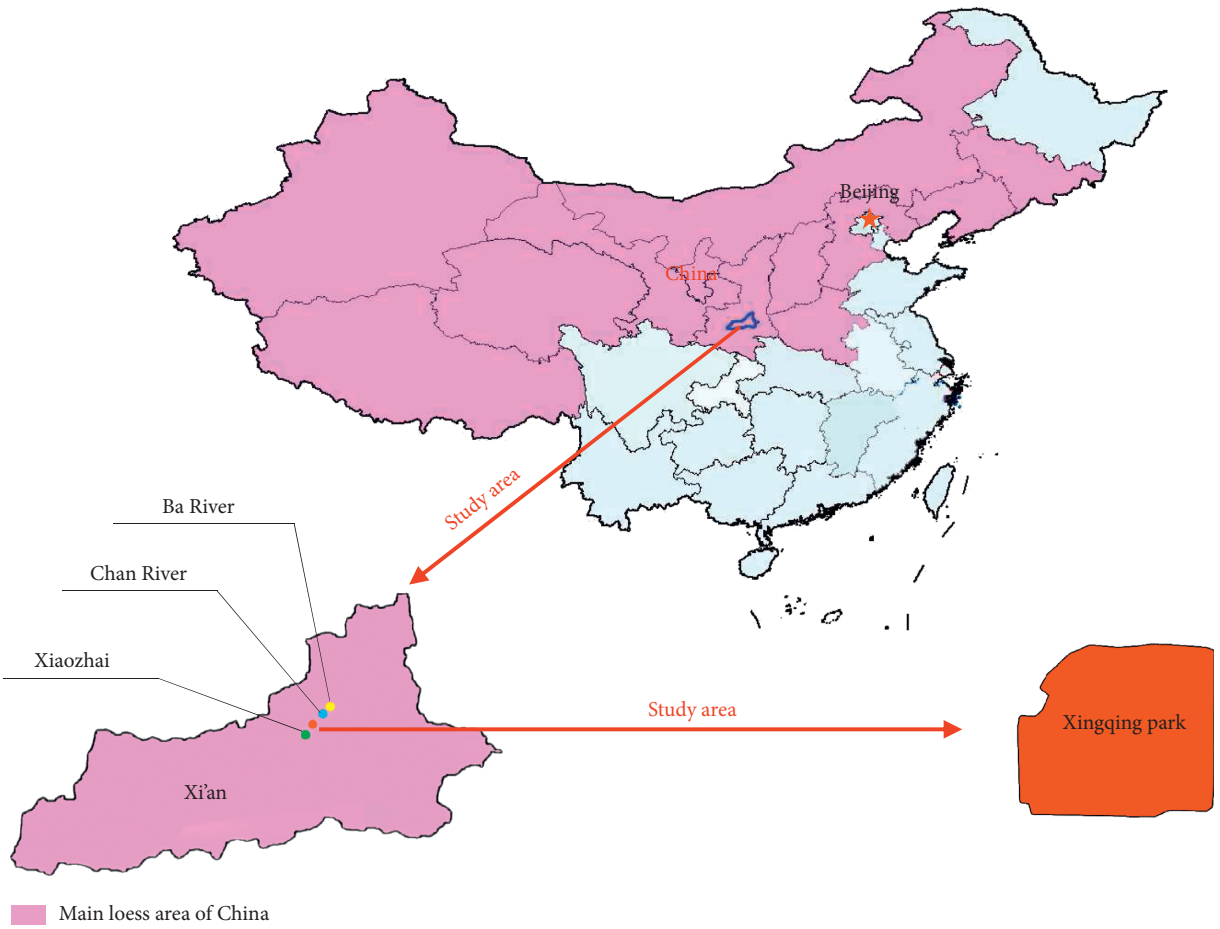

Figure 1: Main distribution of saturated soft loess in Xi'an, China.

analysis of monitoring data has become an effective way to understand deep foundation pits' deformation laws in saturated soft loess.

In recent years, many scholars have analyzed the monitoring of different types of deep foundation pits in loess and soft soil areas. Clough, Long, Moormann C, and others carried out a classification study on the deformation of different foundation pits around the world and obtained the deformation law of foundation pits during construction [9–11]; Mei and Yang analyzed the deformation characteristics and influencing factors of foundation pits in Xi'an, Shanghai, Ningbo, Hangzhou, and other regions, respectively [12–14]; Zhou Yong, Ren Jianxi, Liu, Zhi, Li Zhe, Eibaz, and Wang Guohui studied and analyzed the monitoring data of pile displacement, surface settlement outside the pit, supporting axial force, and groundwater level during the excavation of the foundation pit [15–21]; Xu Jian and Zhang, respectively, compared numerical simulation and monitoring data of foundation pit excavation to analyze the deformation characteristics of foundation pit [22, 23]; Zhang and Di studied the influence of the enclosure structure on ground settlement [24, 25]; Farzi et al. [26] conducted a systematic survey of the complex geotechnical characteristics of Ahwaz, and the displacement value during construction and excavation was checked and evaluated; Wang et al. [27] analyzed the influence of soil structural changes on the horizontal displacement of the retaining structure wall, ground settlement, and adjacent subway tunnels during the excavation of the foundation pit; and Liu et al. [28] analyzed the influence mechanism of rainfall on the deformation of the soft soil foundation pit support structure.

The aforementioned research provides an effective reference for analyzing foundation pit excavation deformation law. However, there is less monitoring and analysis of deep foundation pit construction in saturated soft loess areas with high-water levels. Therefore, this article aimed to analyze and study the deformation laws between the groundwater level, the ground surface, continuous underground walls, and internal supports during the construction of deep and high-level foundation pits in saturated soft loess. The results can provide references for the excavation and the deformation prevention measures of deep foundation pits in similar saturated soft loess areas to ensure the safety and stability of the foundation pit.

2. An Overview of the Test Section

Saturated soft loess has the characteristics of large pore structure, high compressibility, low strength, and flow plastic state, which makes the engineering properties of saturated soft loess poor. These factors increase the construction risk of deep foundation pit excavation in saturated soft loess areas. The

saturated soft loess in Xi'an, China is mainly distributed in Chanhe, Bahe, Xiaozhai, Xingqing Park, and other areas, as shown in Figure 1. As construction progresses, a subway in Xi'an passes through the core area of saturated soft loess in Xingqing Park. As shown in Figure 2, the deep foundation pit of the shield shaft is 28.6 m from the nearest Xingqing Lake. The urban area is dense, and there are old constructions around it. Therefore, the control requirements are very strict. Therefore, the deep foundation pit was selected as the test section for the on-site monitoring test.

The outer size of the deep foundation pit is 26.7 m × 8.6 m, and the open-cut method is adopted. The depth of the foundation pit is 30.45 m, and the thickness of the roof covering is about 11.6 m. According to the geological survey report, the top-down stratum of the site topography is artificial plain fill above the groundwater table, saturated soft loess below the groundwater table, ancient soil, old loess, silty clay, medium sand, and silty clay, as shown in Figure 3. Except for artificial filling, the remaining soil layers are continuously and evenly distributed throughout the site, and the layer thickness is relatively uniform. The physical parameters of soil are shown in Table 1.

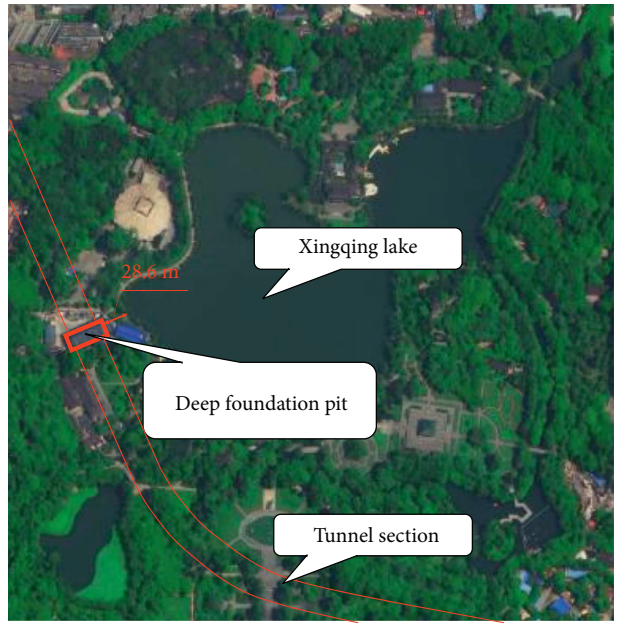

Figure 2: The location of the foundation pit.

3. Test Plan

3.1. The Foundation Pit Support Plan. The dewatering of the foundation pit for this project uses the water-stop curtain combined with the dewatering scheme in the pit. The total number of dewatering wells is 14. There are 4 dredging wells and 10 observation wells. The foundation pit adopts the method of laying wells in the pit, as shown in Figure 4. After the underground diaphragm wall construction is completed, the foundation pit will be excavated when the dewatering meets the design requirements. After the first layer is excavated, the reinforced concrete crown beam and the supporting beam will be erected. After the concrete strength is reached, the second layer will be excavated and erected in time. The steel support will be excavated downward layer by layer.

The supporting structure of the foundation pit adopts the supporting form of a continuous underground wall combined with internal support. The continuous underground wall adopts C30 concrete, the thickness is 1 m, the underground depth is 45 m, and the embedded depth is 14.5 m, as shown in Figure 4.

There are six supports in the foundation pit. The first support is made of C30 concrete. The second to sixth steel supports are supported by steel pipes with a diameter of 609 mm and a thickness of 16 mm. The fifth steel support is set with inverted supports. During the continuous wall construction, the steel plate is embedded in the corresponding position, and the excavation and support are conducted during the earth excavation process. The steel support layout is shown in Figures 5.

3.2. Monitoring Plan. To prevent the excessive deformation of the foundation pit from causing safety problems, it is necessary to monitor the surrounding environment, the continuous underground wall, and the supporting system. The layout of the measuring points is shown in Figures 6 and 4, and the main monitoring items are shown in Table 2.

3.3. Analysis of Working Conditions. The foundation pit monitoring data collection work took 79 days from the erection of the second steel support to the removal of the first steel support. To study the general law of mutual influence among water level, ground settlement, and enclosure structure, the foundation pit was divided into 14 working conditions, as shown in Table 3.

4. Analysis of Monitoring Results

4.1. Analysis of Groundwater Level and Surface Subsidence Data. Before this experiment, the foundation pit had been dewatered for 20 days. After the water level in the pit fell below −31.5 m, the foundation pit began to be excavated. The monitoring data of the longitudinal observation wells GJ3, GJ5, GJ6, and GJ8 of the foundation pit were extracted, and the data from the beginning of the deep foundation pit to when the water level outside the pit stabilized were selected for analysis, which lasted for 64 days. The groundwater-level monitoring curve of the dewatering wells in each pit is shown in Figure 7. It can be seen from the figure that the overall trends of the 4 observation wells were consistent. 36 days ago, due to the continuous precipitation of the foundation pit, the water levels of the 4 observation wells were all decreasing; after 36 days, the water level outside the pit fluctuated due to the occurrence of water gushing; and the water level gradually stabilized after the water gushing problem was solved. The final descending water levels of the observation wells were −3 m, −2.5 m, −4.1 m, and −3.9 m, respectively. The analysis shows that due to the replenishment of the water source, the water levels of the observation

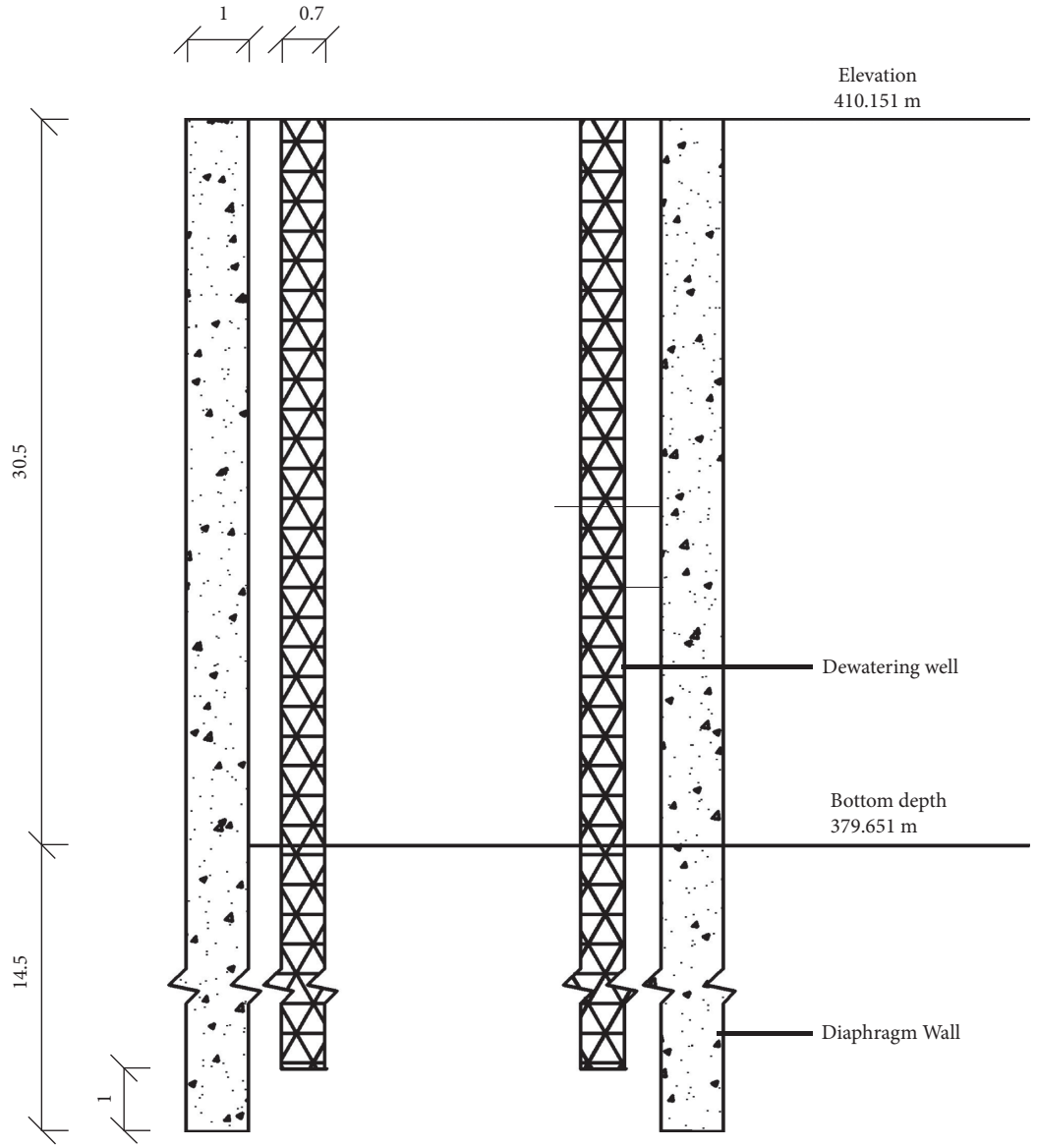

Figure 3: Underground diaphragm wall structure design (unit: m).

Table 1: Physical and mechanical parameters of soil.

Stratum	Dry weight (kN/m^3)	Cohesion (kPa)	Internal friction angle (°)	Permeability coefficient (m/d^{-1})	Poisson's ratio
Plain fill	—	10	12.0	—	0.38
Saturated soft loess	14.7	15	15.0	5	0.37
Paleosol	16.4	20	18.0	4	0.33
Old loess (soft)	16.6	20	18.5	3	0.35
Silty clay	16.0	30	21.0	3	0.30
Nakasago	—	0	32.0	25	0.25

wells GJ3 and GJ5 on the right side of the foundation pit were significantly higher than those on the left side of the foundation pit and the water levels of the observation wells GJ6 and GJ8 on the other hand.

A total of 29 ground subsidence monitoring points were set up in this experiment. Data from CJ1-1 to CJ5-6 were examined. Figure 8 shows the settlement time-history curve of the 3 loops around the foundation pit. The positive value represents the uplift and the negative value represents the settlement. Referring to Figure 4, taking the center of the foundation pit as the dividing line, it can be seen from Figure 8 that due to the replenishment of nearby water sources, the ground surface on the left side of the foundation pit is partially uplifted, and the ground surface on the right side is partially subsided. On the 14th day of the monitoring, a water inrush occurred near the CX2 monitoring point, and

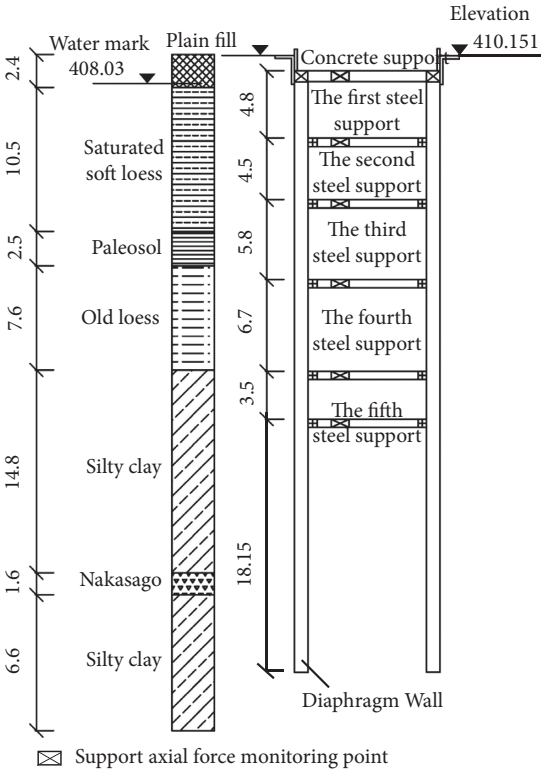

Figure 4: Survey point layout (unit: m).

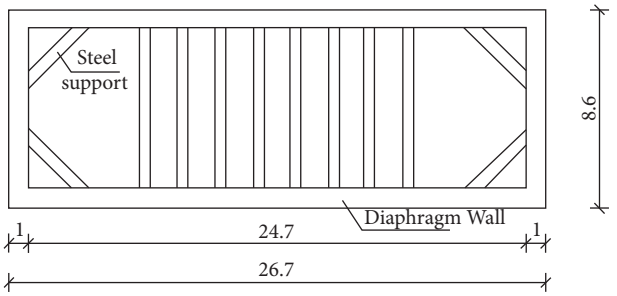

Figure 5: Geological section and cross section of steel support (unit: m).

the data fluctuated and began to disperse. After 7 days, the water inrush problem was solved, and the ground subsidence gradually stabilized. Through the comparative analysis of Figure 8(a)–8(c), as the distance from the foundation pit increased, the settlement or uplift of the ground outside the pit gradually decreased.

Data were extracted from surface monitoring points CJ3-1, CJ3-2, CJ3-3, CJ3-4, and CJ3-5, and the changes were analyzed in surface settlement from the installation of the second steel support to the end of the negative second floor inverted support construction. As shown in Figure 9, it can be seen that due to the water supply on the right side of the foundation pit, the ground surface on the left side of the foundation pit is partially uplifted, and the ground surface on the right side is partially subsided. At the same time, in condition S6, the data begin to change when water inrush occurs, and then the data are stable.

An analysis was conducted from the installation of the second steel support to the removal of the second and first steel supports, the locations of the largest settlement and the largest uplift of the ground surface, as shown in Figure 10. It can be seen from the figure that the foundation pit construction has the greatest impact on CJ5-5 before the water inrush. However, the surface settlement deformation is small, and the deformation is relatively slow. After the water gushing, the uplift value of CJ4-4 is the largest, and the settlement value of CJ2-5 is the largest. The surface uplift and settlement are both experiencing high acceleration until the water gushing problem is solved.

The aforementioned data analysis shows that the water gushing from the foundation pit significantly impacts the groundwater level and surface settlement. During the construction of the foundation pit, attention should be paid to the changes in the groundwater level and ground settlement to avoid water inrush accidents.

Figure 11 shows the maximum settlement (Hz) ratio of the measured points of the actual measurement target section to the maximum excavation depth (H) of the foundation pit. It can be seen from the figure that the surface settlement increases with the increase in the excavation depth of the foundation pit. The maximum surface uplift distribution range is 0.0023%H~0.0215%H, with an average value of 0.0111%H, and the maximum surface subsidence distribution range is 0.0032%H~0.0187%H, with an average value of 0.0096%H. The average value is less than the average value of 0.043%H calculated by the statistics of the Xi'an loess area [12]. This is due to the reduction of surface settlement caused by the water source replenishment near the foundation pit, which is less than the average value of the Xi'an loess area.

Figure 12 is a histogram of the maximum settlement of each measurement point in the actual measurement target section. Figure 12 shows that among all the measurement points in the actual measurement bid section, the maximum uplift value of the surface outside the pit is 6.57 mm, the average value is 2.432 mm, the maximum settlement value is 5.68 mm, and the average value is 1.286 mm. This is due to the replenishment of the water source causing the surface uplift value to be greater than the settlement value.

Through comparison, it is found that the ground settlement caused by deep foundation pit excavation is very different due to the difference in soil quality. Long and Michael [10] studied Hong Kong and other soft soil areas and Hashash [29] studied that the clay layer foundation pit characteristics are not much different. The maximum surface settlement distribution range is distributed between 0.08%H and 0.15%H; Moormann's [11] statistics show that the surface subsidence range of soft clay areas is from 0.5%H to 2%H; the surface subsidence range of Xi'an and other loess areas studied by Mei et al. [12] ranges from 0.0114%H to 0.02%H. Compared with the above-mentioned soil quality, saturated soft loess has higher compressibility and lower strength. When excavating deep foundation pits in saturated soft loess areas, special attention will be paid to changes in the groundwater level during the design and construction stages. Dewatering causes changes in the groundwater

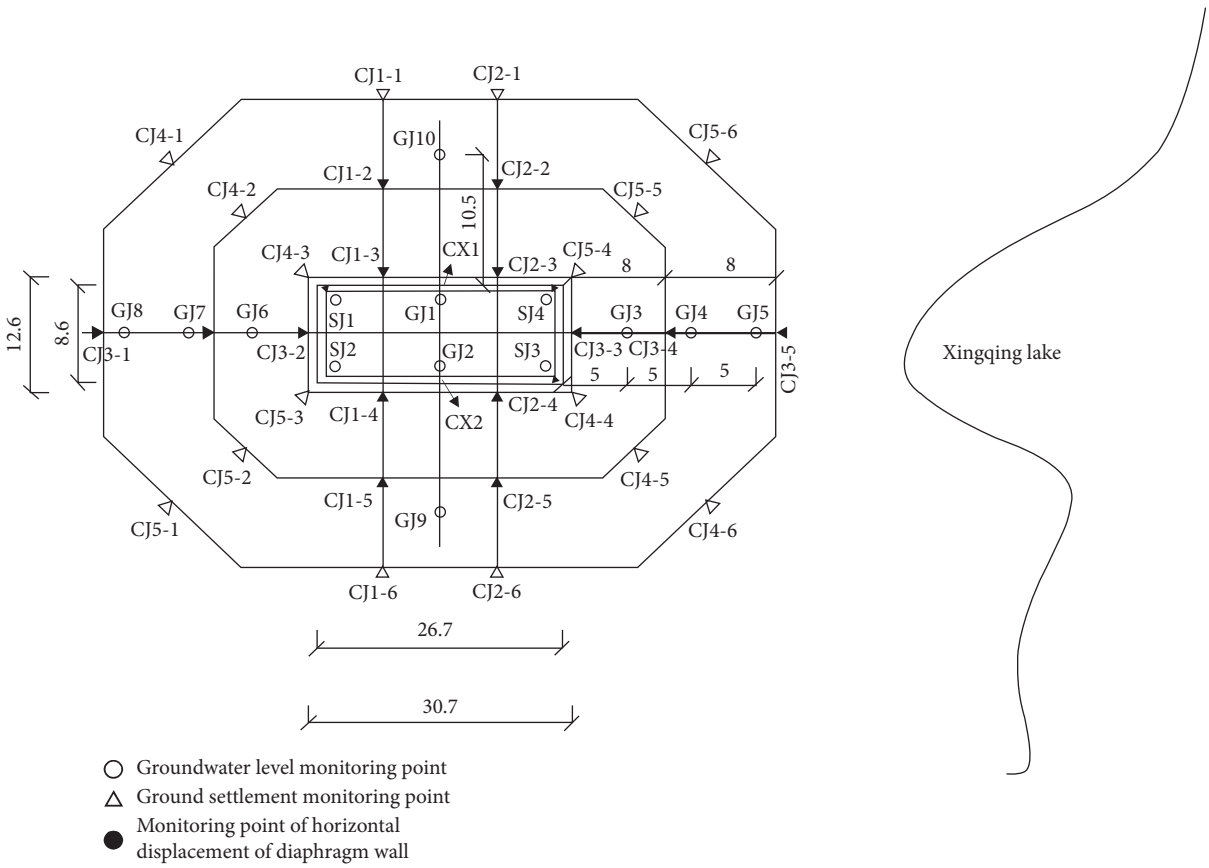

Figure 6: Plan of steel support (unit: m).

Table 2: Main items of foundation pit monitoring.

Serial number	Monitoring items	Monitoring instrument	Measuring point layout	Measurement accuracy	Allowance
1	Surface settlement around the pit	Level	Arrange 2 rings along the circumference of the pit, the first ring is 2.0 m away from the periphery of the foundation pit, the second ring is 8 m away from the periphery of the first ring, and the distance between the measuring points of each ring is 10–20 m	1.0 mm	0.3%H or ≤30 mm, whichever is smaller
2	Horizontal displacement of diaphragm wall	Theodolite Total station	Layout along with the middle and outside corners of the periphery of the foundation pit, with a spacing of no more than 20 m, and no less than 3 underground continuous walls on each side	1.0 mm	0.2%H or ≤30 mm, whichever is smaller
3	Support axial force	Axial force gauge Strain gauge	The deformation of the diaphragm wall is set at the same monitoring section, and the vertical supports at the same section position are set at measuring points	0.15%F.s	0.8f
4	Groundwater level	Water-level pipe Water-level meter	The midpoint of the long and short sides of the foundation pit, and the distance between 20 and 50 m when the foundation pit is large, needs to be combined with the precipitation plan	5.0 mm	

outside the pit, which will cause the pore water pressure in the soil to drop. According to the principle of effective stress, the decrease of pore water pressure in the soil layer will increase the effective stress, leading to the compression of the soil layer and the decrease of porosity. However, the ground subsidence caused by the excavation of the deep

Table 3: Main analysis conditions of foundation pit.

Working condition	Content	Duration/day
S1	Install the second steel support	1
S2	Excavate to 17 m, install the third steel support	3
S3	Excavate to 23 m, install the 4th steel support	4
S4	Excavate to 27 m, install the 5th steel support	3
S5	Excavation to 30.45 m	2
S6	Start gushing water-gushing solution	6
S7	Slab pouring	11
S8	Demolition of the 5th steel support	2
S9	Negative second floor inverted support construction	13
S10	4th steel support removal	2
S11	Construction of sidewall and floor frame beam on the second floor	18
S12	Removal of the 3rd steel support	2
S13	Construction of frame beams on the sidewall of the negative first floor	10
S14	Demolition of the second and first steel supports	2

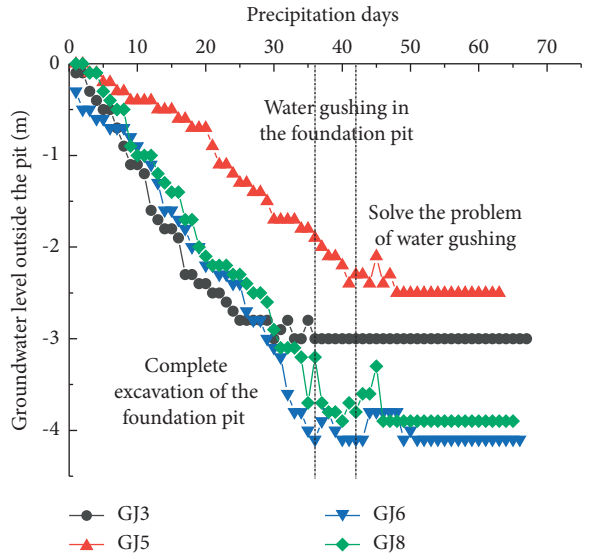

Figure 7: Water-level change curve outside the pit.

foundation pits studied in this paper is smaller than that in other areas. This is due to the special situation of water sources near the test area. Recharge was carried out during the precipitation process, which weakened the impact of precipitation on soil compression.

It can be seen that due to the nearby water supply, the surface settlement caused by deep foundation pit excavation in the saturated soft loess area is smaller than that in other areas. However, it should be noted that the saturated soft loess has greater compressibility and low strength. During the excavation of deep foundation pits, once the water level outside the pit drops too much, the consequences are often serious. Special attention and control of ground settlement should be given during design and construction.

Figure 13 shows the distribution of the maximum surface settlement deformation of the monitored section and the ratio of the distance from the edge of the foundation pit to the excavation depth of the foundation pit during the excavation of the foundation pit. It can be seen that the settlement points caused by the excavation of the foundation pit all fall within the area I summarized by Peck [30]; the average distance between the maximum vertical deformation position of the ground surface and the edge of the foundation pit is 0.341H, which is less than the average value of the Xi'an loess area; and the statistical average is 0.521H [12]. This is because the water level outside the pit in the test area is higher than the average water level in the Xi'an loess area, and the pore pressure of the soil layer is large, resulting in less ground settlement. Therefore, the average distance between the maximum vertical deformation position of the ground surface and the edge of the foundation pit is less than the statistics of the Xi'an loess area. The average value was obtained.

Due to the small excavation area of the foundation pit and the presence of nearby water sources, the groundwater was recharged during the excavation of the foundation pit. So the surface settlement outside the pit is small, but it will cause surface swelling outside the pit. Therefore, during this process, we need to pay attention to the surface subsidence and the surface uplift.

4.2. Data Analysis of Horizontal Displacement of the Diaphragm Wall. Using the CX1 monitoring point as an example to analyze the horizontal displacement of the ground connecting wall, Figure 10 shows the horizontal displacement curve of the diaphragm wall under different working conditions. From Figure 14(a) and 14(b), it can be seen that the horizontal displacement curve of the diaphragm wall under different working conditions has the exact change. Due to the installation and removal of the steel support, the underground diaphragm wall and the middle change are large. Due to the upper concrete and the lower soil support, the deformation at the lower ends of the continuous underground wall is smaller. It can be seen from the figure that as the excavation depth of the foundation pit increases, the deformation of the underground continuous wall is "serrated," which is different from the general "bow" [14]. This is because the preaxial force of the steel support is too large, resulting in the continuous underground wall not being able to bear the force together with the steel support.

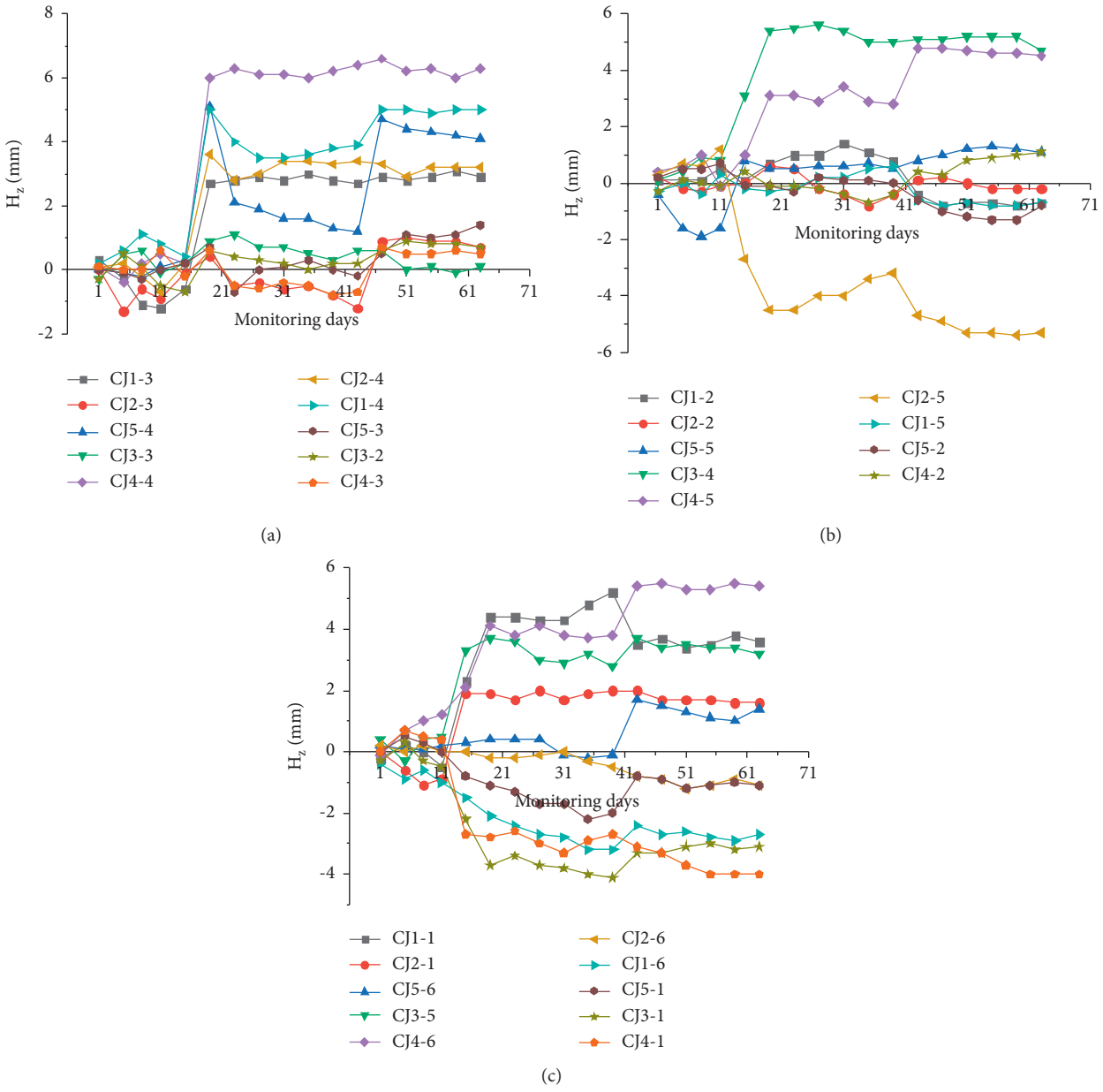

Figure 8: Change curve of surface settlement. (a) First ring. (b) 2nd ring. (c) 3rd ring.

Figure 14(c) shows the relative horizontal displacement curve of the underground diaphragm wall between different working conditions. It can be seen from Figure 14 that the relative horizontal displacement between working conditions is gradually decreasing. It shows that working condition S3 has a greater impact on the diaphragm wall. This is because when the fourth steel support is installed, the preaxial force of the steel support is too large, and the supporting structure does not effectively share the same effect. During the excavation of the foundation pit, the ground connecting wall bears greater lateral pressure of the soil, resulting in the deformation of the ground connecting wall into the pit. Working conditions S9 and S10 have a greater impact on the continuous underground wall due to the negative two of S9. The construction of the layered inverted sidewall makes the continuous underground wall completely expand outward compared to the previous working condition. The above data analysis shows that the water gushing from the foundation pit has a huge impact on the surface settlement.

Therefore, the preaxial force of the steel support should be reasonable so that the supporting structure can effectively work together to avoid excessive deformation of the ground connecting wall. Speeding up the construction of inverted sidewalls, floor frame beams, and sidewall frame beams can alleviate the impact of steel support removal on the continuous underground wall.

Figure 15 shows the cumulative curve of the displacement of the maximum and minimum deformation points of the diaphragm wall over time. It can be seen that in the

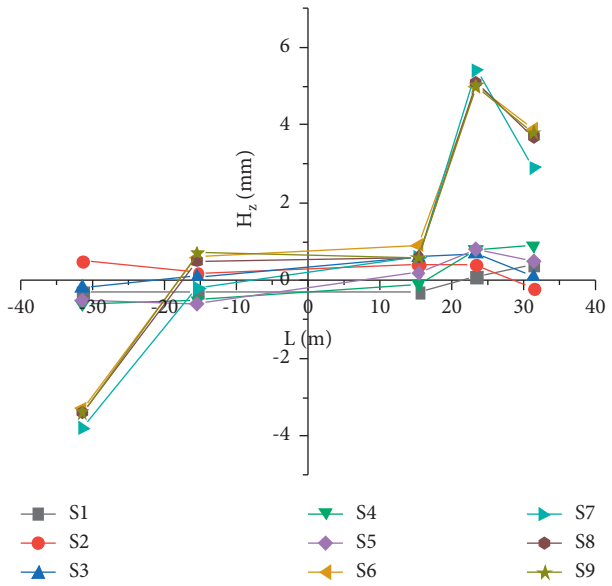

Figure 9: Changes in surface settlement under different working conditions.

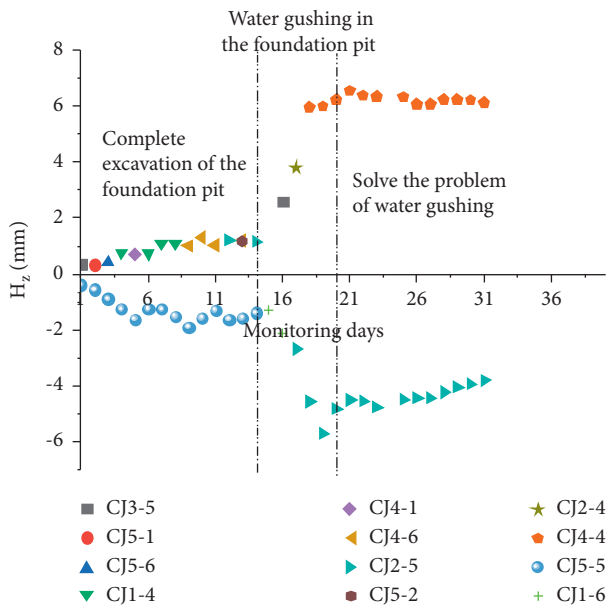

Figure 10: Changes in measurement points of the largest uplift and subsidence on the surface.

S4–S6 stage, the horizontal displacement speed of the ground connecting wall is called S1–S3 and is relatively slow; in the S7–S8 stage, due to the removal of the fifth steel support, the maximum and minimum horizontal deformations of the ground connecting wall are reduced. The underground wall deforms into the pit; the S9–S14 stage: after the negative two-story inverted bracing is completed, the continuous underground wall gradually shifts outward, and with the construction of the inverted brace, the floor frame beam, and the sidewall frame beam, the underground is continuous. The wall is restrained by its rigidity, effectively controlling the development of horizontal deformation of

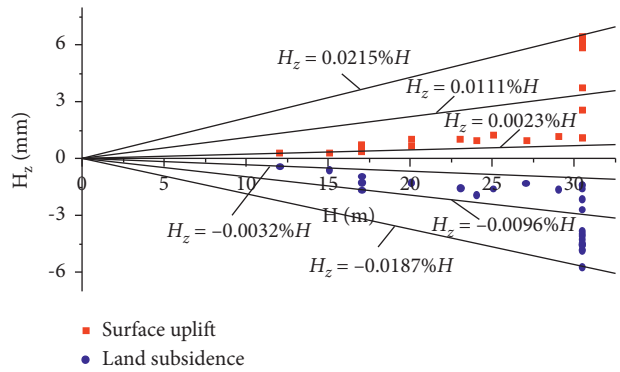

Figure 11: The relationship between the maximum surface uplift, settlement, and excavation depth.

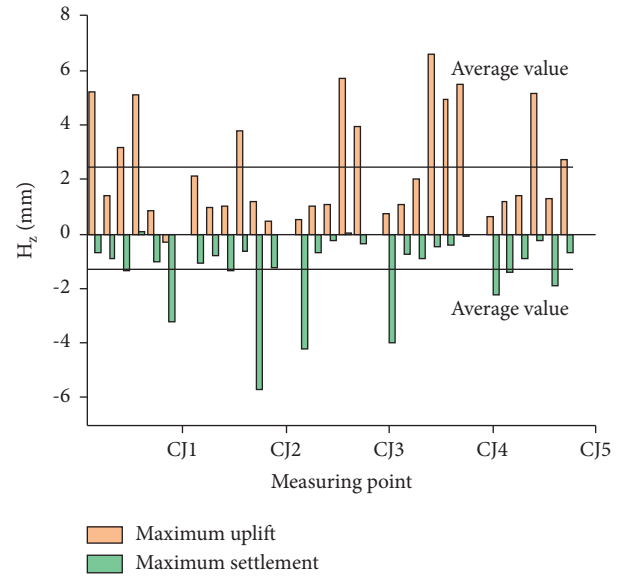

Figure 12: Histogram of the maximum uplift and settlement values outside the pit.

the continuous underground wall. Figure 16 shows that the maximum horizontal displacement of the external wall expansion is mainly distributed at 5 m and 11 m, which is a saturated soft loess area. The saturated soft loess has the characteristics of a large pore structure and high compressibility, so the wall is easy to expand. The maximum horizontal displacement of internal shrinkage is mainly distributed at 17.5 m and 22.5 m, which is the old loess area. The old loess has the properties of a compact structure, high strength, and local flow plastic state, so the wall is easy to shrink. Therefore, it is believed that the horizontal displacement of the wall may be related to the distribution of the soil layer. Given the different properties of various soil types, the ground connecting wall is subjected to different lateral pressures of the soil. Therefore, the pit bottom floor, the inverted support, and the floor slab should be accelerated during the construction process. The construction speed of the frame beams and the sidewall frame beams restrains the deformation of the continuous underground wall. Meanwhile, the deformation monitoring of the continuous

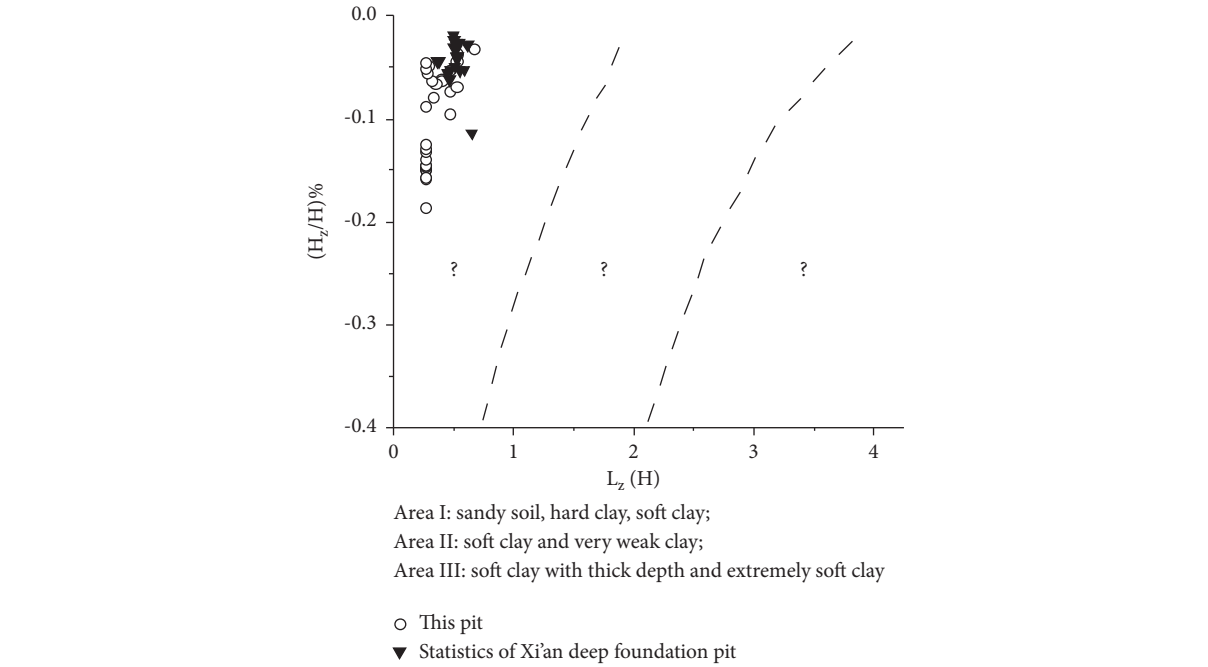

Figure 13: Ground settlement caused by excavation of foundation pit.

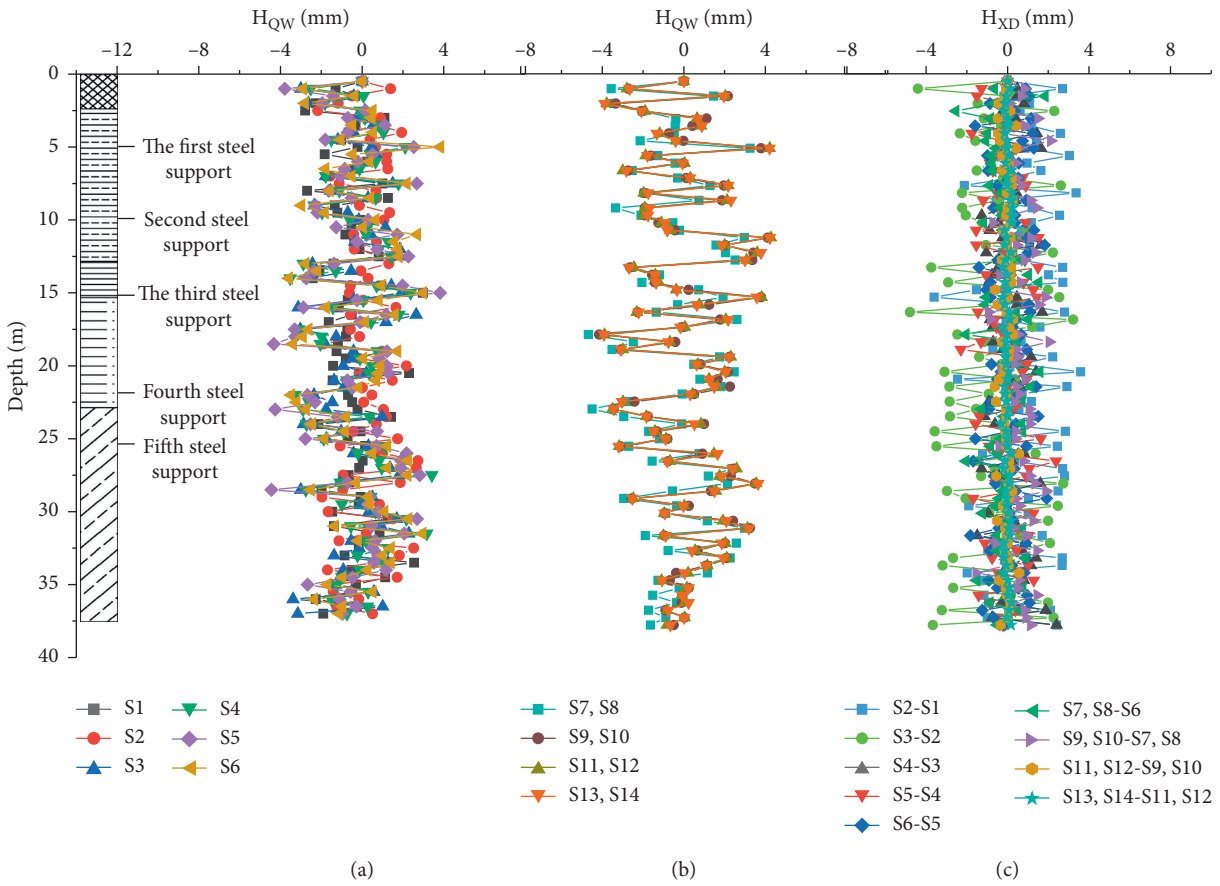

Figure 14: Horizontal deformation of ground connecting wall.

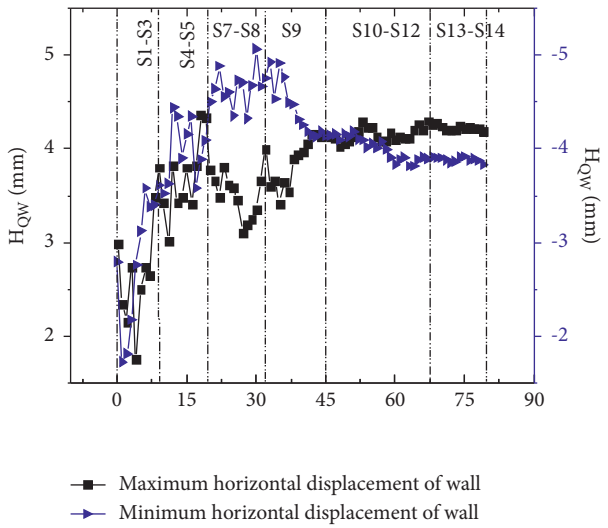

Figure 15: The cumulative curve of the displacement of the maximum and minimum deformation point of the ground connecting wall with time.

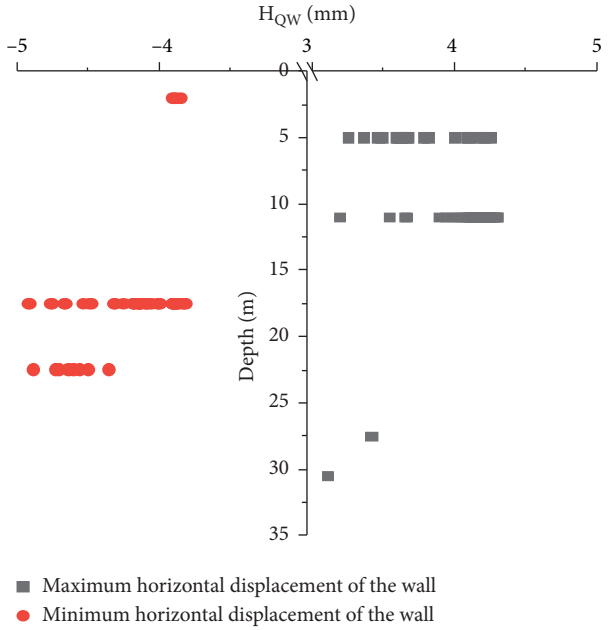

Figure 16: Distribution of the maximum and minimum horizontal displacement of the ground connecting wall.

underground wall should continue until the deformation is stable to ensure the safety of the construction.

Figure 17 shows the ratio of the horizontal displacement of the diaphragm wall (H_{QW}) to the maximum excavation depth (H) of the foundation pit. It can be seen from the figure that the wall deformation increases with the increase of the excavation depth of the foundation pit. The maximum horizontal displacement distribution range of the ground connecting wall outside the pit is 0.0102%H~0.0248%H, with an average value of 0.0133%H. The maximum horizontal displacement distribution range along the pit is 0.0107%H~0.0233%H, with an average value of 0.0141%H.

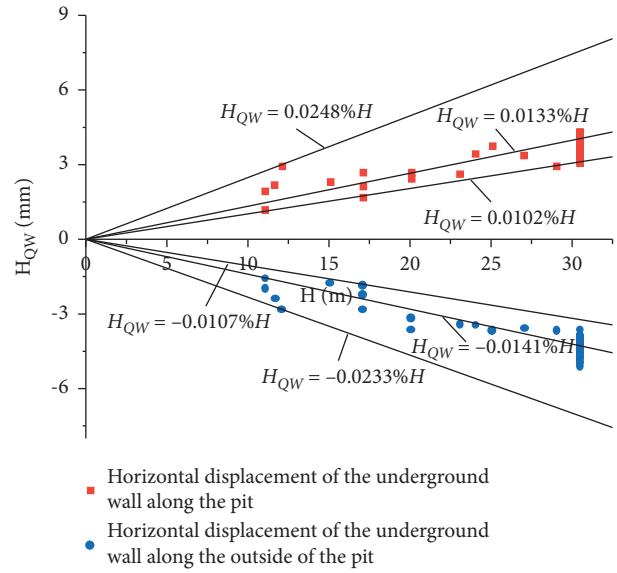

Figure 17: The relationship between the horizontal displacement of the underground wall and the excavation depth.

The distribution range is less than the distribution range of the Xi'an loess area, which is 0.0046%H~0.0994% [12], and the average value is less than the average value of 0.0366%H [12]. This is because the preadded axial force is too large when laying steel supports, which fails the effective interaction of the enclosure structure. Therefore, the average value of the ratio of the horizontal displacement of the underground diaphragm wall (H_{QW}) to the maximum excavation depth (H) of the foundation pit is smaller than Xi'an. The statistics of the loess area obtain the average value.

Therefore, the preadded axial force of the steel support should be reasonable so that the supporting structure can work together to avoid an excessive increase in the axial force of some steel supports.

4.3. The Relationship between the Vertical Deformation of the Ground Surface and the Lateral Deformation of the Diaphragm Wall. During the dewatering and excavation of foundation pits, the earth pressure is unbalanced and the enclosure structure is deformed, while the ground surface behind the envelope structure is also deformed, which causes the surface deformation to be closely related to the lateral deformation of the ground connecting wall. Figure 18 shows the relationship between the maximum surface settlement and the maximum horizontal deformation of the ground connecting wall. The figure shows that the surface settlement increases with the increase of the ground connecting wall deformation, and the main distribution range of the maximum surface settlement is 0.24, $H_{QW\max}$~$1.37H_{QW\max}$. Since the foundation pit studied in this paper is close to the water source and the surface settlement is small, the distribution range of the maximum surface settlement value is smaller than the lower limit of the range calculated by the Xi'an loess area, $0.65H_{QW\max}$ [12].

Through comparison, it is found that the relationship between the vertical deformation of the ground surface and

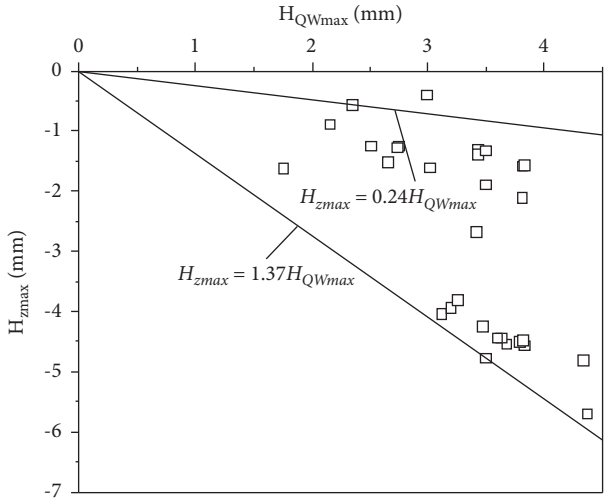

Figure 18: The relationship between the maximum vertical deformation of the ground surface and the maximum lateral deformation of the ground connecting wall.

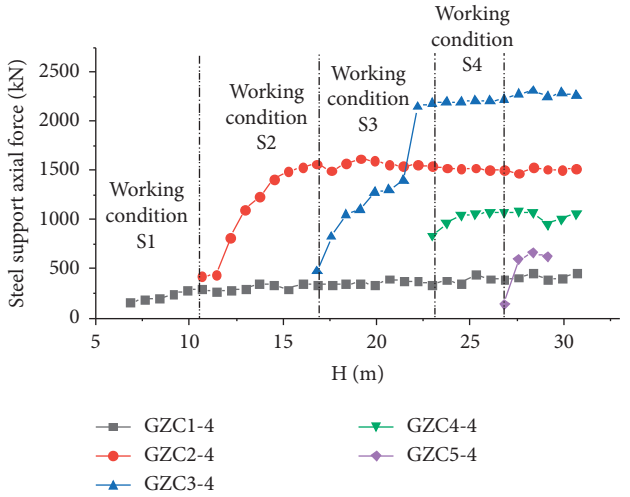

Figure 19: The change of steel support axial force with excavation depth.

the lateral deformation of the diaphragm wall is very different due to the difference in soil quality. Because of this relationship, Clough [9] believes that $H = (0.5\sim1.5)\ H_{QW\max}$ exists in the sand, hard clay, and soft clay areas; Mana [31] believes that $H = (0.5\sim1.0)\ H_{QW\max}$ exists in clay areas; according to Ou [32], there is $H = (0.5\sim0.7)\ H_{QW\max}$ in the Taipei area; Moormann [11] has $H = (0.5\sim2.0)\ H_{QW\max}$ in the soft clay area; Wang et al. [33] analyzed the depth of the soft soil area in Shanghai and, for excavation of foundation pits, considered $H = (0.4\sim2.0)\ H_{QW\max}$; Mei et al. [12] calculated the loess area in Xi'an and considered $H = (0.65\sim2.0)\ H_{QW\max}$; and Xiao et al. [34] analyzed 92 soft soil foundation pits in China, It is considered that there is $H = (0.2\sim2.5)\ H_{QW\max}$. In the saturated soft loess area studied in this paper, the ratio of the surface settlement to the lateral deformation of the diaphragm wall is within the range of Xiao's statistics, but it is smaller than other areas. This is due to the small settlement value of the soil caused by the replenishment of nearby water sources. It can be seen that the deformation of the foundation pit is not only related to soil quality, design, and construction factors, but the special environment of the area may also be an important factor, such as the water source near the test area.

4.4. Steel Support Axial Force Data Analysis. The fourth monitoring section has been used as the main section to analyze the variation of the axial force of each steel support with the excavation depth of the foundation pit, as shown in Figure 19. GZC1-4 indicates the axial force monitoring point of the first support section of the fourth section. Overall, the axial force of the first support is the smallest and gradually stabilized, and the axial force of the second, third, fourth, and fifth steel supports increases with the increase in the excavation depth. This is due to the increased pressure on the front side due to excavating the deep foundation pit. When the soil is unloaded, the passive earth pressure is reduced, and the continuous underground wall along with the pit is deformed, causing the axial force of the steel support to increase.

It can be seen from the figure that the emergence of axial force has the characteristics of "immediateness," and it is generated synchronously with the excavation. At the same time, as the excavation stage S1 progresses, the axial force at GZC1-4 slowly increases, but in stages S3 and S4, as the depth of the excavation further increases, the axial force at GZC2-4 and GZC3-4 appears to be decreasing. The significant increase is due to the "depth effect" of the excavation.

Figure 20 shows the change curve of the measured axial force of the steel support over time. It can be seen from the figure that the steel support can withstand a large axial force in a short time after installation and remains relatively stable. The supporting axial force of the measuring points of the first and eighth cross sections is slightly smaller than that of the fourth cross section. The axial force of the second steel support still increased significantly after installing the third steel support. It indicates that the second steel support shared part of the earth pressure that the third steel support should bear, resulting in the second steel support. The supporting shaft force exceeds its standard value. The axial force of the third steel support tends to be stable after the fourth support is installed. This is because the fourth support shares the lateral pressure of the third steel support. It can be seen from the figure (b) that when the 5^{th} steel support starts to work, the axial force of the 4^{th} support increases faster. This is because the 5^{th} support does not share the pressure of the 4^{th} support. The continued excavation of the pit caused the 4th support to bear greater lateral pressure of the soil, causing the axial force of the 4^{th} support to exceed its standard value. This is because the preadded axial force of the steel support is too large, and the supporting structure does not work together effectively.

Therefore, the preadded axial force of the steel support should be reasonable so that the steel support, the steel purlin, and the ground connecting wall are in contact with each other without any joint force. In the early stages of

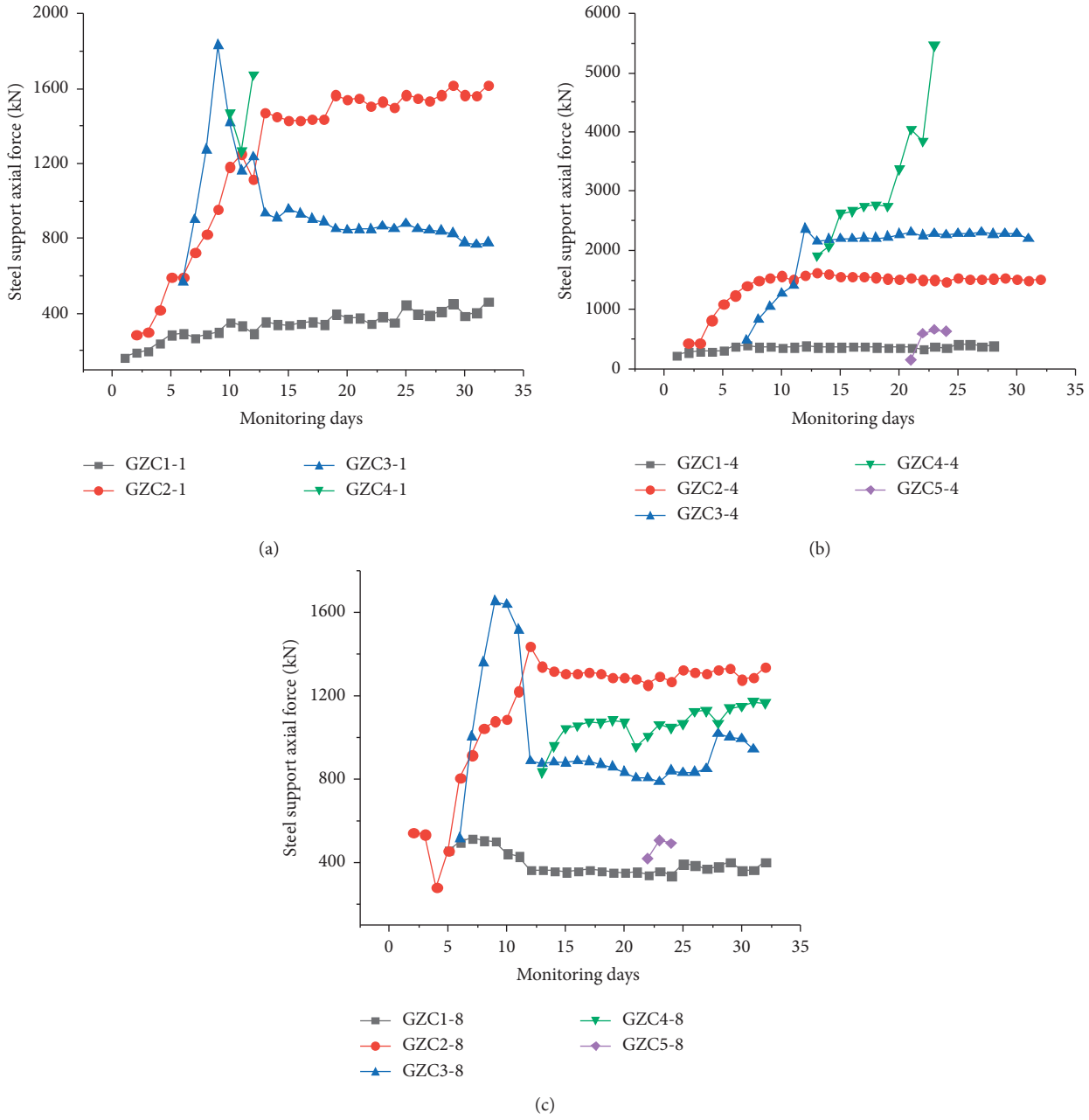

Figure 20: Axial force change curve of steel support. (a) Change of axial force of steel support at No. 1 section measuring point. (b) Axial force change of steel support at No. 4 section measurement point. (c) Change of axial force of steel support at No. 8 section measuring point.

excavation, it is necessary to speed up the deployment of the steel support and increase the monitoring frequency to prevent the smaller number of tracks from increasing the value of the rest of the supporting axis.

4.5. The Relationship between the Horizontal Deformation of the Diaphragm Wall and the Axial Force of the Steel Support. During the excavation process of the foundation pit, the horizontal displacement of the ground-connecting wall is closely related to the axial force of the steel support. The axial force value of GZC2-4 and the horizontal displacement value of the wall corresponding to the depth are analyzed. As shown in Figure 21, the wall deformation along the pit is set as a negative value. It can be clearly seen from the figure that the axial force of the steel support decreases with the decrease of the horizontal displacement of the ground connecting wall, and shows a certain correlation ($R^2 = 0.76$), and the fitting curve generally shows a downward trend. This is because when the earth pressure outside the pit is too large and the wall deforms into the pit, the steel support needs to bear too much earth pressure and the axial force is large. As the wall gradually deforms along the outside of the pit, the steel support does not need to bear it. With a high earth pressure, the axial force gradually decreases.

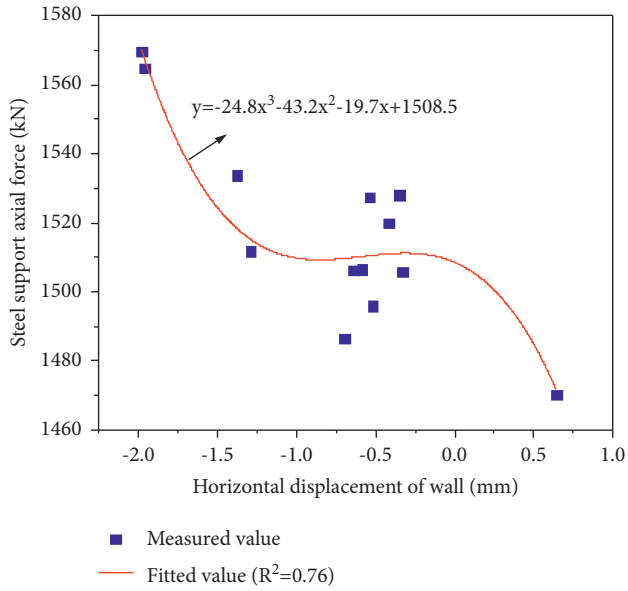

Figure 21: The relationship between wall displacement and steel support axial force.

Therefore, during the construction process, it is necessary to speed up the deployment of steel supports, share the axial force of other steel supports, and avoid excessive deformation of the continuous underground wall.

5. Discussion

This paper systematically analyzes the changes in the groundwater level, ground settlement, horizontal displacement of the diaphragm wall, and the axial force of the steel support during the excavation of deep foundation pits. At the same time, it analyzes the changes in the ground surface settlement, the horizontal deformation of the diaphragm wall, and the excavation depth. The relationships between the surface settlement and the horizontal deformation of the diaphragm wall and the axial force of the steel support provide a reference for the construction plan for the deep foundation pit excavation in the saturated soft loess area. However, due to the particularity of the location of the deep foundation pit and the construction and other factors studied in this paper, it does not apply to all the deformation modes of the deep foundation pit in the saturated soft loess area.

6. Conclusions

Based on a field test of a high-water level deep foundation pit in saturated soft loess, through real-time monitoring and data analysis, the conclusions are as follows:

(1) The average value of the maximum surface uplift outside the pit is 0.0111%H, and the average value of the maximum surface subsidence is 0.0096%H and the average value of the distance between the maximum vertical deformation position of the surface and the edge of the foundation pit is 0.341H, both of which are smaller than the average value obtained by statistics of Xi'an loess area. The main distribution range of the maximum surface subsidence is $0.24H_{QW\max}$~$1.37H_{QW\max}$, which is smaller than the statistical scope of Xi'an loess area. Therefore, in the design and construction stages, the impact of water sources needs to be considered.

(2) The average value of the maximum horizontal displacement along the ground wall outside the pit is 0.0133%H, and the average value of the maximum along the pit is 0.0141%H, both of which are smaller than the average value obtained by statistics of Xi'an loess area. Therefore, during the construction process, the steel supports of the axial force should be reasonable to make the supporting structure effectively work together; speed up the construction speed of the bottom slab, the inverted brace, the floor frame beam, and the sidewall frame beam to restrain the deformation of the continuous underground wall.

(3) The supporting axial force sometimes tends to increase and decrease. Meanwhile, the steel supporting axial force declines with the decrease of the ground connecting wall deformation. Therefore, the preadded axial force of the steel support should be reasonable to make the internal support uniformly stressed to avoid local instability. In the early stage of excavation, it is necessary to speed up the deployment of the steel support and increase the monitoring frequency.

Nomenclature

L: Distance between the measuring point and the center of the foundation pit (m)
L_z: The distance between the maximum vertical deformation point of the surface and the edge of the pit (m)
H: Excavation depth (m)
H_z: Surface subsidence (m)
$H_{z\ \max}$: Maximum surface settlement (mm)
H_{QW}: Cumulative horizontal displacement of diaphragm wall (mm)
$H_{QW\max}$: Maximum horizontal displacement of underground diaphragm wall (mm)
H_{XD}: Relative horizontal displacement of diaphragm wall (mm).

Data Availability

The data used to support the findings of this study are available from the first author upon request.

Conflicts of Interest

The authors declare that there are no conflicts of interest regarding the publication of this paper.

Acknowledgments

This work was supported by the Key Research and Development Project of Shaanxi Province (No. 2021SF-523).

References

[1] Z. Liu, *Loess Mechanics and Engineering*, Shaanxi Science and Technology Press, China, 1997.

[2] Y. Zhang, Z. Song, X. Weng, and Y. Xie, "A new soil-water characteristic curve model for unsaturated loess based on wetting-induced pore deformation," *Geofluids*, vol. 2019, Article ID 1672418, 14 pages, 2019.

[3] Y. Xue, X. Zhang, S. Li et al., "Sensitivity analysis of loess stability to physical and mechanical properties: assessment model," *International Journal of Geomechanics*, vol. 19, no. 7, pp. 06019012.1–06019012.10, 2019.

[4] X. Wang, Y. U. Hongqin, C. Wang, and Y. Yang, "Study on control measures for subgrade settlement of high-speed railway in cold regions of western China," *Subgrade Engineering*, vol. 2017, no. 5, pp. 53–58, 2017.

[5] J. Qiu, Y. Qin, J. Lai et al., "Structural response of the metro tunnel under local dynamic water environment in loess strata," *Geofluids*, vol. 2019, Article ID 8541959, 16 pages, 2019.

[6] N. He, P. Li, S. Shao, J. Li, and Y. Jiao, "Ground settlement monitoring above Xi'an Metro tunnel through the saturated soft loess," *Journal of Earth Sciences and Environment*, vol. 34, no. 1, pp. 96–103, 2012.

[7] J. Yang, "Surface deformation induced by tunnel construction in saturated soft loess strata," *Journal of Xi'an University of Science and Technology*, vol. 38, no. 1, pp. 91–98, 2018.

[8] S. M. Haeri and A. A. Garakani, "Hardening behavior of a hydro collapsible loessial soil," in *Proceedings of the 15th Asian Regional Conference on Soil Mechanics and Geotechnical Engineering*, Fukuoka, Japan, November 2016.

[9] G. W. Clough, "Construction induced movements of in situ walls," *Design & Performance of Earth Retaining Structures*, ASCE, Cornell, 1990.

[10] M. Long, "Database for retaining wall and ground movements due to deep excavations," *Journal of Geotechnical and Geoenvironmental Engineering*, vol. 127, no. 3, pp. 203–224, 2001.

[11] C. Moormann, "Analysis of wall and ground movements due to deep excavations in soft soil based on a new worldwide database," *Soils and Foundations*, vol. 44, no. 1, pp. 87–98, 2004.

[12] Y. Mei, Y.-L. Li, X.-Y. Wang, J. Wang, and C.-M. Hu, "Statistical analysis of deformation laws of deep foundation pits in collapsible loess," *Arabian Journal for Science and Engineering*, vol. 44, no. 10, pp. 8347–8360, 2019.

[13] J. Yang and D. Kong, "Deformation of deep and large foundation pit in soft soil of Fuzhou Subway," *Arabian Journal of Geosciences*, vol. 13, no. 2, 2020.

[14] Y. Mei, D. Zhou, X. Wang et al., "Deformation law of the diaphragm wall during deep foundation pit construction on lake and sea soft soil in the yangtze river delta," *Advances in Civil Engineering*, vol. 2021, no. 11, Article ID 6682921, 11 pages, 2021.

[15] Y. Zhou, X. Wang, Y. Zhu, and S. Gao, "Seepage Stability analysis of deep foundation pit of lanzhou metro under the condition of water level reduction in collapsible loess," *China Railway Science*, vol. 38, no. 1, pp. 86–94, 2017.

[16] J. Ren, J. Ma, J. Bai, and K. Yang, "Research on the deformation laws of center pillar of metro station excavated by semi-covered method," *Journal of Railway Engineering Society*, vol. 34, no. 9, pp. 103–108, 2017.

[17] M. Liu, D. Zhang, F. Qian, and Y. Hou, "Wall and ground movements due to deep excavation of tianjin subway station," *DEStech International Conference on Transportation Infrastructure and Materials*, vol. 2017, Article ID 9944, 2017.

[18] Z. Ding, J. Jin, and T.-C. Han, "Analysis of the zoning excavation monitoring data of a narrow and deep foundation pit in a soft soil area," *Journal of Geophysics and Engineering*, vol. 15, no. 4, pp. 1231–1241, 2018.

[19] Z. Li, M. Han, Y. Li, L. Yang, and W. Liu, "Analysis on continuous deformation process of underground continuous wall of foundation pit of daliang station," *Chinese Journal of Underground Space and Engineering*, vol. 15, no. S1, pp. 367–375, 2019.

[20] K. Elbaz, S.-L. Shen, Y. Tan, and W.-C. Cheng, "Investigation into performance of deep excavation in sand covered karst: a case report," *Soils and Foundations*, vol. 58, no. 4, pp. 1042–1058, 2018.

[21] G. Wang, W. Chen, and Q. Nie, "Impacts of pit excavation on foundation piles in deep silty soil by centrifugal model tests," *Rock and Soil Mechanics*, vol. 41, no. 2, pp. 399–407, 2020.

[22] J. Xu, S. Yang, H. Wu, and L. Zhang, "Monitoring and numerical analysis of pile-anchor supporting structure for deep and large foundation pit in loess area," *Journal of Xi'an University of Architecture and Technology*, vol. 51, no. 4, pp. 517–524, 2019.

[23] W. Zhang, H. Li, Y. Li, R. Zhang, and H. Liu, "Effects of jet grouting slabs on responses for deep braced excavations," *Underground Space*, vol. 6, no. 4, 2020.

[24] D. W. Zhang, J. C. Shu, and J. P. Sun, "Observed deformation characteristics of a deep excavation for the spring area in Jinan, China," *Journal of Mountain Science*, vol. 14, no. 3, 2017.

[25] H. Di, H. Guo, S. Zhou, J. Chen, and L. Wen, "Investigation of the axial force compensation and deformation control effect of servo steel struts in a deep foundation pit excavation in soft clay," *Advances in Civil Engineering*, vol. 2019, no. 6, Article ID 5476354, 16 pages, 2019.

[26] M. Farzi, M. S. Pakbaz, and H. A. Aminpour, "Selection of support system for urban deep excavations: a case study in Ahvaz geology," *Case Studies in Construction Materials*, vol. 8, pp. 121–138, 2018.

[27] C. Wang, D. Ling, and H. Wang, "Influence of soft clay structure on pit excavation and adjacent tunnels," *Journal of Zhejiang University*, vol. 54, no. 2, pp. 264–274, 2020.

[28] C. Liu, F. Ji, G. Zheng, T. Liu, and Y. Liu, "Measurement and mechanism of influences of rainfall on supporting structures of foundation pits in soft soils," *Chinese Journal of Geotechnical Engineering*, vol. 42, no. 3, pp. 447–456, 2020.

[29] Y. M. A. Hashash, A. Osouli, and C. Marulanda, "Central artery/tunnel project excavation induced ground deformations," *Journal of Geotechnical and Geoenvironmental Engineering*, vol. 134, no. 9, pp. 1399–1406, 2008.

[30] R. B. Peck, "Deep excavations and tunneling in soft ground," in *Proceedings of the 7th International Conference on Soil Mechanics and Foundation Engineering*, Mexico, 1969.

[31] A. I. Mana, "Prediction of movements for braced cuts in clay," *Geotechnical Engineering*, vol. 107, 1981.

[32] C.-Y. Ou, P.-G. Hsieh, and D.-C. Chiou, "Characteristics of ground surface settlement during excavation," *Canadian Geotechnical Journal*, vol. 30, no. 5, pp. 758–767, 1993.

[33] J. H. Wang, Z. H. Xu, and W. D. Wang, "Wall and ground movements due to deep excavations in shanghai soft soils,"

Journal of Geotechnical and Geoenvironmental Engineering, vol. 136, no. 7, pp. 985–994, 2010.

[34] H. Xiao, S. Zhou, and Y. Sun, "Wall deflection and ground surface settlement due to excavation width and foundation pit classification," *KSCE Journal of Civil Engineering*, vol. 23, no. 4, pp. 1537–1547, 2019.

Hindawi
Advances in Civil Engineering
Volume 2022, Article ID 6845847, 12 pages
https://doi.org/10.1155/2022/6845847

Research Article

Study on Distribution Characteristics of Metro Stray Current and Evaluation of Cumulative Corrosion Effect

Shan Lin,[1] **Jing Zhang**,[2] **Xuehua Liu**,[2] **Xianwei Zhang**,[2] **Zhichao Cai**,[2] **and Xia Chen**[1]

[1]*Guangzhou Metro Design & Research Institute Co., Ltd., Guangzhou 510010, China*
[2]*School of Electrical and Automation Engineering, East China Jiaotong University, Nanchang 330013, China*

Correspondence should be addressed to Zhichao Cai; czchebut@foxmail.com

Received 14 October 2021; Accepted 13 December 2021; Published 10 January 2022

Academic Editor: Yuan Mei

Stray current directly affects the regular operation of electrical equipment and facilities in the subway DC traction power supply system. Therefore, it is worthwhile to study the stray current distribution characteristics during train operation and the quantitative corrosion of buried pipelines. This paper introduces the traction characteristics of power carriages and power wheelsets of subway vehicles into the DC traction process. A finite element model considering the dynamic distribution of stray current under the actual operation of subway vehicles is established. The interference characteristics of stray current and the contribution of power sources under the multiparticle model are analyzed. The rail insulation damage caused by long service time and the quantitative calculation of rail and buried pipeline corrosion is considered. The model results show that the stray current in the buried pipeline under the multiparticle model is more accurate and more suitable for the protection in the actual subway. The quantitative corrosion of the buried pipeline is stronger than the partial insulation damage environment when the rail is not insulated. The rail and buried pipeline corrosion at both ends of the insulation damage position is relatively severe. The stray current distribution model established in this paper gives full play to the solution advantages of the finite element method and provides a new idea for the quantitative calculation of buried pipeline corrosion.

1. Introduction

With the development of China's national economy and the promotion of urbanization, urban rail transit has been vigorously developed as an effective tool to alleviate traffic congestion. DC electric traction is adopted in urban rail transit systems such as subway and light rail. The train receives power through the pantograph or collector boots, and the rail is used to achieve reflux. In the initial stage of subway operation, the degree of insulation between the steel rail and the underground metal structure is relatively high, the rail-to-ground transition resistance is rather large, and the stray current leaking from the steel rail to the surrounding soil medium is also relatively small. However, with the increase of the working life of the subway, the rail-to-ground insulation performance of the rail decreases, and the stray current leaking from the rail to the surrounding soil medium will increase [1]. Therefore, the metro equipment that has been built and used for a long time is easy to lead to the corrosion of underground metal structures under the interference of rail overpotential and stray current [2–4].

According to the existing subway traction power supply system, domestic and foreign scholars have alleviated the leakage of rail overpotential and stray current by controlling rail return mode [5–7], blocking current leakage [8–15], and protecting affected structural parts [16–23]. For example, increasing the supply voltage is helpful to reduce the rail current [5]. The use of minimizing the distance between DC railway substations helps to shorten the leakage path of track current [5]. A fully insulated rail is installed as a special return rail to transfer the return current from the rail to the special return rail [6, 7]. Concrete sleepers, side column insulators, insulating clips, and rail cushions are used to insulate the track from the ground, blocking or reducing the leakage path of track current [8–10].

Therefore, this paper establishes the finite element distribution model of stray current to analyze the interference quantitatively. The operating parameters of actual subway vehicles are selected to be easy to measure and a dynamic stray current interference calculation example is proposed. The main contributions are as follows:

(1) Considering the current distribution and marshaling configuration inside the train, combined with the actual running state of the subway vehicle, the stray current leakage is analyzed when the bullet train carriage is used as the particle and the train wheel as the particle backflow. Furthermore, the contribution of the leakage degree of each power car provides reference information for additional protection measures such as cathodic protection.

(2) As part of the rail insulation is damaged in the section of the subway with long operating life, the influence of rail insulation damage on the distribution of stray current is analyzed, and the total current density and corrosion area of rail corrosion in the section are analyzed when the location of insulation damage and the size of the damaged area is different.

(3) According to the distribution of rail potential and current density of buried pipeline, the cathode area and anode area of the buried pipeline at any time are determined, and the relationship between current leakage position and buried pipeline corrosion under different conditions is analyzed.

The content of this paper is arranged as follows: Section 2 shows the theoretical analysis modeling process and solution process of corrosion current on the buried pipeline; Section 3 discusses the distribution characteristics of rail potential and stray current under the condition of multiparticle distribution; Section 4 gives the dynamic cathode and anode area changes of stray current, the corrosion accumulation of metal structures, and the insulation damage of some areas causing new stray current interference. Finally, Section 5 gives the conclusion.

2. Model Establishment and Solution

In urban rail transit, the typical configuration of the subway traction power supply system is shown in Figure 1. The power grid powers the subway system, and the main substation is reduced from AC110 kV to AC35 kV by the transformer. Then it is divided into two parts. One part is reduced by the rectifier transformer in the traction substation to AC 1180 v voltage and converted into DC1500V or (DC750V) through a 24 pulse rectifier circuit to supply power to the catenary. After the contact between the pantograph and catenary, it provides traction current to the train and drives the train to run. The other part is reduced to AC voltage of 380 V through the transformer of the station substation, which supplies power to the elevator, ventilation system, lighting, and other electrical equipment in the station.

This paper draws the traction current and running speed curve of the train based on the operational data of the Nanchang Metro Line 1 Metro Central Station to the Qiushui Square Station, as shown in Figure 2. The train has different traction currents at any time so that it can be regarded as a movable current source and the whole loop system as a constant electric field in the model.

2.1. Modeling. According to the analysis of the subway mentioned above power supply system, a finite element solution model including locomotives, stations, tracks, soil, and buried pipelines is established, as shown in Figure 3. The model mainly includes four parts: the construction of geometry, the addition of physical field, meshing, and post-processing. The geometric size of the soil domain is $1500 \times 150 \times 100$ m, the wheel radius is 0.5 m, and the setting size of steel rail is $1500 \times 0.5 \times 0.1$ m. The buried pipeline is located 30 m directly below the rail, with a length of 1500 m and a radius of 1 m. According to the above dimensions, a finite element model is established in COMSOL Multiphysics. Since the train has traction current at any time, the current module is added to treat the train as a current source, and the inner wheel of the train is the input boundary of the traction current as of the terminal of the model. The two ends of the subway section are set as the negative poles of the substation, which are directly grounded to study the distribution of stray current in the soil under the mobile current source and its corrosion effect on buried pipelines. The finite element method divides a continuous solution region into a set of element combinations. It uses the approximate functions of these elements to express the unknown positions of the solution domain. Therefore, the accuracy of the model solution depends on the precision of meshing. According to the computational accuracy and efficiency requirements, the solution domain of the model is divided into 30637 domain elements and 2068 boundary elements through free triangular meshes.

Since this paper considers the distribution of actual subway vehicles, in the process of establishing the model, if other parameters are the same, the multiparticle model 1 is based on the number of power cars in the subway train formation, and the multiparticle model 2 is based on the number of moving wheelsets of the train. The differences of each model are shown in Table 1.

The traction current flows into the wheel from the positive pole of the traction substation through the catenary, pantograph, high-speed circuit breaker, traction inverter, coupling, and gearbox. The wheel current distribution is shown in Figure 4. Since the traction current in Figures 4(a) and 4(b) has the same current size and different directions at the time of acceleration and deceleration, the current path in reflux is very different. At the time of train acceleration (when the current is positive), the traction current is transferred from the connection between the wheel and the axle to the tread where the axle is in contact with the rail. Most of the current is transmitted from both sides of the tread contact surface to the traction substations on the left and right sides through the rail, but very little of the current

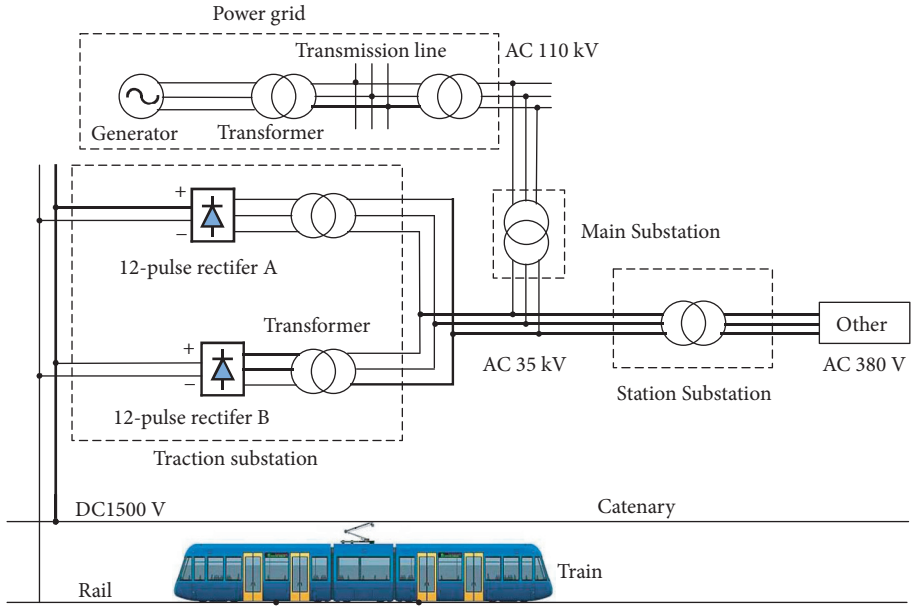

Figure 1: Schematic diagram of subway traction power supply system.

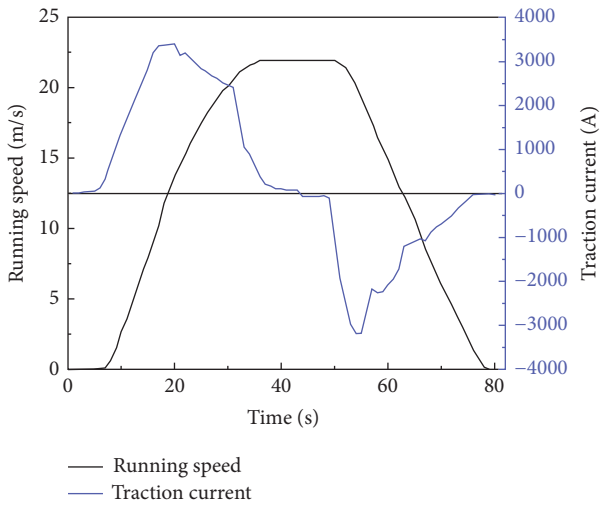

Figure 2: Train running speed and traction current.

leaks from the rail to the soil. At the time of train deceleration (due to the influence of current receiving power, the current is negative at this time), according to the principle of regenerative braking, most of the current is fed back to the positive pole of traction substation through catenary current, to reduce energy loss. However, very little of the current leaks into the soil from the rails, thus corroding the rails and buried pipelines.

Considering that the stray current distribution is a constant electric field problem, some simplifications and assumptions are made that the soil near the pipeline is uniformly distributed and the concentration gradient in the soil is ignored. The finite element method is used to solve the Maxwell equation, and the "AC/DC module" can solve the Maxwell equation.

Governing equation is

$$\begin{aligned} \nabla \times E &= 0, \\ \nabla \cdot J &= 0. \end{aligned} \tag{1}$$

The current density J in soil electrolyte obeys Ohm's law, and its constitutive relation is as follows:

$$J = \gamma E. \tag{2}$$

The interface conditions in the model meet

$$\begin{aligned} E_{1t} &= E_{2t}, \\ J_{1n} &= J_{2n}, \end{aligned} \tag{3}$$

where E represents the electric field strength, J represents the current area density, γ represents conductivity, E_t represents the tangential component of electric field strength, and J_n represents the normal component of current area density.

The soil and buried pipeline are set as constant conductivity, 1 E − 2 S/m and 1 E7 S/m, respectively. For simplicity, the conductivity of metals (such as rails, train wheels) is also set to 1 E7 S/m [24].

2.2. Solution of Corrosion Current Density of Metal Structures under Stray Current Interference. Due to the dynamic changes of underground metal potential during the subway operation period, the metal surface is easy to reach the primary conditions of electrochemical corrosion. Then the buried metal pipelines around the subway and the steel bars in the main structure of the station and section tunnels will be electrochemically corroded. Electrochemical corrosion will shorten the service life of metal pipelines and reduce the strength and durability of the subway's reinforced concrete [25–30].

When the dynamic stray current flows into the pipeline, the pipe section is called the cathode area and will not be corroded. However, cathodic polarization can increase soil

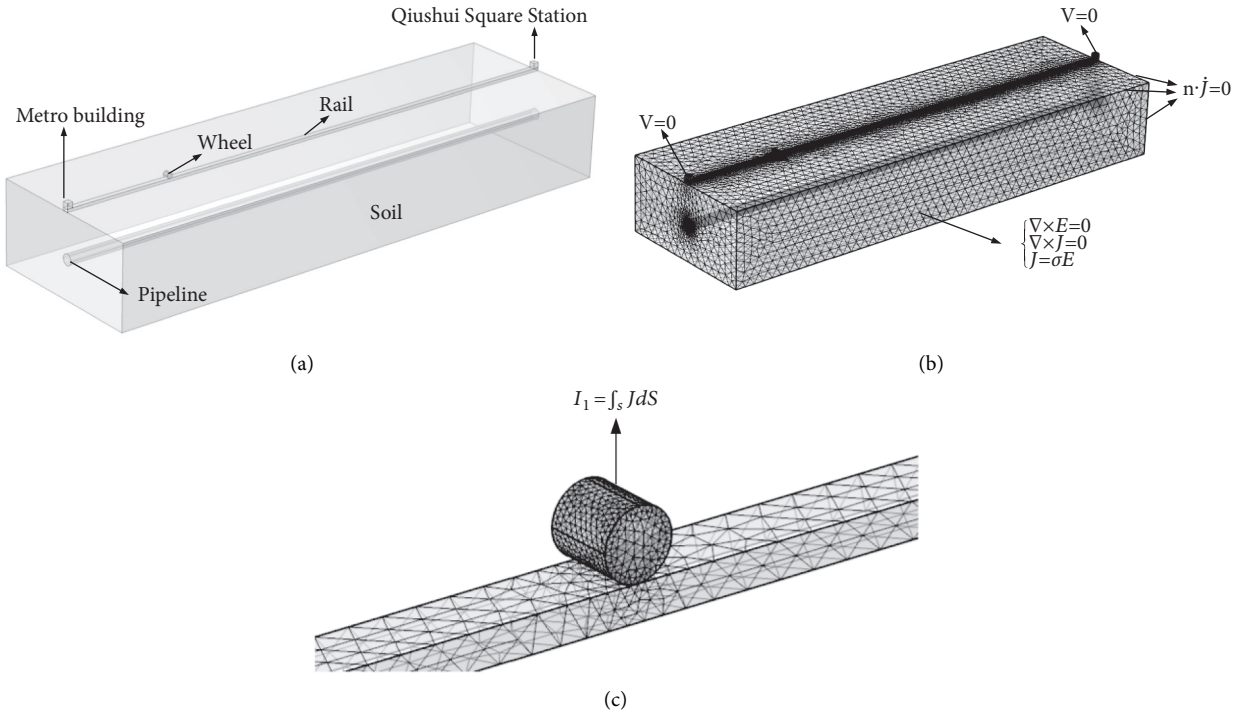

Figure 3: Finite element solution model. (a) Solid geometry diagram. (b) Overall meshing. (c) Local meshing.

Table 1: Modeling methods of different models.

Models	Modeling method
Single particle model	Regard the train as a whole as a particle.
Multiparticle model 1	According to the four-motion and two-drag grouping mode, each power car is regarded as a particle.
Multiparticle model 2	According to the fact that there are two switch machines in each power car to control four moving wheelsets, each wheelset is regarded as a particle.

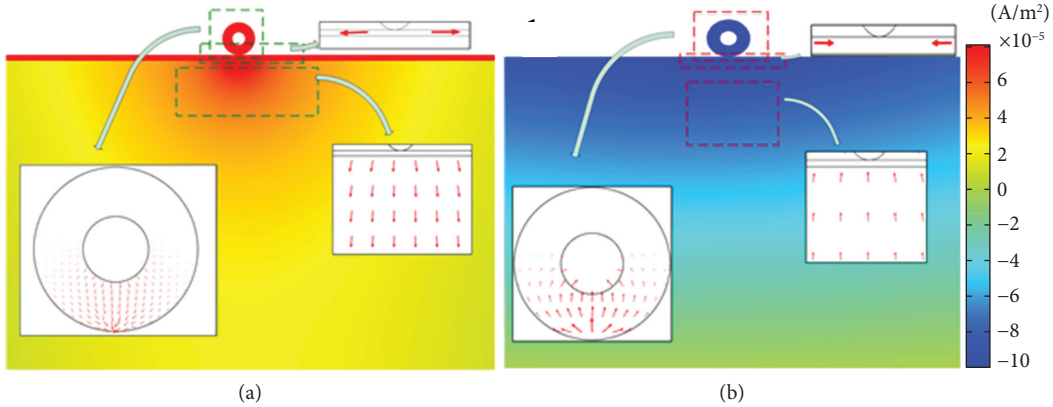

Figure 4: Traction current reflux path. (a) Positive traction current. (b) Negative traction current.

pH value (alkaline) around the damage point of the pipeline anticorrosion layer, which will reduce the adhesion of the anticorrosion layer and the peeling off of the anticorrosion layer. When the density of the DC stray current flowing into the pipeline is too high, it will cause the hydrogen evolution reaction, which may cause hydrogen embrittlement of high-strength pipes. In the area where the stray current flows out (anode area), electrons flow from the anode to the cathode,

while ions flow in the surrounding soil. The oxidation process leads to the dissolution or loss of metal. Therefore, stray current directly leads to the corrosion of steel bars and reduces the reinforced concrete. The service life of the structure is reduced. Since the stray current changes dynamically, there will be alternating changes of the cathode area and the anode area at the same position on the pipeline. It can be seen from Figure 5 that there are mainly two places where the traction current leaks: area A directly below the train during the operation of the subway vehicle and area D directly below the traction substation. At the same time, it is verified that both leakage current and stray current are dynamic changes, and the corrosion of rail and pipeline is interlaced. When electrochemical corrosion occurs at rail A, no corrosion occurs directly below the rail at the corresponding buried pipeline B.

The finite element model can calculate the leakage current density $i(t)$ of the buried pipeline. If the current density in the anode region is $i_1(t)$ and that in the cathode area is $i_2(t)$, the leakage current density of the buried pipeline can be satisfied.

$$i(t) = i_1(t) + i_2(t). \tag{4}$$

Since the current density in the cathode area will not corrode the buried pipeline, considering only the anode corrosion current density $i_1(t)$, the corrosion current density of the pipeline at each moment is $i_f(t)$:

$$i_f(t) = i_1(t). \tag{5}$$

The total current area density of (T) of the cumulative corrosion of the whole pipeline is

$$i_F(t) = \sum_{t=1}^{T} i_f(t) = \sum_{t=1}^{T} i_1(t), \tag{6}$$

where $T = 1s, 2s, \ldots, 83s$, T is the total operation time of the train in a single operation section.

Since all leakage currents are dynamic and the corrosion current density leaked from each rail and buried pipe is a function of time [9], we can define the time integral of the leakage corrosion current density $i_f(t)$ as the total leakage charge Q:

$$Q = \int_{t_1}^{t_2} i_f(t)\mathrm{d}t. \tag{7}$$

According to Faraday's law, the weight of rail corrosion metal is proportional to the total leakage charge [31], so the corrosion current density can be used as an objective parameter to evaluate rail corrosion indirectly.

3. Consider the Effect of Multiple Current Sources on Stray Current

Traditional stray current analysis models generally use a single-particle model (using a vehicle as a current source of particles), common in analytical solutions. Cai et al. [32] studied the influence of the subway track on the stray current of the ground transition resistance under the single-mass model. Xu [33] established a continuous track-drainage network-earth-buried pipeline based on the single-mass model and calculated the pipeline and earth resistance. Yang et al. [34] established a mathematical model of the rail potential distribution of the entire line based on the single-particle model, revealing the subway rail potential distribution law considering the edge effect of the finite boundary. However, simplifying the single-particle model for the train will affect the actual stray current distribution, so introducing a multiparticle model is considered. In a more optimized situation, a power car can be used as a particle current source (multiparticle model 1, considering the relative distance between the power cars) and a set of moving wheels as a particle current source (multiparticle model 2, viewing the close distance between the moving wheels), as shown in Figure 6. By comparing the three models, it is found that the rail potential and the trend distribution of stray current obtained by the calculation are consistent. However, the result of the single-particle solution is slightly larger than that of the multiparticle model, which may happen although the length between the motor cars is shorter than that of an interval, and it cannot be ignored that there still be an impact on the steel pipe potential and stray current. The same problem exists when considering the multiwheel situation. Because the multiparticle model is closer to the actual operation, the result is more relative to the existing subway system, making pipeline corrosion calculation and analysis more accurate.

According to the train formation of the subway vehicles of Nanchang Metro Line 1, the four power cars in the vehicles are concentrated in the central area. The relative distance maintains a car's length. Stray current leakage occurs in each power car, and the leakage position is consistent with the relative position of each carriage. The current is leaked to both sides. The buried pipeline produces the maximum stray current at the relative position between the carriage and the traction substation, as shown in Figure 6. Although the traction current gap in each carriage is minimal, the influence of each power car on the stray current of the whole buried pipeline is significantly different, as shown in Figure 7. Since the multiparticle model 1 analyzes the train carriage as a particle, the four particles from left to right are called power car 1, power car 2, power car 3, and power car 4, respectively. The train runs from left to right. In the initial stage of subway vehicle operation (traction state), the first power car (power car 4) in the forward direction of the subway vehicle has the most significant contribution and drives the train. In the stage of constant speed operation of subway vehicles, the contribution of each power car is the same to keep the train running at a constant speed. In the stop phase (braking phase) of subway vehicles, the fourth power car (power car 1) in the forward direction contributes the most. It is worth noting that the division of the areas mentioned above does not entirely correspond to the operating conditions of subway vehicles. However, the more stray current is indeed leaked from the power cars at both ends of the subway vehicles. In contrast, the stray currents leaked from other power cars are relatively minor. In the operation section, the power car closest to the middle

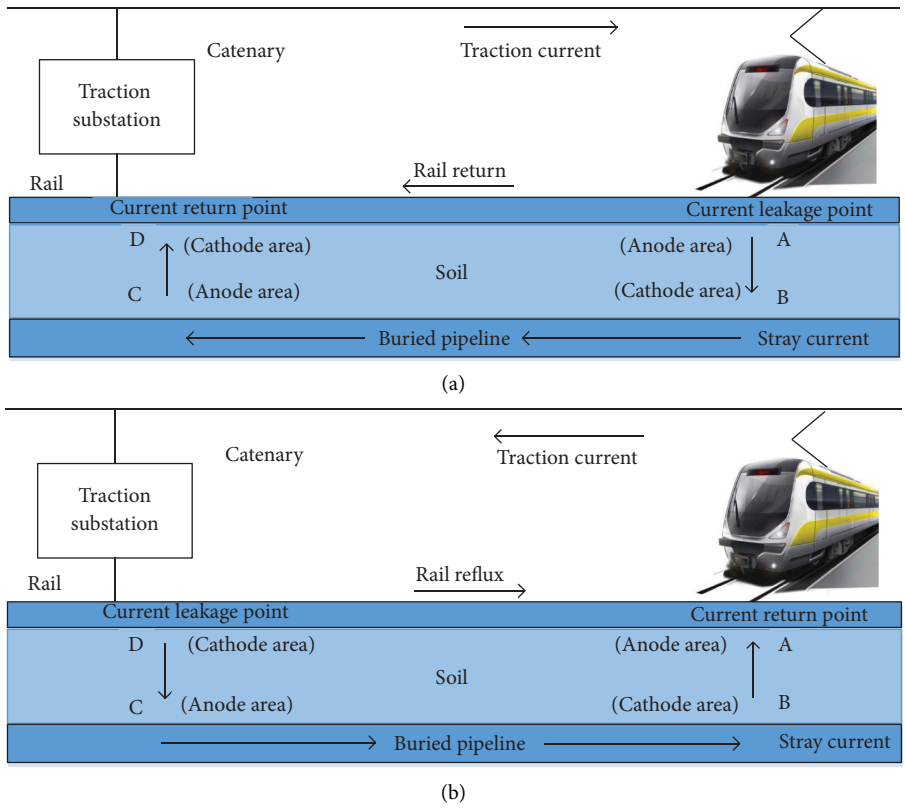

Figure 5: Electrochemical corrosion caused by stray current. (a) Train traction current is positive. (b) Train traction current is negative.

position will return more traction current to the traction substations on both sides through the rails. In contrast, other power cars will return most of the traction current to the traction substations on both sides through the rails. Therefore, a small part of the current leaked into the soil, causing the buried pipeline to be destroyed.

4. Effect of Rail Insulation Damage on Stray Current Distribution

4.1. Quantitative Analysis of Rail Corrosion under Stray Current Interference. Rail corrosion refers to the electrochemical corrosion of the rail at the leakage current, which leads to severe corrosion at the bottom of the rail, and the existing fasteners are not enough to make the corroded rail safely fixed on the sleeper. It is also noteworthy that there are dynamic changes in the position of rail corrosion; that is, where the subway vehicle runs, the relative position of its contact with the rail bottom will produce oxidation reaction and electrochemical corrosion. Theoretically, the wheel is in point-line contact with the rail, and the corresponding corrosion is also point-line corrosion. The oxidation reaction is mainly the loss of electrons, and the more significant the oxidation reaction rate, the greater the number of losses of electrons. Therefore, the more the traction current leaks, the more pronounced the electrochemical corrosion. The specific redox reaction equation is as follows:

$$\begin{aligned}
\text{anode: } & 2Fe - 4e^- = 2Fe^{2+}, \\
\text{cathode: } & 4H^+ + 4e^- = 2H_2\uparrow \text{(anaerobic acidic environment)} \\
& 4H_2O + 4e^- = 4OH^- + 2H_2\uparrow \text{(anaerobic environment)} \\
& O_2 + 2H_2O + 4e^- = 4OH^- \text{(aerobic alkaline environment)}
\end{aligned} \tag{8}$$

The analysis shows that the area of rail leakage current is related to the running state of the train without the insulation between rail and soil. When the train is in the acceleration state, the rail leakage current area is consistent with the contact area of the rail wheelset; when the train is in the deceleration state, the rail leakage current area is consistent with the substation area. When the isolation condition between rail and soil is applied, if damage occurs in a certain area, no matter where the subway vehicle is running, the breakage area or traction substation area will produce current leakage. Therefore, the electrochemical corrosion in the breakage area and the area near the substation will be more serious, as shown in Figure 8. Because the traction current flows in different directions at different times, the potential in the soil changes continuously. When the traction current is in the opposite direction, the potential change in the soil is also just the opposite. The protection of the insulating layer can better guide the loop current on the steel rail and collect it to the negative pole of the traction substation. The difference is that under the condition of no

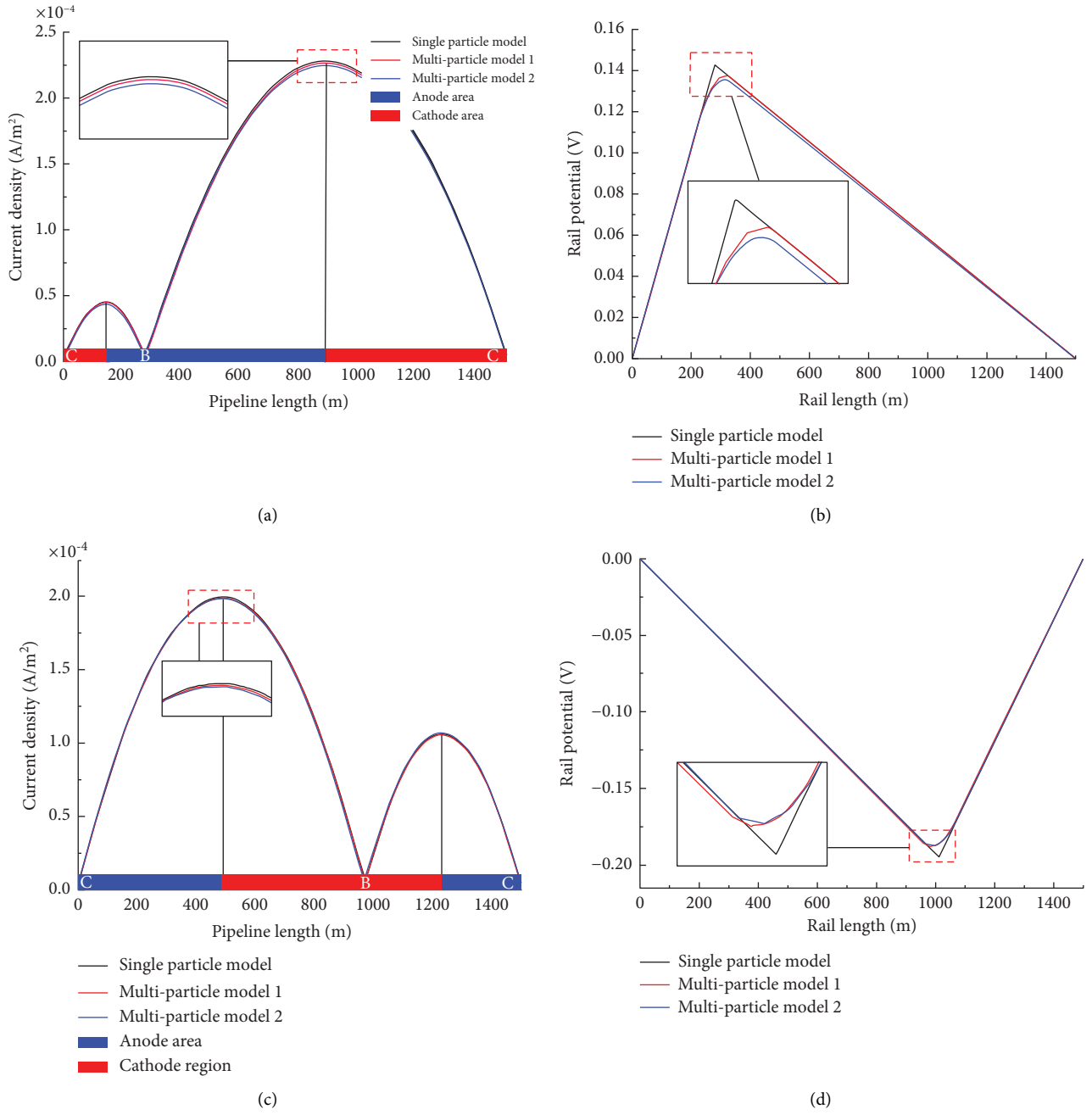

Figure 6: Analysis of the influence of each model on stray current and rail voltage. (a) Pipeline current density ($t = 20$ s). (b) Rail potential ($t = 20$ s). (c) Pipeline current density ($t = 55$ s). (d) Rail potential ($t = 55$ s).

insulation, the leakage area covers the whole rail, while under the condition of insulation, leakage always occurs in the insulation damage area, which accelerates the redox reaction there.

Figure 9 is a comparison diagram of rail corrosion current when the rail is without insulation and when the rail is insulated, but the insulation is damaged at different positions. At this time, the length of the rail damage is the same, and the position is different, as shown in Table 2. When the insulation is added to the rail, the leakage of current in the rail interval can be reduced obviously. When some physical or human factors damage the insulation layer at a specific position, it can be seen that the rail has apparent current leakage at the damaged position. The leakage current makes the oxidation rate of the rail more significant. It accelerates the corrosion of the damaged part of the rail, thereby leading to some hidden safety problems. The rail corrosion current is in a "concave" shape at both ends of the damaged insulation. Compared with the middle of the damaged position, there is more corrosion current leakage at both ends of the damaged insulation. This shows that at the junction of damaged and undamaged insulation, the corrosion current is the largest, leading to the most severe corrosion of the steel rail. Still, it reduces the corrosion of the rail near the traction substation

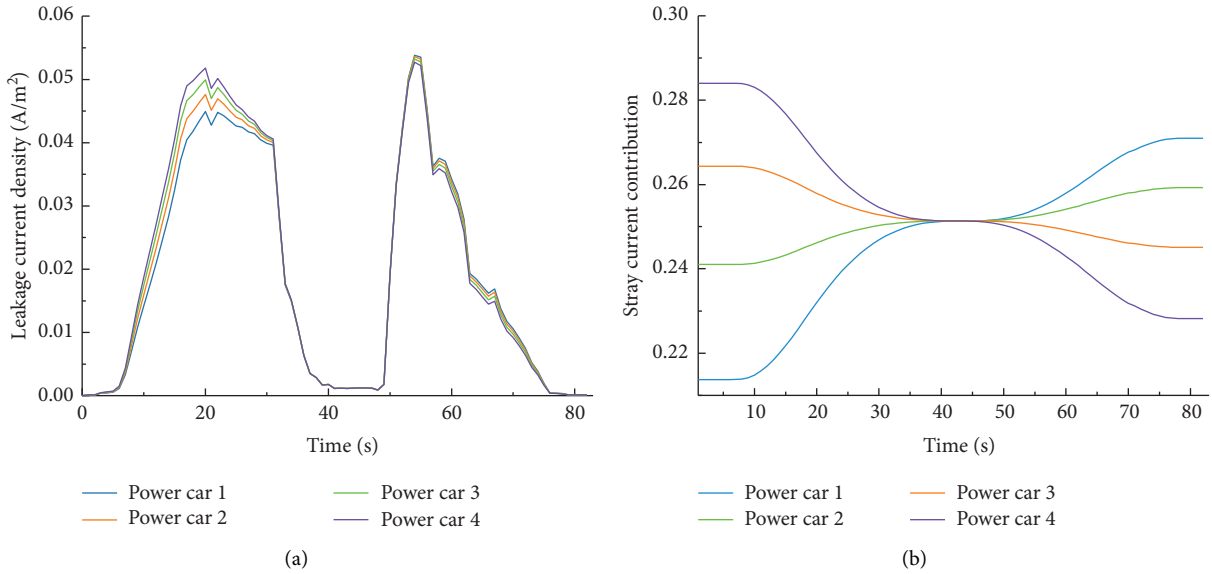

Figure 7: Analysis of the influence of each power car on stray current in the multiparticle model 1. (a) Leakage of each power car. (b) Contribution of power car.

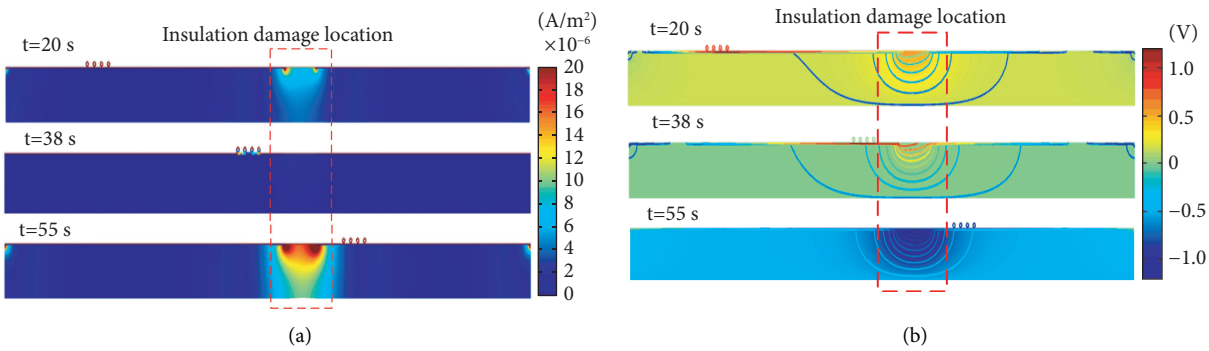

Figure 8: Distribution in soil at different times (when partial insulation is broken). (a) Current leakage. (b) Potential distribution.

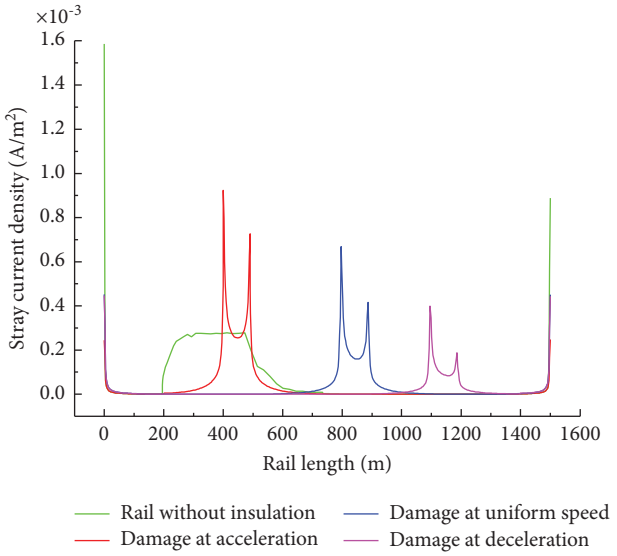

Figure 9: Total corrosion current density of rail under different conditions.

when the rail is not insulated. In the middle of insulation damage, the rail corrosion current is relatively small. When the train runs at both ends, the rail returns current first passes through the junction of insulation damage and sound insulation, resulting in most current leakage at the junction point. In contrast, the damage in the middle is relatively more minor. Affected by the distance and traction current, the current density of damaged rail corrosion is the acceleration, constant, and deceleration time in descending order. The corrosion current density of the rail near the traction substation is just the opposite of the corrosion current density of the damaged place.

If there is a damaged area of rail insulation, with the train running in this section, the damaged area's size is different, leading to the severity of rail corrosion. If the damaged area is tiny and approaches a point, all the stray current leaks at that point, resulting in severe damage to the rail. When the damaged area gradually becomes more extensive, the corrosion current of the rail will be slowed down, but the corrosion area of the rail will increase. As shown in

Table 2: Location and length parameters of rail insulation damage.

Type	Insulation damage location (m)	Insulation damage length (m)
Damaged acceleration	400–490	90
Damaged at constant speed	800–890	90
Damaged at deceleration	1100–1190	90
45 m damaged at acceleration	422.5–467.5	45
180 m damaged at acceleration	355–535	180

Figure 10, taking insulation damage of 45 m, 90 m, and 180 m as examples, as the damage area increases by multiples, the rail corrosion current gradually decreases. When the rail insulation is completely damaged, the corrosion current in the rail section reaches the minimum, but it changes. The corrosion current near the power station reaches its maximum.

4.2. Quantitative Analysis of Buried Pipeline Corrosion under Stray Current Interference. Pipeline corrosion refers to the corrosion problem caused by the stray current in the anode area of buried pipelines. Since the magnitude and direction of the stray current are constantly changing, it will cause dynamic DC stray current interference to the pipeline. At the same time, there are dynamic changes in the location and degree of corrosion of buried pipelines. Therefore, dynamic pipeline corrosion needs to be quantitatively analyzed.

Firstly, the buried pipeline is divided into cathode and anode regions. From the previous distribution of the stray current on the surface of the pipeline at a specific time, it can be seen that there are two peaks of the stray current on the surface of the steel pipe, corresponding to the critical value of the current inflow and outflow of the buried pipeline. When the current flows forward, the rail position corresponding to the inner side of the two wave crests is the cathode area, and the rail position corresponding to the outer side of the two wave crests is the anode area. Conversely, when the current flows in the reverse direction, the rail position corresponding to the inner side of the two wave peaks is the anode area, and the rail position corresponding to the outer side of the two wave peaks is the cathode area, as shown in Figures 6(a) and 6(c). Position B in Figure 6 is the position where the train is located, and position C is the position corresponding to the traction substation, which corresponds to the position in Figure 5.

By comparing noninsulated conditions and insulation damage, the size of the pipeline's cathode area and anode area is the same under noninsulated conditions. In the case of insulation damage, the cathode and anode areas of the pipeline have apparent size changes. When the traction current flows positively, the anode area is larger than the cathode area. On the contrary, the anode area is smaller than the cathode area. It can be concluded that when the traction current is positive, the anode area is inversely proportional to the width of insulation damage, and when the traction current is negative, the anode region is proportional to the width of insulation damage.

According to the division of the cathode and anode areas of the buried pipeline, the leakage current density of the

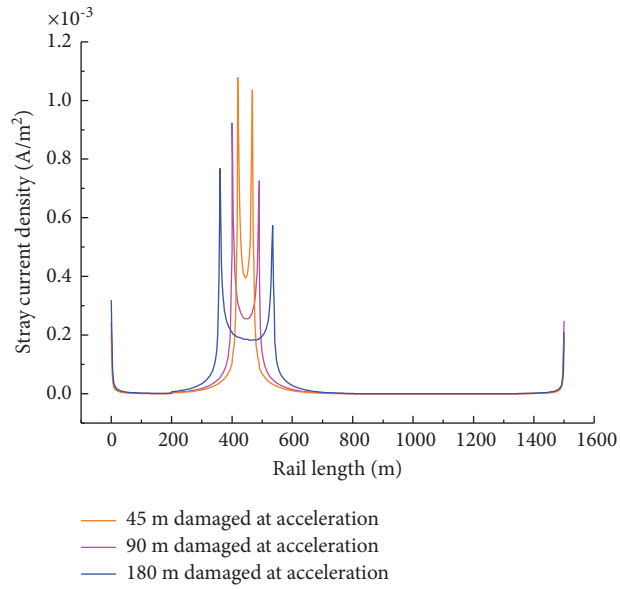

Figure 10: Corrosion current density of rail with different damage length.

anode area is accumulated. The total corrosion current density of the buried pipeline in the section is calculated, forming a dynamic cumulative electrochemical corrosion effect of stray current on the buried pipeline. The calculation flow chart is shown in Figure 11.

Since the calculation of the model can directly obtain the leakage current density in the buried pipeline, the leakage current density of the damaged pipeline at the acceleration is shown in Figure 12(a). According to the calculation process of the flowchart, the corrosion area of the buried pipeline and the corresponding corrosion current density can be obtained at each moment, and the corrosion current density of the buried pipeline damaged at the acceleration is shown in Figure 12(b). By superimposing the corrosion current density of the same area at each time, the corrosion area and the corresponding corrosion current density of the entire buried pipeline in the section can be obtained.

The calculation flow chart of the corrosion current density of the buried pipelines is shown in Figure 13. The corrosion situation of the stray current at the specific location of the pipeline can be obtained, which is convenient for the reasonable evaluation of the quantitative corrosion caused by the subsequent stray current. When there is no insulation, the cathode and anode areas of the pipeline are theoretically the same. The cumulative analysis of the dynamic pipeline corrosion current density shows that there is still a large oxidation reaction interference area, which is

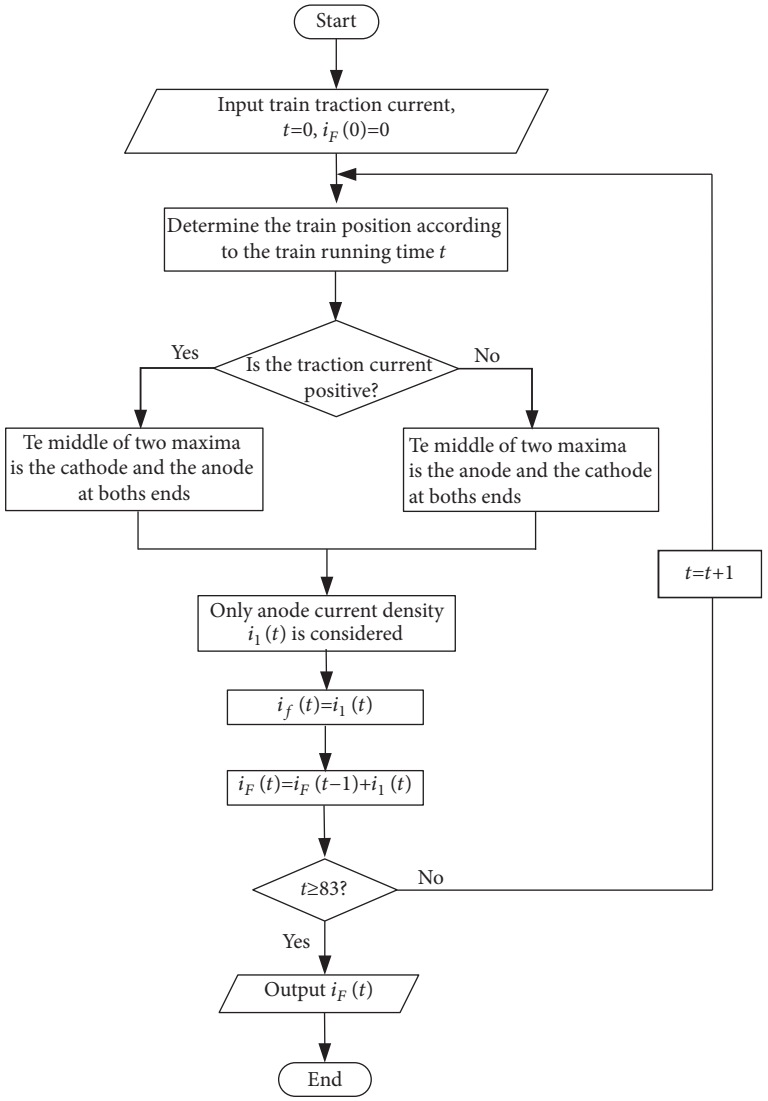

Figure 11: Flowchart for calculation of total corrosion current density of buried pipelines.

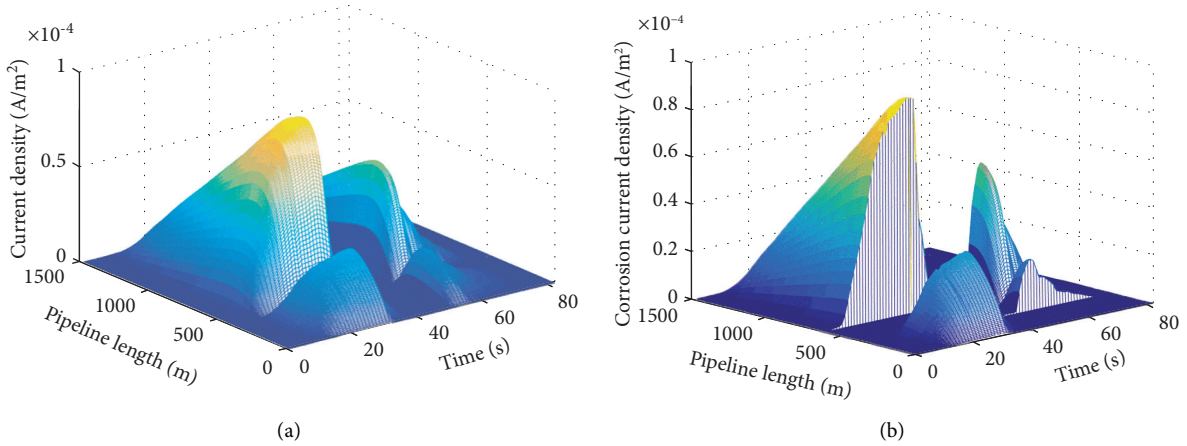

Figure 12: Distribution of current density on the pipeline in the section. (a) Leakage current density of pipeline damaged at acceleration. (b) Corrosion current density of pipeline damaged at acceleration.

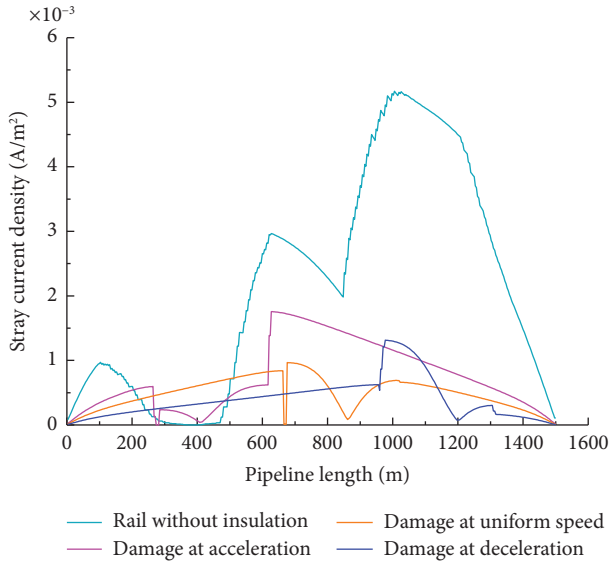

Figure 13: Corrosion of buried pipelines in train operation section.

significantly more potent than the insulation. The dynamic corrosion accumulation caused by insulation damage is relatively fixed; both ends show an increasing trend towards the damaged area. There are rapid increases and decreases around the damaged position. Compared with the insulation damage that occurred in different areas, corrosion accumulation is different, and the cumulative corrosion in the deceleration area is slight.

5. Conclusions

The distribution of stray current is affected by multiparameter variables. This paper considers the distribution and operation of actual subway vehicles and the electrochemical corrosion caused by the failure of relevant mitigation measures to use the stray current finite element model to guide the engineering practice and ensure subway vehicles' safe and stable operation. The main conclusions are as follows:

(1) The multiparticle model is more consistent with the actual running state of subway vehicles than the single-particle model. After solving and comparing, the stray current calculated by the multiparticle model is relatively small and has low pipeline potential. At the same time, the front wheel leakage of the train during the starting phase makes a more significant contribution to the stray current, and the rear wheel leakage during the braking phase makes a more substantial contribution to the stray current.

(2) Rail corrosion is a dynamic corrosion process, and the rail corrosion in the insulation damaged area is more severe than that without insulation. In contrast, the rail corrosion near the substation is just the opposite.

(3) The corrosion of the buried pipeline is closely related to the damaged insulation area. The corrosion of pipelines in areas without damaged insulation is more severe than in some damaged insulation areas. Therefore, buried pipelines' corrosion degree and corrosion area can be reasonably evaluated by effectively detecting damaged insulation areas to guide targeted excavation and maintenance.

Data Availability

The data (experimental results) used to support the findings of this study are included in the article.

Conflicts of Interest

The authors declare that there are no conflicts of interest regarding the publication of this paper.

Acknowledgments

This work was supported in part by the Natural Science Foundation of China under grant 51807065 and in part by the Key Research and Development Plan of Jiangxi Province under grant 20202BBEL53015.

References

[1] S. A. Memon and P. Fromme, "Stray Current Corrosion and Mitigation: a synopsis of the technical methods used in dc transit systems," *IEEE Electrification Magazine*, vol. 2, no. 3, pp. 22–31, 2014.

[2] S. W. Chen, M. Y. Qin, D. X. Liu, and J. H. Gong, "Study on erosion risk prediction of wet gas gathering and transmission pipeline in high sulfur gas field," *Natural gas and oil*, vol. 33, no. 1, pp. 80–83+12, 2015.

[3] Z. F. Zhao, *Study on Dynamic Evaluation Method of Safety for Corrosion protection System of Long-Distance Pipeline*, Xi'an University of Science and Technology, Xi'an, China, 2017.

[4] A. L. Cao, *Study on Stray Current Corrosion protection of Buried Metal Pipelines*, Chongqing University, Chongqing, China, 2010.

[5] M. Niasati and A. Gholami, "Overview of stray current control in DC railway systems," in *Proceedings of the International Conference on Railway Engineering-Challenges for Railway Transportation in Information Age*, pp. 1–6, Hong Kong, China, March 2008.

[6] Y. T. Zhang, "Traction power supply technology for the fourth return track of urban rail transit," *Modern urban transit*, vol. 4, pp. 8–10+125, 2011.

[7] C. Goodman, J. Allan, J. Jin, and K. Payne, "Single pole-to-earth fault detection and location on a fourth-rail DC railway system," *IEE Proceedings - Electric Power Applications*, vol. 151, no. 4, pp. 498–504, 2004.

[8] D. F. Yan, N. Y. Liu, P. B. Yuan, J. Shu, and Y. E. Li, "Corrosion of buried steel pipelines by stray current in Metro maintenance base and protective measures," *Corrosion & Protection*, vol. 34, no. 8, pp. 739–742, 2013.

[9] D. Paul, "DC stray current in rail transit systems and cathodic protection [history]," *IEEE Industry Applications Magazine*, vol. 22, no. 1, pp. 8–13, 2016.

[10] I. Cotton, C. Charalambous, P. Aylott, and P. Ernst, "Stray current control in DC mass transit systems," *IEEE Transactions on Vehicular Technology*, vol. 54, no. 2, pp. 722–730, 2005.

[11] Z. M. Zhang, *Study on protection Measures against Stray Current in Metro*, Southwest Jiaotong University, Chengdu, China, 2015.

[12] N. M. J. Dekker, "Stray current control-an overview of options [DC traction systems]," *IEE Seminar on DC Traction Stray Current Control - Offer a Stray a Good Ohm?* pp. 8-810, 1999.

[13] J. Zhu and C. Q. Zhu, "Study on the distribution of stray current and rail potential in multi-section of urban rail transit," *China Science and Technology Information*, vol. 11, pp. 90-91, 2020.

[14] K. Yu, *Study on Simulation of Metro Stray Current Based on DEGS*, Southwest Jiaotong University, Chengdu, China, 2014.

[15] X. H. Han, W. Liu, and S. F. Jie, "Calculation of cross-sectional area of metro stray current collection network," *Urban Mass Transit*, vol. 18, no. 10, pp. 98–101+105, 2015.

[16] L. Huang, G. F. Du, J. Wang, and J. Tian, "Simulation study on dynamic drainage and rail potential control of urban rail reflux system," *Railway Standard Design*, vol. 63, no. 10, pp. 152–158, 2019.

[17] G. Du, J. Wang, X. Jiang, D. Zhang, L. Yang, and Y. Hu, "Evaluation of rail potential and stray current with dynamic traction networks in multitrain subway systems," *IEEE Transactions on Transportation Electrification*, vol. 6, no. 2, pp. 784–796, 2020.

[18] J. Gu, X. Yang, T. Q. Zheng, Z. Shang, Z. Zhao, and W. Guo, "Negative resistance converter traction power system for reducing rail potential and stray current in the urban rail transit," *IEEE Transactions on Transportation Electrification*, vol. 7, no. 1, pp. 225–239, 2021.

[19] G. F. Du, C. L. Wang, J. H. Liu, G. X. Li, and D. L. Zhang, "Effect of over zone feeding on rail potential and stray current in DC mass transit system," *Mathematical Problems in Engineering*, vol. 2016, Article ID 6304726, 2016.

[20] H. Z. Li, "Calculation of rail potential and stray current based on centralized parameter model of reflux system," *Modern urban transit*, vol. 6, pp. 20–23, 2020.

[21] T. T. Ke, J. M. Fang, Y. H. Qian, and Z. B. Peng, "Effects of metro stray current on cathode protection of buried metal pipelines," *Urban Mass Transit*, vol. 20, no. 3, pp. 90–93, 2017.

[22] K. Zakowski, K. Darowicki, A. Jazdzewska, S. Krakowiak, M. Gruszka, and J. Banas, "Electrolytic corrosion of water pipeline system in the remote distance from stray currents-Case study," *Case Studies in Construction Materials*, vol. 4, pp. 116–124, 2016.

[23] X. Hao and D. L. Li, "New risk to buried steel pipe anti-corrosion system caused by DC stray current of rail transit," *Urban Georgia*, vol. 3, pp. 12–17, 2016.

[24] Z. C. Cai, X. W. Zhang, and J. Zhang, "Research on theoretically modelling and quantitatively calculating stray current corrosion in a subway system," *International Journal of Electrochemical Science*, vol. 2020, no. 15, pp. 6626–6644, 2020.

[25] H. R. Wang, *Design of Stray Current Monitoring System for Urban Rail Transit*, Southwest Jiaotong University, Chengdu, China, 2007.

[26] S. R. Allahkaram, M. Isakhani-Zakaria, M. Derakhshani, M. Samadian, H. Sharifi-Rasaey, and A. Razmjoo, "Investigation on corrosion rate and a novel corrosion criterion for gas pipelines affected by dynamic stray current," *Journal of Natural Gas Science and Engineering*, vol. 26, pp. 453–460, 2016.

[27] A. O. S. Solgaard, M. Carsana, M. R. Geiker, A. Küter, and L. Bertolini, "Experimental observations of stray current effects on steel fibres embedded in mortar," *Corrosion Science*, vol. 74, pp. 1–12, 2013.

[28] Y.-S. Tzeng and C.-H. Lee, "Analysis of rail potential and stray currents in a direct-current transit system," *IEEE Transactions on Power Delivery*, vol. 25, no. 3, pp. 1516–1525, 2010.

[29] Z. Chen, D. Koleva, and K. van Breugel, "A review on stray current-induced steel corrosion in infrastructure," *Corrosion Reviews*, vol. 35, no. 6, pp. 397–423, 2017.

[30] L. Bertolini, M. Carsana, and P. Pedeferri, "Corrosion behaviour of steel in concrete in the presence of stray current," *Corrosion Science*, vol. 49, no. 3, pp. 1056–1068, 2007.

[31] J. G. Yu, "The effects of earthing strategies on rail potential and stray currents in DC transit railways," in *Proceedings of the 1998 International Conference on Developments in Mass Transit Systems Conf. Publ. No. 453)*, pp. 303–309, London, UK, April 1998.

[32] L. Cai, J. G. Wang, and Y. D. Fan, "Influence of the track-to-earth resistance of subway on stray current distribution," *High Voltage Engineering*, vol. 41, no. 11, pp. 3604–3610, 2015.

[33] J. P. Xu, "Analysis of urban rail transit stray current in buried pipeline and protective measures," *Urban Mass Transit*, vol. 20, no. 7, pp. 60–64, 2017.

[34] X. F. Yang, H. K. Wang, and Q. L. Zheng, "Influence of finite boundary fringe effect on the rail potential in DC traction power supply system," *Journal of Beijing Jiaotong University*, vol. 44, no. 3, pp. 1–11, 2020.

Hindawi
Advances in Civil Engineering
Volume 2021, Article ID 7703359, 10 pages
https://doi.org/10.1155/2021/7703359

Research Article

A Principal Component Analysis Control Chart Method for Catenary Status Evaluation and Diagnosis

Shan Lin,[1] **Liping Liu**,[1] **Meiwan Rao**,[1] **Shu Deng**,[1] **Jiaxin Wang**,[2] **Wenfan Zhong**,[2] **and Li Lun**[2]

[1]*Guangzhou Metro Design&Research Institute Co., Ltd., Guangzhou 510010, China*
[2]*School of Electrical and Automation, EastChina Jiaotong University, Nanchang 330013, China*

Correspondence should be addressed to Li Lun; 664313727@qq.com

Received 20 October 2021; Accepted 13 December 2021; Published 24 December 2021

Academic Editor: Yuan Mei

To make accurate and comprehensive evaluation of the catenary and diagnose the causes of the catenary fault, a method of catenary state evaluation and diagnosis based on the principal component analysis control chart was proposed, which can make full use of the multidimensional detection parameters of the catenary. The principal component analysis was used to reduce the dimension of catenary parameters, the principal component T^2 control chart was calculated to show the change of principal component of catenary state data, the residual SPE control chart was calculated to show the change of their correlation, and the contribution rate control chart was calculated to show the cause of abnormal state data. The method can not only transform the multidimensional detection parameters of the catenary into a statistic to realize the simple and intuitive evaluation of the catenary state but also can accurately determine the cause of the abnormal state, so as to provide technical support for the targeted condition-based maintenance of the catenary.

1. Introduction

As the only power supply line for electrified railway, catenary's working environment is harsh, and there is no backup for it, once there is a fault, it will lead to the outage of electrified railway, which will have a huge impact on the railway operation. As a special power supply line, catenary has the following characteristics:

(1) Operating environment is unique. Catenary is erected along the railway, exposed to the air, and is subject to the high-speed impact of locomotive pantograph, the space environment, climate environment, and working environment are unique compared to ordinary transmission lines, which makes the catenary more prone to failure and is greatly affected by the external environment.

(2) There is no backup for catenary. Due to the particularity of the catenary operating environment, there is no backup for catenary, Once the catenary is abnormal, it will lead the electrified railway to fail, resulting in huge economic losses.

(3) There is electromechanical compound effect for catenary. As a complex mechanical structure, the catenary's main function is to ensure a good and stable power supply, it needs to maintain structural stability under various mechanical loads and electrical shocks, thus to provide a good and stable current to the electric locomotive.

(4) There are moving loads for catenary. The pantograph of electric locomotive gets energy by sliding through the catenary, the load of the catenary fluctuates with time, and its position moves dynamically.

The statistical data show that the failure of the traction power supply system is mainly caused by the catenary failure, which accounts for more than 90% of the failure of the traction power supply system [1]. In order to avoid safety and economic losses caused by catenary failures, it needs to maintain the catenary in good working condition. Accurate

evaluation and diagnosis of the catenary status are the prerequisites for realizing the maintenance of the catenary and keeping the catenary in good condition.

The state detection of catenary includes static detection and dynamic detection. Static detection is a routine detection of manual use of portable detection equipment. Dynamic detection measures the parameters of the catenary under the actual operation state by the detection equipment installed on the special detection vehicle.

Static detection is carried out manually, which is intensive, time-consuming, inefficient, and is limited by the time of the skylight. A multifunctional laser measuring instrument was proposed in [2] for the static detection. The multivision technology was proposed to determine the catenary according to the image characteristics captured by the camera and to analyse the pantograph catenary components through intelligent image recognition [3].

Since the catenary is a flexible mechanical suspension system, the pantograph will cause the catenary to rise, so the dynamic parameters of the catenary are different from the static parameters. In the 1950s, Germany and Japan began to develop catenary detection vehicles, which installed various sensors and other equipment on the roof of locomotives, so as to detect the pull-out value and height under dynamic conditions when the train was running [4–6]. With the rapid development of high-speed railways, the relationship between the pantograph and the catenary has gradually become complicated, the catenary detection parameters have also expanded from the height and pull-out value to the pantograph contact force, the vertical acceleration of the pantograph head, and the off-line rate.

China proposes to build a traction power supply safety detection and monitoring system (6C system), which aim to achieve comprehensive detection and monitoring of the traction power supply system in all directions and full coverage [7–10]. The catenary information obtained by the 6C system is more diversified, in addition to the traditional geometric detection parameters of the catenary, it also includes various high-definition pictures, videos, and infrared detection information, and this unstructured information can be processed to extract the structural information of the catenary.

It can be seen that with the development of detection technology, the detection parameters of catenary become more and more comprehensive. How to effectively use these detection data to comprehensively and accurately evaluate the state of the catenary has become a new problem.

At present, the single-threshold comparison method is used to evaluate the state of catenary, which compares each parameter with the corresponding standard value to determine whether a certain parameter of the catenary exceeds the standard [11]. Commonly used catenary parameters include pull-out value and height [12], as well as dynamic parameters such as height difference, hard point, and contact force [1, 13]. With the increasing number of catenary detection parameters, this single-parameter comparison method is inefficient in judgment, and the judgment method is simple, which cannot meet the needs of comprehensive evaluation of the multidimensional parameters of the catenary. At the same time, the single-parameter comparison method does not consider the correlation between the catenary parameters, and there may be conflicting judgment results in some conditions [14].

Different detection parameters reflect the state of the same catenary from different respects. The comprehensive evaluation of the multidimensional parameters can obtain a more comprehensive and accurate evaluation result of the catenary status. For example, the operation quality index CQI was proposed to evaluate the operation quality of the catenary [15], but the index does not consider the influence degree difference of different parameters. On the basis of CQI, [16] used the analytic hierarchy process to determine the weight of each indicator, but it need to specify the importance of each indicator manually, which was highly subjective. In order to use the objective law embodied by the catenary parameters, the entropy method was proposed to determine the weight through the law embodied by the change of the catenary parameters [17, 18], and the fuzzy comprehensive evaluation method was proposed to evaluate the state of the catenary comprehensively. A combination method that combines subjective and objective methods to perform hybrid calculations on the weights of indicators in [19–21]. The above method can determine the degree of influence of catenary parameters on the state of the catenary from a subjective or objective perspective, but the calculation is complicated, and the results are not intuitive enough to reflect the inherent relationship between the catenary parameters. For this reason, [22] carried out cluster analysis on the catenary detection parameters and performed linear regression on each type of data, so as to obtain the mathematical model of the catenary detection parameters, and judge the state of the catenary based on the regression model. The normal cloud model was proposed in [23, 24] to process the detection index, solve the problem of ambiguity and randomness of the evaluation index, and establish a comprehensive evaluation model of the catenary operating state. The set pair analysis method was proposed to determine the degree of connection between each evaluation index and the health status level [25]. These methods can carry out a graded evaluation of the catenary status, but the evaluation results cannot reflect the cause of the abnormal status, so they cannot provide targeted guidance for the catenary maintenance.

Normally, the detection parameters of the catenary fluctuate around its standard value, and there is a certain correlation between the parameters. When the state of the catenary is abnormal, the state parameters of the catenary will deviate from the standard value. At the same time, due to the abnormality of the catenary structure, the original correlation of the catenary parameters will be destroyed. Therefore, the degree of deviation of the catenary detection parameters from the standard value and the change in the correlation between the catenary detection parameters can reflect the abnormality of the catenary status.

Multivariate statistical analysis is a method of comprehensive analysis of multidimensional data, which can analyse the statistical distribution rules and interrelationships of multidimensional parameters. The multivariate statistical

control chart based on multivariate statistical analysis is a commonly used quality management tool [26]. It can directly reflect the change process of detection parameters in graphical form and comprehensively monitor, control, analyse, and evaluate the process with multivariate parameters [27]. This paper combines principal component analysis with multivariate statistical control charts and uses principal component analysis to reduce the dimensions of the multidimensional state parameters of the catenary. By obtaining the principal component space and residual space of the catenary detection parameters, the principal component T^2 control chart and the residual SPE control chart of the catenary detection parameters on this basis are established. The main element T^2 control chart and the residual SPE control chart are used to comprehensively evaluate the status of the catenary and analyse the reasons for the abnormal status of the catenary. The results obtained can be used for targeted guidance on the maintenance of the catenary.

2. Multivariate Statistical Analysis of Catenary Status Based on Principal Component

2.1. Principal Component Analysis. The detection parameters of the catenary are numerous and related to each other. In order to reduce the complexity of processing the catenary detection data and reduce the computational workload, principal component analysis is used to simplify and compares the catenary detection data. The original data space is transformed into the main element subspace and the error subspace to achieve the purpose of data dimensionality reduction. Among them, the principal component subspace is the principal component, which contains most of the data information; the error subspace is the space orthogonal to the principal component subspace and represents the degree of deviation of the data from the principal component subspace [28].

The steps to transform the catenary detection data into the main element subspace and the error subspace are as follows:

(1) Standardize the test data. Due to the differences between the dimensions of each parameter lead to too large deviations between the data, it is necessary to standardize the detection parameters first to obtain the standardized detection data X;

(2) Calculate the correlation coefficient matrix:

$$\sum = X \cdot X^T. \tag{1}$$

(3) Calculate the principal components and load matrix. Find the characteristic equation:

$$\left| \sum -\lambda I \right| = 0. \tag{2}$$

Among them, I is the identity matrix. Solve the p eigenvalues and their corresponding eigenvectors and arrange the eigenvalues in descending order: $\lambda_1 \geq \lambda_2 \geq ,\ldots, \geq \lambda_p$, where p is the dimension of the detection parameter.

(4) Determine the number of principal components of the principal component subspace according to the cumulative contribution rate. When the cumulative sum of eigenvalues is greater than a certain specified value C_R, the selected data information of the k principal components can already include most of the data information, that is, satisfy:

$$\sum_{l=1}^{k} \left(\frac{\lambda_l}{\sum_{i=1}^{p} \lambda_i} \right) \geq C_R. \tag{3}$$

(5) Determine the load matrix P and the principal component space t. The selected eigenvectors corresponding to the k principal components form the load matrix P, and the principal component space t of the detection data is expressed as

$$t = XP. \tag{4}$$

(6) Calculate the score matrix. The score matrix $\widehat{X}$ is the projection of the standardized data X in the principal component space t:

$$\hat{X} = tP^T. \tag{5}$$

Since there is an error between the projection of the data in the principal component space and the actual data, that is, there is an error subspace E in the actual model space and the principal component subspace, the original data can be expressed as

$$X = \hat{X} + E. \tag{6}$$

According to (5) and (6), the error space E under the action of the principal component space:

$$\begin{aligned} E &= X - \widehat{X} \\ &= X - tP^T \\ &= X - XPP^T. \end{aligned} \tag{7}$$

It can be seen from (7) that the principal component space reduces the p-dimension detection parameters of the original data to k-dimension, and there is no correlation between the data. The remaining (p-k) dimensional data constitute the error subspace E, which has not undergone principal component transformation, and E contains the correlation information of the detection parameters.

2.2. Evaluation of Catenary Status Based on Principal Components Control Chart. The control chart is a quality control tool that can monitor and diagnose the process. In order to display the catenary status more intuitively and reflect the development trend of the catenary status, the principal component analysis and the multivariate statistical control chart are combined to obtain the multivariate statistical control chart based on the principal component analysis, which includes principal component T^2 control chart,

residual SPE control chart, and principal component contribution control chart [29].

The main component T^2 control chart uses the T^2 statistics to reflect the change of the main metadata, which can realize the status judgment of the main metadata of the detected data. The SPE control chart uses the residual SPE statistics for statistical testing, which reflects the degree of deviation of the data from the pivot space and can reflect the changes in the correlation between the data. The principal component contribution control chart calculates the contribution rate of each parameter at the abnormal point to the T^2 statistic and the SPE statistic, which can reflect the cause of the abnormality and play a diagnostic role. Different from other types of control charts, the principal component analysis control chart can not only reflect the changes in state data but also accurately diagnose the cause of the abnormality when the state is abnormal, so as to provide guidance for maintenance.

2.2.1. Principal Component T^2 Control Chart. The principal component T^2 control chart is a statistical control chart that monitors the principal components in the principal component space based on the T^2 statistics [30]. It can reflect the change trend and the degree of deviation of the principal components after the dimension reduction of the catenary detection parameters and reflect the change of the data in the principal component space.

Based on the definition of Hotelling T^2 statistic, for the ith detection group, its principal component T_i^2 statistic is expressed as

$$T_i^2 = t_i \Lambda^{-1} t_i'. \tag{8}$$

Among them, t_i represents the principal component of the ith group, Λ represents the diagonal matrix composed of the eigenvalues of the selected k principal components. Since the principal component and the original data satisfy (4), it can be expressed in the form of the original data and load matrix:

$$T_i^2 = X_i P \Lambda^{-1} P^T X_i^T. \tag{9}$$

According to (8) and (9), it can be seen that the principal component T^2 control chart is a manifestation of the change of principal component data in the principal component space on the basis of eliminating the correlation between the detection parameters of the catenary.

The control limit of the T^2 control chart is expressed as

$$T^2UCL = \frac{k(m-1)}{m-k} F_{1-\alpha}(k, m-1). \tag{10}$$

Among them, $F_{1\text{-}\alpha}(k,\ m-1)$ represents the number of principal components of the first degree of freedom k, the second degree of freedom is $m-1$, m is the number of detection parameter groups, and the confidence is the F distribution of α. When $T_i^2 > T^2\text{UCL}$, it means that the main component data fluctuate beyond the normal range, and the catenary status is abnormal.

2.3. Residual SPE Control Chart. The SPE control chart is a control chart that reflects the change of the error between the k principal component information and the p parameter information of the catenary detection parameters [31], which includes the change of the correlation between the catenary detection parameters.

Once the SPE control chart is abnormal in the evaluation process, it means that the deviation between the data and the principal component space is too large at this time, and the data are abnormal. Since the SPE control chart is an error value formed by integrating all parameters, the SPE control chart can not only monitor the deviation of the data relative to the principal element space but also detect the change in the internal correlation of the data. For the ith sample, the SPE statistics are calculated as

$$\begin{aligned} Q_i &= E^T E \\ &= X_i^T \left(I - PP^T\right)^T \left(I - PP^T\right) X_i. \end{aligned} \tag{11}$$

It can be seen from (11) that the Q_i statistic reflects the degree to which the data deviates from the pivot space and at the same time reflects the change in the correlation between the data. The control limit of the SPE control chart is [32]:

$$QUCL = \theta_1 \left[\frac{z_{1-\alpha} h_0 \sqrt{2\theta_2}}{\theta_1} + \frac{\theta_2 h_0 (h_0 - 1)}{\theta_1^2} + 1 \right]^{1/h_0}. \tag{12}$$

Among them, $\theta_i = \sum_{j=n+1}^{p} \lambda_j^i (i = 1, 2, 3)$, $h_0 = 1 - 2\theta_1\theta_3/3\theta_2^2$, $z_{1-\alpha}$ is the $1-\alpha$ quantile of the Gaussian distribution. When $Q_i > QUCL$, it means that the non-principal component part has a large deviation, and the principal component model is out of control and needs to be adjusted.

When the status of the catenary is abnormal, the status parameters of the catenary will shift, and the correlation between the parameters will also change, which will cause the statistics of the T^2 control chart and SPE control chart to exceed the limit. Therefore, the main component T^2 control chart and the residual SPE control chart can be used to judge the status of the catenary.

3. Catenary Status Diagnosis Based on Contribution Rate Control Chart

The T^2 control chart and SPE control chart can reflect the abnormality of the catenary status, but cannot find out the cause of the abnormality. The contribution control chart calculates the sum of the contribution rate of each parameter at the abnormal point to the abnormality, so as to determine the cause of the abnormality [29].

The abnormality in the T^2 control chart is caused by the principal component, and the contribution value of the jth detection parameter X_j is

$$\text{CONTT}_j^2 = \sum_{l=1}^{k} P_{jl} X_j \lambda_l^{-1}. \tag{13}$$

Among them, CONTT_j^2 represents the contribution rate of the jth detection parameter to the principal component

T^2, P_{jl} represents the value of the lth principal component of the jth detection parameter in the load matrix P, and λ_l represents the eigenvalue corresponding to the lth principal component.

For the SPE control chart, the contribution rate at the abnormal point is the error square value at the fault point, and the contribution rate of the jth detection parameter to the SPE statistics is

$$\mathrm{CONTSPE} = \left(X_j^T\left(I - \mathrm{PP}^T\right)\right)^2. \tag{14}$$

The higher the contribution rate of the parameter, the greater the impact on the abnormality of the fault, so the cause of the abnormality of the catenary status can be determined based on this.

Therefore, the establishment of the principal component analysis control chart is divided into two processes. First of all, the detection data are used to construct a principal component analysis control chart model that can correctly evaluate the status of the catenary, determine the number of principal components required, and calculate the control limits of the T^2 control chart and the SPE control chart. Then, on the basis of the control chart, the detection data of other sections of the catenary is analyzed and evaluated, and the corresponding principal component contribution control chart is drawn for the over-limit point to diagnose the cause.

4. Case Analysis

Take the detection data of a certain section of the catenary and use the multivariate statistical control chart to evaluate and diagnose the state of the catenary. Select the lead height $X1$, the pull-out value $X2$, the height difference $X3$, the hard point $X4$, and the contact force $X5$ in the detection parameters as the detection parameters for judging the state of the catenary and constitute the detection parameter $X = (X1, X2, X3, X4, X5)$. The changes of 25 groups of detection parameters of a certain section of catenary are shown in Figure 1. The red line in the figure is the allowable value range determined in accordance with the current "High-speed Railway Catenary Operation and Maintenance Rules".

Table 1 shows the standardization value of the catenary detection parameters in this section.

Calculate the eigenvalues and eigenvectors of the standardized data and arrange them in the descending order of eigenvalues. Calculate the cumulative sum of different eigenvalues, take the cumulative sum criterion $C_R = 85\%$, and the cumulative contribution rate of the first three principal components is 87%. Therefore, the number of principal components is determined to be three, and only the first three principal components can include most of the information in the analysis, so as to achieve the purpose of dimensionality reduction.

According to (9) and (11), the dot values of T^2 control chart and SPE control chart are calculated, as shown in Table 2.

Given the confidence level $\alpha = 0.01$, it is calculated according to (10) that $T^2UCL = 13.50$, calculate that $\theta_1 = \sum_{j=4}^{5}\lambda_j = 0.65$, $\theta_2 = \sum_{j=4}^{5}\lambda_j^2 = 0.29$, $\theta_3 = \sum_{j=4}^{5}\lambda_j^3 = 0.14$, $h_0 = 1 - 2\theta_1\theta_3/3\theta_2^2 = 0.25$. According to (12), the SPE control limit is calculated as $QUCL = 0.61$. Plot the dot values and control limits of the principal component T^2 control chart, SPE control chart, and conventional multivariate T^2 control chart mentioned in this article in the same graph, and the multivariate statistical control chart of the catenary obtained is shown in Figure 2.

It can be seen from Figure 2 that the multivariate statistical control chart can integrate the multidimensional detection parameters of the catenary into a statistical quantity and visually display it in the form of graphics, which makes it easier to judge the state of the catenary. For this section of the catenary, the statistics of its state parameters are all within the control limit, indicating that the detection data X are in a controlled state, and the state of this section of the catenary is normal. At the same confidence level, the principal component T^2 control chart in this paper retains the core principal components and is more sensitive to the fluctuation of the detection parameters than the multivariate T^2 control chart.

Select the detection data of this section of the catenary in another time period and draw the corresponding principal component analysis control chart, as shown in Figure 3.

It can be seen from Figure 3 that the statistics of the 13th group of the T^2 control chart are abnormal, and the statistics of the 13th and 25th groups of the SPE control chart are abnormal. The 13th set of data is abnormal in both the principal component subspace and the error subspace, indicating that the state reflected in this set of data is abnormal and needs to be adjusted. The abnormality of the 25th group of statistics reflects that the data have a large deviation from the principal component space, the correlation between the data has undergone abnormal changes, and the contact network status is abnormal and needs to be adjusted.

In order to find out the reasons for the abnormality of statistics in the 13th and 25th groups, the contribution rate of the abnormal parameter is calculated as shown in Figure 4.

As can be seen in Figure 4, the hard point and height difference in the 13th group have a larger contribution rate, and the 25th group hard point and the leading height have a larger contribution rate. Based on this, it is judged that the state at the position of the catenary reflected by the 13th group of statistics is abnormal, and the factors that cause the abnormal state at this point are hard point and height difference. The factor causing the abnormality of the 25th group of statistics is the change in the correlation between the hard point and the height difference.

Combined with the actual detection parameter changes, the analysis in Figure 1 shows that the principal component analysis control chart does not need to analyse the detection parameters in each detection group separately and can comprehensively evaluate all the detection parameters to evaluate the catenary status. Not only it is more sensitive to data fluctuations, it can detect abnormalities in advance, and it can also detect abnormalities caused by parameter out-of-limits and changes in related relationships. The principal component analysis control chart can not only reflect the

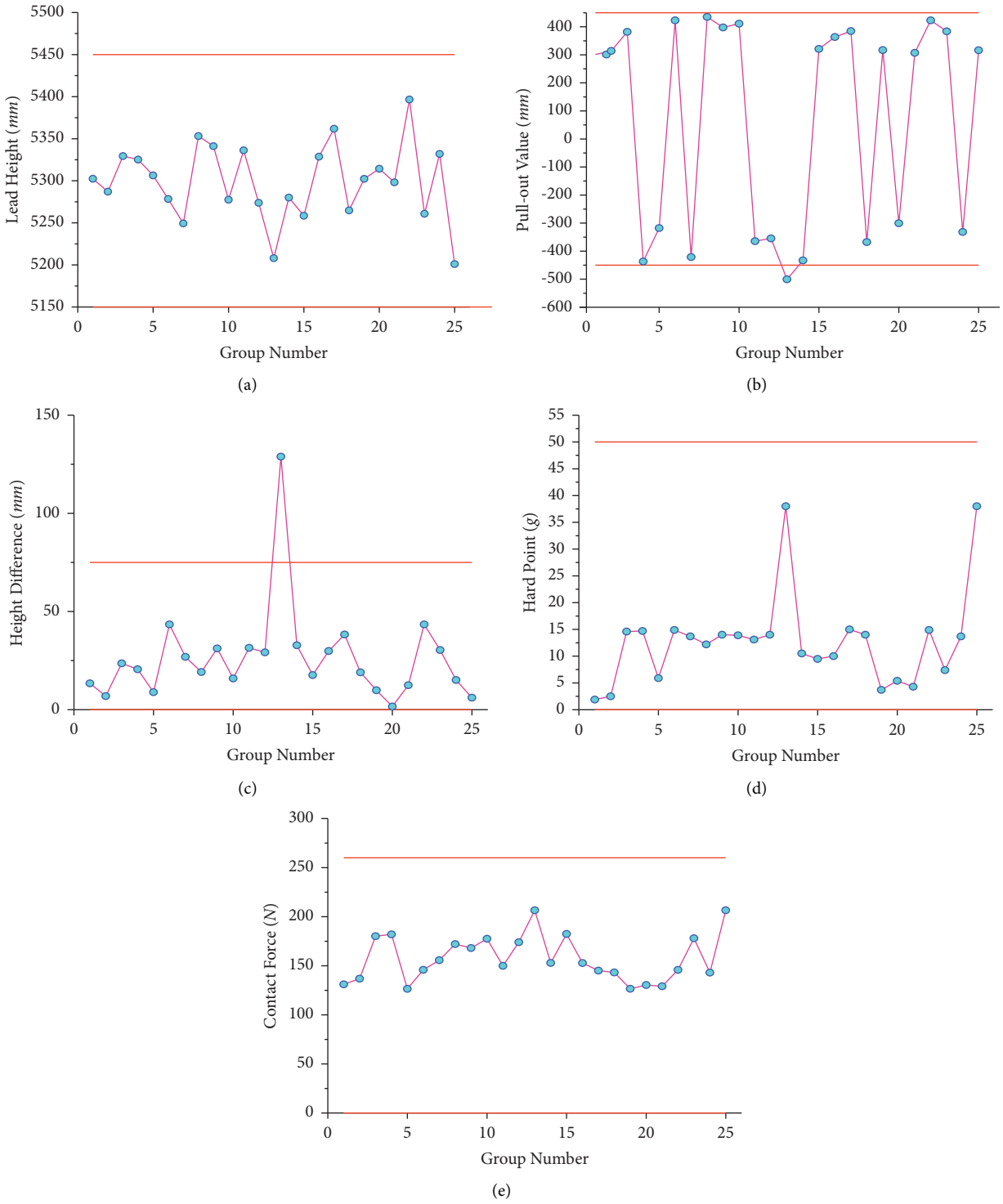

Figure 1: Changes of catenary parameters of one section. (a) Lead Height/mm; (b) pull-out value/mm; (c) height difference/mm; (d) hard point/(g); (e) contact force/(N).

Table 1: Standardized data of the catenary detection parameters in this section.

X1	X2	X3	X4	X5
0.33	0.92	−0.68	−0.68	−0.96
0.40	0.84	−0.95	−1.00	−1.05
0.09	−0.73	−0.79	−0.88	−0.67
1.19	−0.98	−0.72	−0.49	−0.71
−0.60	0.87	0.54	−0.60	−0.63
0.42	0.92	1.93	2.11	−0.36
−0.22	−0.71	−0.99	0.18	0.79
1.64	−1.15	0.55	2.39	1.38
−0.56	1.18	0.14	−0.21	−0.26
0.44	−0.76	−1.32	−0.83	−0.70
0.47	−0.78	−0.91	−0.95	−0.43
0.27	−0.74	−0.53	−0.86	−1.04
−0.08	1.03	0.23	0.70	2.81
−0.27	−1.11	−0.43	−0.24	0.75
0.96	1.14	1.53	0.25	−0.06
−1.00	−1.16	0.23	−0.23	0.73
−1.68	−1.22	1.87	0.19	−0.30
−2.05	−0.93	0.11	−0.06	0.29
1.42	1.17	−0.27	0.05	0.78
0.87	1.00	1.11	0.36	−0.29
−2.17	−1.07	1.34	2.55	2.14
−1.09	1.28	1.01	0.08	−0.07
0.36	0.88	−0.87	−0.73	−0.99
0.49	0.82	−0.92	−0.74	−0.36
0.36	−0.72	−1.22	−0.38	−0.80

Table 2: Rated value of T^2 control chart and SPE control chart.

Group no.	T^2	Q	Group no.	T^2	Q
1	3.40	0.14	14	1.61	0.11
2	2.42	0.12	15	3.15	0.17
3	4.13	0.18	16	1.80	0.20
4	5.72	0.21	17	6.36	0.43
5	2.11	0.01	18	4.63	0.02
6	7.31	0.49	19	2.97	0.00
7	1.86	0.13	20	2.40	0.00
8	9.68	0.01	21	9.46	0.16
9	2.00	0.31	22	2.18	0.03
10	2.91	0.07	23	3.10	0.26
11	1.59	0.07	24	1.32	0.52
12	2.49	0.00	25	2.90	0.19
13	8.48	0.04			

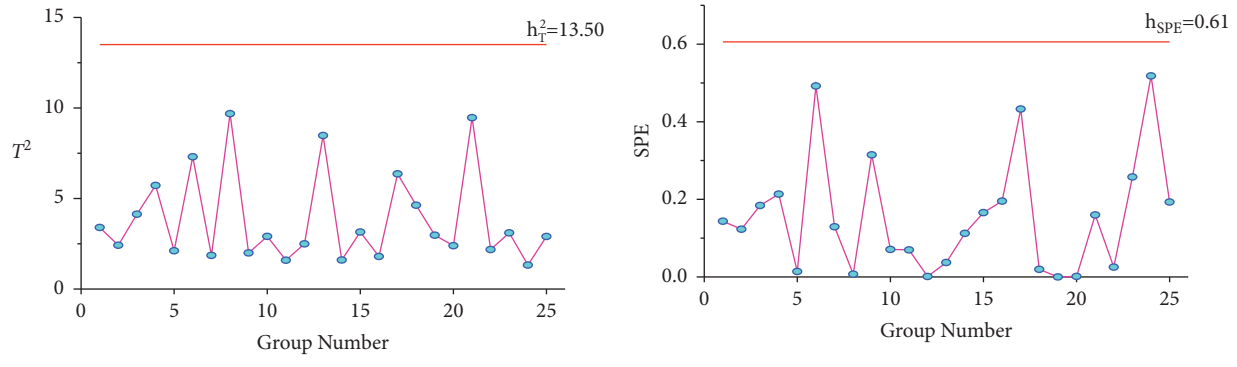

Figure 2: Continued.

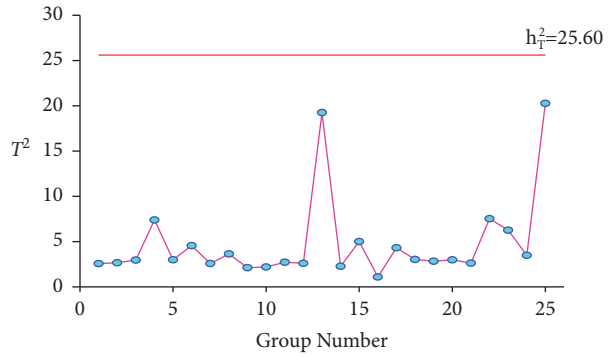

(c)

Figure 2: T^2 control chart and SPE control chart of catenary in normal states. (a) Principal component T^2 control chart; (b) SPE control chart; (c) conventional multiple T^2 control chart.

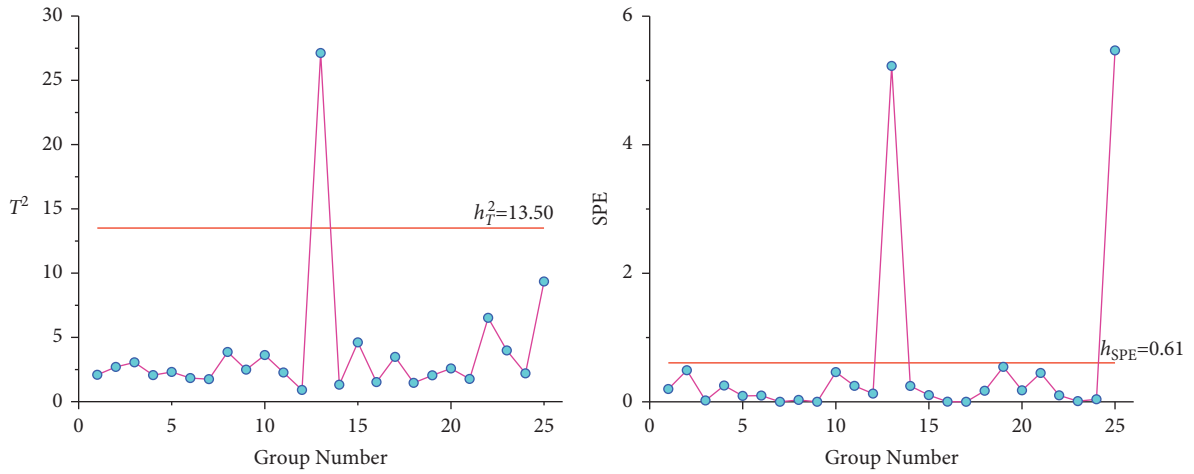

(a) (b)

Figure 3: T^2 control chart and SPE control chart of catenary in abnormal states. (a) Principal component T^2 control chart; (b) SPE control chart.

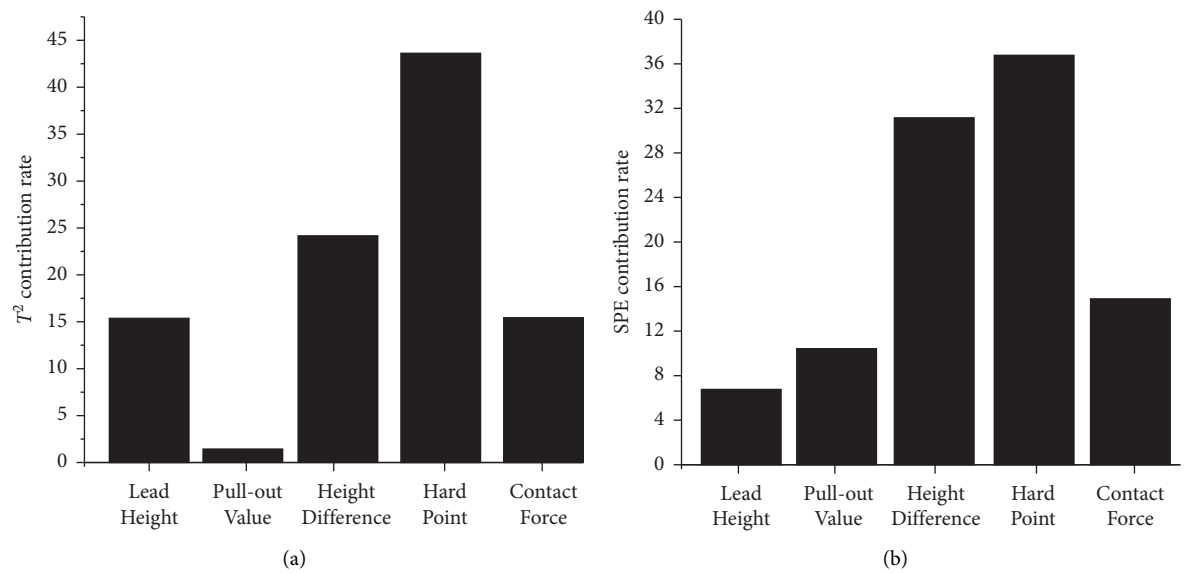

(a) (b)

Figure 4: Continued.

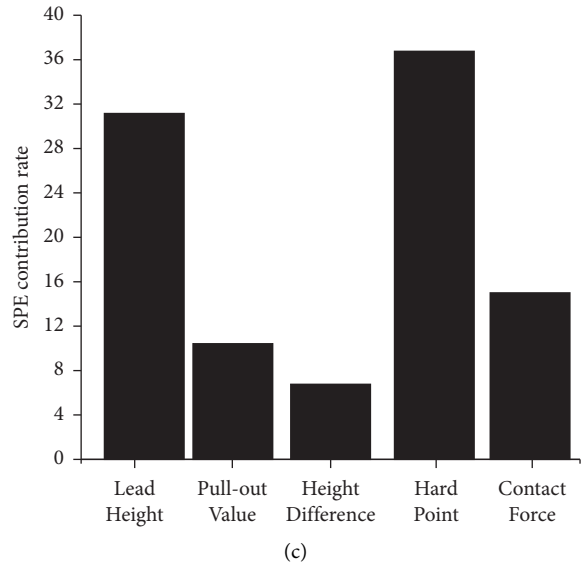

Figure 4: Contribution control chart of group 13 and group 25. (a) T^2 contribution rate chart of group 13; (b) SPE contribution rate chart of group 13; (c) SPE contribution rate chart of group 25.

changes in the principal component space, show the correlation within the data, but also find out the cause of the failure.

5. Conclusion

(1) The main component T^2 control chart can show the degree of fluctuation and deviation of the catenary status parameters. The residual SPE control chart can reflect the changes in the relationship of the catenary state parameters. The main component T^2 control chart and the residual SPE control chart of the catenary parameters can be used to evaluate the state of the catenary.

(2) The principal component T^2 control chart and the residual SPE control chart can convert the multidimensional detection parameters of the catenary into a statistic. It is displayed in the form of graphs, and the relationship between statistics and control limits is used to judge the status of the catenary. The method is simple and the result is intuitive.

(3) The contribution rate control chart can reflect the contribution degree of different parameters to the abnormal state on the basis of the main component T^2 control chart and the residual SPE control chart to realize the abnormal judgment of the catenary state. It can be used to determine the cause of the abnormal state of the catenary, so as to provide targeted guidance for the maintenance of the catenary.

Data Availability

The data sets used or analyzed during the current study are available from the corresponding author on reasonable request.

Conflicts of Interest

The authors declare that there are no conflicts of interest regarding the publication of this paper.

Acknowledgments

This work was supported by the research project of Guangzhou Metro Design and Research Institute Co., Ltd., under grant KY-2021-006.

References

[1] F. Lin, J. Luo, and Z. Li, "Statistical analysis of national electric traction power supply system failures in 2003 and 2004," *Gansu Science and Technology*, vol. 2006, no. 3, pp. 27-28, 2006.

[2] J. Zhou and C. Wu, "Analysis of high-speed railway catenary detection technology," *China High-Tech Enterprise*, vol. 23, no. 3, pp. 110-111, 2017.

[3] W. Zhou, Z. Sun, S. Ren et al., "Measuring method of geometric parameters of catenary based on multi-eye stereo vision," *China Railway Science*, vol. 36, no. 5, pp. 104–109, 2015.

[4] Z. Li, *Research on Non-contact Detection Technology of Catenary Parameters*, East China Jiaotong University, Nanchang, China, 2017.

[5] D. Zhu, "German catenary dynamic detection technology," *Electric Railways*, vol. 17, no. 3, pp. 13-14, 2004.

[6] X. Zhao, X. Wu, and G. Xu, "German high-speed railway catenary detection system," *China Railway*, vol. 38, no. 9, pp. 60–62, 2008.

[7] H. Bai, *Research on the Detection of Catenary Suspension Status of High-Speed Railway*, China Academy of Railway Sciences, Beijing, China, 2016.

[8] R. Zhang, Z. Liu, and Z. Yang, "Research on 6C system information comprehensive application technology scheme," *China Railway*, vol. 48, no. 6, pp. 44–50, 2018.

[9] R. Zhang and Z. Yang, "Research and practice of monitoring system for catenary operation state," *China Railway*, vol. 49, no. 9, pp. 64–70, 2019.

[10] Ministry of Railways of the People's Republic of China, *General Technical Specifications for the High-Speed Railway Power Supply Safety Detection and Monitoring System (6C System)*Power Supply Department, Beijing, China, 2012.

[11] China National Railway Group Co., Ltd, "The outline of the advanced railway planning for a powerful country in the new era," *People's Railway*, no. 2, 2020.

[12] National Development and Reform Commission, *Mid- to Long-Term Railway Network Planning*, National Development and Reform Commission, Beijing, China, 2016.

[13] China Railway Corporation, *High-speed Railway Catenary Technology*, China Railway Publishing House, Beijing, China, 2014.

[14] Q. Qian, S. Gao, Z. He, Q. Chen, and J. Wu, "Key technologies of traction power supply for high-speed railways in China," *China Engineering Science*, vol. 17, no. 4, pp. 9–20, 2015.

[15] J. Wang, "Research on determining the weights of influencing factors of catenary section quality evaluation based on analytic hierarchy process," *China Railway*, vol. 49, no. 4, pp. 60–64, 2019.

[16] H. Cheng, Z. He, H. Hu, B. Wang, and X. Sun, "Entropy weight multi-information comprehensive assessment of the health status of high-speed rail catenary," *Journal of the China Railway Society*, vol. 36, no. 3, pp. 19–24, 2014.

[17] Yi Yin, S. Gao, and M. Wang, "Feature extraction of catenary parameters of high-speed railway," *Electric Railways*, vol. 29, no. 5, pp. 29–32, 2018.

[18] S. Liu, X. Zhu, Y. Zhang, and L. Wu, "Research on the health status assessment of high-speed railway catenary based on grey clustering and combined weighting method," *Journal of the China Railway Society*, vol. 38, no. 7, pp. 57–63, 2016.

[19] D. Zhang, *High-speed Railway Catenary Status Assessment Based on Detection Parameters*, Southwest Jiaotong University, Chengdu, China, 2019.

[20] S. Liu, Z. Chou, and Z. Ma, "Comprehensive evaluation of catenary health status based on variable weight matter element extension model," *Journal of East China Jiaotong University*, vol. 36, no. 1, pp. 125–132, 2019.

[21] Ye Tian, *Application of Data Mining Technology in Data Processing of Catenary Detection*, Southwest Jiaotong University, Chengdu, China, 2005.

[22] H. Wang and K. Feng, "High-speed railway catenary system safety evaluation based on structural entropy weight method and cloud model," *China Railway*, vol. 49, no. 12, pp. 41–46, 2019.

[23] M. Zhang, H. Cheng, X. Wang, and Y. Li, "Evaluation of catenary operation status based on improved variable weight method and cloud model," *Journal of Railway Science and Engineering*, vol. 13, no. 5, pp. 964–970, 2016.

[24] D. Zhang, Z. Han, Z. Liu, S. Gao, and H. Wei, "Assessment of the health status of the high-speed rail catenary based on set pair analysis and evidence theory," *Journal of the China Railway Society*, vol. 42, no. 5, pp. 58–65, 2020.

[25] X. Xu and L. Ma, "Control chart recognition based on transfer learning and convolutional neural network," *Computer Applications*, vol. 38, no. S2, pp. 290–295, 2018.

[26] J. Zhao, "The application of statistics in quality control," *Statistics and Management*, vol. 35, no. 5, pp. 6-7, 2015.

[27] J. Jiang, X. Jiang, Y. Feng, and S. Deng, "Comparative study of multivariate statistical control charts," *Aviation Standardization and Quality*, no. 1, pp. 17–21, 2017.

[28] Y. Qin, H. Huang, F. Jian, and Y. Chen, "Transformer fault diagnosis based on FCM and improved PC," *High Voltage Apparatus*, vol. 54, no. 12, pp. 262–267, 2018.

[29] B. Wen, *Research on Fault Detection and Diagnosis Based on Principal Component Analysis*, Nanjing Normal University, Nanjing, China, 2011.

[30] C. Wen, F. Lv, Z. Bao, and M. Liu, "Overview of data-driven micro-fault diagnosis methods," *Acta Automatica Sinica*, vol. 42, no. 9, pp. 1285–1299, 2016.

[31] Y. Chang, S. Wang, F. Wang, and J. Fu, "Process monitoring method based on multi-PCA model," *Chinese Journal of Scientific Instrument*, vol. 35, no. 4, pp. 901–908, 2014.

[32] Z. Xiao and X. Ran, "Process control and diagnosis using principal component analysis," *Journal of Chongqing University of Technology (Natural Science)*, vol. 28, no. 1, pp. 96–101, 2014.

Hindawi
Advances in Civil Engineering
Volume 2021, Article ID 3606389, 9 pages
https://doi.org/10.1155/2021/3606389

Research Article

Selection of the Key Segment Position for Trapezoidal Tapered Rings and Calculation of the Range of Jack Stroke Differences with a Predetermined Key Segment Position

Wencui Zhang,[1] **Jian Zhang**,[1] **Jingru Yan**,[1] **and Yaohong Zhu**[2,3]

[1]*College of Civil Engineering and Architecture, Henan University of Technology, Zhengzhou, China*
[2]*School of Civil and Environmental Engineering, Ningbo University, Ningbo, China*
[3]*Collaborative Innovation Center of Coastal Urban Rail Transit, Ningbo University, Ningbo, China*

Correspondence should be addressed to Jian Zhang; 1214977789@qq.com

Received 3 November 2021; Accepted 8 December 2021; Published 24 December 2021

Academic Editor: Yuan Mei

It is generally accepted that selecting the key segment position for trapezoidal tapered rings and controlling the shield machine advancement are challenging tasks for shield tunneling projects. In this work, we propose a method for calculating the key segment position based on the shield tail gap, jack stroke difference, and lining trend. To calculate all possible key segment positions other than that corresponding to the straight joint configuration, the shield tail gap that remains after segment assembly and the jack stroke difference corresponding to the advancement of the segmental lining and lining trend were computed; then, values and importance coefficients were assigned to these factors according to current operating conditions. To ensure that the segmental lining can be assembled successfully with the calculated key position, we established a model to calculate the change in the shield tail gap before and after shield machine advancement based on the spatial relationships of the shield machine, the currently installed segmental rings, and the segment to be installed. Further, we propose a method for calculating the range of jack stroke differences when the predetermined "permitted shield tail gap" and key position are provided. The method is based on the change in the shield tail gap calculated with the above model and the positional relationship between the shield machine's actual axis and the designed tunnel axis after the current segmental ring has been assembled. The calculated range of jack stroke differences may then be used to control the advancement of the shield machine. We validated the viability of our methods by using the data of Phase 1 works on Line 2 of the Ningbo Rail Transit system.

1. Introduction

In the field of urban tunnel construction, shield tunneling has become the preferred method, as it causes minimal ground disturbance and allows for fast construction. The trapezoidal tapered ring is a tunnel lining method that is becoming increasingly popular because of its cost-effectiveness, simple construction, and adaptability for a wide range of radius curves [1]. However, a tapered ring has many potential key segment positions (or key positions), which makes their selection a challenging task. If the key positions are not selected correctly, the segments will not fit the designed tunnel axis. This can cause the shield machine to deviate from the designed tunnel axis or damage the segmental lining. In addition, the advancement of the shield machine directly affects segment installation. If the advancement of the shield machine is not controlled as per operating conditions, it may become impossible to install the segmental ring with its calculated key position, which will subsequently affect the quality of the construction. Therefore, studies on selecting the key position and controlling shield machine advancement with a predetermined key position are very important for engineering applications.

A number of important research findings have been obtained in China and abroad about the key position selection for trapezoidal tapered rings and shield machine advancement. In studies on technologies for the construction of tapered rings, Song used the least-squares method to

optimize the selection of the segment posture [2]. Li et al. created an algorithm for calculating the coordinates of the key position on planar and vertical curves, a bisection algorithm for calculating the ideal key positions of a tunneling route, and a computational geometry algorithm for a spatially arbitrary point rotating around an arbitrary axis [3]. Zhao et al. optimized the design of the ring thickness, overall ring deflection, ring segmentation/joint positioning, and segment assembly methods [4]. Song et al. analyzed the principles that underlie the design of ring segmentation, key position, and ring dimensions [5]. Zhang et al. used the coordinate system transformation theory to derive a method for segment typesetting that is based on the positional parameters of segment erectors in segment assembly processes [6]. Hu proposed a classification method based on a restrained support vector machine, which can regulate the position of the key segments by utilizing historic engineering data [7]. Zhang et al. calculated the advancement of the segmental lining in different directions and analyzed the influencing factors that need to be considered in the layout design for universal segmental lining combined with actual construction experience [8]. Besides, Li and He simulated segment lining with the beam-spring model and calculated loads acting on segment lining with the load-structure model [9]. Yang et al. chose three test sections with different geological conditions to study the segment internal force during the construction of the shield tunnel [10]. Chen and Mo analyzed a tunnel with 9 segment rings by the three-dimensional finite element method [11]. The loads include injected pressure, jacking force, and squeezing action of the tail of shield machine. The analytical results indicate that during the construction stage, the difference of loads along longitudinal direction causes various displacements and stress distributions in different segment rings.

In studies on shield machine advancement, Xu et al. developed a method for calculating the thrust force of Earth pressure balance (EPB) shield machines and investigated the factors that affect this force based on the excavation mechanisms of these machines [12]. Dai divided the total buoyancy force experienced by the rings behind the shield machine into static and dynamic components based on the assumptions of ideal simultaneous backfill grouting and negligible changes in grout characteristics [13]. The static component is generated by the envelopment of the liquid grout, while the dynamic component changes with the ground conditions and buried depth of the tunnel. Formulas to calculate these buoyancy force components were also derived. Li et al. experimentally studied how Earth pressures inside and outside the soil chamber are correlated with changes in the cutter disc torque and thrust, as well as factors that influence this correlation [14]. In addition, they studied the effects of the cutter disc's opening ratio on the total thrust of the shield machine and the torque of the cutter disc.

In addition to the above studies, a large amount of basic research has been performed on selecting segmental linings, calculating the key position, axial line fitting, and the mechanical properties of segmental linings [15–28]. Although a number of important results have been obtained, the vast majority of studies on tapered rings have focused on segment measurement, structural optimization, correcting the segment typesetting process, or the selection of segment types. Studies on controlling shield machine advancement have been relatively scarce.

In most of the above studies, the distance between the fitted center of the segment assembly plane and the target point of the designed tunnel axis was often the sole consideration to calculate the key position. Other operating conditions were simply overlooked. Furthermore, many of the proposed methods cannot fully prevent the occurrence of straight joints, which reduce the applicability of the calculated key position. Even after the key position of the segment to be installed has been determined, a mature and reliable method for controlling shield machine advancement toward the next segmental ring does not currently exist. Consequently, ring assembly in the calculated key position may be impossible under certain circumstances. In this work, we constructed a model for calculating the change in shield gap before and after shield machine advancement, and we propose a method for calculating the key position based on the shield tail gap, jack stroke difference, and lining trend. These methods are based on the spatial relationship between the shield machine, current segmental ring, and ring to be installed as well as a careful review of the existing literature. We also established a method for calculating the range of jack stroke differences for shield machine advancement to the next ring when the key positions are fully determined and a "permitted shield tail gap" has been defined. This method is based on the positional relationship of the shield machine's actual axis with the designed tunnel axis after the current ring has been assembled.

2. Calculation of Key Positions in Tapered Rings

2.1. Factors That Affect the Key Position Calculation. The shield tail gap, jack stroke difference, and lining trend were selected as the most important factors for calculating the key position based on actual field conditions and spatial relationships between the segmental lining, shield machine, and designed tunnel axis during shield machine advancement.

2.1.1. Shield Tail Gap. The segment is assembled into a ring at the shield tail and then ejected. However, the shield machine always deviates slightly during the tunneling process. Therefore, a gap between the shield housing and the outer surface of the segment (i.e., the "shield tail gap"), as shown in Figure 1, is necessary to ensure that the next ring can be safely assembled. The shield tail gap is defined as the shortest distance from the outer ring at the front end of the assembled segmental ring to the inner ring of the shield housing.

In theory, there is an ideal value for the shield tail gap in the top, bottom, left, and right directions. However, during the tunneling and assembly processes, the shield tail gap changes because of the jack stroke difference and advancement corresponding to each key position. The shield tail gap (a_2) after the segmental ring assembly consists of two parts: the shield tail gap of the previous segmented ring a_1 and the change in the shield tail gap d:

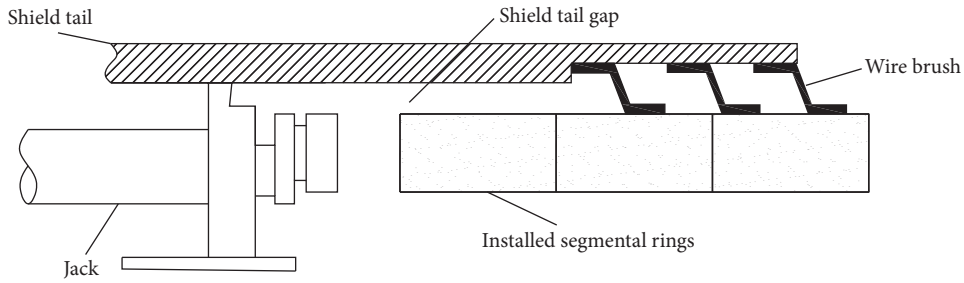

Figure 1: Schematic diagram of the shield tail gap.

$$a_2 = a_1 + d. \tag{1}$$

The total change in the shield tail gap d consists of changes in the shield tail gap that are caused by jack stroke differences d_1 and the key position of the segment to be installed d_2:

$$d = d_1 + d_2, \tag{2}$$

where

$$d_1 = \pm \frac{\Delta s B}{D_j}. \tag{3}$$

$$d_2 = \begin{cases} \pm \dfrac{\delta B}{2D_r} \cos\left[\dfrac{\pi}{8}\left(N_1 - 1\right)\right] \\ \pm \dfrac{\delta B}{2D_r} \sin\left[\dfrac{\pi}{8}\left(N_1 - 1\right)\right] \end{cases} \tag{4}$$

Here, Δs is the stroke difference of the jack (mm), B is the width of the segment (mm), D_j is the diameter of the jack (mm), D_r is the segment diameter (mm), δ is the taper of the tapered ring (mm), and N_1 is the key position of the segment to be installed. Equations (4) calculate the vertical and horizontal changes, respectively, in the shield tail gap. D_1 and d_2 are positive for shield tail gaps at the top and right sides of the segmental ring and negative for gaps at the bottom and left sides.

The shield tail gap of the previous segmental ring is obtained using an automated measurement system. The above equations are then used to calculate the postassembly shield tail gap. If the postassembly shield tail gaps in the top, bottom, left, and right directions are greater than permitted, this position may then be selected for ring assembly. If the postassembly shield tail gaps do not meet the above criterion, then this position cannot be selected for ring assembly.

2.1.2. Jack Stroke Difference. The jack stroke difference can vary significantly during the tunneling process of a shield machine. If the jack stroke difference is very large, the segmental rings will be subjected to excessively large force differentials, and the attitude of the shield machine also becomes difficult to control. Therefore, the effects of the jack stroke difference should be considered when selecting the key position for the next segmental ring. Because the advancement of the segmental ring (due to the selected key position) should match the intended advancement of the designed tunnel route, the advancement of each possible key position should be calculated in the horizontal and vertical directions by using (5) and (6), respectively. A threshold value may then be defined for the jack stroke difference according to the operating conditions. A key position should not be selected if the resulting postassembly stroke difference exceeds this threshold value.

$$\Delta r_v = -\delta \cos\left[\frac{\pi}{8}\left(N_1 - 1\right)\right], \tag{5}$$

$$\Delta r_l = \delta \sin\left[\frac{\pi}{8}\left(N_1 - 1\right)\right]. \tag{6}$$

2.1.3. Lining Trend. During the advancement of a shield machine, the assembled segments should fit the designed tunnel axis in both distance and angle. The lining trend is defined as the distance and angular deviations of the segment axis from the designed tunnel axis. Hence, the main objective when selecting the key position is to minimize the distance and angular deviations between the segment axis and the designed tunnel axis to ensure that the segmental rings are closely aligned with the latter axis.

It is easy to observe that distance deviations induced by the key position are equivalent to changes in the shield tail gap. Therefore, distance deviations can be calculated with equations (4). Angular deviations induced by the key position in the vertical and horizontal directions may be calculated with (7) and (8), respectively:

$$\arcsin\left\{\frac{\delta}{2D_r} \cos\left[\frac{\pi}{8}\left(N_1 - 1\right)\right]\right\} \approx \frac{\delta}{2D_r} \cos\left[\frac{\pi}{8}\left(N_1 - 1\right)\right], \tag{7}$$

$$\arcsin\left\{\frac{\delta}{2D_r} \sin\left[\frac{\pi}{8}\left(N_1 - 1\right)\right]\right\} \approx \frac{\delta}{2D_r} \sin\left[\frac{\pi}{8}\left(N_1 - 1\right)\right]. \tag{8}$$

Because the key position should be selected to minimize distance and angular deviations between the segment axis and designed tunnel axis, the lining trend needs to be minimized. This is performed by calculating and comparing the distance and angular deviations induced by different possible key positions in various practical settings.

2.2. Segment Position Selection and Software Development. Visual Basic was used to develop an automated position selection program to calculate key positions for segmental ring assembly. After the shield tail gap, jack stroke difference, and lining trend are measured or calculated, each candidate key position is assigned a value based on the principles of key position selection. This value indicates the "selectability" of a candidate key position according to the previously described conditions. Candidate key positions that are suitable for selection have a value of 1, while positions that cannot be selected have a value of 0.

2.2.1. Shield Tail Gap. The shield tail gaps are calculated in the top, bottom, left, and right directions after the assembly of the next segmental ring. If the gaps in all directions are greater than some defined limit, a value of 1 is then assigned to this candidate key position. If the gap in some direction is less than the limit, a value of 0 is then assigned to the candidate key position.

2.2.2. Jack Stroke Difference. The jack stroke differences are calculated in the horizontal and vertical directions after the assembly of the next segmental ring. If these stroke differences fall within a certain limit, a value of 1 is then assigned to the candidate key position; a value of 0 is assigned otherwise.

2.2.3. Lining Trend. Distance and angular deviations in the horizontal and vertical directions after the assembly of the next segmental ring are calculated. If the values of these deviations fall within a certain range of limits, a value of 1 is then assigned to the candidate key position; a value of 0 is assigned otherwise.

The above limits should be selected rationally according to actual operating conditions. In special circumstances (e.g., an excessively large jack stroke difference), a larger value should be assigned to the selectable key positions. This is because the attitude of the shield machine is very poor in this instance, and the jack stroke difference needs to be corrected in a timely manner. A larger value is thus assigned to the selectable key positions. In this case, all selection factors other than the jack stroke difference may be neglected until it has been reduced to an acceptable value.

Each candidate position has three assigned values V_{1i}, V_{2i}, and V_{3i}, which correspond to the shield tail gap, jack stroke difference, and lining trend, respectively. The overall value of each candidate position is the sum of these factors multiplied by their corresponding importance coefficients I_{1i}, I_{2i}, and I_{3i}.

The overall value of each position is

$$J_i = V_{1i}I_{1i} + V_{2i}I_{2i} + V_{3i}I_{3i}, \tag{9}$$

where J_i is the overall value of a candidate position; V_{1i}, V_{2i}, and V_{3i} are the values associated with the shield tail gap, jack stroke difference, and lining trend, respectively; I_{1i}, I_{2i}, and I_{3i} are the important factors associated with the shield tail gap, jack stroke difference, and lining trend, respectively; and i represents a candidate position.

The importance coefficients are selected as follows. The shield machine operator selects the importance coefficients of the factors according to his or her judgment of the current situation; certain factors may be assigned larger values if a problematic situation is encountered. For example, if the shield tail gap is currently very poor while the jack stroke difference and lining trend are satisfactory, a larger importance coefficient is assigned to the shield tail gap. The degree of importance, therefore, depends on the judgment and selection of the shield machine operator.

The above calculations can be used to calculate n selectable candidate key positions for the next segmental ring by using the key position of the previous segmental ring. The overall calculated values of these n positions are then compared, and the next ring is then assembled with the key position having the greatest overall value. The Visual Basic programming language was used to write a program that performs our key position calculations.

3. Calculating the Range of the Jack Stroke Differences in Tapered Rings

Even after the key positions are fully determined, assembling the segments in the calculated key positions during the tunneling process may not be possible, or the segments may simply break after being assembled. This is caused by a lack of theoretical research on the advancement of shield machines toward the next ring. To address this issue, we propose a method for controlling the advancement of a shield machine by calculating the range of Jack stroke differences needed to reach the next ring.

3.1. Calculation of the Shield Tail Gaps before and after Shield Machine Advancement. The shield tail gap is the most important factor for determining whether a segment can be assembled successfully. If the shield tail gap is too small, the shield tail will interfere with the segment during shield machine advancement. A minimal level of interference will increase resistance against the advancement of the shield machine, whereas a severe level of interference can lead to dislocations or damage in the segmental ring that will subsequently induce tunnel leakage or surface settlement. Because the shield tail gap has a significant impact on the advancement process, this factor was selected as the controlling index for calculating Jack stroke differences.

3.1.1. Shield Tail Gap after the Current Ring Has Been Released from the Shield Tail at the End of the Shield Machine's Advancement. Figure 2 illustrates the calculation of the shield tail gap after a segmental ring is released at the end of the shield machine's advancement. The contact between the installed segmental ring and jack is the datum plane, and the manually measured shield tail gap of the previous segmental ring after the advancement of the shield machine is a_1. If the shield tail gap after the current segmental ring is released from the tail is a_3 and all shield machine displacements

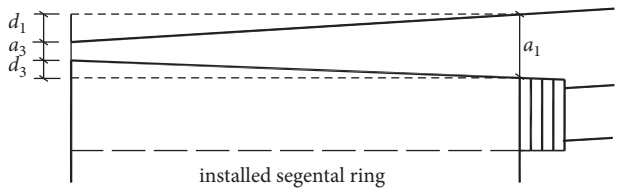

Figure 2: Diagram of the shield tail gap upon the release of a segmental ring at the end of the shield machine's advancement.

caused by other factors are negligible, the following equation may then be obtained from the geometric relationship between the shield machine and segmental lining:

$$a_3 = a_1 - d_1 - d_3, \tag{10}$$

where d_1 is calculated from Equation (3) and d_3 is the change in the shield tail gap caused by the installed segmental ring. The vertical and horizontal components of this change may be calculated using equation (11), respectively:

$$d_3 = \begin{cases} \pm \dfrac{\delta B}{2D_r} \cos\left[\dfrac{\pi}{8}\left(N_1 - 1\right)\right] \\ \\ \pm \dfrac{\delta B}{2D_r} \sin\left[\dfrac{\pi}{8}\left(N_1 - 1\right)\right] \end{cases}, \tag{11}$$

where N_2 is the key position of the installed segment. All other symbols retain their previous definitions.

3.1.2. Shield Tail Gap at the Segment after the Next Segmental Ring Has Been Fully Assembled. Further constraints may be applied to the jack stroke difference by considering the shield tail gap after the next segmental ring has been assembled. The shield tail gap after the assembly of the next segmental ring (a_2) can be calculated using equations (1)–(4).

The vertical top-side shield tail gap is taken as an example here. Substituting (3) and (11) into (3) and (10) and (4) into (1) yields

$$a_3 = a_1 - \Delta s \frac{B}{D_j} - \frac{\delta B}{2D_r} \times \cos\left[\frac{\pi}{8}\left(N_1 - 1\right)\right], \tag{12}$$

$$a_2 = a_1 + \Delta s \frac{B}{D_j} + \frac{\delta B}{2D_r} \times \cos\left[\frac{\pi}{8}\left(N_1 - 1\right)\right]. \tag{13}$$

3.2. Calculating the Range of Jack Stroke Differences with Predetermined Key Positions. A reasonable range of values for the shield machine's jack stroke difference may be acquired by applying constraints based on the shield tail gap. Determining the range of jack stroke differences is effectively a method for controlling shield machine advancement that is compatible with segment typesetting schemes.

Boundary conditions are added to (12) and (13). The shield tail gap when the current ring is released from the shield tail (a_3) and the shield tail gap after the next segmental ring is assembled (a_2) should not be smaller than ε (i.e., $a_2 = a_3 \geq \varepsilon$). By setting $a_2 = a_3 = \varepsilon$, the range of the jack stroke difference Δs, which is represented by $[x_1, x_2]$, may then be calculated with equations (12) and (13). The minimum requirements of the upper shield tail gap on the top side are satisfied when $\Delta s \in [x_1, x_2]$. The range of Δs for the shield tail gap on the bottom side, which is represented by $[x_3, x_4]$, may be calculated in the same way. The results of $[x_1, x_2] \cap [x_3, x_4]$ are then denoted as $[x_{\min}, x_{\max}]$. When all other factors are negligible, $[x_{\min}, x_{\max}]$ is the vertical range of jack stroke differences that satisfies the minimum shield tail gap. Similarly, the horizontal range of jack stroke differences that satisfies the minimum shield tail gap may be calculated by using the minimum shield tail gaps on the right and left sides of the shield tail.

To further minimize the calculated range of jack stroke differences, the positional relationship between the actual axis of the shield machine and the designed tunnel axis needs to be considered. The initial stroke difference in the vertical direction after the current segmental ring is assembled is denoted as Δs_0, and the height deviations of the shield machine and shield tail are denoted as h_1 and h_2, respectively. These height deviations are positive if the shield machine is above the designed tunnel axis and negative if the shield machine is below the designed tunnel axis. The goal is to keep the shield machine moving along the direction of the designed tunnel axis.

When $\Delta s_0 \in [x_{\min}, x_{\max}]$, the following values define the vertical range of jack stroke differences that satisfies the minimum shield tail gap:

When $h_1 < h_2$, $\Delta s \in [x_{\min}, \Delta s_0]$;

When $h_1 > h_2$, $\Delta s \in [\Delta s_0, x_{\max}]$;

When $h_1 = h_2$,

If $h_1 > 0$ and $h_2 > 0$, then $\Delta s \in [\Delta s_0, x_{\max}]$;
If $h_1 < 0$ and $h_2 < 0$, then $\Delta s \in [x_{\min}, \Delta s_0]$;
If $h_1 = h_2 = 0$, then $\Delta s = \Delta s_0$.

If $\Delta s_0 \notin [x_{\min}, x_{\max}]$, the requirements of the shield tail gap need to be prioritized to ensure that the segmental lining does not break or crack. Hence, the constraints imposed by the need to fit the designed tunnel axis are abandoned in this instance, and the value of Δs_0 remains within $[x_{\min}, x_{\max}]$.

The range of jack stroke differences in the horizontal direction may be calculated in a similar manner. The Visual Basic programming language was used to write the software for calculating the range of Jack stroke differences.

4. Case Study

4.1. Project Overview. Project TJ2101 (Phase 1 in Line 2 of the Ningbo Rail Transit system) covers the section from Lishe Station up to Yinzhou Avenue Station. Shield tunneling was used to construct this section. The design lengths of the up and down lines were 1463.318 and 1445.695 m, respectively. The running tunnel has a minimum buried depth of 5.8 m and a maximum buried depth of 21.6 m. Most of the tunnel is situated in (2) 2 gray silty clay, (4) 1 silty clay, (5) 1 clay, and (5) 1a sandy silt clay. The soil layers are therefore weak and unstable, so they are prone to uneven settlement and large deformations.

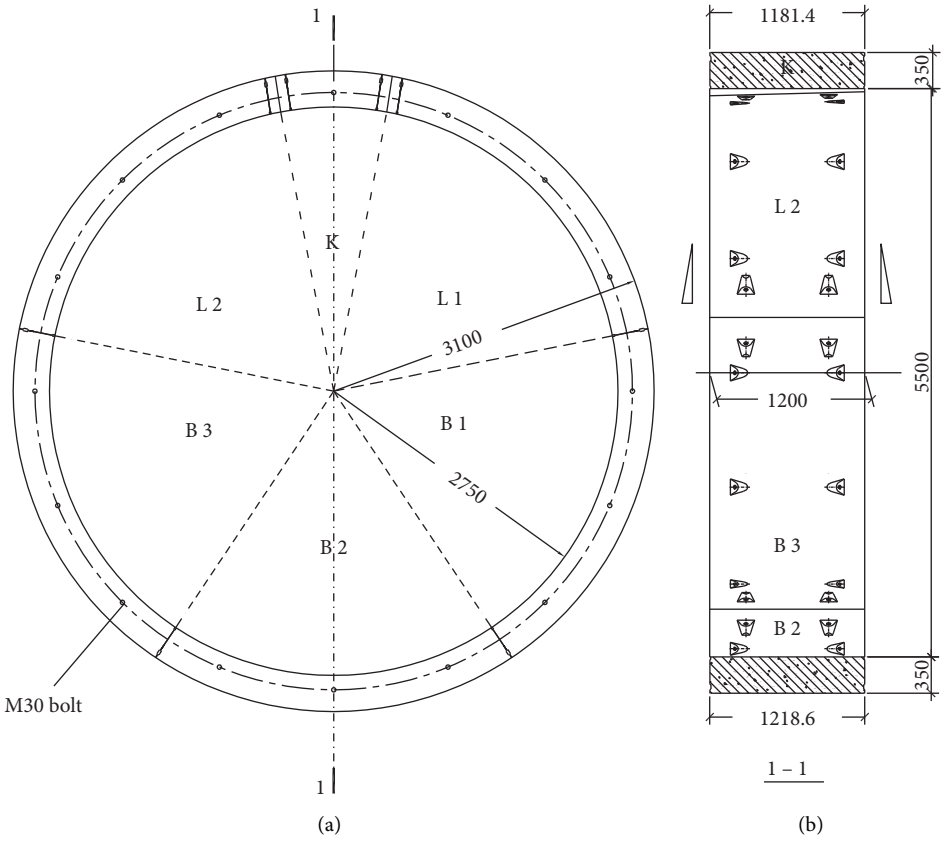

Figure 3: Schematic of a tapered ring (dimensions: mm). (a) Front view and (b) sectional view.

A Komatsu TM634PMX shield machine (Japan) was used for this project. This shield machine has a length of 8680 mm and an outer diameter of 6340 mm. The jack group consists of 22 cylinders and has a diameter of 5850 mm. The tapered ring has an inner diameter of 5500 mm, an outer diameter of 6200 mm, a thickness of 350 mm, and an annular width of 1200 mm. The segments were designed as doubly tapered segments with a maximum taper of 37.2 mm and a tapering angle of $20'37.59''$ for each segment. Each segmental ring was composed of six segments: one key segment (F), two countersegments (L1, L2), and three regular segments (B1, B2, B3). Each ring had a total of 16 possible key positions for segment assembly, and a tongue and groove construction was used for the joints of the segmental ring. The structure of the segmental ring is shown in Figure 3.

4.2. Example of Key Position Selection. The key positions selected by our program and actually selected during the project were compared. Twenty-five samples from a linear section of the down line were used, which corresponded to rings 104–116 and 129–140. This area of the tunnel was mainly excavated in a single stratum of (2) 2 gray silty clay, and no damage or leakage was observed in these 25 segmental rings. This implies that the shield machine operator chose the key positions of these segmental rings in a rational manner according to all operating conditions and factors. These selections may therefore be used as a reference for comparison. The data input and parameter configuration interfaces are shown in Figures 4 and 5, respectively. Table 1 compares the actual key positions with those selected by our program.

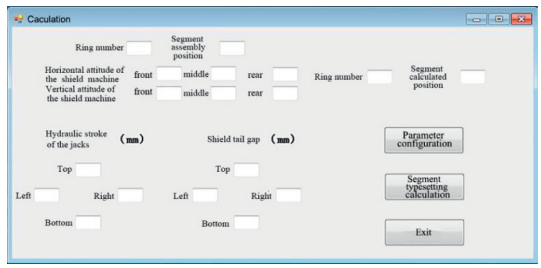

Figure 4: Data input interface.

The key positions computed by our program for these 25 segmental rings are very similar to the key positions that were actually selected. There are 17 instances where the same position was selected, which accounts for 68% of all selections. Therefore, the results of our program are highly reliable. Because the importance coefficients of the shield tail gap, jack stroke difference, and lining trend were set to 1 : 3 : 2 in all of the calculations, some of the calculated positions significantly differed from the actual positions used for segment assembly. Therefore, the importance coefficients need to be chosen according to the actual operating conditions prior to each calculation.

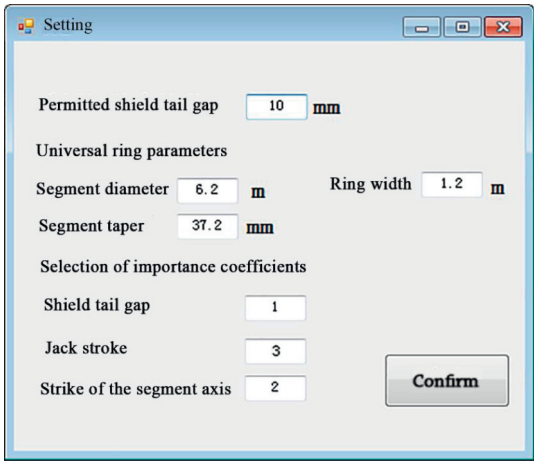

Figure 5: Parameter configuration interface.

Table 1: Comparison of the calculated and actual positions for segment assembly.

Ring number	104	105	106	107	108	109	110	111	112
Actual key position	13	5	13	5	13	5	13	11	13
Calculated key position	13	5	7	5	7	5	13	5	13
Ring number	113	114	115	116	129	130	131	132	133
Actual key position	5	3	5	13	5	13	5	13	15
Calculated key position	11	13	5	13	14	13	5	13	15
Ring number	134	135	136	137	138	139	140		
Actual key position	13	5	13	5	7	5	13		
Calculated key position	13	11	13	5	7	5	16		

4.3. Example Calculation for the Range of Jack Stroke Differences. In this case, the key position of the ring currently being assembled was assumed to be Position 5, while Position 13 was predicted to be the key position for assembling the next ring. The current shield tail gap (which may be measured by using a specialized instrument or manual measurements) was 20 mm on the top, 30 mm on the bottom, 18 mm on the left, and 33 mm on the right. The permitted shield tail gap was set to 10 mm. The current stroke difference of the shield machine was 15 mm in the horizontal direction and −20 mm in the vertical direction. The horizontal and vertical deviations in the attitude of the shield machine were 5 and −15 mm, respectively, at the cutter head and 15 and −30 mm, respectively, at the shield tail. Figure 6 shows the calculated range of jack stroke differences for a permitted shield gap of 10 mm. These ranges were 49 mm to −20 mm in the vertical direction and 15–56 mm in the horizontal direction. These ranges are clearly too large to be of any use for shield machine operators. This is because the attitude of the shield machine is currently in a good state, and the permitted shield tail gap was too small. Consequently, the range of jack stroke differences was not restricted in a meaningful manner. This calculation was therefore performed again with an adjustment to the permitted shield tail gap.

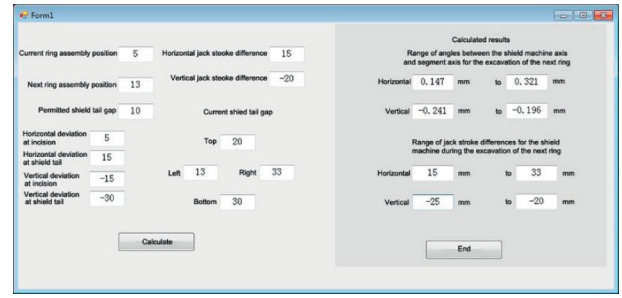

Figure 6: Calculated range of jack stroke differences when the permitted shield tail gap is 10 mm.

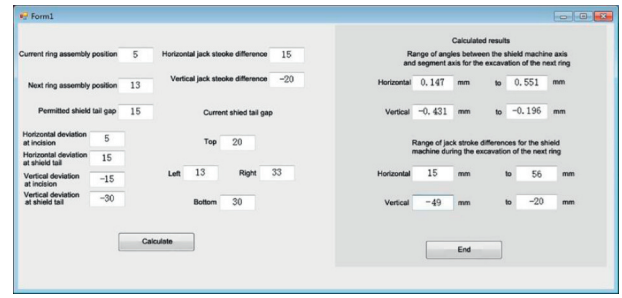

Figure 7: Recalculated range of jack stroke differences when the permitted shield tail gap is adjusted to 15 mm.

The permitted shield tail gap was adjusted to 15 mm, and the recalculated range of jack stroke differences is shown in Figure 7. The results were −25 to −20 mm in the vertical direction and 15–33 mm in the horizontal direction. The range of stroke differences was significantly reduced compared to the previous example, and this range is sufficiently precise for practical applications.

The case study showed that the calculated range of stroke differences is closely related to the permitted shield tail gap. Hence, the shield machine operator should select a suitable permitted shield tail gap according to the actual project conditions. The attitude of the shield machine may then be maintained in a good state by the operator using the range of jack stroke differences calculated by the program to control the advancement of the shield machine.

5. Conclusion

Based on a review of previous relevant studies, we propose a method for key position selection based on the shield tail gap, jack stroke difference, and lining trend. We also constructed a method for calculating the range of jack stroke differences with predetermined key positions and a user-defined permitted shield tail gap to ensure that a segmental ring can be safely installed in the calculated key position. Comparisons with a case study showed that the calculation results of our method are highly reliable.

Our automated key position selection program (based on our algorithm) accounts for the impacts of the three

most important factors for shield tunneling, and the importance coefficients of these factors can be adjusted according to actual operating conditions. This program is therefore viable for practical applications. When the program was used in an engineering application, the importance coefficients of the shield tail gap, jack stroke difference, and lining trend were found to affect the quality of the calculated results to some extent. Therefore, the shield machine operator should select importance coefficients for each factor according to the actual operating conditions.

The range of jack stroke differences was calculated by using the shield tail gap as the controlling index. The calculated ranges based on the permitted shield tail gap are sufficiently precise for practical applications, and the calculations are straightforward to perform. In the validation experiment, the range of jack stroke differences corresponding to a permitted shield tail gap of 10 mm was very large. Increasing the shield tail gap to 15 mm significantly reduced the range of Jack stroke differences to be sufficiently precise for practical requirements, which proved the viability of this method. Therefore, the permitted shield tail gap needs to be selected according to actual operating conditions in practical applications.

Segment floating often occurs during shield construction, especially under the condition of crossing soft soil layer. In this paper, we do not consider the influence of the segment floating on the key position selection as well as the calculation of jack stroke differences. This point will be studied with an emphasis on our future research.

Data Availability

All the data used to support the findings of this study are included within the article.

Conflicts of Interest

The authors declare that there are no conflicts of interest regarding the publication of this paper.

Acknowledgments

The research was financially supported by the Natural Science Project of Henan University of Technology (31401085) and the Basic Scientific Research Special Funds of Provincial Colleges and Universities (2017QNJH06).

References

[1] S. A. M. U. E. L. Swartz, S. H. I. M. I. Tzobery, and B. Gary, "Trapezoidal tapered ring-key position selection in curved tunnels," in *17th Rapid Excavation and Tunneling Conference. Seattle WA:Society for Mining, Metallurgy and Exploration*, pp. 957–969, San Diego, California, USA, June 2005.

[2] S. O. N. G. Ruiheng, *Development of Software for Composition and Dynamic Deviation Correction of Universal Segments for Shield Tunnel*Shanghai Jiao Tong University, SHANG HAI, 2008.

[3] L. I. Weiping and Z. H. E. N. G. Guoping, "Study on core algorithm of typesetting system for universal wedge segments of shield tunnels," *Modern Tunnelling Technology*, vol. 45, no. 5, pp. 34–37, 2008, 43.

[4] Z. H. A. O. Guoxu and H. E. Chuan, "Tunneling lining segment design optimization analysis," *China Railway Science*, vol. 24, no. 6, pp. 61–66, 2003.

[5] S. O. N. G. Chenghui, "Study on structure design for universal shield segments of metro in soft soil," *Chinese Journal of Underground Space and Engineering*, vol. 7, no. 4, pp. 733–740, 2011.

[6] Z. H. A. N. G. Wencui, M. U. Shixu, L. I. Jiatao, H. Changming, and W. Kai, "Research on layout design and deviation correction of the general segment in shield tunnels," *Construction Technology*, vol. 42, no. 13, pp. 89–92, 2013.

[7] H. U. Min, H. A. N. Zhanwei, S. U. N. Xiangyang et al., "Key position selection in universal trapezoidal tapered rings of shield tunnels," *Modern Tunnelling Technology*, vol. 46, no. 5, pp. 13–18, 2009, 22.

[8] Z. H. A. N. G. Zhihua, Z. H. U. Guoli, and L. O. N. G. Si, "Study on calculating method for composition of segments for shield tunnels," *Chinese Journal of Underground Space and Engineering*, vol. 9, no. 5, pp. 1040–1044, 2013, 1086.

[9] L. I. Wei and H. E. Chuan, "Study on mechanical behavior and controlling assembling modes of universal segment lining for shield tunnel," *Journal of the China Railway Society*, vol. 29, no. 2, pp. 77–82, 2007.

[10] Y. A. N. G. Guangwu, L. I. Xinggao, W. U. Xiaojun et al., "Study of the segment internal force during the construction of shield tunnel," *China Railway Science*, vol. 30, no. 3, pp. 57–62, 2009.

[11] C. H. E. N. Junsheng and M. O. Haihong, "Three-dimensional finite element analysis of mechanical behaviors of shield tunnel segment during construction," *Chinese Journal of Rock Mechanics and Engineering*, vol. 25, no. Supplement 2, pp. 3482–3489, 2006.

[12] X. U. Qianwei, Z. H. U. Hehua, L. I. A. O. Shaoming et al., "Analysis of reasonable thrust force during tunnel excavation in homogeneous soft ground by use of earth pressure balance shield machine," *Chinese Journal of Geotechnical Engineering*, vol. 30, no. 1, pp. 79–85, 2008.

[13] D. A. I. Zhiren, "The mechanism and control principle of upward movements of sements at the rear of shield tail," *China Railway Science*, vol. 34, no. 1, pp. 59–66, 2013, Chinese.

[14] L. I. Xianghong and F. U. Deming, "Experimental study on excavation behavior using model EPB shield with a diameter of 1.8 m," *Chinese Journal of Geotechnical Engineering*, vol. 28, no. 9, pp. 1101–1105, 2006, Chinese.

[15] L. I. Yujie, H. E. Ping, and Q. I. N. Dongping, "Force analysis of segment for shield tunnel based on elastoplastic damage constitutive model of concrete," *China Railway Science*, vol. 33, no. 1, pp. 47–53, 2012.

[16] L. I. U. Chun, J. I. N. G. Yi, W. A. N. G. Xiexian et al., "Rings prediction model inconstruction of long-distance tunnel shield and its computer system realization," *Journal of Geodesy and Geodynamics*, vol. 28, no. 6, pp. 112–116, 2008.

[17] P. E. N. G. Zhiyong, L. I. U. Weining, D. I. N. G. Deyun, and X. Yang, "Experimental study on the mechanical properties of the interface on partitioned key segment of large-diameter shield tunnel," *China Railway Science*, vol. 34, no. 5, pp. 39–45, 2013.

[18] G. U. A. N. Linxing, "Effect of segment width on behavior of shield tunnel assembled in staggered pattern," *Chinese Journal*

of Underground Space and Engineering, vol. 11, no. 4, pp. 852–858, 2015.

[19] Z. H. A. N. G. Heng, C. H. E. N. Shougen, T. A. N. Xinrong, and Z. Yubao, "Research on mechanical behaviour of segmental structure of shield tunnel in different strata," *Chinese Journal of Underground Space and Engineering*, vol. 11, no. 4, pp. 845–851, 2015.

[20] Y. A. N. Jingru and Z. H. A. N. G. Wencui, "Study on the calculation of position selection of universal ring segment in shield tunneling construction," *Chinese Journal of Underground Space and Engineering*, vol. 15, no. S2, pp. 577–582, 2019.

[21] F. E. N. G. Tianwei, Z. H. O. U. Jiamei, Z. H. A. N. G. Jun et al., "Research on risk assessment system of segments dislocation in metro tunnel," *Chinese Journal of Underground Space and Engineering*, vol. 13, no. 4, pp. 1066–1072, 2017.

[22] R. U. A. N. Chengzhi, "Research on the analysis method for segment layout in shield tunnelling," *Modern Tunnelling Technology*, vol. 58, no. 4, pp. 224–228, 2021.

[23] W. U. Haibin, H. E. Chuan, Y. A. N. Qixiang et al., "A study on curve fitting algorithm of curved shield tunnels assembled by universal wedge segments and its application," *Journal of the China Railway Society*, vol. 38, no. 10, pp. 90–98, 2016.

[24] H. U. Changming, Z. H. A. N. G. Wencui, M. E. I. Yuan et al., "Calculation of jack stroke difference range and advancing control of shield machine under known point position of universal ring segment," *China Railway Science*, vol. 36, no. 3, pp. 51–57, 2015.

[25] P. A. N. Guorong and R. O. N. G. Yifu, "Simplified calculation of general segment composition and correction control," *Journal of Geodesy and Geodynamics*, vol. 34, no. 1, pp. 55–58, 2014.

[26] X. U. Chong, "Research on the mechanical behavior of shield lining on granular soil across yellow river," *Journal of Railway Engineering Society*, vol. 37, no. 6, pp. 64–69, 2020.

[27] H. U. A. N. G. Kan, S. U. N. Yiwei, Z. H. A. O. Lei et al., "Mechanical properties of segments when shield passes through upper-soft and lower-hard composite strata," *Journal of Central South University*, vol. 51, no. 5, pp. 1371–1383, 2020.

[28] D. O. N. G. Xiuzhu, Z. H. U. Zhankui, S. O. N. G. Xiaolong et al., "Study on calculation method of the deviation of lining ring axis for shield tunnel," *China Civil Engineering Journal*, vol. 52, no. S2, pp. 149–154, 2019.